Extreme Wave Loads on Monopiles: Identification, Reproduction and Detailed Investigation

Ghadirian, Amin

Publication date:
2018

Document Version
Publisher's PDF, also known as Version of record

Extreme Wave Loads on Monopiles: Identification, Reproduction and Detailed Investigation

Department of Wind Energy PhD Report 2018

Amin Ghardirian

DTU Wind Energy PhD-0092(EN)
DOI number:10.11581/dtu:00000041

October 2018

DTU Wind Energy
Department of Wind Energy

Authors: Amin Ghadirian

Title: Extreme Wave Loads on Monopiles: Identification, Reproduction and Detailed Investigation

Department: Wind Energy

2018

Project Period:

1 November 2015 – 31 October 2018

Education:

PhD

Supervisor:

Professor Henrik Bredmose

DTU Wind Energy is a department of the Technical University of Denmark with a unique integration of research, education, innovation and public/private sector consulting in the field of wind energy. Our activities develop new opportunities and technology for the global and Danish exploitation of wind energy. Research focuses on key technical-scientific fields, which are central for the development, innovation and use of wind energy and provides the basis for advanced education.

DTU Wind Energy has a staff of approximately 240 and a further 35 PhD-students, spread across 38 different nationalities. The variety of research, education, innovation, testing and consultancy is reflected in the employment profile which includes faculty with research and teaching responsibilities, researchers and technical academic staff, highly skilled technicians and administrative staff.

Our facilities are situated at DTU Risø Campus and at DTU Lyngby Campus. Furthermore the department is running the national test stations in Høvsøre and Østerild.

Technical University of Denmark
Department of Wind Energy
Frederiksborgvej 399
Building 118
4000 Roskilde
Denmark

www.vindenergi.dtu.dk

Extreme Wave Loads on Monopiles: Identification, Reproduction and Detailed Investigation

by
Amin GHADIRIAN

Submitted to the Department of Wind Energy in partial fulfillment of the requirements for the degree of

Doctor of Philosophy

in the

Department of Wind Energy
Technical University of Denmark

Supervisor:
Prof. Henrik BREDMOSE
October 31, 2018

Preface

This thesis is submitted in partial fulfilment of the *Doctor of Philosophy* degree from the Technical University of Denmark. The work is performed at the Fluid Mechanics Section of Department of Wind Energy at the Technical University of Denmark, in the period November 2015 to October 2018.

The focus of the study is extreme wave loads on monopiles, while it investigates the subject in three themes of identification, reproduction and detailed investigation. The work is divided into two main parts. In the first part an extensive introduction is given to each discipline of extreme wave loads on monopiles and in the second part six papers, looking into each branch, are presented.

The study has been performed under the supervision of professor Henrik Bredmose. This work was funded by the Innovation Fund Denmark and other partners as part of DeRisk project with grant number 4106-00038B.

Amin Ghadirian

October 2018, Copenhagen

Acknowledgements

Firstly, I would like to thank my supervisor, Professor Henrik Bredmose. Without his help, guidance and support I would have not been able to finish this work. I also am very grateful for his patience in explaining and discussing many subjects that he taught me during these last three years. Professor Harry Bingham has been very helpful with note on calculations in OceanWave3D and open to discussions and understandings of the results. In addition, I would like to thank Professor Emeritus Jørgen Juncher Jensen and Ju Hyuck Choi for their help about the application of reliability methods and interpretation of related results. Bjarke Larsen and Xerxes Mandviwalla have helped me a lot with the OpenFOAM calculations. Their help is gratefully appreciated. I am also very grateful for professor Paul Taylor's and associate professor Thomas Adcock's very helpful discussions on wave physics, harmonic separation and for hosting me in Oxford University. I am very grateful for the welcome and help I received during the stay.

I am very thankful of the support that I received while doing this work in the Fluid Mechanics Section of Wind Energy Department. This work was funded by the Innovation Fund Denmark and other partners as part of De-Risk project with grant number 4106-00038B. This support is gratefully acknowledged. The partners of this project are also thanked for numerous useful discussions.

I am also grateful for the support and love my friends and my amazing girlfriend Gesine Wanke have given me. Finally, I would like to thank my family. They have believed in me and supported me my whole life and for that and for their love I am extremely grateful.

Abstract

This thesis focuses on the extreme wave loads on monopiles from three different perspectives. Namely, reproduction, identification and local flow investigation of such wave impacts. A state of the art CFD model is used in addition to a fully nonlinear potential flow solver to validate cases compared to experimental measurements. The validation cases include breaking focused waves with and without directional spreading in different depths. Good consistency between the measurements and numerical results is found for the free surface elevation, in-line force and wave-induced pressures. The wave-structure interaction including the secondary load cycle and wave scattering around the structure are well reproduced using the coupled solver. The validation is then extended to the measured wave episodes which are associated with the two largest peak moments of a 3 hour test. It is observed that for small values of the inline force, the CFD results provides good agreement with the measurements. For the larger values of inline force, however, the consistency decreases largely due to different breaking processes in the numerical domain relative to the experiments. In addition, the vastly validated models are then used to investigate the source of the secondary load cycle and to demonstrate the applicability of an analytical slamming wave load model.

The well known pressure impulse theory is used to calculate the slamming wave load for an incompressible and inviscid fluid. The geometry of the impacting wave is simplified as a block of water in Cartesian coordinates and as a wedge in cylindrical coordinates. The pressure impulse on a vertical flat plate and on a vertical circular cylinder is next calculated as analytical solutions to the Laplace equation. Parameter studies are performed for each case of slamming wave impact on a flat plate in the 3D domain and on a monopile. The results of the parameter studies clarify the behaviour of the pressure impulse distribution in relation to each parameter including the length of the impacting water block and the diameter of the cylinder. The pressure impulse distribution of a slamming wave on a monopile in the state of the art CFD model is compared to the results from the suggested model and good consistency is observed.

To identify the expected extreme wave episodes that creates a target inline force on the monopile the First Order Reliability Method is used in combination with first- and second-order wave theories and Morison type force models. The calculated expected extreme wave episodes are validated against experiments and a good agreement is observed. Such wave episodes can be used in the design process for the Ultimate Limit State cases. The method is extended to incorporate a fully nonlinear potential flow solver (OceanWave3D) for the incident wave kinematics. Significant improvement relative to first-order and second-order results is observed. The average deviation between the model results and the wave averaged measurements is about 10In

addition to the applicability of this method to extreme wave episode identification, it has the benefit of flexibility with topography of the bed. Hence, the effect of the bed slope on extreme wave episodes is investigated by combination of FORM and the nonlinear potential flow solver. It is observed that in the low Ursell number cases, force histories are very similar between flat bed and sloped bed. However, in the high Ursell number cases, larger skewness is observed in inline force time histories for flat bed. The exceedance probabilities for the same peak inline force are larger on sloped bed cases. The investigation is the most systematic investigation of the bed slope influence on the extreme wave loads to the author's knowledge.

The source of the Secondary Load Cycle is studied in large extends. The source of this event, which has been a matter of speculation for some time, is important for reduction of uncertainties in load calculation as some researchers claim that it can contribute to ringing of the structure. To conduct the investigation experimental and numerical results were extensively studied. Especially the state of the art CFD model is used to separate each important term in the momentum equation that creates the secondary load cycle. A thorough explanation for the source of the secondary load cycle is given which relates this phenomena to a suction region below the water column created behind the cylinder by diffraction as the outer wave disappears. The suction is created by the need for a sudden downward acceleration of the column. The author considers this part of the thesis the most detailed investigation of secondary load cycle event to date.

Dansk Resumé

Nærværende afhandling omhandler ekstreme bølgelaster på monopæle med fokus på reproduktion, identifiktation og detaljeret analyse af lokale strømningsfænomener. En state-of-the-art CFD model, koblet med en fuldt ikke-lineær potentialmodel benyttes og valideres mod eksperimentelle målinger. Valideringen inkluderer fokuserede brydende bølger med og uden retningsspredning på varierende dybder. Der er opnået god konsistens mellem de eksperimentelle og numeriske resultater for overfladeelevation, in-line kraft og bølge-inducerede tryk. Også bølge-struktur-interaktionen inklusiv den sekundære last-cyklus og diffrakterede bølger er reproduceret med god nøjagtighed i den koblede løser. Valideringen udvides efterfølgende til målte bølgeepisoder, der fører til de største momenter ved havbunden i en tre-timers test. For små værdier af inline-kraften er CFD resultaterne i god overensstemmelse med målingerne. For større værdier af inline-kraften falder nøjagtigheden på grund af forskelle i brydningsprocessen, numerisk og eksperimentelt. Den validerede, koblede model bruges efterfølgende til at undersøge årsagen til den sekundære last-cyklus og til at påvise anvendeligheden af en analytisk slamming last model.

Den velkendte impuls–tryk teori benyttes til at beregne slamming lasten for et inkompressibelt og inviskost bølge-anslag. Geometrien af den anslående bølge approximeres som en rektangulær blok i Kartesiske koordinater og som en kile i cylindriske koordinater. Impulstryklasten for en vertikal plade og en vertikal cylinder beregnes dernæst gennem analytiske løsninger til Laplace ligningen. Modellens parametre undersøges for både 3D blok- og monopæl-konfigurationen. Afhængigheden af blokkens længde og monopældiameter belyses og modellen valideres succesfuldt mod resultater fra en CFD model.

Formen af bølgeepisoder der producerer en givet in-linekraft er identificeret gennem kombineret anvendelse af FORM (First-Order Reliability Method) metoden, første- samt anden-ordenskinematik og Morisons ligning. De fundne bølgeepisoder er valideret med god overensstemmelse mod ensemble-midlede eksperimentelle resultater. Bølge-episoder af denne type er velegnede til design for ULS (Ultimate Limit State) bølger. Metoden er udvidet til fuldt ikke-lineær kinematik fra OceanWave3D bølgemodellen med god forbedring i forhold til første- og anden-ordens resultaterne. Den gennemsnitlige afvigelse mellem de numeriske og eksperimentelt midlede resultater er omkring 10

Udover identifikation af ekstreme bølge-episoder, giver metoden mulighed for anvendelse på forskellige bund-variationer. Dette udnyttes til at undersøge effekten af bundhældning for de ekstreme bølge-episoder. For små værdier af Ursell-parameteren er tidshistorierne for kraft meget ens. For store Ursell-parametre ses en større vertikal asymmetri (skewness) i krafthistorierne for flad bund. Overskridelsessandsynligheden for fastholdt peak

kraft er større for skrå bund end for flad bund. Studiet udgør efter forfatterens overbevisning den mest systematiske undersøgelse af effekten af bundhældning på ekstrembølgelaster.

Årsagen til den sekundære last-cyklus er undersøgt i stor detalje. Dette har været et emne med en del spekulation gennem de sidste årtier og er vigtigt i forhold til at reducere usikkerhederne i lastberegninger, idet nogle forskere mener at det kan bidrage til ringing-effekter for offshore-strukturer. En omfattende analyse af eksperimentelle og numeriske resultater er foretaget. Specielt er en state-of-the-art CFD model blevet anvendt til at separere de enkelte led i momentumligningen der danner den sekundære last-cyclus. En tilbundsgående forklaring på last-cyclens dannelse er opnået. Last-cyclen skyldes et undertryk, der dannes på bagsiden af cylinderen når den ydre bølge forsvinder og efterlader en søjle af vand skabt af diffraktionseffekter. Undertrykket skabes af den pludselige nødvendige nedad-rettede acceleration af vandsøjlen. Denne del af afhandlingen udgør efter forfatterens overbevisning det mest detaljerede studie af den sekundære last-cyklus til dato.

Contents

Preface iii

Acknowledgements v

Abstract vii

Dansk Resumé ix

I Overview and summary 1

1 Introduction 3
1.1 Motivation and Objectives . . . 7
1.2 Thesis structure . . . 9

2 Field overview 13
2.1 Wave models and hydrodynamic load calculations . . . 13
2.2 CFD modelling of water waves impact on surface piercing cylinders . . . 17
2.3 Expected extreme wave episodes . . . 19
2.4 The effect of the bed slope . . . 20
2.5 The source of the Secondary Load Cycle . . . 21
2.6 Slamming wave loads . . . 21

3 Theoretical background 27
3.1 Linear wave theory . . . 27
3.2 Irregular waves . . . 28
3.3 New Wave . . . 32
3.4 Linear wave maker theory . . . 32
3.5 Second order contributions . . . 34
3.6 First order reliability method . . . 35

4 Numerical methods 41
4.1 Fully nonlinear potential flow solver (OceanWave3D) . . . 41
4.2 Two-phase incompressible Navier-Stokes solver (waves2Foam) . . . 43
4.3 Coupled OceanWave3D-waves2Foam . . . 44

5 Summary of the papers 47

II Papers **53**

1 Breaking phase focused wave group loads on offshore wind turbine monopiles **55**

2 Extreme wave impacts on monopiles: re-analysis of experimental data by a coupled CFD solver **69**

3 Prediction of the shape of inline wave force and free surface elevation using First Order Reliability Method (FORM) **85**

4 Investigation of the effect of the bed slope on extreme waves using First Order Reliability Method **107**

5 Detailed force modelling of the secondary load cycle **145**

6 Pressure impulse theory for a slamming wave on a vertical circular cylinder **179**

Part I

Overview and summary

Chapter 1

Introduction

The biggest challenge facing the human species is currently the environmental risk from the global warming. The most effective solution scientists have come up with is to limit the fuel consumption as much as possible and replace the non-renewable energy resources with renewable forms such as solar, hydro-power and wind energy. This transition from the fuel sources of energy to clean energy also creates many new jobs and is positively influential on the economy in the international scale (Ferroukhi et al. 2017). Hence, the Danish government, for example, has set national targets of meeting 50% of Denmark's energy demand by renewable energy in 2030 and becoming independent of fossil fuels by 2050 (International Energy Agency 2017).

One of the fastest growing renewable energy forms during the last decade has been wind energy as shown in figure 1.1. Wind energy is also the natural candidate for the transition to renewable energy resources in Denmark's climate. In Denmark the average wind speed onshore at a height of 100 meters is between 6 and 10 m/s while the average offshore wind speed is between 9 and 11 m/s. Highest wind speeds occur at the western coasts. In 2012, Denmark set a goal so that by 2020, 50% of electricity consumption should be supplied by wind power. Wind energy was already providing 42% of the electricity consumption in 2016 and is expected to provide 48% of the electricity by 2020 (International Energy Agency 2017). So it is anticipated that

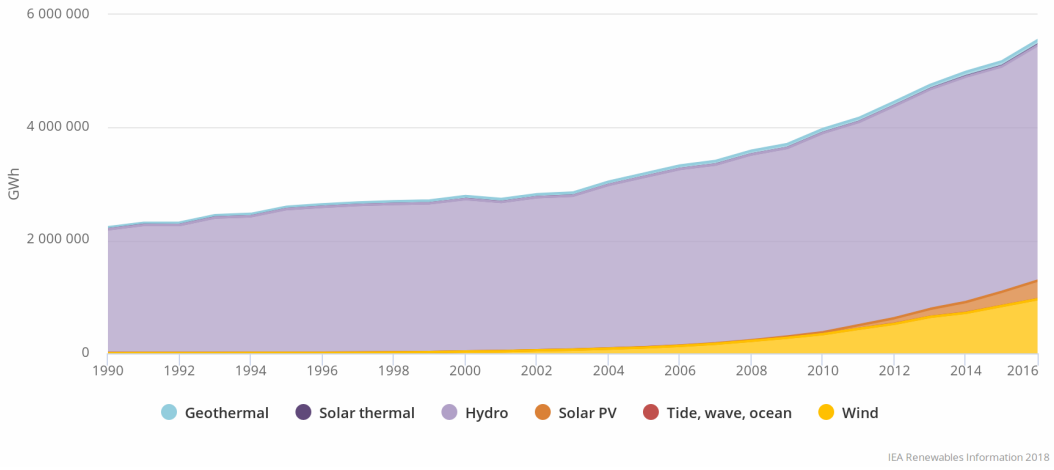

FIGURE 1.1: Electricity generation from renewables by source. World 1990 - 2016 (International Energy Agency 2018).

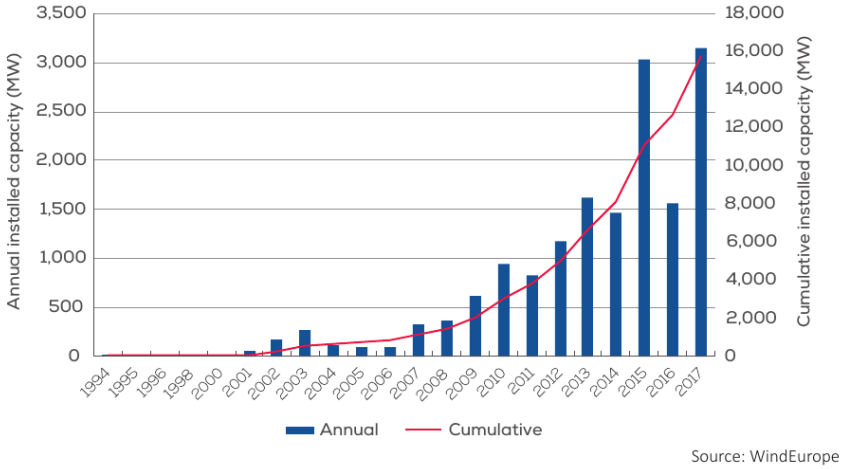

FIGURE 1.2: Cumulative and annual offshore wind energy installation (Wind Europe 2018)

wind energy continues to be the primary renewable energy resource in Denmark. In 2015, the Danish Energy Agency performed sensitivity analyses, which demonstrated that it is technically possible to design energy systems, consisting of only renewable energy forms, largely wind-based, independent of fossil fuels (International Energy Agency 2017).

There is a larger potential capacity in offshore because of uninhabited body parts and higher average wind speeds. In addition, the wind climate is more stable offshore. Larger wind turbines and wind farms can be installed offshore and there are fewer or no restrictions from municipalities and neighbouring citizens. Denmark has more than 7300 km of coastline with low average sea depth which is ideal for offshore wind energy. Data from the last few years show that the interest in offshore wind energy is increasing more rapidly than onshore wind energy (REN21 2017). Figure 1.2 shows the annual offshore wind energy installed capacity since 1994. The recent years data also show that the cost of offshore is decreasing in the Danish market which is tender driven.

Between the different designs of foundations for offshore wind turbines monopiles are the most commonly used type because of the simplicity in design and production. Monopile foundations are circular tubes hammered into the sea bed piercing the surface of water. A transition piece at the top of the monopile connects the monopile and the wind turbine tower. Mass production of monopile foundations is uncomplicated, which makes monopiles the most cost efficient type of foundation for offshore wind turbines at depth up to 40 m. In figure 1.3 the share of different substructure types for grid-connected wind turbines up to 2017 is shown. More than 80% of the grid-connected offshore wind turbines are installed on monopiles.

One disadvantage of the monopile foundations is their small structural stiffness and structural damping because of their slender shape. To increase the stiffness in larger water depth (longer monopiles), the diameter should be increased which implies more expensive substructures. Hence, the use of

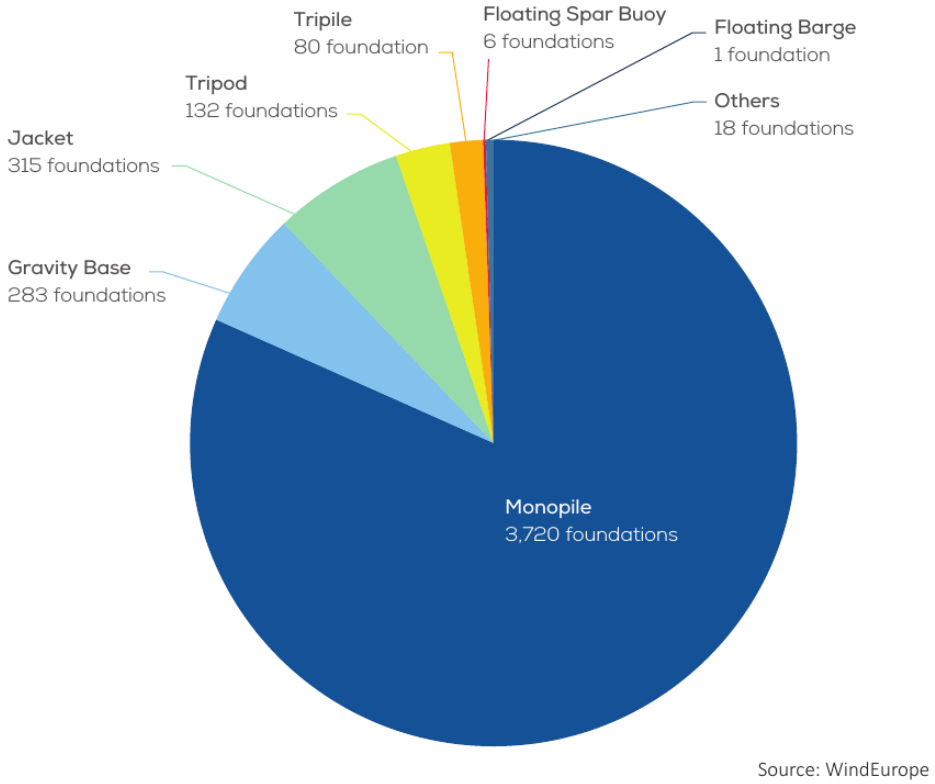

FIGURE 1.3: Share of substructure types for grid-connected wind turbines (units) (Wind Europe 2018).

monopile foundations is limited to water depths of $h < 30 - 40m$. At deeper water the jacket foundation is a suitable alternative to the monopile because of its large structural stiffness. Complicated production process, which includes significant amount of high quality welding, makes mass production of jacket structures difficult.

The average water depth and distance to shore of offshore wind farms under construction during 2017 is shown in figure 1.4. Most of the offshore wind farms under construction in 2017 are going to be installed in depth of 30 - 40 m. Because of increasing cost of the foundation and installation, it is anticipated that future offshore wind turbines will be placed at intermediate and shallow water depths as long as there are suitable areas at these depths to be exploited. Therefore, the monopile foundations will remain the most used type of foundation for several years to come. Thus in this thesis, wave loads on bottom mounted surface piercing circular cylinder, with properties similar to the monopile foundation is investigated.

The monopiles of offshore wind turbines are exposed to highly non-linear hydrodynamic loads from intermediate and shallow water waves including breaking waves. The wave load on offshore monopiles are of most importance during violent storms, when the largest wave forces are expected and the wind turbine is parked so there is no aerodynamic damping and the structure is practically un-damped. At these conditions, large wave impacts, lay a real risk to the safety of the monopile (Kuik et al. 2016). Therefore,

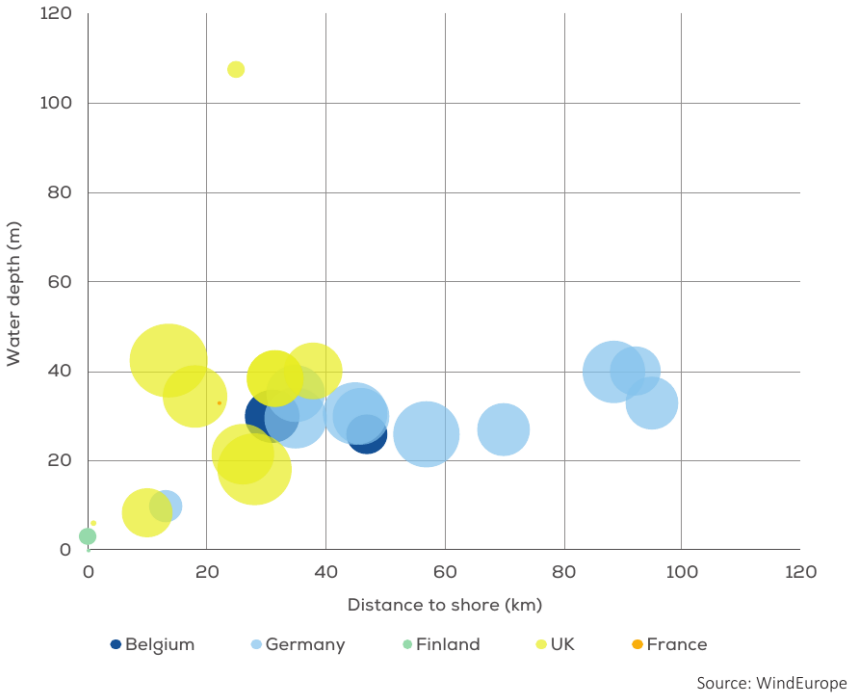

FIGURE 1.4: Average water depth and distance to shore of offshore wind farms under construction during 2017. The size of the bubble indicates the overall capacity of the site (Wind Europe 2018).

extreme waves and the associated Ultimate Limit State (ULS) loads can be determining for the design parameters of the monopile.

To reduce the cost of offshore wind energy Megavind (2013) identified improved design models with lowered risk and uncertainty as a key element. In addition, the foundations of offshore wind turbines typically make out 20% of the total cost of energy (Technology Innovation Needs Assessment (TINA) 2012). Hence, reduction in uncertainties of monopile design can play an important role in the offshore wind energy cost reduction. By reduced risk and uncertainty, over-engineered design can be avoided, less raw material would be used in the production and the cost-efficiency of the substructures would improve.

The currently common methods used in the industry for wave load prediction on offshore wind support structures is described in the *IEC 61400-3* (2009) design code among other handbooks. The methods are originated in the deep-water oil and gas industry assuming a flat bed. In these methods extreme waves are represented by simplistic regular wave solutions. The physical effects of wave non-linearity, 3D effects and wave-current interaction are, therefore, excluded from these methods. The load calculations in these methods are largely based on the assumption that the extreme wave loading is associated with the highest wave. However, recently an increasing awareness within the offshore industry has come up that the largest wave-induced load is not necessarily associated with the largest wave but is greatly influenced by wave steepness, non-linearities and breaking. These effects are

not included in the common engineering models. Therefore, more advanced methods such as CFD and reliability methods can be used to predict and reproduce the waves which pose the largest loads on the structures.

In the recent years the ringing response of the monopile structures has caught attention as a possible threat to offshore wind turbines which can damage them drastically (Grue 2013). As the size of the wind turbines increases the foundation diameter increases and there is a bigger concern about ringing. Unfortunately not only there is no engineering model for this phenomena, the physics of it is also unknown to a great extent. Hence, there is an urgent need for clarification of the increased ringing risk and for validated engineering models that can possibly predict the local nonlinear loading on the cylinder.

1.1 Motivation and Objectives

This thesis aims to satisfy five needs.

1. Further validation of efficient yet accurate numerical wave load models are needed in order to spread their usage in the industry. Such models can help to reduce the uncertainties in the design process of foundations for offshore wind turbines and ultimately decrease the cost of offshore wind energy.

2. A more generalized extreme wave event is needed in the design process that is not limited to the first order phase focused linear waves or the stream function waves with symmetric shape. New Wave (Tromans, Anatruk, and Hagemeijer 1991) has been used as the extreme wave event in the design process of offshore wind turbines while it suffers from simplicity. More accurate expected extreme waves for given exceedance probabilities are needed to reduce the uncertainty of the design process in the ULS cases.

3. The effect of the bed slope on the extreme waves and their probability needs to be investigated as laboratory tests are often done at a too strong slope. It is important to account for the bed slope in the design process of the ULS cases.

4. Deeper knowledge about wave impacts on surface piercing circular cylinders, the local nonlinear events around the cylinder and the secondary load cycle (Grue, Bjørshol, and Strand 1994) is needed. The secondary load cycle might contribute to ringing in the foundation of offshore wind turbines in some cases. Knowledge about the source of the secondary load cycle is needed to eventually develop force models which include its effects.

5. An engineering slamming wave load model is needed in the design process that focuses on the pressure impulse. The commonly used models focus on the maximum force due to the slamming waves and

the force time series while pressure impulse is usually a more important parameter in calculating the response of the structure.

In this thesis significant contributions to the aforementioned needs are made.

Further validation of a state of the art CFD model The coupled OceanWave3D and waves2Foam package (Paulsen 2013) is used to reproduce phase focused waves in intermediate water depth. Waves2Foam is a package wrapped around the InterFoam solver of OpenFOAM for easy generation of surface waves in relaxation zones close to the boundaries (Jacobsen, Fuhrman, and Fredsøe 2012). InterFoam uses a volume of fluid (VOF) method to treat the free surface flows (Hirt and Nichols 1981). The solver has been previously verified against experimental measurements, convergence has been proven by grid refinement towards a fully nonlinear analytical solution by Paulsen, Bredmose, and Bingham (2012) and Paulsen (2013). The domain decomposed model presented by Paulsen (2013) is used in several new cases to validate this model further for the case of breaking focused waves with and without directional spreading in different depths. In addition, the numerical solver is used to investigate the source of the secondary load cycle and validate the analytical slamming wave load model. An extensive emphasis is given to utilization of the state-of-the-art CFD for each phenomena of interest.

Expected extreme wave episodes The First Order Reliability Method (FORM) wrapped around the first order Airey theory and the second order Sharma and Dean (1981) theory is used to find the expected wave that creates a target inline force on the monopile. FORM has been previously used in determination of the wave with a target crest height, known as the New Wave, analytically (Tromans and Suastika 1998) and to find the wave creating a certain response of offshore structures in the sea (Jensen and Capul 2006; Jensen 2007; Jensen 2008). However, to the author's knowledge it has not been used to find extreme waves in terms of inline force on a monopile using first and second order wave models. The developed method is validated against experiments and a good agreement is shown. The method can be used in the design process in the ULS cases where usually linear New Wave or stream function waves are used. The method is then extended to include the fully nonlinear potential flow solver OceanWave3D. Such a model can include different topographies which may be crucial to take into account in the design process.

The effect of the bed slope The extended model of FORM around the fully nonlinear potential flow solver, OceanWave3D, is then used to investigate the effect of bed slope on the extreme waves in relation to inline force on a monopile. The results are validated against measurements on a flat and sloped sea bed and the exceedance probabilities are compared between the model results and the experiments and between model results on sloped versus flat sea bed. This is a unique method that allows us to investigate the

differences in the time and frequency domain and calculate the exceedance probability for each target force in each sea state. This method responds to the need of systematic investigation of the bed slope on the extreme waves since such investigation is not found in the literature.

The source of the Secondary Load Cycle The origin of the local event called the Secondary Load Cycle is still unresolved and has until now remains a matter of discussion. The secondary load cycles is seen by some researchers as a strong indicator of a "ringing" event. Understanding this phenomenon is important for reduction of uncertainties and risks related to offshore wind energy. We use experimental and simulation results extensively and perform detailed analysis to separate the flow in different terms and identify the source of the secondary load cycle. A thorough explanation for the source of the secondary load cycle is given in this thesis. The author considers this part of the thesis as the most detailed investigation of secondary load cycles event and a major contribution to the ongoing discussion about the nature of this phenomenon.

Slamming wave load model based on pressure-impulse An analytical breaking wave load model is presented based on the pressure impulse model ofy Cooker and Peregrine (1995) for calculating the pressure impulse on a flat plate. The theory is extended to calculate the pressure impulse on a cylinder. The commonly used analytical breaking wave models such as Goda, Haranaka, and Kitahata (1966) and Wienke and Oumeraci (2005) estimate the peak slamming force and the duration of the breaker effect on the cylinder. In many cases the exact force history is less important for the excitation of high-frequency modes of the structure than the integrated effect. Yet, the distribution in space is still needed. This motivates the development of such a pressure impulse model for steep breaking wave loads on a vertical cylinder. The presented model, therefore, responds to the need of a breaking load model that includes the pressure impulse instead of impulsive force history.

1.2 Thesis structure

The thesis is divided into two parts. In Part I an overview and summary of the thesis is given while Part II consists of a collection of six papers. In the first part a general overview of the research context, motivation and objectives and the structure of the thesis has been presented in Chapter 1. In Chapter 2 a short background of the addressed needs and the current state of the art is provided. The used background theory and numerical methods are presented in Chapter 3 and Chapter 4. The important results and a brief summary of each paper is presented in Chapter 5. The six papers are appended in Part II.

References

Cooker, Mark J. and Howell Peregrine (1995). "Pressure-impulse theory for liquid impact problems". In: *Journal of Fluid Mechanics* 297, p. 193.

Ferroukhi, Rabia et al. (2017). *Renewable Energy and Jobs: Annual Review 2017*. Tech. rep. International Renewable Energy Agency, p. 16.

Goda, Yoshimi, Suketo Haranaka, and Masaki Kitahata (1966). *Study on impulsive breaking wave forces on piles*. Tech. rep. 5, pp. 1–30.

Grue, John (2013). *Windmills at sea can break like matches*.

Grue, John, Gunnhild Bjørshol, and Øivind Strand (1994). "Nonlinear wave loads which may generate "Ringing" responses of offshore structure". In: *Workshop on Water Waves and Floating Bodies*.

Hirt, C. W and B. D Nichols (1981). "Volume of fluid (VOF) method for the dynamics of free boundaries". In: *Journal of Computational Physics* 39.1, pp. 201–225.

IEC 61400-3 (2009).

International Energy Agency (2017). *Energy Policies of IEA Countries - Denmark Review*. Tech. rep. International Energy Agency (IEA), p. 213.

— (2018). *IEA Statistics*.

Jacobsen, Niels Gjøl, David R Fuhrman, and Jørgen Fredsøe (2012). "A wave generation toolbox for the open-source CFD library: OpenFoam". In: *International Journal for Numerical Methods in Fluids* 70.9, pp. 1073–1088.

Jensen, J. Juncher (2008). "Extreme value predictions and critical wave episodes for marine structures by FORM". In: *Ships and Offshore Structures* 3.4, pp. 325–333.

Jensen, Jørgen Juncher (2007). "Efficient estimation of extreme non-linear roll motions using the first-order reliability method (FORM)". In: *Journal of Marine Science and Technology* 12.4, pp. 191–202.

Jensen, Jørgen Juncher and Julien Capul (2006). "Extreme response predictions for jack-up units in second order stochastic waves by FORM". In: *Probabilistic Engineering Mechanics* 21.4, pp. 330–337.

Kuik, G. A. M. van et al. (2016). "Long-term research challenges in wind energy – a research agenda by the European Academy of Wind Energy". In: *Wind Energy Science* 1.1, pp. 1–39.

Megavind (2013). *The danish wind power hub*. Tech. rep. Megavind, pp. 1–52.

Paulsen, Bo Terp (2013). "Efficient computations of wave loads on off shore structures". PhD thesis.

Paulsen, Bo Terp, H Bredmose, and H B Bingham (2012). "Accurate computation of wave loads on a bottom fixed circular cylinder". In: *International Workshop on Water Waves and Floating Bodies* m, pp. 137–140.

REN21 (2017). *Renewables 2017: global status report*. Tech. rep. Renewable Energy Policy Network for the 21st century (REN21).

Sharma, Jagat N. and Robert G. Dean (1981). "Second-Order Directional Seas and Associated Wave Forces." In: *Society of Petroleum Engineers journal* 21.1, pp. 129–140.

Technology Innovation Needs Assessment (TINA) (2012). *Technology Innovation Needs Assessment (TINA) Offshore Wind Power Summary Report*. Tech.

rep. February 2012. Low Carbon Innovation Coordination Group, pp. 1–18.

Tromans, P S and I K Suastika (1998). *Spectral response surfaces, designer waves and the ringing of offshore structures*.

Tromans, Peter S, A R Anatruk, and Paul Hagemeijer (1991). "A New Model for the Kinematics of Large Ocean Waves Application as a Design Wave". In: *Proceedings of the First International Offshore and Polar Engineering Conference* 8.August, pp. 64–71.

Wienke, J. and H. Oumeraci (2005). "Breaking wave impact force on a vertical and inclined slender pile - Theoretical and large-scale model investigations". In: *Coastal Engineering* 52.5, pp. 435–462.

Wind Europe (2018). "Offshore Wind in Europe Offshore Wind in Europe". In:

Chapter 2

Field overview

Monopiles are frequently exposed to stormy climate in the open sea. During storms wind turbines are parked and the aerodynamic damping is absent. Hence, the extreme wave loads play an important role in the Ultimate Limit State (ULS) strength calculations of the structure. In this chapter an overview over the ULS calculations is given. The chapter is divided into five sections and in each section the current common practice and the latest advancements in the subject is presented.

2.1 Wave models and hydrodynamic load calculations

The current recommended practice for calculation of hydrodynamic loads, including the ULS cases, is presented in *IEC 61400-3* (2009). The first step to calculate the hydrodynamic loads is to choose the appropriate wave model. The different wave theories provide approximate solutions to the same differential equations and boundary conditions with different accuracies. Figure 2.1 shows the wave diagram proposed as a guideline for wave theory selection. The horizontal and vertical axis in the diagram are the normalized depth and wave height. As shown in this diagram breaking criteria changes for shallow and deep water as for a deep water wave the wave steepness mostly defines if a wave breaks, $H/L \gtrapprox 0.14$, while in shallow water the ratio of the wave height to the water depth is critical $H/d \gtrapprox 0.78$. Here H is the wave height, L is the wave length, d is the water depth, T is the wave period and g is the gravitational constant.

If the linear wave theory is selected to calculate the wave kinematics, stretching methods such as Wheeler or Delta method should be used to calculate the kinematics from the still water level to the free surface. The Morison's equation (Morison 1953) is used to calculate the hydrodynamic forces from the wave kinematics calculated from the appropriate wave theory. The Morison's equation for a static member is:

$$F = \frac{1}{2} C_D \rho D |U| U + C_M \rho A \dot{U} \tag{2.1}$$

where F is the force per unit length of the member, C_D is the drag coefficient, C_M is the inertial coefficient, ρ is the density, D is the member diameter, A

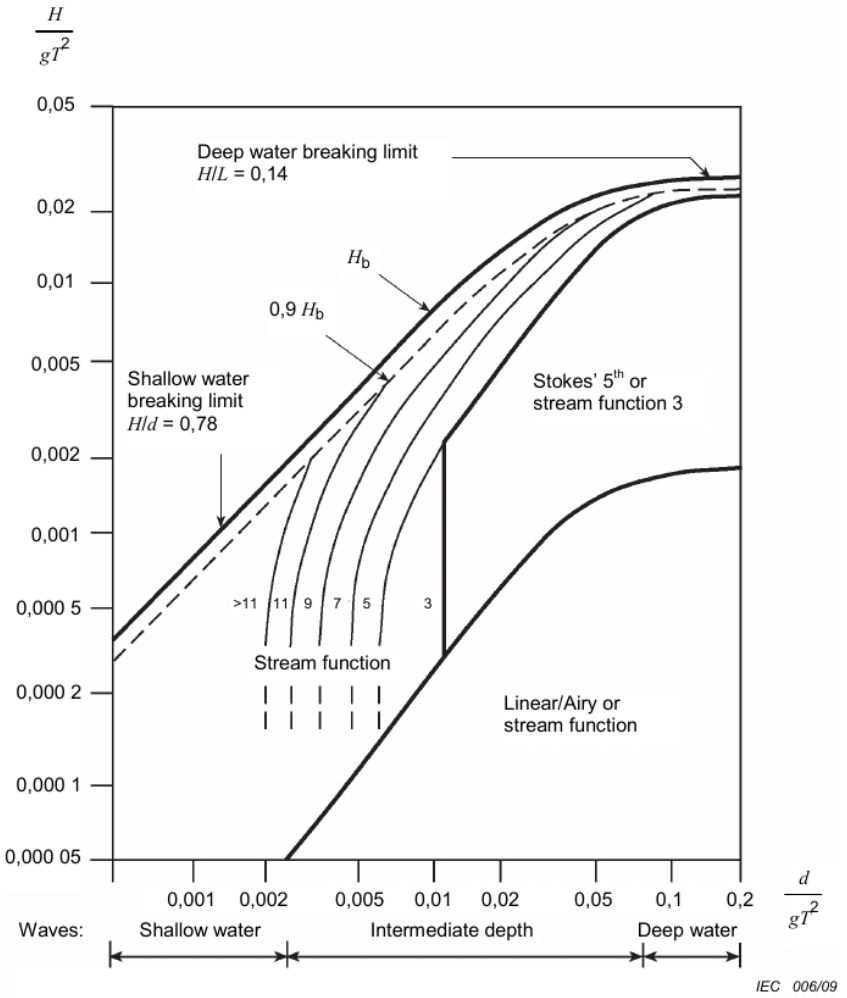

FIGURE 2.1: Regular wave theory selection diagram (*IEC 61400-3* 2009).

is the cross sectional area of the member and U and $\dot{U}$ are the velocity and acceleration of the flow resolved normal to the member. If the flexibility of the structure is important the relative velocity and acceleration should be used in the equation and Morison's equation can be written as

$$F = \frac{1}{2} C_D \rho D |U_r| U_r + C_m \rho A (\dot{U} - \dot{U}_s) + \rho A \dot{U} \tag{2.2}$$

where U_r is the relative velocity of the flow normal to the member, $\dot{U}_s$ is the acceleration of the structure resolved normal to the member and $C_m = C_M - 1$ is the added mass coefficient.

In the cases where the structure dimension is large relative to the wave length, $D > 0.2L$, where D is the diameter of the structure and L is the wave length, the diffraction is so large that the Morison's equation is not directly applicable. For the more conventional case of a vertical surface piercing cylinder the diffraction problem is solved analytically by MacCamy R. (1954) for linear problems in which the horizontal force per unit length may

be written as the inertia part of Morison's equation:

$$f_x = \frac{2\rho g H}{k} \frac{\cosh(ks)}{\cosh(kd)} \frac{1}{\sqrt{A_1(ka)}} \cos(\omega t - \alpha), \tag{2.3}$$

$$A_1(ka) = J_1'^2(ka) + Y_1'^2(ka), \tag{2.4}$$

$$\alpha = arctan\left(\frac{J_1'(ka)}{Y_1'(ka)}\right) \tag{2.5}$$

where s is the elevation above the bed at a phase lag of α, d is the water depth, a is the member's radius and J and Y are the first and second kind Bessel functions. This solution should be used in case of significant diffraction waves with cylindrical surface piercing structures.

The current common method of hydrodynamic load calculation in the wind energy can be found in guidelines such as *IEC 61400-3* (2009) among others. In *IEC 61400-3* (2009) four approaches are recommended for calculation of hydrodynamic loads in the cases of extreme events to take into account the effect of the stochastic nature of the wave loading, the flexibility of the structure and the nonlinear nature of the waves. The four recommended approaches can be summarized as:

1. **Explicit approach.** The first, most intuitive approach is to use irregular, non-linear, short crested wave kinematics created in models such as a Boussinesq solver. However, because some of the load cases include long time series of the marine conditions to capture the largest loads, this method is not vastly used in the industry.

2. **Wave non-linearity factor approach.** For this approach, *IEC 61400-3* (2009) recommends to use flexible structures and turbulent wind with irregular linear wave theory and take the non-linearities into account with a set of load factors. In this approach the calculations with the aforementioned models are performed, then the maximum load wave episodes are selected and the corresponding wind velocity and wave height are calculated. For each selected force two sets of simulations with rigid body and wind inflow are performed with regular non-linear and linear waves; then the ratio of the maximum force between them is calculated as the wave non-linearity factor. The maximum forces from the original simulation with irregular waves are multiplied with the wave non-linearity factor.

3. **Regular wave approach.** As a third approach *IEC 61400-3* (2009) suggests to use flexible structures with steady wind inflow and regular non-linear waves. In this approach the simulations with no waves and turbulent wind inflow are performed initially to calculate the correct aerodynamic forces on the turbine. Hereafter, simulations with steady wind are performed with scaled up wind velocity to get the same aerodynamic force in the two simulations. Finally, the simulations with the

corrected steady wind velocity, flexible structure and regular non-linear waves are conducted with durations shorter than three times the duration of the waves to avoid non-physical response from the structure.

4. **Constrained wave approach.** In this approach the kinematics of the waves are calculated with embedding one regular non-linear wave into a time series of irregular linear waves. In this method the extreme waves based on the wave height can also be replaced with a New Wave episode used with a stretching method. The directional spreading of the waves can also be taken into account in this approach. This is the most commonly used method in the industry.

With the increasing capacity of computers, numerical models which solve the single or double-phase momentum equation and continuity are used more often than before. Hence, the explicit approach recommended in *IEC 61400-3* (2009) is getting more attention. Bingham and Zhang (2007) suggested a finite difference solution for the nonlinear water waves which was extended by Engsig-Karup, Bingham, and Lindberg (2009) to a flexible-order model in three-dimensions. They validated the model for 3D steep nonlinear wave problems and a shoaling problem against experimental measurements and other calculations from the literature. Schløer (2013) used the model to investigate the fatigue and extreme wave loads on bottom fixed offshore wind turbines. Later Paulsen (2013), validated the model for more cases and used it to initiate a Navier-Stoke's model which includes water and air fluids. He used this coupled solver to calculate forces on a surface piercing cylinder for regular and phase focused irregular steep breaking waves (Paulsen, Bredmose, and Bingham 2014).

Use of Navier-Stoke's two phase numerical models is becoming more common during the last few years. Christensen, Bredmose, and Hansen (2005) studied the wave run-up and wave forces on offshore wind turbine foundations. The analyses were based on numerical investigations using a Navier-Stokes solver. The free surface was resolved with a Volume of Fluid technique (VOF) in OpenFOAM®. Jacobsen, Fuhrman, and Fredsøe (2012) extended the open-source CFD library OpenFOAM® with a generic wave generation and absorption method termed 'wave relaxation zones'. The model was validated using two benchmark test cases, which show its capability to model wave propagation and wave breaking. Filip (2013) studied the behaviour of turbulence in the proximity of the free surface using direct numerical simulations (DNS) and large-eddy simulations (LES). Hildebrandt and Sriram (2014) used a commercial Navier-Stokes solver to model phase focused wave groups and investigated the pressure distribution and vortex shedding around a cylinder due to steep waves.

2.2 CFD modelling of water waves impact on surface piercing cylinders

Although usage of CFD simulations for the reproduction of extreme waves around surface piercing cylinder is not common in the industry, validation cases in the literature can be found especially during the last decade. The application of such cases can be divided into validation of the inline force caused by the wave events and detailed investigation of the flow-structure interaction including the run-up on the monopile. Christensen, Bredmose, and Hansen (2005) studied the wave run-up and inline forces on offshore wind turbines using an in-house developed Navier Stokes solver called NS3 and concluded that the run-up and forces on the monopile are strongly influenced by the breaking process. They validated the model with measurements conducted by Kriebel (1992) for non-breaking and breaking waves. The computations were carried out with a slip boundary condition at the cylinder wall thus with no representation of the structural boundary layer. Bredmose et al. (2006) extended the study for the extreme wave loads on offshore wind turbines in an irregular sea state with current and proved that the model is capable of such complicated cases too. Later Bredmose and Jacobsen (2010) investigated breaking wave impacts from focused wave groups on offshore wind turbine monopiles using OpenFOAM and validated the numerical model with linear wave forcing. They concluded that the more developed breaking is the smaller the effect of it on the force history gets. In addition, Bredmose and Jacobsen (2011) investigated wave impacts on offshore wind turbine inspection platforms and illustrated the potential of CFD calculations for violent wave loads. They reported that the natural frequency of the structure might be excited during the wave impacts on the inspection platforms.

Filip (2013) and Filip and Maki (2015) used Large Eddy Simulations (LES) to model the forces from the free surface flow of steep non-breaking regular waves and validated them with experiments. They extended the study by modelling breaking waves and showed that the prediction of forces on a vertical circular cylinder are improved by the use of the extended LES model for multiphase free surface flow using Volume of Fluid method. Filip (2013) was one of the first to include the effects of turbulence in calculation of the wave forces on the surface piercing cylinder. Paulsen, Bredmose, and Bingham (2014) developed and presented results of the domain decomposition method (Paulsen 2013) for modelling of wave loads on surface piercing circular cylinders. They showed that the method works very well by validating extensively against experiments. The validation cases included breaking and non-breaking regular and focused waves. In addition, they were the first to report the reproduction of the Secondary Load Cycle in the numerical results. Paulsen et al. (2014) then focused more on the detailed investigation of the flow-structure interaction and studied the forcing of a bottom-mounted circular cylinder by steep regular water waves at finite depth. They especially focused on the source of the Secondary Load Cycle in the inline force history. The numerical results were accompanied with experimental measurements

of the non-breaking regular waves. Even though they investigated the local flow around the cylinder, its boundary layer was neither resolved nor modelled. Chen et al. (2014) investigated the performance of OpenFOAM when applied to non-linear wave interactions with offshore structures for 4 cases of regular and 4 cases of irregular phase focused wave groups. They concluded that OpenFOAM is very capable of accurate modelling of nonlinear waves interaction with structure as validated by experiments of non-breaking regular and focused waves conducted at DHI Denmark. The study included inline force, free surface elevation, local event of secondary load cycle and sub- and super-harmonics of the free surface elevation and inline force time series. This study was the first numerical investigation of waves and monopile interaction including a no-slip boundary conditioned monopile.

Hildebrandt and Sriram (2014) looked into the pressure distribution and vortex shedding around a cylinder due to a steep non-breaking wave using measurements and numerical modelling. Pressure was measured on the surface of the cylinder in different heights and azimuths, and was compared to the numerical results. The used model in this study was ANSYS-CFX with Reynolds Averaged $k\omega$-SST turbulence modelling. They concluded that the model is suitable for local flow investigation around a surface piecing cylinder in waves. Choi, Lee, and Gudmestad (2015) used the dynamic amplification method to account for the structures response due to breaking wave impacts. The paper showed that the in-house developed 3D numerical model performs well in modelling the breaking wave phenomenon and producing reliable results including approximated structure response. An in-house developed Navier Stokes solver, REEF3D, which incorporates a level set method to capture the free surface was used by Alagan Chella (2016) and Alagan Chella et al. (2016) to simulate the free surface waves and to conduct a detailed investigation of the shape of the wave breaker and local events around the cylinder. The model was validated by comparison to experiments of breaking waves on a sloped bed. They reported pile-up of a water column (mound) behind the cylinder and related it to the depth of water. The cylinder wall included a no-slip boundary condition with wall functions to account for the values of k and ω in the $k\omega$ turbulence model.

Devolder, Rauwoens, and Troch (2017) extended and applied a buoyancy-modified $k\omega$-SST turbulence model to simulate wave run-up around a monopile subjected to regular waves using OpenFOAM. They showed that usage of modified $k\omega$-SST increases the consistency of the numerical methods to conserve the shape of regular waves. Then they used this to calculate the run up and compare with experiments. The included wave cases were non-breaking and the boundary layer on the cylinder wall was modelled using wall functions. Jose et al. (2017) conducted a comparison of numerical simulations of breaking wave forces on a monopile structure using finite difference and finite volume models. They used a method to refine the mesh around the free surface elevation locally. They reported that the secondary load cycle is caused by the hydrostatic effect of the water column. A good

consistency of the numerical results is shown in this work with a $k\omega$-SST turbulence model in validations against experiments for both numerical models. Veic and Sulisz (2018) analysed the impact pressure distribution on a monopile structure excited by two irregular breaking wave episodes. They reported similar mechanisms of the breaking wave impact, in the sense of pressure distribution, in both impact cases and showed that the value of the peak slamming coefficient is approximately equal to $Cs = 2\pi$. They presented force time histories, free surface elevation and pressure distribution on the cylinder during the slamming.

Based on this literature review the secondary load cycle in the numerical model time history of inline force of free surface waves interacting with a surface piercing cylinder was first reported by Paulsen, Bredmose, and Bingham (2014) and then reported frequently by different research groups using different numerical models. Using a no-slip boundary condition on the cylinder wall was firstly incorporated by Chen et al. (2014) and to this day has been repeated a few times. Taking turbulence into account in these cases was also firstly done by Filip (2013). However, usage of LES models has not been repeated since then and only RANS type models, especially $k\omega$-SST, have been used a few times. Most of the literature includes numerical results incorporating Volume of Fluid method for capturing the free surface elevation which has showed a good agreement with experiments. From this literature review it is clear that there has been a shift in the usage of the numerical models for validation purposes towards use of the models for detailed investigation during the last decade.

2.3 Expected extreme wave episodes

If the fourth approach, constrained wave approach, is chosen in the design process the extreme waves, selected based on wave height, should be replaced by either stream function waves (Fenton 1988) with the same height or a New Wave group (Tromans, Anatruk, and Hagemeijer 1991). Both of these theories are associated with limitations, the most important one of which is the symmetry of these waves around the wave crest. To avoid the limitations and to estimate a more realistic extreme wave, other theories and methods have been suggested in the recent years. One such method is the "designer" wave denoted firstly by Grice, Taylor, and Taylor (2014). This wave is the average shape of measured waves that can create an extreme event of choice. This method requires some initial experiments or simulations to estimate the extreme wave shape. Another approach to find an extreme wave event is to apply the First Order Reliability Method (FORM) to calculate the shape of the most probable wave episode which exceeds a certain maximum crest height or inline force. The New Wave group is developed based on the solution of the FORM problem around the linear wave theory which is solved analytically. Use of FORM to estimate the extreme event in a given sea state using higher order wave theories is limited. Jensen (2008) used FORM to calculate the most probable wave sequence for extreme loads on a jack-up structure, the roll response of a ship and the motion of a TLP floater.

2.4 The effect of the bed slope

All the wave theories mentioned in figure 2.1 are derived based on the flat bed assumption. *IEC 61400-3* (2009) suggests to use a corrected wave height distribution in shallow water which includes corrections for the sea bed slope. This formulation of Battjes and Groenendijk (2000) wave height distribution is a function of the depth and slope of the sea bed:

$$F(h) = Pr(\underline{h} < h) = \begin{cases} F_1(h) = 1 - exp\left(-\left(\frac{h}{h_1}\right)^2\right) & h \leq h_{tr} \\ F_2(h) = 1 - exp\left(-\left(\frac{h}{h_2}\right)^{3.6}\right) & h \geq h_{tr} \end{cases} \tag{2.6}$$

where the constants h_1 and h_2 are given based on experiments and h_{tr} is the normalized transition wave height and can be calculated as

$$h_{tr} = \frac{H_{tr}}{H_{rms}}, \tag{2.7}$$

$$H_{tr} = (0.35 + 5.8\tan(\alpha))d, \tag{2.8}$$

$$H_{rms} = 2.69\sqrt{m_0} + 3.24\frac{m_0}{d}. \tag{2.9}$$

Here d is the water depth, α is the bed slope and variance of the sea surface elevation is m_0.

Another early study to investigate the effect of the bed slope on wave characteristics was conducted by Nelson (1982). He showed that the effect of the bed slope is minimal on wave celerity and potential energy but considerable on crest and trough skewness and the asymmetry of the wave. These parameters might be influential in the load calculations on the substructures in large inertia dominant waves. Nwogu (1993) presented similar conclusions about horizontal and vertical asymmetry of the waves caused by increased lower- and higher-frequency wave harmonics. He concluded based on a newly form of Boussinesq-type equations with the velocity variable in an arbitrary depth. The model was validated against measurements. The first study to investigate the effect of the bed slope on the inline forces on a monopile directly was performed by Schløer, Bredmose, and Bingham (2011). They investigated the statistical distribution of the maximum inline forces numerically on two bed slopes of 1:25 and 1:100 and concluded that a larger bed slope results in largest maximum crest height, inline force and bending moment. The work included numerical simulation of one sea state only. In particular, for the case of the constrained wave approach the effect of the bed slope on the extreme wave loads is of interest where more nonlinear models might be used.

Nevertheless there has been no study to investigate the effect of the bed slope on the wave episodes creating the extreme loads on a monopile. In the methodology described in the constrained wave approach, the wave height is used to select the extreme waves even though the highest wave may be not the wave episode with the largest load on the structure.

2.5 The source of the Secondary Load Cycle

As powerful as the Morison's equation is, it includes some simplifications including exclusion of the non-linear wave-structure interactions. Batchelor and Young (1968) suggested corrections to the Morison's equation to consider the convective effect of the water particle acceleration. Rainey (1989), Manners and Rainey (1992) and Rainey (1995) suggested corrections including an axial divergence term and an extra point force around the surface which accounts for the change of wetted area around the cylinder. Faltinsen, Newman, and Vinje (1995) derived the boundary-value problem for the nonlinear potential of third order to calculate the wave loads on a vertical cylinder with slender body (considering diffraction effects up to third order) in deep water. Kristiansen and Faltinsen (2017) later extended this method to arbitrary depth. Nevertheless, none of these methods is able to capture all the local events around the cylinder. A secondary load cycle in the force time history is one of such events which not only is still not captured in the analytical methods but also its source is a matter of debate. Grue, Bjørshol, and Strand (1994) were the first to report the existence of what was initially called a secondary oscillation in the force-recordings. They attributed the local event to a suction region one diameter below the still water level concluded from the free surface measurements. Rainey (2007) associated the secondary load cycle with the violent motion of the water surface and a cavity bubble formed behind the cylinder which then collapses to give the secondary load cycle. Paulsen et al. (2014) showed by visual observation and a simplified analytical model that the secondary load cycle is caused by the free surface which drives a return flow from the back of the cylinder towards the front side after the passage of the wave crest. Nevertheless, there is still no agreement on the nature of the secondary load cycle and the governing physics.

2.6 Slamming wave loads

In today's common practice of the hydrodynamic load calculations in the offshore industry, after calculating the wave kinematics based on the appropriate model mentioned in figure 2.1 the breaking waves should be identified using the breaking criteria. The breaking type (spilling, plunging and surging) principally depends on the deep water wave steepness and sea bed slope. Spilling waves are usually broken by the given condition, such as focusing on the same depth or wind effects, and retain their original steep-sided profile. The wave profile and their kinematics may be described using a higher order stream function wave. Plunging breakers usually occur when a wave with moderate initial steepness is made to break by running up a sea floor slope. The wave height might increase above the limiting regular wave height for the local water depth and a tongue shaped spout forms at the wave crest. Surging waves occur when very long waves with small height shoal up a slope such as a beach. Such waves are unlikely to be important in the offshore wind turbine design.

In case of a breaking wave at the location of the structure the effect of slamming should be taken into account in the force calculation. *IEC 61400-3* (2009) defines a slam event as engulfing of an almost horizontal member by rising water surface of a wave and a slap event as impact of a breaking wave with a member in the plane perpendicular to the wave direction. In both cases the force is applied impulsively and is important for the structure response. Since the method of calculation for both of these events are identical, the slap and slam loads are used interchangeably in industry and through out this document.

The suggested formulation to calculate the slam force per unit height in *IEC 61400-3* (2009) is written as

$$F = \frac{1}{2} C_s \rho D U^2 \tag{2.10}$$

where C_s is the slam coefficient and typically between π and 2π, ρ is the density, D is diameter of the member and U is the velocity of the water particles at the point of impact.

It should be mentioned that (2.10) is the impact force at the first moment of impact and as a function of time the theory from the work of Wienke and Oumeraci (2005) is recommended to be used. According to Wienke and Oumeraci (2005) the effect of the slamming can be added linearly to the inertia and drag terms in the Morison equation. The theory developed by Wienke and Oumeraci (2005) can be used with any inclination of the structure relative to the wave front and only the celerity of the wave is needed. In this formulation the initial impact of this formulation corresponds to $C_s = 2\pi$. Prior to Wienke and Oumeraci (2005), several other methods were developed to calculate the initial force and the time series of a breaking wave impact force on a cylinder. Wagner (1932) proposed a theoretical 2D-model for the peak pressure which built the foundation for further development by Wienke and Oumeraci (2005). Wagner (1932) described the flow by a potential flow approach. The flow was assumed to be incompressible, inviscid and irrotational. The surface tension of the flow and the forces due to gravity were neglected. In addition, the theory neglected the nonlinear velocity term in the Bernoulli equation so it only provides the peak pressure similar to (2.10). Goda, Haranaka, and Kitahata (1966) developed a method that is vastly used in coastal engineering

$$F_I(t) = \lambda \eta_b \pi \rho R C^2 \left(1 - \frac{C}{R} t\right), \tag{2.11}$$

where $\lambda \eta_b$ is the area of impact and C is the wave celerity.

This formulation is based on the assumption that the breaker front is vertical and moves with the celerity of the wave. However, Goda, Haranaka, and Kitahata (1966) calculated C_s to be equal to π. Based on the work done by Wagner (1932), Cointe (1989) considered a more general problem where the breaker front can be non-normal relative to the cylinder axis. He used the method of matched asymptotic expansions to solve the resulting boundary

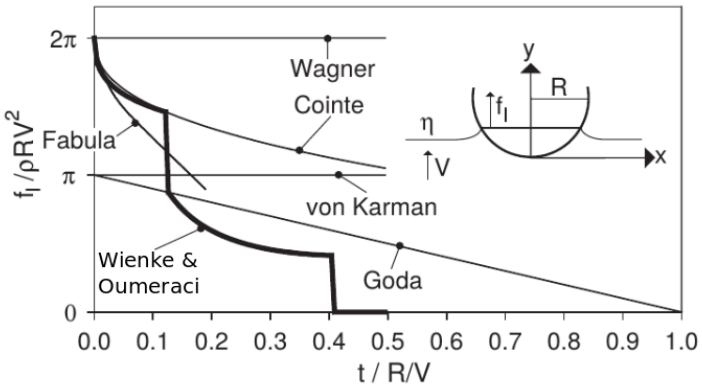

FIGURE 2.2: Time histories of the line force according to different theories (Wienke and Oumeraci 2005).

value problem for small penetration depth. The model accounted for nonlinear features such as the creation of a jet at each waterline. Wienke and Oumeraci (2005) presented a comparison of the normalized inline force per length from the slamming wave based on several different theories which is presented in figure 2.2. The slamming coefficient can take the value of either π or 2π based on different theories while the time histories also differ significantly between the investigated theories.

In the literature and the current industry procedure the maximum pressure or inline force and the time series of such force is estimated. However, another approach is to focus on the time integral of the impact pressure during the impact.

References

Alagan Chella, Mayilvahanan (2016). "Breaking Wave Characteristics and Breaking Wave Forces on Slender Cylinders Breaking Wave Characteristics and Breaking Wave Forces on Slender Cylinders". PhD thesis.

Alagan Chella, Mayilvahanan et al. (2016). "Breaking solitary waves and breaking wave forces on a vertically mounted slender cylinder over an impermeable sloping seabed". In: *Journal of Ocean Engineering and Marine Energy* 3.1, pp. 1–19.

Batchelor, G. K. and A. D. Young (1968). "An Introduction to Fluid Dynamics". In: *Journal of Applied Mechanics* 35.3, p. 624. arXiv: 9780471202318.

Battjes, J A and H W Groenendijk (2000). "Wave height distribution on shallow foreshores". In: p 161–182.

Bingham, Harry B. and Haiwen Zhang (2007). "On the accuracy of finite-difference solutions for nonlinear water waves". In: *Journal of Engineering Mathematics* 58.1-4, pp. 211–228.

Bredmose, Henrik and Niels G Jacobsen (2010). "Breaking Wave Impacts On Offshore Wind Turbine Foundations: Focusedwave Groups And CFD".

In: *Proceedings of the ASME 29th 2010 International Conference on Ocean, Offshore and Arctic Engineering OMAE2010 June 6-11, 2010, Shanghai, China*.

Bredmose, Henrik and Niels G Jacobsen (2011). "Vertical wave impacts on offshore wind turbine inspection platforms". In: *Proceedings of the ASME 2011 30th International Conference on Ocean, Offshore and Arctic Engineering OMAE2011 June 19–24, 2011, Rotterdam, The Netherlands*. Vol. 436. 1896, pp. 13–32.

Bredmose, H. et al. (2006). "Numerical reproduction of extreme wave loads on a gravity wind turbine foundation". In: *International Conference on Offshore Mechanics and Arctic Engineering, OMAE*, pp. 1–9.

Chen, L. F. et al. (2014). "Numerical investigation of wave-structure interaction using OpenFOAM". In: *Ocean Engineering* 88, pp. 91–109.

Choi, Sung Jin, Kwang Ho Lee, and Ove Tobias Gudmestad (2015). "The effect of dynamic amplification due to a structure's vibration on breaking wave impact". In: *Ocean Engineering* 96, pp. 8–20.

Christensen, Erik Damgaard, Henrik Bredmose, and Erik Asp Hansen (2005). "Extreme wave forces and wave run-up on offshore wind-turbine foundations". In: *Proceedings of Copenhagen Offshore Wind Conference* 1995, pp. 1–10.

Cointe, R (1989). "Two-DImensional Water-Solid Impact". In: *Offshore Mechanics and Arctic Engineering* 111, pp. 109–114.

Devolder, Brecht, Pieter Rauwoens, and Peter Troch (2017). "Application of a buoyancy-modified k-ω SST turbulence model to simulate wave run-up around a monopile subjected to regular waves using OpenFOAM®". In: *Coastal Engineering* 125.June 2016, pp. 81–94.

Engsig-Karup, A. P., H. B. Bingham, and O. Lindberg (2009). "An efficient flexible-order model for 3D nonlinear water waves". In: *Journal of Computational Physics* 228.6, pp. 2100–2118.

Faltinsen, O. M., J. N. Newman, and T. Vinje (1995). "Nonlinear wave loads on a slender vertical cylinder". In: *Journal of Fluid Mechanics* 289.-1, p. 179.

Fenton, J.D. (1988). "The numerical solution of steady water wave problems". In: *Computers & Geosciences* 14.3, pp. 357–368.

Filip, G and K Maki (2015). "Evaluation of Advanced Turbulence Models for High-Reynolds Number External Flow". In: 354.

Filip, Grzegorz P (2013). "High-Resolution Numerical Simulation of Turbulent Interfacial Marine Flows". PhD thesis.

Goda, Yoshimi, Suketo Haranaka, and Masaki Kitahata (1966). *Study on impulsive breaking wave forces on piles*. Tech. rep. 5, pp. 1–30.

Grice, J R, P H Taylor, and R Eatock Taylor (2014). "Second-order statistics and ' designer ' waves for violent free-surface motion around multi-column structures Subject Areas :" in:

Grue, John, Gunnhild Bjørshol, and Øivind Strand (1994). "Nonlinear wave loads which may generate "Ringing" responses of offshore structure". In: *Workshop on Water Waves and Floating Bodies*.

Hildebrandt, A and V Sriram (2014). "Pressure Distribution and Vortex Shedding Around a Cylinder due to a Steep Wave at the Onset of Breaking

from Physical and Numerical Modeling". In: *The Twenty-fourth International Ocean and ...* 3, pp. 405–410.

IEC 61400-3 (2009).

Jacobsen, Niels Gjøl, David R Fuhrman, and Jørgen Fredsøe (2012). "A wave generation toolbox for the open-source CFD library: OpenFoam". In: *International Journal for Numerical Methods in Fluids* 70.9, pp. 1073–1088.

Jensen, J. Juncher (2008). "Extreme value predictions and critical wave episodes for marine structures by FORM". In: *Ships and Offshore Structures* 3.4, pp. 325–333.

Jose, Jithin et al. (2017). "A comparison of numerical simulations of breaking wave forces on a monopile structure using finite difference and finite volume models". In: *Ocean Engineering* m.1, pp. 1–26.

Kriebel, D. L. (1992). "Nonlinear wave interaction with a vertical circular cylinder. Part II: Wave run-up". In: *Ocean Engineering* 19.1, pp. 75–99.

Kristiansen, T and O M Faltinsen (2017). "Higher harmonic wave loads on a vertical cylinder in finite water depth". In: pp. 773–805.

MacCamy R., Fuchs R. (1954). *Wave forces on piles: A diffraction theory*. Tech. rep.

Manners, W. and Rod C. T. Rainey (1992). "Hydrodynamic Forces on Fixed Submerged Cylinders". In: *Proceedings of the Royal Society A: Mathematical, Physical and Engineering Sciences* 436.1896, pp. 13–32.

Morison, J. R. (1953). *The Force Distribution Exerted by Surface Waves on Piles*. Tech. rep., p. 16.

Nelson, R. C. (1982). "The Effect of Bed Slope on Wave Characteristics". In: pp. 555–572.

Nwogu, Okey (1993). "Alternative Form of Boussinesq Equations for Nearshore Wave Propagation". In: *Journal of Waterway, Port, Coastal, and Ocean Engineering* 119.6, pp. 618–638.

Paulsen, Bo Terp (2013). "Efficient computations of wave loads on off shore structures". PhD thesis.

Paulsen, Bo Terp, Henrik Bredmose, and Harry B. Bingham (2014). "An efficient domain decomposition strategy for wave loads on surface piercing circular cylinders". In: *Coastal Engineering* 86, pp. 57–76.

Paulsen, Bo T. et al. (2014). "Forcing of a bottom-mounted circular cylinder by steep regular water waves at finite depth". In: *Journal of Fluid Mechanics* 755, pp. 1–34.

Rainey, R. C. T. (1995). "Slender-body expressions for the wave load on offshore structures". In: *Proceedings of the Royal Society of London* 450.1939, pp. 391–416.

Rainey, R. C.T. (1989). "A new equation for calculating wave loads on offshore structures". In: *Journal of Fluid Mechanics* 204.WW3, pp. 295–324.

Rainey, Rod C T (2007). "Weak or strong nonlinearity: The vital issue". In: *Journal of Engineering Mathematics* 58.1-4, pp. 229–249.

Schløer, S. (2013). *Fatigue and extreme wave loads on bottom fixed offshore wind turbines*.

Schløer, S., H. Bredmose, and H. B. Bingham (2011). "Irregular Wave Forces on Monopile Foundations: Effect of Full Nonlinearity and Bed Slope". In: *International Conference on Ocean, Offshore and Arctic Engineering*.

Tromans, Peter S, A R Anatruk, and Paul Hagemeijer (1991). "A New Model for the Kinematics of Large Ocean Waves Application as a Design Wave". In: *Proceedings of the First International Offshore and Polar Engineering Conference* 8.August, pp. 64–71.

Veic, Duje and Wojciech Sulisz (2018). "IMPACT PRESSURE DISTRIBUTION ON A MONOPILE STRUCTURE EXCITED BY IRREGULAR BREAKING WAVE". In: 25, pp. 29–35.

Wagner, Herbert (1932). "Über Stoß- und Gleitvorgänge an der Oberfläche von Flüssigkeiten". In: *Zeitschrift für Angewandte Mathematik und Mechanik* 12.4.

Wienke, J. and H. Oumeraci (2005). "Breaking wave impact force on a vertical and inclined slender pile - Theoretical and large-scale model investigations". In: *Coastal Engineering* 52.5, pp. 435–462.

Chapter 3

Theoretical background

In the calculations conducted in this thesis, the wave generation is based on the linear wave theory, linear irregular waves, New Wave theory and the linear theory of wave generation. In addition the most probable shape of the waves and the effect of bed slope on the extreme waves were investigated. These models and the theories which are the backbone of the thesis investigations are described in this chapter.

3.1 Linear wave theory

The linear wave theory expresses the wave by its free surface elevation, $\eta(x,y,t)$, and velocity potential , $\Phi(x,y,z,t)$. Laplace equation should be considered in the whole domain in $-h \leq z \leq 0$, where h is the water depth.

$$\Phi_{xx} + \Phi_{zz} = 0 \tag{3.1}$$

The boundary conditions include kinematic boundary conditions on the free surface and the bed, stating that the particles on the free surface will remain on the free surface, and, expressing that the particles do not pass through the bed, and a dynamic boundary condition on the free surface imposing the pressure to be zero at the free surface.

$$\Phi_z = \eta_t \quad at \quad z = 0 \tag{3.2}$$

$$\Phi_z = 0 \quad at \quad z = -h \tag{3.3}$$

$$\Phi_t + g\eta = 0 \quad at \quad z = 0 \tag{3.4}$$

Using separation of variables in $\eta(x,y,t)$ and $\Phi(x,y,z,t)$ general form of the solution can be derived as

$$\eta(x,y,t) = \frac{H}{2}\cos(\omega t - kx), \tag{3.5}$$

$$\Phi(x,y,z,t) = -\frac{H}{2}\frac{\omega}{k}\frac{\cosh(k(z+h))}{\sinh(kh)}\sin(\omega t - kx) \tag{3.6}$$

for progressive modes and

$$\eta_E(x,y,t) = \sum_{n=1}^{\infty} a_n \exp(-\kappa_n x)\cos(\omega t), \tag{3.7}$$

$$\Phi_E(x,y,z,t) = \sum_{n=1}^{\infty} a_n \frac{\omega}{\kappa_n}\frac{\cosh(\kappa_n(z+h))}{\sinh(\kappa_n h)}\exp(-\kappa_n x)\sin(\omega t) \tag{3.8}$$

for the evanescent modes. The linear dispersion relation is

$$\omega^2 = gk\tanh(kh) \tag{3.9}$$

$$\omega^2 = -g\kappa\tanh(\kappa h) \tag{3.10}$$

for the progressive modes and evanescent modes respectively. Evanescent modes are provoked by the local boundary conditions like close to a submerged steady or moving body, close to a wave maker or close to an abrupt bottom change.

Linear shoaling theory Shoaling is the process waves undergo when running up (or down) a slope from deeper to shallow water. The linear shoaling theory was also used, although not directly compared to the nonlinear effect, to estimate the shoaling effect. The theory is based on the assumption that waves transfer energy with a constant rate propagating from one depth to another. The wave height changes as

$$\frac{H_2}{H_1} = \sqrt{\frac{(1+G_1)\tanh(k_1h_1)}{(1+G_2)\tanh(k_2h_2)}}, \tag{3.11}$$

where

$$G = \frac{2kh}{\sinh(2kh)},$$

and k is the wave number.

3.2 Irregular waves

In the ocean the waves are irregular and random with measurable spectra of the free surface elevation. Since one focus of this work was also the ocean waves which might create extreme loading on the substructures the theory of linear irregular waves was used several times in this work. Random or irregular waves may be considered as a linear superposition of several linear waves as a first approximation. As a simple summation this superposition can be presented as

$$\eta(t) = \sum_{n=1}^{N_{freq}} \sqrt{S_n df}\,(a_n \cos(\omega_n t - k_n x) + b_n \sin(\omega_n t - k_n x))\,, \tag{3.12}$$

$$\Phi(x,z,t) = \sum_{n=1}^{N_{freq}} \frac{-\omega_n}{k_n \sinh(hk_n)} \cosh(k_n(z+h))$$
$$\sqrt{S_n df}\,(a_n \sin(\omega_n t - k_n x) - b_n \cos(\omega_n t - k_n x))\,, \tag{3.13}$$

$$u(x,z,t) = \sum_{n=1}^{N_{freq}} \frac{\omega_n}{\sinh(hk_n)} \cosh(k_n(z+h))$$
$$\sqrt{S_n df}\,(a_n \cos(\omega_n t - k_n x) + b_n \sin(\omega_n t - k_n x))\,, \tag{3.14}$$

$$\omega_n = 2\pi f_n, \quad f_n = ndf, \quad S_n = S(f_n),$$

where df is the frequency increment and S is the wave spectrum. The coefficients a_n and b_n are independent sets of independent zero-mean Gaussian variables of unit variance. A commonly used wave spectrum is the JONSWAP spectrum calculated as

$$S(f) = m_0 a f^{-5} \exp(-bf^{-4}) \gamma^{\Omega(f)} \tag{3.15}$$

$$f = ndf, \quad a = 5f_p^4, \quad b = \frac{5}{4} f_p^4, \tag{3.16}$$

$$\Omega(f) = \exp\left(-\frac{1}{2}\left(\frac{f - f_p}{\sigma f_p}\right)^2\right) \tag{3.17}$$

where m_0 is the zero moment of the wave spectrum which is equal to the variance of the sea surface elevation, f_p is the peak frequency of the wave spectrum, σ is either 0.07 or 0.09 for $f \leq f_p$ and $f > f_p$ respectively and γ is the peak shape parameter chosen based on H_s and T_p. A simplified, approximate version of (3.12) is used extensively in offshore engineering as

$$\tilde{\eta}(t) = \sum_{n=1}^{N_{freq}} \sqrt{2S_n df}\,(\cos(\omega_n t - k_n x + \psi_n))\,, \tag{3.18}$$

where ψ_n is a set uniformly distributed over the interval $(0, 2\pi)$. Note that $\tilde{\eta}$ is never exactly a Gaussian random variable because the random variables a_n and b_n are replaced by $\sqrt{2}$ (Naess and Moan 2012).

In directionally spread sea states the multi-directional spectrum represents the distribution of wave energy not only over frequencies but also in the direction. The general expression for multi-directional spectrum is $\Upsilon(f,\theta)$ often decomposed as $S(F)D(\theta)$ in the interval $\theta_{min} \leq \theta \leq \theta_{max}$. In the field (ocean) the limits are

$$\theta_{min} = -\pi \quad \text{and} \quad \theta_{max} = \pi, \tag{3.19}$$

but in the laboratory the limits are usually much smaller and linked tot he facilities shape and width.

One of the most popular directional spreading distributions is the cosine distribution shown as

$$D_c^*(\theta) = \left(\cos(\frac{\theta - \theta_0}{2})\right)^{2s}, \tag{3.20}$$

$$\Xi_2 = \int_{\theta_{min}}^{\theta_{max}} D^*(\theta) d\theta, \tag{3.21}$$

$$D_c(\theta) = \frac{D_c^*(\theta)}{\Xi_2} \tag{3.22}$$

where s is the spreading constant.

Both a single summation and a double summation method were used in this work for generation of multi-directional random waves. The double summation formulation of the irregular linear waves intuitively can be written as

$$\eta(x,y,t) = \sum_{n=1}^{N_{freq}} \sum_{m=1}^{M_{dir}} \sqrt{S_{nm} df d\theta} (a_{nm} \cos(\omega_n t - k_{nmx} x - k_{nmy} y) + b_{nm} \sin(\omega_n t - k_{nmx} x - k_{nmy} y)), \tag{3.23}$$

$$\Phi(x,y,z,t) = \sum_{n=1}^{N_{freq}} \sum_{m=1}^{M_{dir}} \frac{-\omega_n}{\kappa_{nm} \sinh(h\kappa_{nm})} \cosh(\kappa_{nm}(z+h)) \sqrt{S_{nm} df d\theta} \left(a_{nm} \sin(\omega_n t - k_{nmx} x - k_{nmy} y) - b_{nm} \cos(\omega_n t - k_{nmx} x - k_{nmy} y)\right) \tag{3.24}$$

$$u(x,y,z,t) = \sum_{n=1}^{N_{freq}} \sum_{m=1}^{M_{dir}} \frac{k_{nmx}\omega_n}{\kappa_{nm} \sinh(h\kappa_{nm})} \cosh(\kappa_{nm}(z+h)) \sqrt{S_{nm} df d\theta} \left(a_{nm} \cos(\omega_n t - k_{nmx} x - k_{nmy} y) + b_{nm} \sin(\omega_n t - k_{nmx} x - k_{nmy} y)\right) \tag{3.25}$$

$$v(x,y,z,t) = \sum_{n=1}^{N_{freq}} \sum_{m=1}^{M_{dir}} \frac{k_{nmy}\omega_n}{\kappa_{nm} \sinh(h\kappa_{nm})} \cosh(\kappa_{nm}(z+h)) \sqrt{S_{nm} df d\theta} \left(a_{nm} \cos(\omega_n t - k_{nmx} x - k_{nmy} y) + b_{nm} \sin(\omega_n t - k_{nmx} x - k_{nmy} y)\right) \tag{3.26}$$

where

$$k_{nmx} = \kappa_{nm} \cos(\theta_m), \tag{3.27}$$
$$k_{nmy} = \kappa_{nm} \sin(\theta_m). \tag{3.28}$$

However, since the double summation leads to spatial variations in the statistical properties of the generated time series, the single summation was also used formulated as

$$\eta(x,y,t) = \sum_{n=1}^{N_{freq}} \sqrt{S_n df}(a_n \cos(\omega_n t - k_{nx}x - k_{ny}y) + b_n \sin(\omega_n t - k_{nx}x - k_{ny}y)), \tag{3.29}$$

$$\Phi(x,y,z,t) = \sum_{n=1}^{N_{freq}} \frac{-\omega_n}{\kappa_n \sinh(h\kappa_n)} \cosh(\kappa_n(z+h)) \sqrt{S_n df}\left(a_n \sin(\omega_n t - k_{nx}x - k_{ny}y) - b_n \cos(\omega_n t - k_{nx}x - k_{ny}y)\right) \tag{3.30}$$

$$u(x,y,z,t) = \sum_{n=1}^{N_{freq}} \frac{k_{nx}\omega_n}{\kappa_n \sinh(h\kappa_n)} \cosh(\kappa_n(z+h)) \sqrt{S_n df}\left(a_n \cos(\omega_n t - k_{nx}x - k_{ny}y) + b_n \sin(\omega_n t - k_{nx}x - k_{ny}y)\right) \tag{3.31}$$

$$v(x,y,z,t) = \sum_{n=1}^{N_{freq}} \frac{k_{ny}\omega_n}{\kappa_n \sinh(h\kappa_n)} \cosh(\kappa_n(z+h)) \sqrt{S_n df}\left(a_n \cos(\omega_n t - k_{nx}x - k_{ny}y) + b_n \sin(\omega_n t - k_{nx}x - k_{ny}y)\right) \tag{3.32}$$

where

$$k_{nx} = \kappa_n \cos(\theta_n), \tag{3.33}$$
$$k_{ny} = \kappa_n \sin(\theta_n). \tag{3.34}$$

Here θ_n is randomly chosen for each frequency based on random uniform distribution of variables from zero to unity assigned to the cumulative probability distribution of the directional spreading

$$P(\theta) = \int_{\theta_{min}}^{\theta} D(\phi) d\phi. \tag{3.35}$$

3.3 New Wave

A combination of several number of realizations of random waves might lead to an extreme event with an extreme wave crest and an associated wave profile. Such wave, which is a result of focusing different waves at one point in time and space, is focused wave group also known as the New Wave. Tromans, Anatruk, and Hagemeijer (1991) developed the theory for such cases in connection with Gaussian processes (linear sea states with independent waves). The associated wave profile in a sea state with spreading is shown as

$$\eta(x,y,t) = \sum_{n=1}^{N_{freq}} \sum_{m=1}^{M_{dir}} \frac{\eta_{crest}}{m_0} S_n D_m df d\theta \cos(\omega_n(t-t_0) - k_{nmx}(x-x_0) - k_{nmy}(y-y_0)) \tag{3.36}$$

where $\eta_{crest} \gg \sigma$ and σ is the standard deviation of the free surface elevation time series. It should be noticed that the New Wave theory formulation can describe the shape of the extreme event, but not the magnitude. In addition, double summation method is used in the case of the focused waves groups.

3.4 Linear wave maker theory

In the cases where numerical models were used, after knowing the desired analytical linear free surface elevation, the paddle motion signal in terms of velocity was required to set the correct boundary conditions for the simulations. To calculate the wave makers paddle motion signal linear wave maker theory was used (Dean 2013). The governing equation for the velocity potential in the domain is the Laplace equation where the linearized forms of the dynamic and kinematic free surface and bed boundary conditions are the same as stated in Section 3.1. However, in the case of the domain with the wave maker the lateral boundary conditions are changed. At x = 0, a new kinematic condition must be satisfied on the wavemaker stating that there is no flux through the moving paddle. In the simplest case the horizontal displacement of the wavemaker is described as

$$x = \frac{S(z)}{2} \sin(\sigma t) \tag{3.37}$$

where σ is the wavemaker frequency and S is the amplitude of the stroke of the piston type wavemaker. Therefore, the final lateral boundary condition after using the truncated Taylor series around the mean position of the piston ($x = 0$) is

$$u(0,z,t) = \frac{S}{2}\sigma \cos(\sigma t). \tag{3.38}$$

With the specified boundary conditions there are infinite number of solutions to the Laplace equation including progressive and evanescent modes as

$$\begin{aligned}\Phi =& A_p \cosh(k_p(h+z)) \sin(k_p x - \sigma t) + \\ & \sum_{n=1}^{\inf} C_n \exp(-\kappa(n)x) \cos(\kappa(n)(h+z)) \cos(\sigma t).\end{aligned} \tag{3.39}$$

The first term represents a progressive wave, while the second series of waves are standing waves (evanescent waves) which decay away from the wavemaker 2 to 3 water depth from the wavemaker. A_p and C_n are evaluated by the lateral boundary condition at the wavemaker using the orthogonality of trigonometric functions. Hence we have

$$A_p = \frac{-\int_{-h}^{0} \frac{S(z)}{2} \sigma \cosh(k_p(h+z))dz}{k_p \int_{-h}^{0} \cosh^2(k_p(h+z))dz} \tag{3.40}$$

and

$$C_m = \frac{-\int_{-h}^{0} \frac{S(z)}{2} \sigma \cos(\kappa_m(h+z))dz}{\kappa_m \int_{-h}^{0} \cos^2(\kappa_m(h+z))dz}, \tag{3.41}$$

for a sinusoidal moving piston type wavemaker.

The wave height for the progressive wave at far field, away from the evanescent waves, is determined by evaluating the free surface elevation

$$\begin{aligned}\eta = \frac{1}{g}\frac{\partial \Phi}{\partial t}\|_{z=0} =& -\frac{A_p}{g}\sigma \cosh(k_p h) \cos(k_p x - \sigma t) \\ =& \frac{H}{2} \cos(k_p x - \sigma t) \quad x \gg h.\end{aligned} \tag{3.42}$$

Substituting for A_p, we find the ratio of wave height to stroke of the piston as

$$\frac{H}{S} = \frac{2(\cosh(2k_p h) - 1)}{\sinh(2k_p h) + 2k_p h}. \tag{3.43}$$

For a desired wave far from the wavemaker (3.43) can be used to calculate the amplitude of motion of the piston. In addition linear superposition can be used to extend this theory to generate any linear random time series of free surface elevation. In the case of three-dimesional wavemakers, A_p for each paddle can be calculated by dividing the A_p in (3.40) by $\cos(\theta)$ where θ is the angle between the wave front orthogonal and the x direction.

3.5 Second order contributions

The second order wave theory was initially developed by Stokes for regular waves and adapted for the random irregular sea states by Sharma and Dean (1981). The second order contribution to the free surface elevation separated for sub- and super-harmonic is

$$\eta^{(2)}_{sub} = \sum_{p=1}^{N-1}\sum_{m=1}^{N-p} G^{-}_{p+m,m}\left(A^{-}_{p+m,m}\cos(\theta_{p+m}-\theta_m)+B^{-}_{p+m,m}\sin(\theta_{p+m}-\theta_m)\right), \quad (3.44)$$

$$\eta^{(2)}_{sup} = \sum_{p=2}^{N}\sum_{m=1}^{M} G^{+}_{p-m,m}\left(A^{+}_{p-m,m}\cos(\theta_{p-m}+\theta_m)+B^{+}_{p-m,m}\sin(\theta_{p-m}+\theta_m)\right). \quad (3.45)$$

Here the sub-harmonic contribution shown in (3.44) is between the two waves frequencies $n = p + m$ and m and the super-harmonic contribution shown in (3.45) is between the couple of waves with frequencies $n = p - m$ and m. The limits in (3.44) and (3.45) are corrected to comply with the frequency limits and avoid repetitions. In the sub-harmonic cases $p \leq N-1$ because $1 \leq n \leq N$, $1 \leq m \leq N$ and $p = n - m$. Another limit in the sub-harmonic contribution calculation is $p \geq 1$ so each value of p only sets the upper limit of the second wave frequency $m \leq N - p$. In the super-harmonic cases $p = n + m$ so $p \geq 2$ and $p \leq N$. In addition, the summation of the two frequency components should not be larger than the total number of frequencies N so $1 \leq m \leq p-1$. However, since the summation of frequencies are interchangeable the upper limit was corrected so that the effect of each couple is not taken into account twice. By choosing only the pair in which $n \geq m$ the limit $m \leq p/2$ is obtained as

$$M = \begin{cases} \frac{p}{2} & \text{(p even)}, \\ \frac{p-1}{2} & \text{(p odd)}. \end{cases} \quad (3.46)$$

Number of the frequency components is denoted by N. The amplitudes are expressed by

$$A^{\pm}_{n,m} = \nu^{\pm}_{nm}\left(\frac{\mathbf{a}_n\mathbf{a}_m \mp \mathbf{b}_n\mathbf{b}_m}{h}\right), \quad B^{\pm}_{nm} = \nu^{\pm}_{nm}\left(\frac{\mathbf{a}_m\mathbf{b}_n \pm \mathbf{a}_n\mathbf{b}_m}{h}\right),$$

$$\nu^{-}_{nm} = 1, \quad \nu^{+}_{nm} = 1 \text{ for } n \neq m, \quad \nu^{+}_{nm} = \frac{1}{2} \text{ for } n = m.$$

Note that in this context $\mathbf{a}_n$ and $\mathbf{b}_n$ are already multiplied by the nth frequency amplitude of the linear wave. Hence, in the case of a random linear wave shown in (3.12) they are independent sets of independent zero-mean Gaussian variables of $\sqrt{S_n df}$ variance, so

$$\mathbf{a}_n = \sqrt{S_n df} a_n, \tag{3.47}$$

$$\mathbf{b}_n = \sqrt{S_n df} b_n. \tag{3.48}$$

The transfer functions are defined by

$$\begin{aligned} G^{\pm}_{nm} =& \frac{gh}{\beta^{\pm}_{nm}} (\omega_n \pm \omega_m) \cosh(h\kappa^{\pm}_{nm}) \\ & \left(\omega_n \left(\kappa_m^2 \pm \mathbf{k}_n \cdot \mathbf{k}_m\right) \pm \omega_m \left(\kappa_n^2 \pm \mathbf{k}_n \cdot \mathbf{k}_m\right)\right) \\ & + \frac{h\kappa^{\pm}_{nm}}{\beta^{\pm}_{nm}} \sinh(h\kappa^{\pm}_{nm}) \left(\pm g^2 \mathbf{k}_n \cdot \mathbf{k}_m + \omega_n^2 \omega_m^2 \mp \omega_n \omega_m \left(\omega_n \pm \omega_m\right)^2\right), \end{aligned} \tag{3.49}$$

$$F^{\pm}_{nm} = \frac{h}{\beta^{\pm}_{nm}} \left(\pm \omega_n \omega_m (\omega_n \pm \omega_m) \left((\omega_n \pm \omega_m)^2 \mp \omega_n \omega_m\right)\right) \tag{3.50}$$

$$- \frac{hg^2}{\beta^{\pm}_{nm}} \left(\omega_n \left(\kappa_m^2 \pm 2\mathbf{k}_n \cdot \mathbf{k}_m\right) \pm \omega_m \left(\kappa_n^2 \pm 2\mathbf{k}_n \cdot \mathbf{k}_m\right)\right) \tag{3.51}$$

where

$$\beta^{\pm}_{nm} = \pm 2\omega_n \omega_m \left((\omega_n \pm \omega_m)^2 \cosh(h\kappa^{\pm}_{nm}) - g\kappa^{\pm}_{nm} \sinh(h\kappa^{\pm}_{nm})\right). \tag{3.52}$$

Here upper sign shows the super-harmonics and the lower sign denotes the sub-harmonics. The second order contribution to the velocity potential is

$$\begin{aligned} \phi^{(2)}_{sub} =& \sum_{p=1}^{N-1} \sum_{m=1}^{N-p} F^{-}_{p+m,m} \cosh(\kappa^{-}_{p+m,m}(z+h)) \\ & \left(A^{-}_{p+m,m} \cos(\theta_{p+m} - \theta_m) + B^{-}_{p+m,m} \sin(\theta_{p+m} - \theta_m)\right), \end{aligned} \tag{3.53}$$

$$\begin{aligned} \phi^{(2)}_{sup} =& \sum_{p=2}^{N} \sum_{m=1}^{M} F^{+}_{p-m,m} \cosh(\kappa^{+}_{p-m,m}(z+h)) \\ & \left(A^{+}_{p-m,m} \cos(\theta_{p-m} + \theta_m) + B^{+}_{p-m,m} \sin(\theta_{p-m} + \theta_m)\right) \end{aligned} \tag{3.54}$$

which can be used to calculate the second order contribution kinematics.

3.6 First order reliability method

Reliability is defined as the probability of a failure surface function, $g(\mathbf{X})$, to be greater than zero. A failure function is a relation which shows the status of a system (e.g. failed/not failed) in terms of input variables. For example, $g(F, S) = S - F$, where S is the yield strength of a beam and F is a load acting on the beam, is a failure surface function. Such beam will "fail" if it bears a

load, F, larger than its strength, S, which means $g(F,S) \leq 0$ and is "reliable" if $g(F,S) > 0$.

Hence, the reliability is computed by

$$R = P\{g(\mathbf{X}) > 0\} = \int_{g(\mathbf{X})>0} f_{\mathbf{X}}(\mathbf{X}) d\mathbf{X} \tag{3.55}$$

where $f_{\mathbf{X}}(\mathbf{X})$ is the joint *pdf* of $\mathbf{X}$, the input variables. Note that "surface" in the term failure surface function, refers to a hyper surface with one dimension fewer than the number of dimensions of the input variables.

The probability integration in (3.55) is visualized in Figure 3.1 for a case the failure function only depends on two random variables X_1 and X_2. All the points on each contour have the same probability density, $f_{\mathbf{X}}(\mathbf{X}) = c$. The integration boundary, failure surface $g(\mathbf{X})$, is also plotted on $X_1 - X_2$ plane. The reliability is the volume underneath $f_{\mathbf{X}}(\mathbf{X})$ on the side of the safe region, where $g(\mathbf{X}) > 0$.

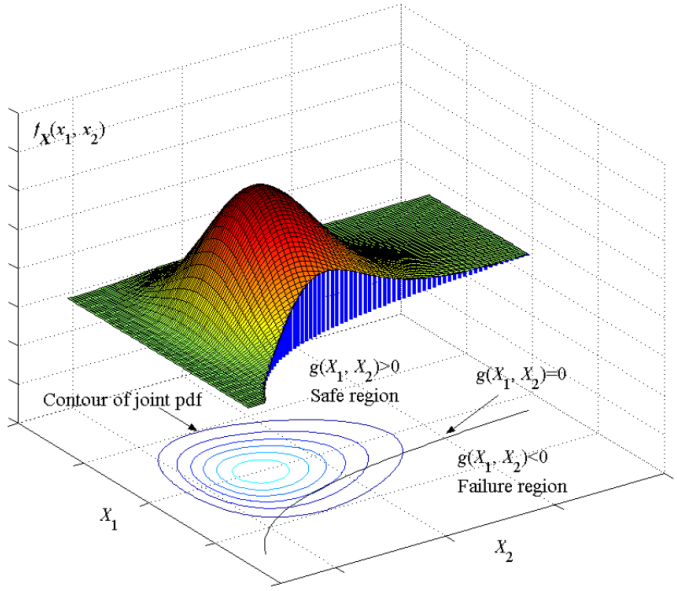

FIGURE 3.1: Probability integration (Du 2005).

Direct evaluation of the probability integration in (3.55) is very difficult because of high dimensionality of the typical engineering problems, complexity of the joint probability distribution function $f_{\mathbf{x}}(\mathbf{x})$ and nonlinearity of the integration boundary $g(\mathbf{X}) = 0$ (Du 2005). In many of the engineering applications the failure function $g(\mathbf{X})$ is a black-box model (or simulation model) such as finite element analysis, dynamic simulation, and computational fluid dynamics. To avoid these difficulties, approximate methods such as FORM are developed. FORM term is used when the failure function is approximated by the first order Taylor expansion (linear) (Du 2005). In this thesis the FORM combined with the first and second order wave theories

and a fully nonlinear potential flow solver was used to estimate the most probable shape of extreme waves on flat and sloped sea bed.

The approximation methods include two steps which firstly transform the random variables from their original random space into a standard normal space and secondly approximates the integration boundary. In the first step usually Rosenblatt transformation (Rosenblatt 1952) is used to transform the variables from any distribution to standard normal distribution on the condition that the cumulative distribution function of the random variables remain the same before and after the transformation. The Rosenblatt transformation is expressed by

$$F_{x_i}(x_i) = \Phi(u_i) \tag{3.56}$$

where $\Phi(.)$ is the *cdf* of the standard normal distribution.

The transformed standard normal variable is then denoted by

$$U_i = \Phi^{-1}\left[F_{x_i}(x_i)\right]. \tag{3.57}$$

For example, for a normally distributed random variable $X \in N(\mu, \sigma)$, (3.57) can be rewritten as

$$U = \Phi^{-1}\left[F_x(X)\right] = \Phi^{-1}\left[\Phi\left(\frac{X-\mu}{\sigma}\right)\right] = \frac{X-\mu}{\sigma}. \tag{3.58}$$

So X can simply be replaced by $\mu + \sigma U$. In this thesis the random variables, (for example a_n and b_n in (3.12)), were normally distributed with zero mean and unit variance.

After the transformation, the probability integration is expressed as

$$R = P\{g(U) > 0\} = \int_{g(\mathbf{U})>0} \Phi_{\mathbf{U}}(\mathbf{U}) d\mathbf{U} \tag{3.59}$$

where $\Phi_{\mathbf{U}}(\mathbf{U})$ is the joint pdf of $\mathbf{U}$. The joint *pdf* can be calculated as the product of the individual *pdf*s of standard normal distribution because of the independency of the random variables. Hence the integration can be written as

$$R = P\{g(U) > 0\} = \int_{g(u_1,u_2,\ldots,u_n)>0} \cdots \int \prod_{i=1}^{n} \frac{1}{\sqrt{2\pi}} \exp\left(-\frac{1}{2}u_i^2\right) \mathrm{d}u_1 \mathrm{d}u_2 \ldots \mathrm{d}u_n \tag{3.60}$$

which does not differ from (3.55) in accuracy.

In the second step the FORM uses a linear approximation (the first order Taylor expansion) to simplify the limits of the probability integral

$$g(\mathbf{U}) \approx L(\mathbf{U}) = g(\mathbf{u}^*) + \nabla g(\mathbf{u}^*)(U - u^*)^T \tag{3.61}$$

where $L(\mathbf{U})$ is the linearized performance function, $\mathbf{u}^* = (u_1^*, u_2^*, ..., u_n^*)$ is the

expansion point, T is transpose operator and $\nabla g(\mathbf{u}^*)$ is the gradient of $g(\mathbf{U})$ at $\mathbf{u}^*$. To minimize the accuracy loss, the expansion is performed around the most probable point (MPP) on the failure surface. This approximation is acceptable because as the integration goes away from the expansion point, the integrand function values will quickly diminish. To locate the MPP the following mathematical model has to be solved

$$\begin{cases} \max\limits_{u} \prod\limits_{i=1}^{n} \frac{1}{\sqrt{2\pi}} \exp\left(-\frac{1}{2}u_i^2\right) \\ \\ \text{subject to } g(\mathbf{u}) = 0 \end{cases}. \tag{3.62}$$

We have

$$\prod_{i=1}^{n} \frac{1}{\sqrt{2\pi}} \exp\left(-\frac{1}{2}u_i^2\right) = \frac{1}{\sqrt{2\pi}} \exp\left(-\frac{1}{2}\sum_{i=1}^{n} u_i^2\right) \tag{3.63}$$

therefore maximizing the left hand side of (3.63) is equivalent to minimizing the right hand of the same equation. Hence

$$\begin{cases} \min\limits_{u} \|\mathbf{u}\|^2 \\ \\ \text{subject to } g(\mathbf{u}) = 0 \end{cases} \tag{3.64}$$

is the model for finding the MPP, where $\|.\|$ is the Euclidean norm (magnitude) of a vector.

The solution to the model given in (3.64) is given in figure 3.2 for the two-dimension example case previously depicted in figure 3.1. Figure 3.2 shows that the MPP is the shortest distance from the failure function $g(\mathbf{u})$ to the origin. This distance, usually denoted by β, is called the reliability index.

The first order Taylor expansion of $g(\mathbf{U})$ is then used at MPP. Note that since $L(\mathbf{U})$ is a linear function of standard normal variables and so is itself normally distributed. Therefore, the probability of failure can be evaluated by

$$p_f \approx P\{L(\mathbf{U}) < 0\} = \Phi(-\beta) \tag{3.65}$$

and the reliability, integral in (3.60), is given by

$$R = 1 - p_f = 1 - \Phi(-\beta) = \Phi(\beta). \tag{3.66}$$

In the cases used in this thesis we were only interested in the combination of the random variables, $\mathbf{u}$, and the reliability index.

The Second Order Reliability Method (SORM) uses the second order Taylor expansion to approximate the performance function at the MPP. Figure 3.3 illustrates the difference between FORM and SORM method in approximating the limits of the integral in a simple case with two input variables. The actual limit of the integral in (3.55) is $g(\mathbf{U})$ which is shown in black while

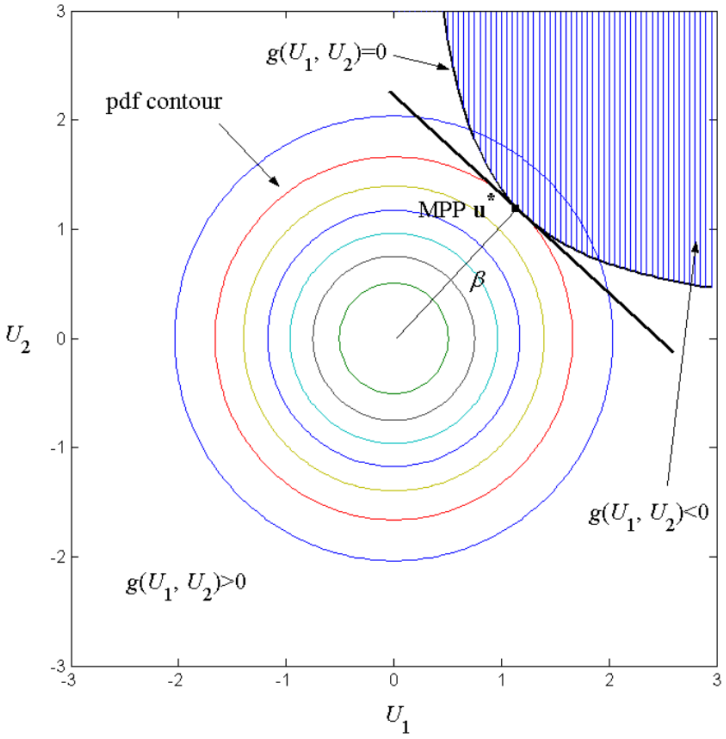

FIGURE 3.2: Probability integration in FORM (Du 2005).

FORM estimates this limit by a straight line, blue, and SORM approximation is a second order curve, red. As shown in this figure there is no difference between the MPP and the reliability index, β, in the two methods.

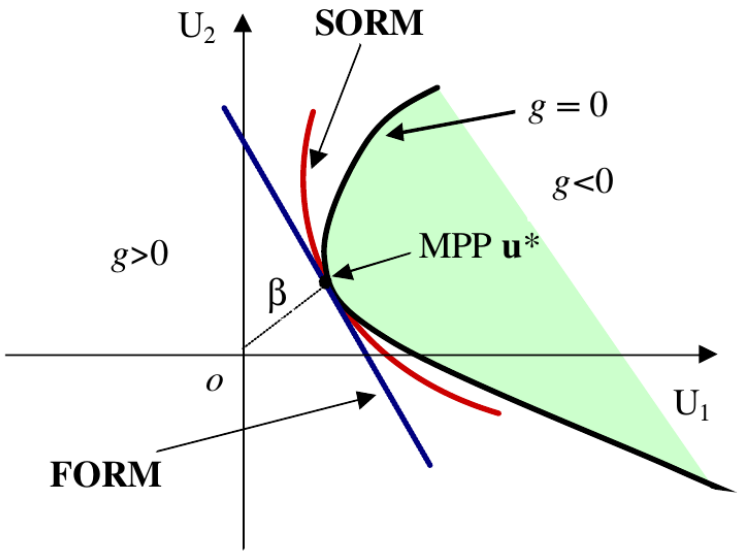

FIGURE 3.3: Comparison of FORM and SORM (Du 2005).

References

Dean, Robert (2013). *Water wave mechanics for engineers and scientists*. Vol. 53. 9, pp. 1689–1699. arXiv: arXiv:1011.1669v3.

Du, Xiaoping (2005). *Probabilistic Engineering Design*.

Naess, Arvid and Torgeir Moan (2012). *Stochastic Dynamics of Marine Structures*. Cambridge: Cambridge University Press.

Rosenblatt, Murray (1952). "Remarks on a Multivariate Transformation". In: *The Annals of Mathematical Statistics* 23.3, pp. 470–472.

Sharma, Jagat N. and Robert G. Dean (1981). "Second-Order Directional Seas and Associated Wave Forces." In: *Society of Petroleum Engineers journal* 21.1, pp. 129–140.

Tromans, Peter S, A R Anatruk, and Paul Hagemeijer (1991). "A New Model for the Kinematics of Large Ocean Waves Application as a Design Wave". In: *Proceedings of the First International Offshore and Polar Engineering Conference* 8.August, pp. 64–71.

Chapter 4

Numerical methods

Two numerical models were used through out this work for numerical computation of free surface flow, namely OceanWave3D (Engsig-Karup, Bingham, and Lindberg 2009) and waves2Foam (Jacobsen 2011). OceanWave3D is a fully nonlinear potential flow solver using a flexible order finite difference method. waves2Foam is a package for introducing and sampling free surface waves in the open source CFD toolbox OpenFOAM. In addition, the coupled version of OceanWave3D and waves2Foam solver (Paulsen 2013) was used in this thesis to reproduce the experimentally produced waves. In the coupled solver, information is transferred from the OceanWave3D to the waves2Foam domain to initiate and set the boundaries in the waves2Foam domain. The governing equations of the potential flow solver, OceanWave3D, are presented in section 4.1. In this section the used boundary conditions are also presented. The governing equations and boundary conditions for the Navier-Stokes solver, waves2Foam, are presented in section 4.2.

4.1 Fully nonlinear potential flow solver (OceanWave3D)

Engsig-Karup, Bingham, and Lindberg (2009) extended the development of a three-dimensions fully nonlinear potential flow solver, OceanWave3D, based on the model developed by Bingham and Zhang (2007). The numerical solver is capable of propagating fully nonlinear water waves up to the point of breaking. Flexible-order finite difference stencils are used to discretize the three dimensional Laplace equation. The velocity potential, ϕ, and the free surface elevation, η are used to describe the problem of non-breaking free surface waves. The free surface elevation is measured relative to the still water level. The gradient of the velocity potential $(\partial_x\phi; \partial_y\phi; \partial_z\phi)$ is used to calculate the physical fluid particle velocities. The evolution of the free surface is governed by boundary conditions. Kinematic and dynamic boundary conditions on the free surface are expressed as

$$\partial_t\eta = -\nabla\eta\cdot\nabla\tilde{\phi} + \tilde{w}(1+\nabla\eta\cdot\nabla\eta), \tag{4.1}$$

$$\partial_t\tilde{\phi} = -g\eta - \frac{1}{2}(\nabla\tilde{\phi}\cdot\nabla\tilde{\phi} - \tilde{w}^2(1+\nabla\eta\cdot\nabla\eta)) \tag{4.2}$$

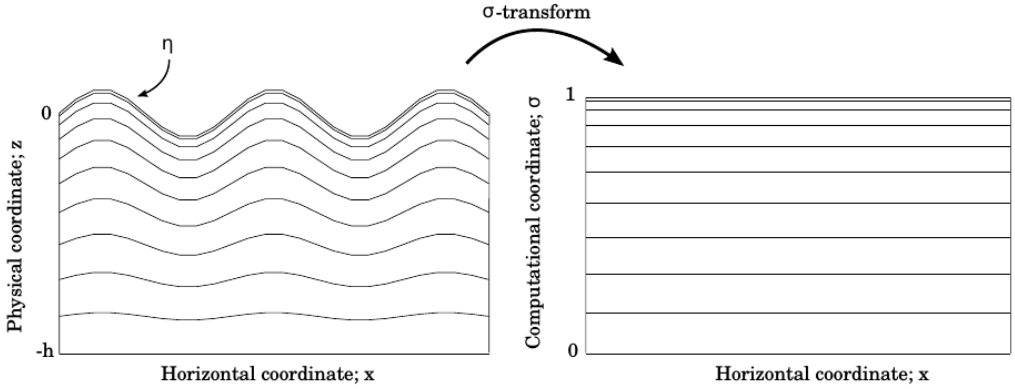

FIGURE 4.1: Sketch of the OceanWave3D mesh grid in physical coordinates and in the computational σ-domain respectively (Paulsen 2013).

where $\tilde{\phi} = \phi(\mathbf{x}, \eta)$ and $\tilde{w} = (\mathbf{x}, \eta)$ are the free surface quantities. Equation 4.1 expresses that on the free surface no out of plane velocities exist so a fluid particle located at the free surface must remain on the free surface. Equation 4.2 states that the pressure on the free surface is zero. Note that (4.2) is dependent on time and forces the wave to evolve in time. The velocity potential in the fluid volume, ϕ, must be calculated by solving the Laplace equation together with the bottom and free surface conditions. The bottom kinematic condition states that the flow cannot pass through the bottom:

$$\phi = \tilde{\phi}, \quad z = \eta \tag{4.3}$$

$$\nabla_H^2 \phi + \partial_{zz}\phi = 0, \quad -h \leq z < \eta \tag{4.4}$$

$$\partial_z \phi + \nabla_H h \cdot \nabla_H \phi = 0, \quad z = -h. \tag{4.5}$$

Here $h = h(x)$ is the water depth measured from still water level to the seabed. At all vertical boundaries, homogeneous Neumann boundary conditions are applied. The Laplace equation, (4.4), is solved by a flexible order finite difference scheme in a time-invariant $(\mathbf{x}, \sigma)$-domain. The non-conformal transformation in (4.6) is used to transform the time-dependent domain into a structured time-independent domain:

$$\sigma = \frac{z + h(\mathbf{x})}{\eta(\mathbf{x}, t) + h(\mathbf{x})}. \tag{4.6}$$

It is recommended to cluster the computational grid near the free surface where the largest gradients of the velocity potential are expected. A sketch of the clustered grid in the physical and computational σ-domain is presented in figure 4.1. Note that the transformation must change in each time step as $\eta(\mathbf{x}, t)$ changes in (4.6). From (4.6), the σ-transformation would break down when wave slope is vertical, breaking starts to occur or the free surface has more that one value at a location in the domain. Hence the method is only valid when η is single valued. A compact spatial Savitzky-Golay filter which

locally dissipates energy while averaging the velocity potential in a stencil of the domain is used to ensure the stability of the solver in the case of breaking and near breaking waves (Engsig-Karup, Bingham, and Lindberg 2009). The filter is not representative of the physical wave breaking.

For the potential flow solver wave generation and absorption, a source relaxation method following the work of Larsen and Dancy (1983) is used. A desired target solution is introduced gradually over a certain length in the domain termed as relaxation zone. The same approach is applied to the wave absorption to avoid reflections from the domain boundaries. Moreover, Paulsen (2013) implemented an inhomogeneous time varying Neumann boundary condition at the inlet boundary. By the means of this implementation, wave generation directly at the boundary is possible without the use of relaxation zones which reduces the domain size. The boundary condition of the Laplace (4.4) is given in

$$\frac{\partial \phi}{\partial x} = u \tag{4.7}$$

where $u = u(y, z, t)$. This type of wave generation is also convenient for numerical reproduction of experimental measurements. In such cases u corresponds to the linear representation of the velocity of the wave paddle.

4.2 Two-phase incompressible Navier-Stokes solver (waves2Foam)

OpenFOAM (Greenshields 2018) is a library of C++ codes that can solve partial differential equations. OpenFOAM is most commonly used for solving fluid dynamic problems. InterFoam is one of the OpenFOAM solvers that uses a volume of fluid (VOF) method to treat the free surface flows (Hirt and Nichols 1981). Waves2Foam is a wrapper around the InterFoam solver of OpenFOAM which uses relaxation zones to induce incident gravity waves (Jacobsen, Fuhrman, and Fredsøe 2012) in the domain.

InterFoam solves the continuity equation coupled with the momentum equations for incompressible fluids as given by

$$\frac{\partial u_i}{\partial x_i} = 0 \tag{4.8}$$

$$\frac{\partial \rho u_i}{\partial t} + u_j \frac{\partial \rho u_i}{\partial x_j} = -\frac{\partial p^*}{\partial x_i} - g_j x_j \frac{\partial \rho}{\partial x_i} + \frac{\partial}{\partial x_j}\left(2\mu_{\text{eff}} S_{ij}\right) + \sigma_T \kappa \frac{\partial \alpha}{\partial x_i} \tag{4.9}$$

$$S_{ij} = \frac{1}{2}\left(\frac{\partial u_i}{\partial x_j} + \frac{\partial u_j}{\partial x_i}\right). \tag{4.10}$$

where u_i are the velocities in the different directions, x_i are the coordinate directions, ρ is the local fluid density, p^* is the pressure excluding the hydrostatic potential $\rho g_j x_j$, g_j is the gravitational acceleration, μ_{eff} is the local effective dynamic viscosity and S_{ij} is the mean strain rate tensor. In this formulation the difference between a laminar and a turbulent flow is the calculated $\mu_{eff} = \mu + \mu_t$ where μ if the local fluid dynamic viscosity and μ_t is the turbulent dynamic viscosity. For the laminar case μ_t is equal to zero while for the turbulent cases it is calculated using a turbulence model. The fluid fraction is denoted by α which can take values between 0 and 1 for full air and water occupation of the cells respectively. Local fluid properties can be calculated by $\Phi = \alpha\Phi_{water} + (1-\alpha)\Phi_{air}$. Hence, for example, $\mu_{eff} = \alpha\mu_{water} + (1-\alpha)\mu_{air} + \mu_t$ in each cell. Note that the linear combination of water and air properties is a non-physical approximate method.

The last term in the (4) takes the surface tension, σ_T, into account by considering the surface curvature, κ, in the border of the two phases where the gradient of α is none-zero.

The transport equation of α is

$$\frac{\partial \alpha}{\partial t} + \frac{\partial \alpha u_j}{\partial x_j} + \frac{\partial}{\partial x_j}\left(\alpha(1-\alpha)u_j^r\right) = 0 \tag{4.11}$$

where u_i^r has the unit of velocity and is in the normal direction to the air-water interface. The last term compresses the region where α is between 0 and 1 and sharpens the free surface numerically. However, even with this term the free surface is spread between a few cells in the VOF model. Even though the equations are solved by a conservative finite volume scheme and the momentum of the fluid domain is conserved the kinematics in the interface region is usually inconsistent with single fluid wave theories.

For the simulations with turbulence modelling the kω–SST model implemented in OpenFOAM was used in this thesis. The implementation of the kω–SST model in OpenFOAM is based on Menter, Kuntz, and Langtry (2003). It should be noted that the density is removed from the incompressible fluid transport equations in the OpenFOAM implementation which was added again similarly to the work of Brown et al. (2014) and Devolder, Rauwoens, and Troch (2017).

4.3 Coupled OceanWave3D-waves2Foam

In this thesis the coupled solver OceanWave3D-OpenFOAM (Waves2Foam) developed by Paulsen (2013) was used to reproduce the experiment. The wave paddle signals were created from the first order wave generation (Dean 2013) similarly to the experiments and then the velocity of movement of the paddles were used as flux boundary condition in the nonelinear solver OceanWave3D to produce the waves. This method of generation is linearly consistent with the piston wave generation in laboratories. Differences at

higher order are expected because no piston or boundary movement is included in the numerical model. Nevertheless, good consistency with experiments using this approach, are presented in earlier works (Paulsen, Bredmose, and Bingham 2014; Bredmose and Jacobsen 2010; Bredmose and Jacobsen 2011) and as part of the DeRisk project (Bredmose et al. 2016; Ghadirian, Bredmose, and Dixen 2016; Ghadirian, Bredmose, and Schløer 2017).

Paulsen (2013) utilized the generic implementation of relaxation zones provided by the waves2Foam utility for the one-way coupling of OceanWave3D and waves2Foam solvers. The coupling zones are merely relaxation zones with the target solution ψ_{target} calculated by the potential flow solver. In the coupling zones, the velocity field and the free surface elevation, as the water volume fraction α, are updated at each time step based on the solution of the potential flow solver by

$$\psi = \chi\psi_{target} + (1-\chi)\psi_{com}, \quad \psi \in \{u, v, w, \alpha\} \tag{4.12}$$

where ψ_{target} is the target solution in time and space given by the potential flow solver, and ψ_{com} is the computed quantity obtained by solving the continuity and momentum equations (3), (4), and (6) in the OpenFoam, waves2Foam domain. The weighting factor, is defined as

$$\chi(\zeta) = 1 - \frac{exp(\zeta\beta) - 1}{exp(1) - 1} \tag{4.13}$$

where $\zeta \in [0; 1]$ is the local coordinate, with values from zero to one, where it is 0 at the outer edge of the coupling zone facing the potential flow solver and 1 at the inner edge. In the present work the shape factor $\beta = 3.5$ was used based on Paulsen (2013).

It may be noted that in the air-phase, where the solution is unknown in the potential flow solver, the fluid is assumed at rest and the target values of kinematics and volume fraction are set to zero in each time step. At the end of the OpenFoam domain, any scattered or reflected waves from the inner domain are gradually damped towards the potential flow solution in another coupling zone. This method minimizes the artificial reflections from the boundaries of the OpenFoam domain. In the coupling zones only the diffracted field should be removed as the undisturbed flow field is known from the potential flow solver (Paulsen 2013).

References

Bingham, Harry B. and Haiwen Zhang (2007). "On the accuracy of finite-difference solutions for nonlinear water waves". In: *Journal of Engineering Mathematics* 58.1-4, pp. 211–228.

Bredmose, Henrik and Niels G Jacobsen (2010). "Breaking Wave Impacts On Offshore Wind Turbine Foundations: Focusedwave Groups And CFD". In: *Proceedings of the ASME 29th 2010 International Conference on Ocean, Offshore and Arctic Engineering OMAE2010 June 6-11, 2010, Shanghai, China*.

Bredmose, Henrik and Niels G Jacobsen (2011). "Vertical wave impacts on offshore wind turbine inspection platforms". In: *Proceedings of the ASME 2011 30th International Conference on Ocean, Offshore and Arctic Engineering OMAE2011 June 19–24, 2011, Rotterdam, The Netherlands*. Vol. 436. 1896, pp. 13–32.

Bredmose, H. et al. (2016). "DeRisk - Accurate prediction of ULS wave loads. Outlook and first results". In: *Energy Procedia*. Vol. 94. Elsevier, pp. 379–387.

Brown, S.A et al. (2014). "An Evaluation Of Rans Turbulence Closuremodels For Spilling Breakers". In: *Coastal Engineering*. 1995, pp. 1–12.

Dean, Robert (2013). *Water wave mechanics for engineers and scientists*. Vol. 53. 9, pp. 1689–1699. arXiv: arXiv:1011.1669v3.

Devolder, Brecht, Pieter Rauwoens, and Peter Troch (2017). "Application of a buoyancy-modified k-ω SST turbulence model to simulate wave run-up around a monopile subjected to regular waves using OpenFOAM®". In: *Coastal Engineering* 125.June 2016, pp. 81–94.

Engsig-Karup, A. P., H. B. Bingham, and O. Lindberg (2009). "An efficient flexible-order model for 3D nonlinear water waves". In: *Journal of Computational Physics* 228.6, pp. 2100–2118.

Ghadirian, A., H. Bredmose, and M. Dixen (2016). "Breaking phase focused wave group loads on offshore wind turbine monopiles". In: *Journal of Physics: Conference Series* 753.9, p. 092004.

Ghadirian, Amin, Henrik Bredmose, and Signe Schløer (2017). "Prediction of the shape of inline wave force and free surface elevation using First Order Reliability Method (FORM)". In: *Energy Procedia* 00.January, pp. 18–20.

Greenshields, C J (2018). *OpenFOAM*.

Hirt, C. W and B. D Nichols (1981). "Volume of fluid (VOF) method for the dynamics of free boundaries". In: *Journal of Computational Physics* 39.1, pp. 201–225.

Jacobsen, Niels Gjøl (2011). "A Full Hydro- and Morphodynamic Description of Breaker Bar Development". PhD thesis, p. 200.

Jacobsen, Niels Gjøl, David R Fuhrman, and Jørgen Fredsøe (2012). "A wave generation toolbox for the open-source CFD library: OpenFoam". In: *International Journal for Numerical Methods in Fluids* 70.9, pp. 1073–1088.

Larsen, Jesper and Henry Dancy (1983). "Open boundaries in short wave simulations — A new approach". In: *Coastal Engineering* 7.3, pp. 285–297.

Menter, FR, M Kuntz, and R Langtry (2003). "Ten years of industrial experience with the SST turbulence model". In: *Turbulence, heat and mass transfer*, p. 8.

Paulsen, Bo Terp (2013). "Efficient computations of wave loads on off shore structures". PhD thesis.

Paulsen, Bo Terp, Henrik Bredmose, and Harry B. Bingham (2014). "An efficient domain decomposition strategy for wave loads on surface piercing circular cylinders". In: *Coastal Engineering* 86, pp. 57–76.

Chapter 5

Summary of the papers

Paper 1: Breaking phase focused wave group loads on offshore wind turbine monopiles

This article has the aim of validating previously developed models at DTU, namely the OceanWave3D potential flow wave model and a coupled solver of OceanWave3D-OpenFOAM, against measurements of focused wave group impacts on a monopile. Four highly nonlinear cases are considered, based on two sea states with and without directional spreading. Free surface elevation, inline force and pressure time series on the cylinder wall are compared for the model results and experimental measurements. In addition, the wave-induced pressure is defined as the pressure excluding the hydrostatic pressure below the still water level and its distribution on the monopile is examined at the time of peak force and discussed in terms of shape and magnitude.

Good consistency between the measurements and model results for the free surface elevation, in-line force and wave-induced pressures is found. The OceanWave3D inline force results, obtained by application of the Rainey force model, follow the experimental force history closely, although no representation of wave-structure interaction is visible. The inline force results from the coupled CFD solver, show slight under-prediction of the peak forces for the 2D and 3D groups of smallest amplitude, while the peaks for the main waves of the two large groups are reproduced more consistently. The wave-structure interaction including the secondary load cycle of in-line force are well reproduced using the coupled solver. Point pressure measurements are also reproduced by the coupled OceanWave3D-OpenFOAM solver consistently, even above SWL. The spatial pressure fields for the largest 2D and 3D wave groups at the time of maximum force show that the steep but non-breaking 2D impact created a strong run-up at the cylinder front, and a pronounced simultaneous pressure at the back side by stagnation of water. In the 3D impact results similar strong pressures at the front side are visible, but with no counter-acting stagnation pressure at the back is visible.

Paper 2: Extreme wave impacts on monopiles: re-analysis of experimental data by a coupled CFD solver

In this paper the two numerical models, OceanWave3D and OceanWave3D-waves2Foam, are used to reproduce measured extreme events in one sea state. The measured wave episodes which are associated with the two largest peak moments of a 3 hour test (exceedance probability of 0.05% and 0.3%) are selected. Both these wave episodes have larger maximum inline force and bending moment than a focused wave group ($H = 1.86H_s$) in the same sea state even though they have similar wave height to the focused wave group. Time series of free surface elevation, depth integrated forces, bending moment at the sea bed and pressure time series at 5 different heights on the cylinder are compared for two episodes between the measurements and the numerical models. In addition, the numerical pressure field on the monopile at impact is analysed and stagnation pressures at the back side of the cylinder, in addition to the main impact pressure at the front side are observed.

A good agreement between the OceanWave3D free surface elevation results and the measurements in the reproduction of the first selected wave episode is observed. However, the OceanWave3D free surface elevation results for the larger selected event, has smaller crest height than the measurements. For small values of the inline force, the waves2Foam results provides good agreement with the measurements. For the larger values of inline force, the consistency decreases largely due to different breaking than the experiments. The sensitivity of the strong impact loads to the state of wave breaking is well known. This is also observed in the numerical results, where sensitivity to the start time before the main impact is visible. Here the best matching results for event 2 are shown.

Paper 3: Prediction of the shape of inline wave force and free surface elevation using First Order Reliability Method (FORM)

The focus of this paper is on identifying the extreme wave episodes which create a certain maximum crest height or inline force. FORM is used systematically to estimate the time history of the most likely extreme wave shapes. Two parameters of maximum crest height and maximum inline force are used to define the extreme events. FORM is applied to first and second-order irregular waves with and without directional spreading of the waves. The application is validated against, the New Force model, which is introduced as the force counter part of the New Wave theory, and the New Wave theory. The results of FORM and New Force are identical for first-order irregular waves as expected and show minor deviations at second order.

The FORM results are validated against wave averaged measurements of the same criteria for crest height and peak force value. Relatively good agreement between the FORM results of free surface elevation including the second-order effects, and the wave averaged measurements is observed. Qualitative agreement is also observed in the inline force time series reproduced using the numerical method, however, the discrepancies are larger than for the free surface elevation. The discrepancies between the FORM results and the measurements is found to be a result of more nonlinearity in the inline force calculation and exclusion of the drag forces above still water level in the present analysis. The relative error between the reproduced second-order free surface elevation and the measurements is larger for more nonlinear target values so it is expected that with a more nonlinear model the agreement between the FORM results and the measurements will improve. This paper is one step towards more precise prediction of extreme wave shape and maximum load and is followed up by the next paper in this thesis, where the FORM methodology is applied to fully nonlinear force calculations. Such waves can replace the stream function wave or New Wave theory that are used in ULS calculations in offshore structure design process since the current commonly used wave theories suffer from limitations such as symmetry around the crest.

Paper 4: Investigation of the effect of the bed slope on extreme waves using First Order Reliability Method

The effect of the bed slope on the force statistics and the shape of the force time history is investigated in this paper using the fully nonlinear wave model, OceanWave3D, and FORM analysis. The wave averaged experimental force and free surface elevation time series are used to validate the model results. A good improvement over first-order and second-order results is observed by the use of the fully nonlinear wave model. The average deviation between the model results and the wave averaged measurements is about 10%. The order statistics for force peaks are also calculated for the measurements and compared to the exceedance probabilities calculated from the model results. For given exceedance probability value a close agreement is observed between the measurements and the model peak forces.

The investigation is then extended to two numerical domains on flat or sloping bed and the time history of the inline force and free surface elevation of the most probable wave episode with a target force peak is compared between the two model results. The diameter, depth at the structure and significant wave height are kept the same between the two model domains. It is observed that in the low Ursell number cases force histories are very similar between flat bed and sloped bed. However, in the high Ursell number cases larger skewness is observed in the flat bed cases inline force time series. The exceedance probabilities for the same peak inline force are larger on sloped bed cases. The ratio of exceedance probability is found to increase with force level except for the sea states with larger Ursell number where the numerical results are affected by strong nonlinearity.

The four-phase separation is next used to isolate the higher-harmonic contributions. The relative contribution from the higher-harmonic force components increase with the force peak level. The relative contribution from the first, second and third harmonic are similar between flat bed and sloped bed. The spurious second-harmonic is stronger in the flat bed cases. It is also observed that the phase shift between different harmonics is constant and does not change with the depth, force peak or the slope.

This paper shows the capability of FORM method in combination with the fully nonlinear solver for determination of design waves. The combination of FORM and a fully nonlinear wave model, such as OceanWave3D, enable designers to get the average probability levels and time histories for extreme events with more certainty.

Paper 5: Detailed force modelling of the secondary load cycle

The cause of the secondary load cycle is the focus of this paper. Initially a two-phase free-surface RANS solver is validated against generic cases of turbulent flow over a wall, wave-boundary layer flow for $1 \cdot 10^4 < Re < 1 \cdot 10^7$, 2D drag on a cylinder for $1 \cdot 10^2 < Re < 2.5 \cdot 10^5$ and 2D oscillatory flow for three sets of flow parameters $Re = \{5.8 \cdot 10^4, 9 \cdot 10^4, 1.7 \cdot 10^5\}$ and $KC = \{6, 12, 18\}$. Afterwards a measured wave-averaged focused wave group impact is reproduced using the RANS solver and an excellent match is observed in inline force and free surface elevation time series between the model results and measurements. Also, a good match is observed for the measured front face pressures.

The numerical solution is next analysed in more detail. It is understood that the secondary load cycle event is confined to an upper region ranging from just above the still water level and 1.5 diameter down. It is caused from suction effects around the still water level on the back side, $\frac{D\rho u_z}{Dt}$ term. The suction is due to the rapid decrease of water level below the generated water column at the back of the cylinder, which at this time has only just begun its downward motion. The preceding force dip is aided by the hydrostatic pressure from the water column and the succeeding dip is aided by wash-down effects on the front side.

The effect of the vortices behind the cylinder are also investigated separately by comparing results of computations with slip and no-slip conditions on the cylinder wall. Vortices give rise to a slight force increase and they last over the whole span of the secondary load cycle. They are, therefore, not correlated to the secondary load cycle. The investigation shows that the global force history is not strongly affected by the boundary layer as previously anticipated.

Paper 6: Pressure-impulse of a breaking wave on a monopile

A pressure impulse model of a wave impact on vertical cylinders is presented in this paper. A simplistic geometry is used to represent the wave impact. Initially 3D box generalization of the 2D wall case is investigated and a closed form solution is given for this case. Afterwards, a wedge shaped impact on a cylinder is used to model the impact of a wave on a vertical circular cylinder. The effective variables in the model which can be identified from the wave parameters are denoted and their effect on the pressure impulse is visualized.

We find that as the crest length increases the pressure impulse increases towards an asymptotic value, as is also the case for the 2D wall problem. For small cylinder radius, the pressure impulse increases with radius of the cylinder due to the larger impact absorbing area and decreases again as the inner radius approaches the outer radius. This is explained with the decrease of the initial momentum of the impacting water. Finally, the pressure impulse increases with the horizontal width of the impact zone in the 3D box model and in the wedge impact on the cylinder model. Since the extend of the impact on the cylinder is not usually known the maximum angle of impact is kept as a free parameter which can be used to tune the model.

The model is next validated against numerical results for a wave impact for a phase- and direction-focusing wave group. As suggested previously, the maximum impact angle is determined by calibration against the force impulse. A good match of the pressure impulse fields is found between the CFD results and the suggested model in terms of vertical and azimuthal variation. The integrated force impulse is also calculated from the CFD model, the suggested model and two most commonly used models in marine engineering and better consistency than other methods is observed between the suggested model and the CFD results for a sensible value of $\theta_{max} = \pi/3$. The suggested model is simple and yet sufficiently accurate for impact problems and it provides a robust representation of the pressure impulse field, based on a limited number of input parameters.

Part II

Papers

Paper 1

Breaking phase focused wave group loads on offshore wind turbine monopiles

* *This paper is published in the* ***Journal of Physics: Conference Series 753 (2016) 092004*** *as part of the proceedings of the conference* ***The Science of Making Torque from Wind (TORQUE 2016)****.*

Amin Ghadirian[1], Henrik Bredmose[1], Martin Dixen[2]
[1] DTU Wind Energy, Nils Koppels Alle Building 403, DK-2800 Kgs. Lyngby, Denmark
[2] DHI, Agern Alle 5, DK-2970 Hørsholm, Denmark
E-mail: amgh@dtu.dk

Abstract

The current method for calculating extreme wave loads on offshore wind turbine structures is based on engineering models for non-breaking regular waves. The present article has the aim of validating previously developed models at DTU, namely the OceanWave3D potential flow wave model and a coupled OceanWave3D-OpenFOAM solver, against measurements of focused wave group impacts on a monopile. The focused 2D and 3D wave groups are reproduced and the free surface elevation and the in-line forces are compared to the experimental results. In addition, the pressure distribution on the monopile is examined at the time of maximum force and discussed in terms of shape and magnitude. Relative pressure time series are also compared between the simulations and experiments and detailed pressure fields for a 2D and 3D impact are discussed in terms of impact type. In general a good match for free surface elevation, in-line force and wave-induced pressures is found.

Introduction

Cost-reduction for the substructures is an important part in reducing the cost of offshore wind energy. A central element here is an accurate determination

of the Ultimate Limit State wave loads with limited uncertainty. The current method for calculating such loads is to use the stream function theory (Dean 1965) combined with a background sea state time series. This method is easy to implement and benefits from limited complexity in the parameters that should be chosen. However, the stream function theory is associated with assumptions such as 2D wave motion, symmetry in the crest of the waves, periodicity and a flat sea bed. This approach also neglects the effect of breaking waves which is the focus of this study. To overcome these, other nonlinear models are developed. However these models are not still vastly used in the industry, partly because of only limited validation against design cases.

Christensen, Bredmose, and Hansen 2005 investigated the wave forces and wave run-up from large regular waves on an offshore wind-turbine foundation on a sloping bed by application of an in-house developed Navier-Stokes solver. They used the Volume Of Fluid method (VOF) to capture the free surface. The free surface elevation and run-ups reproduced by the model showed a good agreement with experimental reference results. A good agreement was also found between the small wave height maximum force with linear diffraction theory and the Morison equation (Sumer and Fredsøe 1997).

Bredmose et al. 2006 investigated the impact of irregular waves on a current on a gravity wind turbine foundation. The results were compared to experiments. Furthermore, Bredmose and Jacobsen 2010 used the InterFOAM solver of OpenFOAM to perform a numerical investigation of breaking wave impacts on an offshore wind turbine foundation in intermediate water depth. In this study they used the focused wave group technique to reproduce the most probable extreme wave in the given sea state. The resulting in-line forces were compared to results from the linear theory and the Morison equation. It was seen that the in-line forces estimate by the latter method gave smaller peaks than the CFD results. They also extended the study (Bredmose and Jacobsen 2011) by investigating the vertical wave impacts on offshore wind turbine inspection platforms. However, both studies lacked the validation of the numerical results against experiments.

Hildebrandt and Schlurmann 2012 used Ansys CFX model to reproduce wave breaking local pressures and forces on a tripod support structure. The study investigated the interaction of different types of breaking waves with the structure. A good agreement was shown for most of the cases between the impact pressure distributions seen in the experiments and in the numerical simulations.

The main goal of the present article, as part of the DeRisk project (Bredmose et al. 2016), is to provide systematic validations for two other open source models specially in case of breaking waves. One validated model is the fully nonlinear potential flow solver OceanWave3D (Engsig-Karup, Bingham, and Lindberg 2009) which is able to create 3D nonlinear waves in a relatively big domain. This model has also been coupled to the OpenFOAM tool box, Waves2FOAM (Jacobsen, Fuhrman, and Fredsøe 2012) , by Paulsen, Bredmose, and Bingham 2014; Paulsen 2013. This coupled solver is investigated in this study as the second model. Validation cases for regular waves

and the Waves2FOAM toolbox have already been presented by Paulsen et al. 2014 which also studied the mechanism for creation of the secondary load cycle, that creates an additional force peak after the main wave impact. The paper of Paulsen, Bredmose, and Bingham 2014 presents validation cases of the coupled solver for four cases of regular, irregular and 2D phase focused waves and 2D focused wave group tests of Zang, Taylor, and Tello 2010.

In the present paper, we provide further validation of the OceanWave3D and the coupled solver against new systematic measurements of focused wave group impacts on a monopile. Time series of free surface elevation and depth integrated forces are compared for two 2-dimensional and two 3-dimensional groups. Also the pressure distribution over the cylinder at the moment of impact by the focused wave is discussed. Computational pressure time series are further compared to measurements. Finally, the detailed pressure fields of a 2D and a 3D impact are discussed and linked to the type of impact.

Methodology

The experiments

The experiments were conducted in the shallow water basin at DHI Denmark at a scale ratio of 1:50. The full scale diameter of the monopile was 7 m and the full-scale depth of water was 33 m. The monopile was mounted on two force transducers — one at the top and one at the bottom — to measure the in-line force and the moment. Pressure sensors were installed facing the incident wave direction. In addition 31 wave gauges were installed to measure free surface elevation for the wave propagation towards the cylinder and around it. The monopile was placed 7.3 m from the wave makers (lab scale) and phase focused wave groups were created with their nominal linear focus point at the monopile center so that breaking and ringing forces could be measured. The wave generator was a piston wave maker driven with linear wave generation theory.

The numerical model

The coupled OceanWave3D and OpenFOAM solver (Paulsen 2013) was used to reproduce the phase focused waves. Waves2Foam is a package added to OpenFOAMs InterFoam solver to allow generation of surface waves in relaxation zones close to the boundaries (Jacobsen, Fuhrman, and Fredsøe 2012). InterFoam uses a volume of fluid (VOF) method to treat the free surface flows (Hirt and Nichols 1981).

To reproduce the experimental results the wave paddle velocity signal of the lab was used to produce the waves nonlinearly by the OceanWave3D solver. The signals were used as a flux boundary condition in the OceanWave3D domain. While this method of generation is linearly consistent with the piston generation in the lab, differences at the second and higher orders can be expected due to the lack of piston movement in the numerical

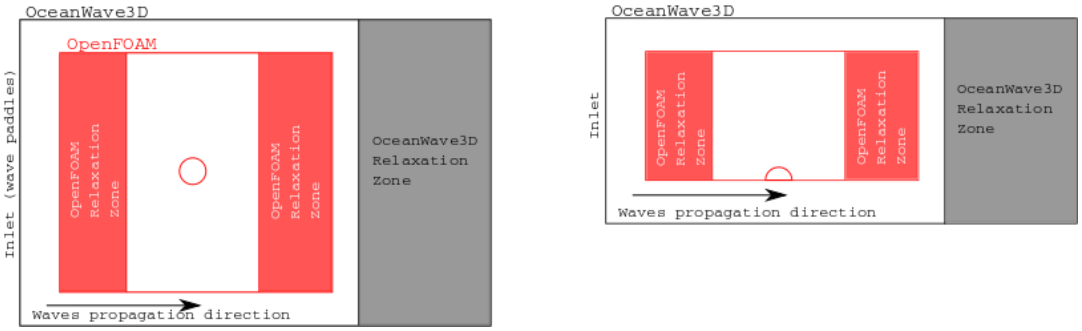

FIGURE 1: The computational domain for 3D (left) and 2D (right) phase focused wave groups.

TABLE 1: Characteristics of the waves

	Full scale				Lab scale				
Case	h [m]	Hs [m]	Tp [s]	Spread angle [deg]	Ursell	$k_pH_{ma:}$	k_ph	$\frac{h}{gT_p^2}$	$\frac{H_{max}}{gT_p^2}$
204	33	7.5	12	13	13.3	0.49	1.1	0.023	0.0102
206	33	9.5	12	13	16.9	0.63	1.1	0.023	0.0129
209	33	7.5	12	0	13.3	0.49	1.1	0.023	0.0102
211	33	9.5	12	0	16.9	0.63	1.1	0.023	0.0129

model. Good results with this approach, however, have been obtained in earlier works (Paulsen et al. 2014; Bredmose and Jacobsen 2010; Bredmose and Jacobsen 2011) and also in the context of the present campaign (Bredmose et al. 2016). In figure 1, top views of the computational domains are shown for the 3D and 2D phase focused wave groups cases. For the 2D wave groups cases, the symmetry of the solution was utilized to reduce the OpenFOAM domain to half size. Even though the 3D focused wave group cases are also symmetric, a full domain was applied. In both cases, the embedded OpenFOAM domain was next driven with waves from OceanWave3D through a relaxation zone (Jacobsen, Fuhrman, and Fredsøe 2012).

Results

In table 1 the characteristics of the investigated wave groups are summarized. For all cases, a JONSWAP wave spectrum was used. The characteristic wave number, k_p, of each case was calculated using the given peak wave period, T_p, and the linear dispersion relation. The theoretical maximum wave height, H_{max}, was calculated using the relation $H_{max} = 1.86H_s$ (Clauss, Schmittner, and Hennig 2006) where H_s is the significant wave height. The spreading angle is defined as the maximum angle at which the wave components moved toward the nominal focus point in 3D for the focused wave groups. Obviously the spreading angle is zero for the 2D phase focused wave groups.

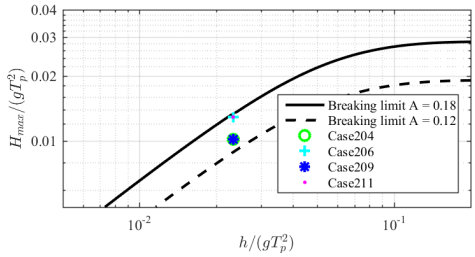

FIGURE 2: Characteristics of the investigated phase focused wave groups in relation to breaking criteria.

The Ursell number, $Ur = \frac{HL^2}{h^3}$, in table 1 represents the nonlinearity of the waves while the $k_p H_{max}$ measures the steepness of the waves. The cases 206 and 211 thus contained the most nonlinear and the steepest waves. The last two columns provide input to an assessment of the investigated waves in relation to a breaking criteria. This breaking criteria is calculated using the following equation (Goda 2010).

$$\frac{H_b}{gT_p^2} = A\{1 - \exp(-1.5\pi\frac{h}{L_p})\}\frac{\tanh(kh)}{2\pi} \tag{1}$$

Here H_b is the breaking wave height, T_p and L_p are the peak wave period and the peak wave length assuming a linear dispersion and constant water depth. Wave breaking for irregular waves occurs for $0.12 < A < 0.18$.

The wave conditions of the four tests are plotted together with the breaking criterion (1) in figure 2. Looking at this plot it can be seen that the cases 204 and 209 included less probable waves to break in 33 m deep water compared to cases 206 and 211. However all of the wave groups are predicted to contain breaking at some point.

Free surface elevation

In figure 3 non-dimensional time series of the free surface elevation for all the investigated wave groups are presented. The cases on the left hand side, namely cases 209 and 211, are 2D focused wave groups while the ones on the right hand side, cases 204 and 206, are the 3D phase focused wave groups. It should be mentioned that the wave gauges in these cases are located 0.2 m upstream from the cylinder in both the physical and computational domains.

Looking at the blue curves in this figure, the wave gauges in the basin show the passage of the focused wave groups clearly by the increase in the oscillation amplitude of free surface elevation until the focus time. After the focus time the amplitude of surface elevation decreases again to reach $\eta = 0$. The time axis of all the plots have been shifted such that the focus time occurs at $\frac{t}{Tp} = 0$. It is clear that the focus wave height is larger in the cases 206 and 211, consistent with the larger significant wave height for these cases.

For the waves in figure 3 it can be seen that after the passage of the largest waves, a small crest occur within the next trough. After investigating the celerity of these bumps, using time series from neighboring wave gauges,

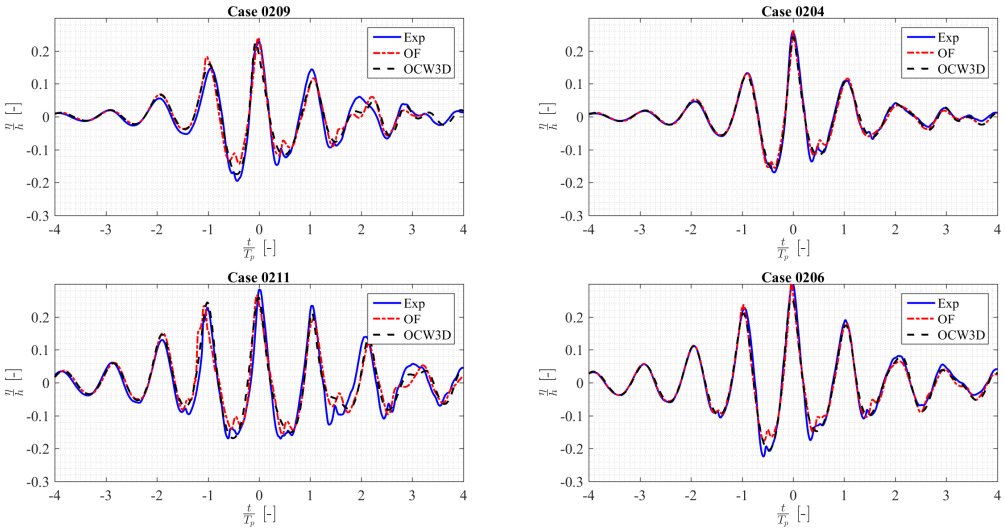

FIGURE 3: Non-dimensional free surface elevation time series at 7.1 m from the wave paddles.

and assuming a linear dispersion relation, it was found that the period of these small waves are about one third of the main incident waves. It was thus concluded that the nature of these small waves is the third-harmonic reflections of the main waves from the cylinder.

It is also worth mentioning that from the plots, the growth of surface elevation to the focus wave is more gradual in the 2D cases. This can be explained by knowing the process of phase focusing, in which a focused wave is created by superposition of many waves. In 3D cases these waves can come from different directions and simply join at the focus point, while for the 2D cases, all wave components come from the same direction and therefore have to focus through differences in phase speed.

From figure 3 it is clearly seen that in all of the cases the free surface elevation calculated by OceanWave3D is consistent with the ones from measurements in relation to phases and amplitude. Only minor differences can be seen between the OceanWave3D generated curves and the measurements.

However, it is seen that after the main wave groups pass the focus point, the surface elevation calms down in the measurements but the surface elevation in the OceanWave3D keeps oscillating for a longer time. A likely reason for this is reflection of waves from the lateral boundaries of the OceanWave3D model which were modelled as slip-walls.

Comparing the measurements and the OpenFOAM simulations in the same figure it is seen that the phases and the amplitudes of the OpenFOAM surface elevations are generally consistent with the measurements. However it can be seen that the surface elevation was marginally over-predicted in the troughs of the waves by OpenFOAM in all cases.

It is worth mentioning that the third order harmonic reflected waves can also be seen in the OpenFOAM simulations with the same order of magnitude and phase as in the measurements. In the OceanWave3D computations, however, these waves cannot be seen as no monopile was present in the domain of OceanWave3D.

In-line forces

Figure 4 shows the non-dimensional in-line force time series of the investigated cases. Similarly to the previous figure, the plots on the left hand side are for the 2D wave groups while the plots on the right hand side are for the 3D wave groups.

The measured in-line force time series show the same general behavior as the surface elevation plots presented in figure 3. It should be mentioned that unlike surface elevations that were measured and computed at 7.1 m from the wave paddles, the forces are measured and computed at the monopile location, 7.3 m from the wave paddles. Even though the surface elevations are measured 0.2 m up stream the monopile the in-line force time series maximize almost at the surface elevation focus time, $\frac{t}{Tp} = 0$. This is expected as the flow is inertia dominated. The Keulegan-Carpenter (KC) number is smaller than 6 in all cases (Sumer and Fredsøe 1997). For inertia dominated flows the force is in phase with $\dot{u}$ so 90 deg to u and η. Hence, the force peak can be expected to occur earlier than the arrival of the wave crest. For OceanWave3D, the in-line force was computed with the Morison force model (Sumer and Fredsøe 1997) with input of the undisturbed wave kinematics at x=7.3 m. The drag and inertia coefficient were 0.5 and 1.98 respectively, selected from experiment tables, Sumer and Fredsøe 1997. The OpenFOAM forces were obtained by direct pressure integration over the cylinder area.

Additionally to the main force peak, the force peak of the largest waves is seen to be followed by an additional peak, occuring in the trough of the force signal. These loads can be explained by the secondary load cycle (Paulsen et al. 2014; Grue and Huseby 2002).

In addition, by comparison of the in-line force time series in figure 4 and the free surface elevation time series in figure 3 it is interesting to see that even though the waves are temporally symmetric, the forces time series are leaning backward. This can be explained by the effect of the inertia terms in the in-line forces, which is a well known feature of nonlinear wave loads.

Looking at figure 4 generally a good agreement between the measurements and forces computed in OceanWave3D can be seen. There are only seldom inconsistencies between the measurements and the numerical results. These inconsistencies are seen mostly at the troughs of the in-line force time series. However, a general inconsistency between the OceanWave3D results and the preceding wave crests can be seen in all cases except case 211. At this point the OceanWave3D result is always above the experiment results. This can be seen in the peak before the preceding peak of case 211 too ($\frac{t}{T_p} = -2$).

The most significant difference between the experiments and the OceanWave3D results is observed in the preceding trough of the focus wave in case 211 and the crest before that. Investigating the videos from the experiments it was observed that the wave breaks at this time and hence fills in the coming trough. This, obviously, cannot happen in the potential flow solver.

Comparing the measurements and the OpenFOAM results we can see that the CFD simulations of all cases are mostly consistent with the measurements. The only two inconsistencies are observed in the main focused wave

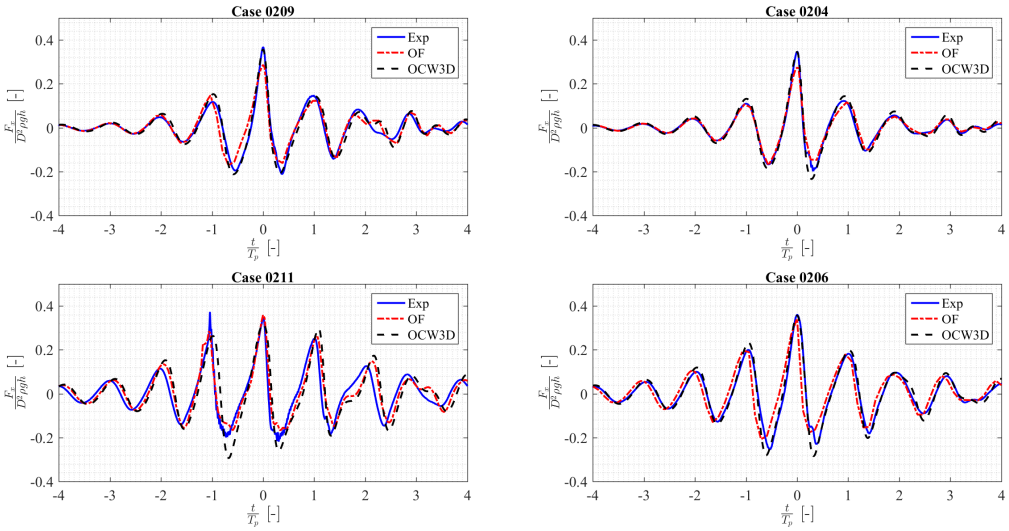

FIGURE 4: Non-dimensional in-line force time series at the location of the cylinder (7.3 m from the wave paddles).

in cases 209 and 204. In these cases the crests of the in-line forces of the focus waves are under predicted in CFD simulations.

For the steeper cases 206 and 211 the waves are breaking at impact time in the former case and is highly non-linear in the latter case. The peak loads, however, are predicted with good accuracy by the Navier-Stokes solver.

The additional peaks in the troughs of the in-line force time series, observed in the measurements, are also reproduced in the OpenFOAM simulation as seen in figure 4. It can also be seen that the backward inclination of the in-line forces are reproduced in the OceanWave3D and OpenFOAM simulation results.

It is worth mentioning that the preceding wave in case 211 shows the same behavior in the CFD results as in the experiments. A small crest on top of the crest can be seen which in the CFD solution, where the impacting wave is broken and have broken up to a series of smaller surface rollers on top of the main wave. However, the crest of the in-line force is under predicted in the OpenFOAM simulation. Another major inconsistency between the OpenFOAM results and the experiments is in the case of 206 in which the preceding and the following troughs of the focus wave are predicted to produce larger in-line forces.

To investigate these inconsistencies, the pressure distribution and time series are compared between the OpenFOAM results and the experiments.

Wave-induced pressure distribution at the cylinder

In figure 5to 6 (left hand side) the contour plots of the wave induced pressure on the half cylinder is shown for the cases 211 and 206 for the time instant of

maximum in-line force. The wave-induced pressure is here defined as

$$p_{\text{wave induced}} = \begin{cases} p_{\text{physical}} + \rho_{\text{water}} g z & z < 0 \\ p_{\text{physical}} & z > 0 \end{cases} \tag{2}$$

and is thus the physical pressure minus the pressure that would be present in case of still water. In the same plots the locations of the pressure sensors mounted on the cylinder in the experiments are marked with black circles. It should be noticed that in this plot the horizontal axis is the azimuthal position in relation to the cylinder. The cylinder faced the wave paddle at $\theta = 180\,\text{deg}$.

On the right hand side the wave induced pressure time series measured and computed from the OpenFOAM results are presented in five plots.

For the 2D wave (case 211) of figure 5, the pressure time series at the location of sensors below SWL show a similar behavior as the surface elevation time series. The time series related to the sensors above SWL, however, are sometimes hit by water (when the surface elevation is high enough) and sometimes they output constant zero pressure. It can be seen in these plots that the higher the location of the sensor is, the fewer waves in the wave group can reach to that height. Hence fewer peaks in the wave induced pressure time series is visible. Further, the magnitude of the peak pressure at the time of maximum in-line force ($t/T_p \approx 0$) decreases with height for the sensors above SWL.

For the two bottom sensors, the measured and computed pressure histories have the same general shape and magnitude, although with some over-prediction of the pressures in the troughs before and after the main focused wave.

For the next 2 sensors (located 0.08 m and 0.12 m above the SWL) there are only marginal inconsistencies between the measurements and computational results. The largest inconsistency can be seen at the location of the highest sensor, 0.16 m over SWL. In this case the time history and peak pressure for the main focused wave is reproduced correctly in the CFD solution, while pressure of the the preceding and the following waves are under-estimated. This behavior, however, is consistent with the in-line force of the preceding wave shown in figure 4 which is at a broken stage at the time of impact.

A similar comparison of experimental and numerical pressures for the 3D wave of case 206 is provided in figure 6. Similarly to the 2D case, the wave induced pressure in the troughs before and after the main focused wave are over-predicted in the numerical solution. This can explain the over prediction of in-line force in figure 4 case 206 in the preceding and the following wave troughs of the focus wave. Another significant difference between the OpenFOAM computed pressure and the measurements can be seen in the crest of the preceding waves at the location of the three sensors above the SWL. Both the experimental and numerical pressure signals contain multiple peaks following each other at a rapid time scale within the same wave event. While this indicates that the impacting wave is breaking, the breaking behaviour is seen to be differently distributed in height, since the experimental

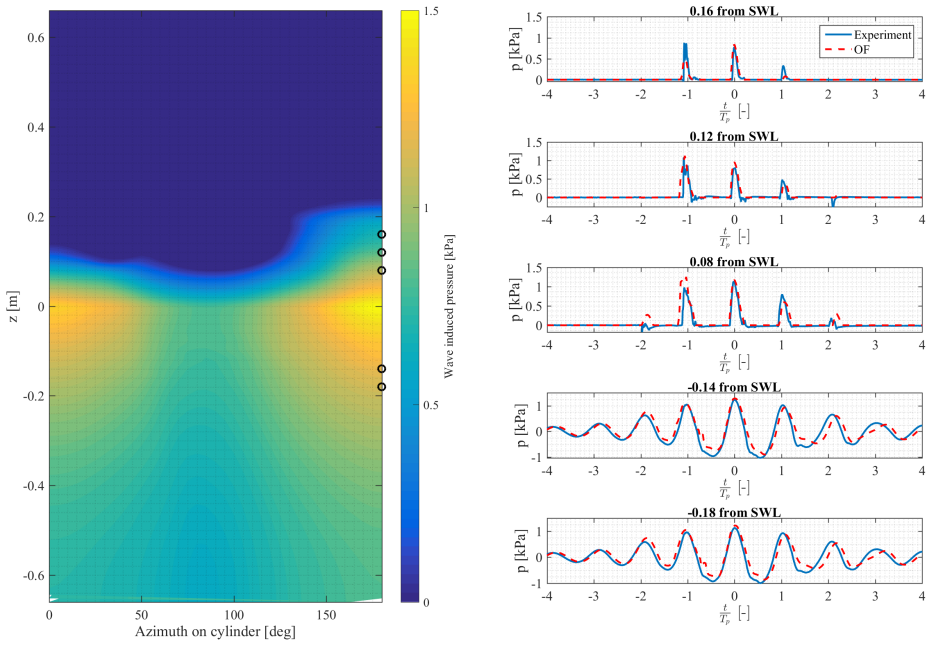

FIGURE 5: Dynamic pressure distribution contour plot (left hand side) and pressure time series measured and computed in the OpenFOAM at five different heights (right hand side). Case 211.

breaking is visible at the sensor at $z = 0.12$ m, while the numerical solution shows signs of breaking at the lower sensor at $z = 0.08$ m.

In figure 7 two snapshots of the impact of the focus waves for cases 211 and 206 are shown. In both snapshots the direction of the transmission of the waves is from right to left. On the left hand side, case 211, the build up of a water column behind the cylinder can be seen at the time of the impact. Subsequent back wash of the water around the cylinder is known to create the secondary load cycles. In the present case, the water column is created earlier than case 206. This can probably explain the high pressure region on the back side of the cylinder at the impact time shown in the contour plot in figure 5.

In the 3D case 206, the right hand side snapshot in figure 7, the wave is breaking at the impact time. At this time the backside stagnation pressure has not yet built up. Hence the pressure field is dominated by the front side as shown in the contour plot in figure 6.

Conclusion

In the present paper, wave impacts of steep and breaking focused wave groups have been investigated. Two numerical models have been used to reproduce four cases of focused wave groups; a potential flow solver (OceanWave3D) and a Navier-Stokes solver (OpenFOAM, using the toolbox

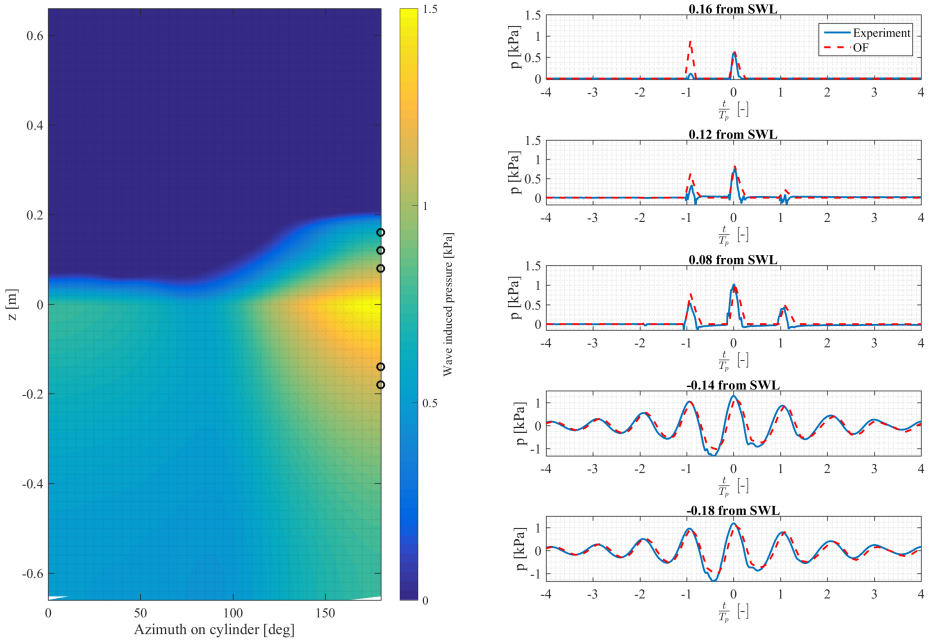

FIGURE 6: Dynamic pressure distribution contour plot (left hand side) and pressure time series measured and computed in the OpenFOAM at five different heights (right hand side). Case 206.

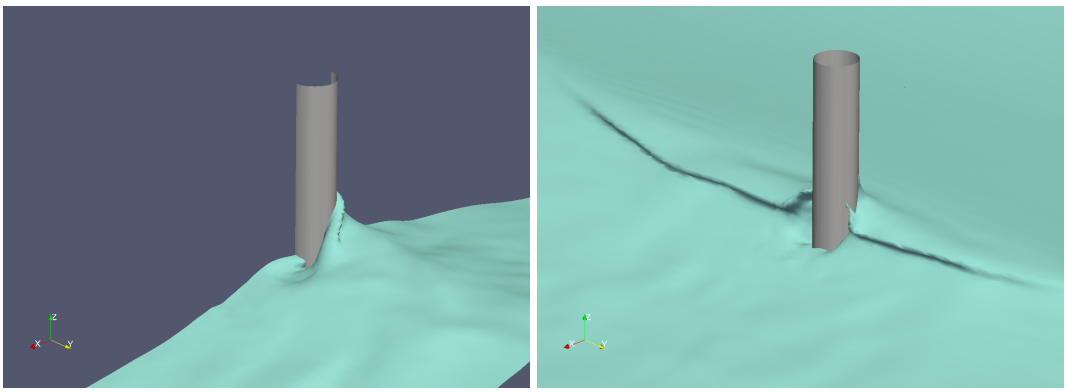

FIGURE 7: Snapshots of the free surface at the time of impact of the focus wave for cases 211 (left) and 206 (right).

Waves2FOAM). The waves were highly nonlinear and breaking. Two of the cases were 2D wave groups and two of them 3D wave groups. Both solvers provided a good reproduction of the free surface elevation for all four tests with only minor errors. Also for the in-line forces, a good match was found. Here, the OceanWave3D results, obtained by application of the Morison equation, followed the experimental force history closely, although no representation of wave-structure interaction can be achieved. The coupled solver, showed a slight under-prediction of the peak forces for the 2D and 3D groups of smallest amplitude, while the peaks for the main waves of the two large groups were well captured. The coupled solver further allowed a detailed reproduction of the wave-structure interaction which for the steep 2D case included the secondary load cycle of in-line force.

Point pressure measurements were also reproduced by the CFD solver and generally showed a good agreement with the tests, even above SWL. The spatial pressure fields for the largest 2D and 3D wave groups at the time of maximum force were discussed. The steep but non-breaking 2D impact created a strong run-up at the cylinder front, and a pronounced simultaneous pressure at the back side by stagnation of water. The 3D impact was breaking with similar strong pressures at the front side, but with no counter-acting stagnation pressure at the back. More investigation, for pressure distributions at the cylinder wall is therefore intended for a larger range of wave conditions.

The coupled solver allows computation of wave impacts for realistic open ocean wave fields. Further development of the model includes a refined breaking filter within the OceanWave3D solver which might improve the accuracy for cases where the waves that break inside the coupling zone between the two models. These investigations, together with further analysis of bending moments and pressure fields will contribute to improved accuracy in the numerical prediction of ULS wave loads for offshore wind turbines.

Acknowledgement

The present research was partly funded by the DeRisk project of Innovation Fund Denmark, grant number 4106-00038B. Further funding was provided by Statoil, DHI and DTU. All funding is gratefully acknowledged.

References

Bredmose, Henrik and Niels G Jacobsen (2010). "Breaking Wave Impacts On Offshore Wind Turbine Foundations: Focusedwave Groups And CFD". In: *Proceedings of the ASME 29th 2010 International Conference on Ocean, Offshore and Arctic Engineering OMAE2010 June 6-11, 2010, Shanghai, China*.

— (2011). "Vertical wave impacts on offshore wind turbine inspection platforms". In: *Proceedings of the ASME 2011 30th International Conference on Ocean, Offshore and Arctic Engineering OMAE2011 June 19–24, 2011, Rotterdam, The Netherlands*. Vol. 436. 1896, pp. 13–32.

Bredmose, H. et al. (2006). "Numerical reproduction of extreme wave loads on a gravity wind turbine foundation". In: *International Conference on Offshore Mechanics and Arctic Engineering, OMAE*, pp. 1–9.

Bredmose, H. et al. (2016). "DeRisk - Accurate prediction of ULS wave loads. Outlook and first results". In: *Energy Procedia*. Vol. 94. Elsevier, pp. 379–387.

Christensen, Erik Damgaard, Henrik Bredmose, and Erik Asp Hansen (2005). "Extreme wave forces and wave run-up on offshore wind-turbine foundations". In: *Proceedings of Copenhagen Offshore Wind Conference* 1995, pp. 1–10.

Clauss, Gunther F., Christian E. Schmittner, and Janou Hennig (2006). "Systematically Varied Rogue Wave Sequences For The Experimental Investigation of Extreme structures". In: *OMAE2006*.

Dean, Robert G. (1965). "Stream function representation of nonlinear ocean waves". In: *Journal of Geophysical Research* 70.18, pp. 4561–4572.

Engsig-Karup, A. P., H. B. Bingham, and O. Lindberg (2009). "An efficient flexible-order model for 3D nonlinear water waves". In: *Journal of Computational Physics* 228.6, pp. 2100–2118.

Goda, Yoshimi (2010). "Reanalysis of Regular and Random Breaking Wave Statistics". In: *Coastal Engineering Journal* 52.01, pp. 71–106.

Grue, John and Morten Huseby (2002). "Higher-harmonic wave forces and ringing of vertical cylinders". In: *Applied Ocean Research* 24.4, pp. 203–214.

Hildebrandt, Arndt and Torsten Schlurmann (2012). "Breaking Wave Kinematics, Local Pressures, and Forces on a Tripod Structure". In: *Coastal Engineering Proceedings* 1.33.

Hirt, C. W and B. D Nichols (1981). "Volume of fluid (VOF) method for the dynamics of free boundaries". In: *Journal of Computational Physics* 39.1, pp. 201–225.

Jacobsen, Niels Gjøl, David R Fuhrman, and Jørgen Fredsøe (2012). "A wave generation toolbox for the open-source CFD library: OpenFoam". In: *International Journal for Numerical Methods in Fluids* 70.9, pp. 1073–1088.

Paulsen, Bo Terp (2013). "Efficient computations of wave loads on off shore structures". PhD thesis.

Paulsen, Bo Terp, Henrik Bredmose, and Harry B. Bingham (2014). "An efficient domain decomposition strategy for wave loads on surface piercing circular cylinders". In: *Coastal Engineering* 86, pp. 57–76.

Paulsen, Bo T. et al. (2014). "Forcing of a bottom-mounted circular cylinder by steep regular water waves at finite depth". In: *Journal of Fluid Mechanics* 755, pp. 1–34.

Sumer, B M and J Fredsøe (1997). *Hydrodynamics Around Cylindrical Structures*. Advanced series on ocean engineering. World Scientific.

Zang, Jun, Paul H Taylor, and M Tello (2010). "Steep Wave and Breaking Wave Impact on Offshore Wind Turbine Foundations - Ringing Re-visited". In: *International Workshop on water waves and floating bodies IWWWFB2010*.

Paper 2

Extreme wave impacts on monopiles: re-analysis of experimental data by a coupled CFD solver

* *This paper is published as part of the* ***Proceedings of the ASME 2017 36th International Conference on Ocean, Offshore and Arctic Engineering OMAE 2017 June 25-30, 2017, Trondheim, Norway****.*

Amin Ghadirian[1], Henrik Bredmose[1], Signe Schløer[1], Martin Dixen[2]
[1] DTU Wind Energy, Nils Koppels Alle Building 403, DK-2800 Kgs. Lyngby, Denmark
[2] DHI, Agern Alle 5, DK-2970 Hørsholm, Denmark
E-mail: amgh@dtu.dk

Abstract

Two different numerical models, OceanWave3D and a coupled solver, OceanWave3D OpenFOAM (Waves2Foam), are used to reproduce extreme events in one sea state. The events are chosen as, the measured event that generates the largest peak moment (exceedance probability of 0.05%) and one event with a slightly smaller peak moment (exceedance probability of 0.3%). Time series of free surface elevation, depth integrated forces, bending moment at the sea bed and pressure time series at 5 different heights on the cylinder are compared for two events between the measurements and the numerical models. The numerical pressure field on the monopile at impact is analyzed and stagnation pressures at the back side of the cylinder, in addition to the main impact pressure at the front side are observed. There is a good agreement between the OceanWave3D results and the measurements in the reproduction of the first selected event. However, for the larger selected event, OceanWave3D results in the peaks of time series are smaller than the measurements. This illustrates the sensitivity of the strong impact loads to the state of wave breaking. For small values of the inline force, the OpeanFOAM results provided good agreement with the measurements. The secondary

load cycles are observed in the measured force and bending moment time series and the reproduced times series using OpenFOAM.

Introduction

CFD computation of extreme wave loads is used to an increasing extent for the design of offshore wind turbine monopiles. The approach makes it possible to reduce the uncertainties in the more common processes of design and also to validate the currently used engineering models.

Some of the studies using CFD computation of extreme wave loads include the earlier works of Christensen, Bredmose, and Hansen 2005; Bredmose et al. 2006 to the recent works of Bredmose and Jacobsen 2010; Bredmose and Jacobsen 2011; Hildebrandt and Schlurmann 2012. In all of these studies the Volume of Fluid (VOF) method was used to capture the free surface. In these studies irregular and regular large waves were considered. In some cases the breaking waves were of most interest. Inline forces, run ups, vertical forces or pressure distributions were investigated. Some of the works included validations against experiment while the others used analytical models to validate the numerical results. However, more systematic validation of the inline force, bending moment and pressure time series results of CFD numerical models for irregular breaking waves against measurements is still needed.

Ghadirian, Bredmose, and Dixen 2016 used a potential flow solver, OceanWave3D, and a coupled Navier-Stokes solver, OceanWave3D OpenFOAM, to reproduce measured focused wave groups, designed to break on a monopile. The authors compared the free surface elevation, inline force and pressure distribution on the cylinder with measurements. A good agreement between the numerical simulations and the measurements was shown. The effect of directional spreading was also investigated. This work further showed that even though the focused wave groups were the most probable linear realization of extreme crest height, they were not necessarily the extreme waves in the sea states in relation to the wave induced pressure.

The main goal of the present article is to apply the models of Ghadirian, Bredmose, and Dixen 2016 to reproduce extreme events in relation to the bending moment on a monopile. Similarly to Ghadirian, Bredmose, and Dixen 2016, this paper is part of the DeRisk project (Bredmose et al. 2016). The first used numerical model is the fully nonlinear potential flow solver OceanWave3D (Engsig-Karup, Bingham, and Lindberg 2009) which is able to create 3D nonlinear waves in a relatively big domain. A coupled version of this model with the OpenFOAM tool box, Waves2FOAM (Jacobsen, Fuhrman, and Fredsøe 2012) , by Paulsen, Bredmose, and Bingham 2014; Paulsen 2013 is the second numerical model used in the present paper. Paulsen validated the OpenFOAM solver for regular waves (Paulsen et al. 2014). He also studied the creation of the secondary load cycle, and the effective physics behind it Paulsen et al. 2014. Paulsen, Bredmose, and Bingham 2014 also presented validation of the coupled solver for more cases including

regular, irregular and 2D phase focused waves and 2D focused wave group tests performed and published by Zang, Taylor, and Tello 2010.

In the present paper, we provide validation of the OceanWave3D and the coupled solver against measurements of extreme events, in terms of bending moment of the monopile at the sea bed, extracted from a random sea state. The sea state parameters are identical to the ones associated with the focused wave group of Ghadirian, Bredmose, and Dixen 2016. The paper can thus be seen as a continuation of this work. Time series of the free surface elevation, depth integrated forces, bending moment at the sea bed and pressure time series measured and extracted at 5 different heights on the cylinder are compared for two events in same sea state.

The experiments

The tests were conducted at DHI Denmark at a scale of 1:50. Each test consisted of a 6 hour random times series of one specific sea state. The measurements of one of the 6 hour random sea tests are used in the present paper. The measured time series of inline force, bending moment and surface elevation were later used to calculate exceedance probabilities. Based on the probabilities of bending moment two extreme events were chosen and a short period between 44 s to 77 s around each event was selected and extracted for reproduction in the numerical models. The diameter of the monopile was 0.14 m in lab-scale and it was located 7.3 m from the wave paddles in the wave basin. The monopile was installed on two force transducers, mounted at the top and the bottom, to measure both inline force and bending moment while keeping a very rigid structure to avoid resonance in the investigating frequency range.

Figure 1 shows the investigated sea state case in relation to the Goda breaking criterion (Goda 2010).

$$\frac{H_b}{gT_p^2} = A\{1 - \exp(-1.5\pi\frac{h}{L_p})\}\frac{\tanh(kh)}{2\pi} \tag{1}$$

Here H_b is the breaking wave height, T_p and L_p are the peak wave period and the peak wave length assuming a linear dispersion and constant water depth. The breaking limit is shown in this plot for both $A = 0.12$ and $A = 0.18$. H_{max} in this plot is chosen $1.86 \times H_s$.

The numerical model

The coupled solver OceanWave3D-OpenFOAM (Waves2Foam) (Paulsen 2013) was used to reproduce the extreme events. Waves2Foam is an added package to OpenFOAM's InterFoam solver which uses relaxation zones close to the boundaries to induce incident gravity waves (Jacobsen, Fuhrman, and Fredsøe 2012). InterFoam uses a volume of fluid (VOF) method to treat the free surface flows (Hirt and Nichols 1981).

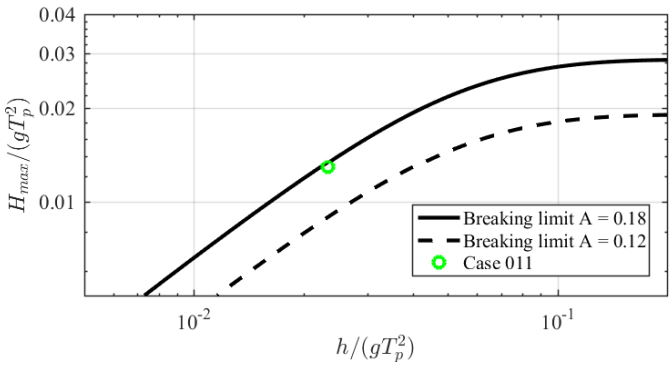

FIGURE 1: Wave diagram showing the investigated sea state and breaking criteria.

To reproduce the measurements, the target wave paddle velocity signals of the lab in the selected time periods were used to produce the waves non-linearly by the OceanWave3D solver. The paddle signals were used to create a flux boundary condition in the OceanWave3D domain. This method of generation is linearly consistent with the piston generation in the lab. Differences at second order and higher are expected because no piston movement is included in the numerical model. However, good results with this approach, are presented in earlier works Paulsen et al. 2014; Bredmose and Jacobsen 2010; Bredmose and Jacobsen 2011 and as part of DeRisk project Bredmose et al. 2016; Ghadirian, Bredmose, and Dixen 2016.

A top view of the computational domains are shown in Fig. 2. The symmetry of the setup was utilized to reduce the OpenFOAM domain to half size. The embedded OpenFOAM domain was driven with waves generated in OceanWave3D through a relaxation zone (Jacobsen, Fuhrman, and Fredsøe 2012). A Courant number of 0.2 was used to limit the time steps of the OpenFOAM simulations. The same grid resolution was used as by Paulsen et al. 2014. Since the reproduced waves have about the same wave length in both studies, the grid convergence study conducted by Paulsen et al. is also valid for the current study.

We found that the results were sensitive to the time period the simulations start before the selected event (warm-up time). While our ultimate goal is to deduce a robust and recommended value for the warm-up time, we have in the present paper chosen to present the results that match the measurements best. Hence, the first selected event had a warm-up time of 33 s in the OceanWave3D domain and 8 s in the OpenFOAM domain, while the second selected event had a warm-up time of 66 s in OceanWave3D and OpenFOAM domains. This means that the OpenFOAM simulation started 25 s after when the OceanWave3D simulation started in the reproduction of the first selected event. Given that the chosen events are extreme and therefore rare, sensitivity to the state of wave breaking can be expected. The state of wave breaking, in turn can be affected by the numerical setup.

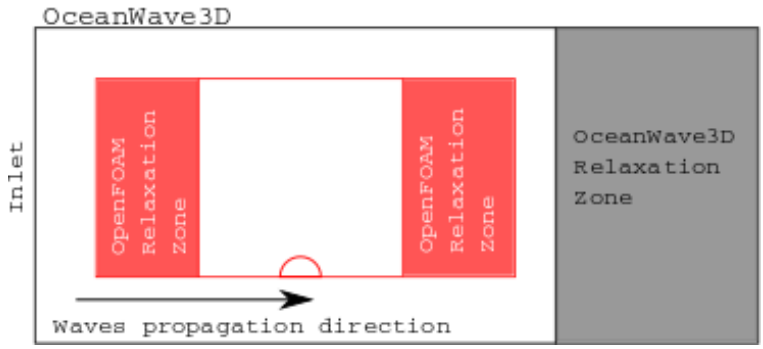

FIGURE 2: The computational domain.

TABLE 1: The characteristics of these selected events and the sea state.

	Max Bending Moment [Nm]	Exceedence Probability	Depth [m]	H_s [m]	H [m]	T_p [s]	T [s]
1. reproduction target	32	3×10^{-3}	33	9.5	15.2	12	12
2. reproduction target	45	5×10^{-4}	33	9.5	18.2	12	12

Reproduced events

In Fig. 3, the exceedance probability of the maximum bending moment from each wave is shown. In the same figure the measured maximum bending moment of a corresponding focused wave for the same sea state is shown with a red circle. The focused wave group was produced with a target wave height of $1.86 \times H_s$ (3 hour return period) and was tested specially as part of the experiments. From the figure the bending moment related to the focused wave was not a vastly extreme event in this sea state. The corresponding exceedance probability of such a bending moment is about 1%. About 20 waves created larger moments. The largest one is associated with an exceedance probability of 0.05%. Two of these waves, shown by blue and green dots in the figure, were selected for numerical reproduction. Table 1 shows the characteristics of these selected events and the sea state from which they are selected.

Figure 4 shows free surface elevation of the selected events in addition to the focused wave group wave group result, carried out as a separate test and modeled in Ghadirian, Bredmose, and Dixen 2016. The maximum crest height of the focused wave group is between the two selected events. The trough heights are very close in all cases.

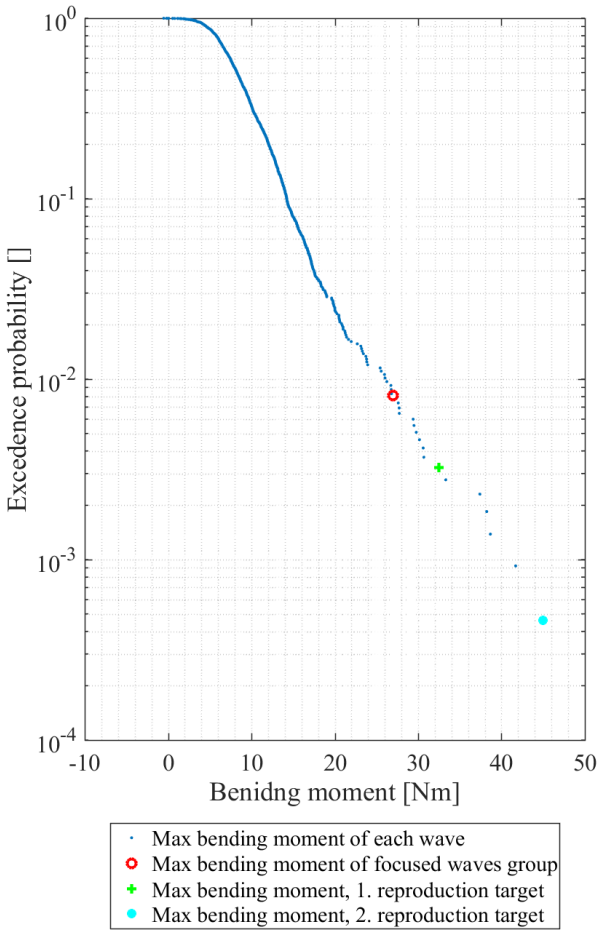

FIGURE 3: Exceedance probability of maximum bending moment in each wave in the studied sea state.

A better correlation with the moment size is seen for the slope of the free surface elevation leading up to the peak. Here the slope for the second selected event is largest while it is smallest for the focused wave group. This makes sense, since for the present structure, loads are inertia dominated and thus strongly linked to the fluid acceleration.

In Fig. 5, top plot, the free surface elevation of the first targeted wave, the blue point in Fig. 3, is shown. The figure shows the free surface elevation 0.2 m upstream of the monopile.

The time axis is shown in terms of $\frac{(t-t_{peak})}{T_p}$ where t_{peak} is the peak time of the bending moment time series and T_p is the peak period of the sea state. It can be seen that the wave is almost symmetric in shape although with a steeper upward slope before the crest relative to the downward slope after the crest. Small fluctuations on top of the crest are visible which might be due to the spilling breaking of the wave on top or vibrations of the wave gauge. Third harmonic reflections from the cylinder can be seen in the troughs of the

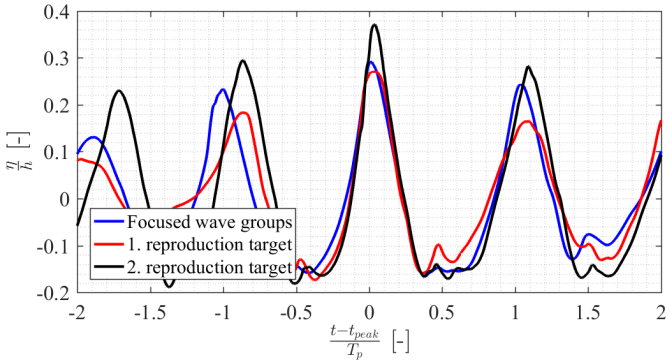

FIGURE 4: The free surface elevation comparison between the selected events and focused wave groups in the same sea state.

wave elevation signal.

It can be seen that the numerical simulations follow the general shape of the time series with fair agreement. The phases and the amplitude of the numerical results from OceanWave3D is generally consistent with the experiments. The results from OpenFOAM, show larger discrepancies in the amplitude of the main crest. The preceding wave amplitude is reproduced better than OceanWave3D. The third harmonic reflections can be observed in the OpenFOAM time series but not in the OceanWave3D time series since the OceanWave3D domain does not contain any cylinder.

Figure 5, middle plot, shows the measured and numerically reproduced inline force time series of the same wave. From this plot and the top plot, it is visible that the ratio of the main peak value to the neighboring breaks is larger in the inline force time series than in the free surface elevation time series. This is a special property of the present event since it was not found for the focused wave group (Ghadirian, Bredmose, and Dixen 2016) or the second selected event (figure 6).

Based on this plot it can be seen that the slope of the inline force time series is larger close to the maximum force time. In addition, the inline force time series include backward leaning cycles from trough to trough.

From comparison between the numerically reproduced results and the measurements, it can be seen that the numerical models reproduced the amplitude and the phases of the inline force time series generally consistently. The OceanWave3D results have a good agreement in amplitude in all times. The calculation of inline force using kinematics extracted from the potential flow solver, OceanWave3D, included the Morison equation and Rainey corrections (Sumer and Fredsøe 1997; Rainey 1995). The OpenFOAM results also show same consistency through the time series. The secondary load cycle can be seen in the trough following the main peak in the measurements and OpenFOAM time series.

Figure 5, bottom plot, shows the measured and numerically reproduced bending moment time series of the event. The maximum measured bending moment is 32 Nm. The general behavior of the measurements is the same as for the inline force time series in terms of shape and phases. The growth of

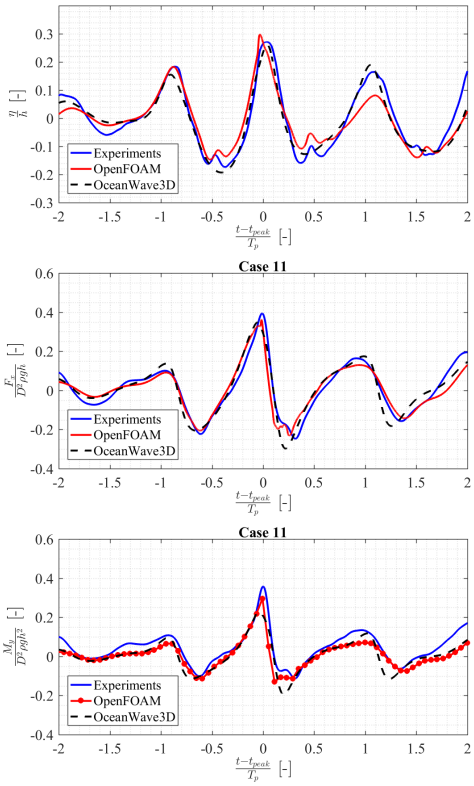

FIGURE 5: Free surface elevation (top), inline force (middle) and bending moment (bottom) comparison between experiments, openfoam and oceanwave3d for the first selected event with maximum bending moment of 32Nm.

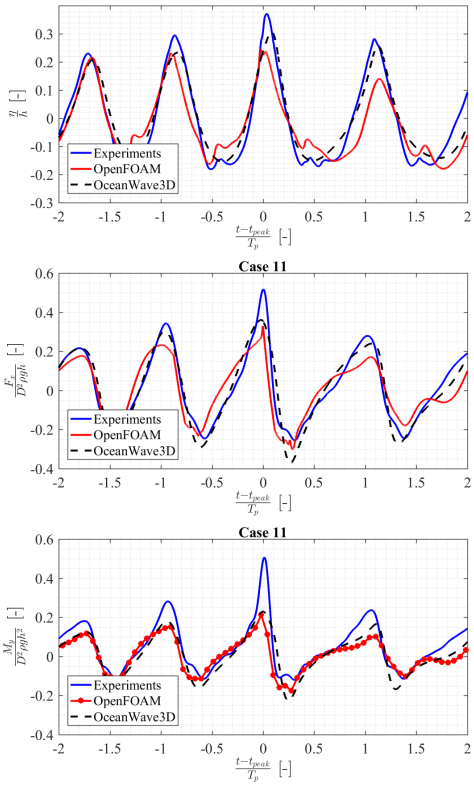

FIGURE 6: Free surface elevation (top), inline force (middle) and bending moment (bottom) comparison between experiments, openfoam and oceanwave3d for the second selected event with maximum bending moment of 45Nm.

the peak value however at the peak time compared to the other peaks in the time series is stronger compared to the inline force time series.

From the OceanWave3D results it can be seen that the numerically generated bending moments present the same general behavior and have the correct phases. The largest discrepancy is observed in the main peak and the following trough of the time series.

The OpenFOAM results show generally good consistency in phase and amplitude for most of the time. The amplitude of the main peak of bending moment time series is predicted with very good agreement with the measurements. The OpenFOAM results of the bending moment were extracted from the saved simulation results after the runtime, hence the time resolution of the time series is lower than the other cases. For this reason the illustration of the bending moment time series from OpenFOAM includes asterisk to show the time resolution. The error between the peak values might be lower in a finer output resolution.

Results for the second selected event are shown in figure 6. The top plot shows the free surface elevation. The time axis is scaled similarly to Fig. 5. From this plot the main wave is almost symmetric in shape though with slight slope asymmetry similar to the previous case.

The numerical simulations follow the general shape of the time series consistently. The phases of the numerical results from OceanWave3D is generally consistent with the experiments but the amplitude is smaller than the measurements. The deviation is more visible for the main peak and the preceding crest.

The results from OpenFOAM, show larger discrepancies both in phase and amplitude. At $t = -1s$, the crest height is reproduced consistently in comparison to OceanWave3D results and smaller than the experiments, with a visible phase difference. However, the deviation between the OpenFOAM results and measurements and OceanWave3D results increase in amplitude after this time. Unlike the previous event, after investigating the results from OpenFOAM it was observed that several preceding waves before the main wave were breaking. After the main wave however, the waves become too small to break.

Figure 6, middle plot, shows the measured and numerically reproduced inline force time series of the event 2. Similarly to the previous event, the relative difference between the main peak value and the following and preceding peaks is larger in the inline force time series than in the free surface elevation time series.

The numerical models reproduced the amplitude and the phases of the inline force time series generally well. The OceanWave3D result has lower amplitude at the time of the main peak of the time series. The magnitude of the trough values in the inline force time series is always over predicted similar to the previous event.

The OpenFOAM results show a less peaky force for the main wave, though with an additional spike towards the end of the main peak. This spike is due to wave breaking and leads to a maximum force value close to the one of OceanWave3D. Both values, however, are about 30% smaller than the measured peak force. The secondary load cycle can be seen in the following trough of the main peak in the measurements and OpenFOAM time series as in the previous event.

Figure 6, bottom plot, shows the bending moment time series. The OceanWave3D results present the same general behavior as the measurements and have the correct phases. The peak values, however, are predicted to be smaller than the measurements in all times. The trough magnitudes in the OceanWave3D results are predicted to be larger than the experiments. This trend was also observed in the bending moment time series of the previous event and the inline force time series of both events.

OpenFOAM results also show generally good consistency in phase in all time. Although the peak values of the time series are predicted to be smaller than the measurements, the trough values are predicted with better accuracy by the OpenFOAM simulations than OceanWave3D simulations. Similar to the previous event, the most significant discrepancy is seen in the prediction of the peak value of the bending moment time series at zero in x axis where the relative error is up to 50%. The results of the bending moment were extracted in the same way as the previous event, from the saved simulation

results after the runtime. The error between the peak values might be lower in a finer output resolution.

Impact pressures

Further insight to the impact flow is provided by analysis of the pressure data in OpenFOAM and 5 different height on the cylinder where the pressures were measured in the experiments. In Fig. 7 a contour plot of the wave induced pressure is shown on the half cylinder at the impact time for the event 1. The wave-induced pressure is defined as

$$p_{\text{wave induced}} = \begin{cases} p_{\text{physical}} + \rho_{\text{water}} g z & z < 0 \\ p_{\text{physical}} & z > 0 \end{cases} \tag{2}$$

Thus, it is the physical pressure, minus the hydrostatic pressure in still water conditions. It can be seen that the wave induced pressure on the impact side (180 degrees) is maximum (1.2 kPa) at the still water level while a high pressure area behind the cylinder is caused by a stagnation point. The position of the pressure sensors in the experiments is shown with black circles facing the wave paddles (180 degrees).

In Fig. 8 a contour plot of the wave induced pressure is shown on the half cylinder at the impact time for event 2. The wave induced pressure on the impact side (180 degrees) is maximum (1.7 kPa) at the still water level while, also for this impact, a high pressure area behind the cylinder is caused by a stagnation point. The magnitude of the pressure is, however, larger than the previous event. In addition, larger areas on the cylinder have high wave induced pressure. However, because of the large back side pressures in event 2 the maximum reproduced bending moment at the impact time is smaller than in event 1 (look at the main peak of the red curves in figure 5 and figure 6 bottom plots).

Figure 9 shows the measured and numerically reproduced pressure time series with target bending moment of 32 Nm. As it can be seen from the measurements the pressure for the sensors below still water level fluctuate with a mean slightly higher than 0 kPa while the sensors above still water level show nonzero values only when the water level comes up to the sensor location. It should be noticed that the pressure time series, measured by sensors above still water level, are forward leaning unlike the inline force and bending moment time series. The slope of the time series measured above still water level preceding the main peak is very high which implies sudden impact of a package of water over the sensors. This indicates for slamming of the wave on the monopile. Also the maximum peak value between the time series is seen at the sensor 0.08 m above the still water level. After the main pressure peaks, undulations are seen for the transducers below still water level. It is currently an open question if these are related to the secondary load cycle, which by Paulsen et al. 2014 was found to be associated with separation and vortex generation at the back side of the cylinder.

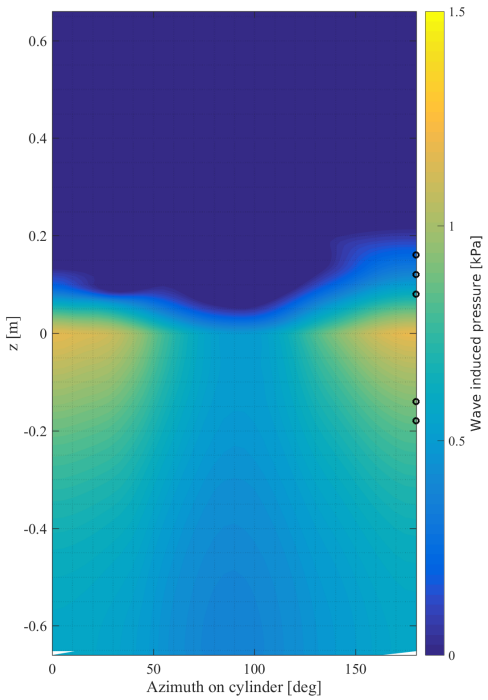

FIGURE 7: Wave induced pressure is shown on the half cylinder at the impact time with the target bending moment of 32 NM.

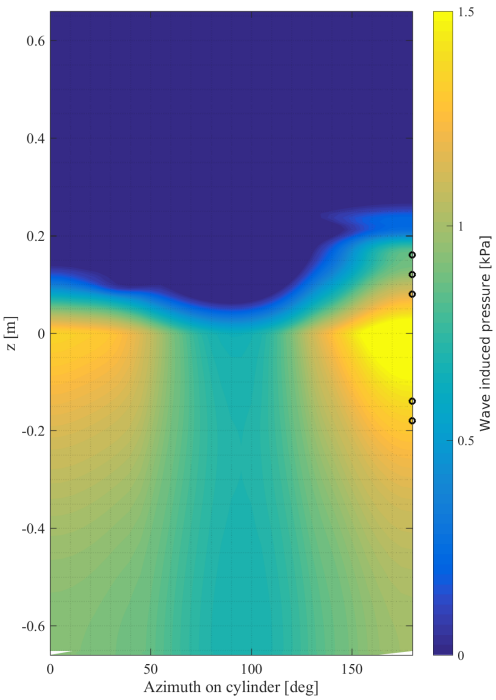

FIGURE 8: Wave induced pressure is shown on the half cylinder at the impact time with the target bending moment of 45 NM.

Based on comparison of the numerically reproduced time series, using OpenFOAM, it can be seen that in the sensors below still water level there is a very good agreement in amplitude between the measurements and the simulation results. In the sensors above still water level the same consistency between the two set of time series can be seen. The measured pressure time series show that the wave is breaking at the peak bending moment time while this is also observed in the results of OpenFOAM simulations.

Figure 10 shows the measured and numerically reproduced pressure time series of event 2. Similar behavior as the previous event can be seen in the wave induced pressure time series.

There is a small phase difference between the two results and the magnitude of the troughs is predicted smaller than the measurements. In the sensors above still water level, the peak amplitude of the numerically reproduced time series show decreasing agreement with height. The large steepness of the time series can only be seen in the OpenFOAM results in the time series from the first sensor above still water level and not in the other sensors results. It can be concluded that the wave is not breaking as violently, and not reaching to the same height as in the measurements. The comparison thus illustrates the sensitivity of the strong impact loads to the state of breaking, see also Bredmose and Jacobsen 2010.

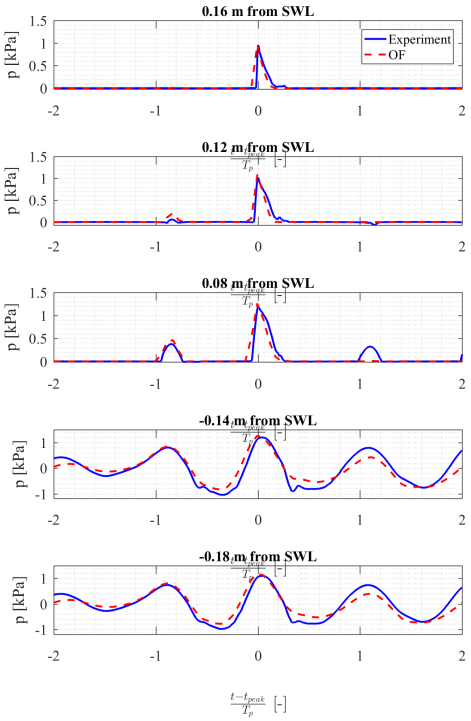

FIGURE 9: The measured and numerically reproduced pressure time series with target bending moment of 32 NM.

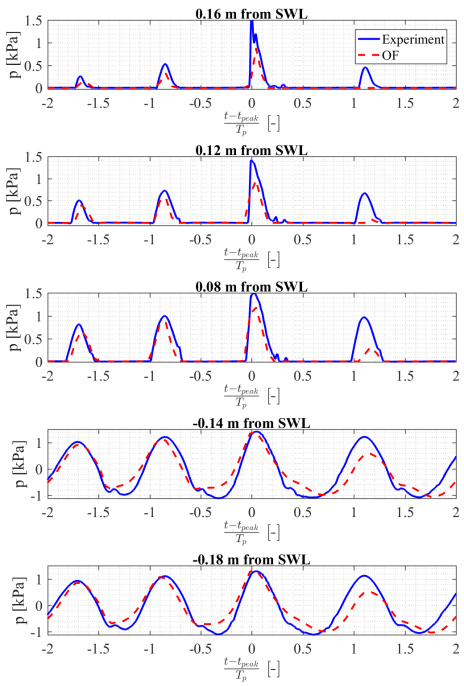

FIGURE 10: The measured and numerically reproduced pressure time series with target bending moment of 45 NM.

Discussion

In both events, the ratio of the main peak value to the neighboring peaks is larger in the inline force time series than in the free surface elevation time series and is the largest in the bending moment time series (look at Fig. 5 and Fig. 6). This is expected from the increasing (hyperbolic in the linear case) behavior of the wave kinematics in regard to height. Velocities and accelerations, which are the main contributors to inline force, are increasing function of height from the sea bed.

The secondary load cycles were observed in the measurement time series of inline force and bending moment and undulations were observed in the pressure time series. These may be related to the vortices associated with the creation of the secondary load cycle as discussed by Paulsen et al. 2014.

Based on the measured free surface elevation, inline force and bending moment time series it can be seen that the variability between the two selected events and the focused wave group is smaller in the trough values. This is also true for the OpenFOAM results but not seen in the OceanWave3D results. The OceanWave3D results over predicted the trough values of inline force and bending moment in all the cases.

In summary, there is a good agreement between the OceanWave3D results and the measurements in the reproduction of the first selected event except for the main peak bending moment in which the OceanWave3D results show

a smaller peak value. For the second selected event the under prediction of OceanWave3D compared to the measurements is visible for almost all the peak values of the free surface elevation, inline force and bending moment. In this case the magnitude of trough values of inline force and bending moment are over predicted. The OpeanFOAM results for event 1 provide good agreement between the measured inline force and bending moment time series. However, for event 2, the large discrepancies between the peak values of OceanWave3D and the measurements are also observed between OpenFOAM results and the measurements.

In Ghadirian, Bredmose, and Dixen 2016, authors compared the measurements of the focused wave group in the same sea state as the present paper (case 0211 in the cited paper) with its reproduction in OceanWave3D and OpenFOAM. Since the bending moment was not reported in that paper only the free surface elevation, inline force and pressure time series can be compared with the present results. From Fig. 4 it can be seen that the focused wave studied in Ghadirian et. al. has about the same height as the first selected and studied event in the present paper. From the free surface elevation, inline force and pressure time series of the first selected event in the present paper and the case 0211 investigated in Ghadirian, Bredmose, and Dixen 2016. the same quality of agreement is found between the measurements and the two numerical models' results.

We thus observe good reproduction for the focused group event and one more extreme event (event 1) while the most extreme event of the measured 6 hour realization shows stronger deviations. On the other hand, the most extreme event is a demanding test for the model since the event is rare by definition. The observed under prediction might be explained by limitations of OceanWave3D regarding reproduction of breaking waves. The waves in the second selected event are very large and the numerical breaking filter is observed to be active from the beginning of the domain. Since this breaking filter is not based on a physical model it might smear out some of the waves which have large vertical acceleration right after the numerical wave paddles but they are not breaking in the laboratory. This leads to an under prediction of free surface elevation and consequently inline force and bending moment. Since the OpenFOAM model is initialized from the OceanWave3D domain the under prediction passes on to the OpenFOAM results.

The sensitivity of the strong impact loads to the state of wave breaking is well known. This was also observed in the numerical results, where sensitivity to the start time before the main impact was observed. We have here chosen to show the best matching results for event 2, and leave for further research to deduce a generally recommended value of the warm-up time.

This is part of the present research to reproduce the OpenFOAM results in future with implementing the wave paddle signals extracted from the measurements directly in the OpenFOAM domain. An improved, analytical or empirical breaking model implementation in the OceanWave3D results also might improve the results for OceanWave3D and the coupled solver.

Further investigation of the pressure distribution in none-breaking waves and the secondary load cycles creation is also of interest as the next steps.

Acknowledgement

The present research was partly funded by the DeRisk project of Innovation Fund Denmark, grant number 4106-00038B. Further funding was provided by Statoil, DHI and DTU. All funding is gratefully acknowledged.

References

Bredmose, Henrik and Niels G Jacobsen (2010). "Breaking Wave Impacts On Offshore Wind Turbine Foundations: Focusedwave Groups And CFD". In: *Proceedings of the ASME 29th 2010 International Conference on Ocean, Offshore and Arctic Engineering OMAE2010 June 6-11, 2010, Shanghai, China*.

— (2011). "Vertical wave impacts on offshore wind turbine inspection platforms". In: *Proceedings of the ASME 2011 30th International Conference on Ocean, Offshore and Arctic Engineering OMAE2011 June 19–24, 2011, Rotterdam, The Netherlands*. Vol. 436. 1896, pp. 13–32.

Bredmose, H. et al. (2006). "Numerical reproduction of extreme wave loads on a gravity wind turbine foundation". In: *International Conference on Offshore Mechanics and Arctic Engineering, OMAE*, pp. 1–9.

Bredmose, H. et al. (2016). "DeRisk - Accurate prediction of ULS wave loads. Outlook and first results". In: *Energy Procedia*. Vol. 94. Elsevier, pp. 379–387.

Christensen, Erik Damgaard, Henrik Bredmose, and Erik Asp Hansen (2005). "Extreme wave forces and wave run-up on offshore wind-turbine foundations". In: *Proceedings of Copenhagen Offshore Wind Conference* 1995, pp. 1–10.

Engsig-Karup, A. P., H. B. Bingham, and O. Lindberg (2009). "An efficient flexible-order model for 3D nonlinear water waves". In: *Journal of Computational Physics* 228.6, pp. 2100–2118.

Ghadirian, A., H. Bredmose, and M. Dixen (2016). "Breaking phase focused wave group loads on offshore wind turbine monopiles". In: *Journal of Physics: Conference Series* 753.9, p. 092004.

Goda, Yoshimi (2010). "Reanalysis of Regular and Random Breaking Wave Statistics". In: *Coastal Engineering Journal* 52.01, pp. 71–106.

Hildebrandt, Arndt and Torsten Schlurmann (2012). "Breaking Wave Kinematics, Local Pressures, and Forces on a Tripod Structure". In: *Coastal Engineering Proceedings* 1.33.

Hirt, C. W and B. D Nichols (1981). "Volume of fluid (VOF) method for the dynamics of free boundaries". In: *Journal of Computational Physics* 39.1, pp. 201–225.

Jacobsen, Niels Gjøl, David R Fuhrman, and Jørgen Fredsøe (2012). "A wave generation toolbox for the open-source CFD library: OpenFoam". In: *International Journal for Numerical Methods in Fluids* 70.9, pp. 1073–1088.

Paulsen, Bo Terp (2013). "Efficient computations of wave loads on off shore structures". PhD thesis.

Paulsen, Bo Terp, Henrik Bredmose, and Harry B. Bingham (2014). "An efficient domain decomposition strategy for wave loads on surface piercing circular cylinders". In: *Coastal Engineering* 86, pp. 57–76.

Paulsen, Bo T. et al. (2014). "Forcing of a bottom-mounted circular cylinder by steep regular water waves at finite depth". In: *Journal of Fluid Mechanics* 755, pp. 1–34.

Rainey, R. C. T. (1995). "Slender-body expressions for the wave load on offshore structures". In: *Proceedings of the Royal Society of London* 450.1939, pp. 391–416.

Sumer, B M and J Fredsøe (1997). *Hydrodynamics Around Cylindrical Structures*. Advanced series on ocean engineering. World Scientific.

Zang, Jun, Paul H Taylor, and M Tello (2010). "Steep Wave and Breaking Wave Impact on Offshore Wind Turbine Foundations - Ringing Re-visited". In: *International Workshop on water waves and floating bodies IWWWFB2010*.

Paper 3

Prediction of the shape of inline wave force and free surface elevation using First Order Reliability Method (FORM)

* *This paper is published in the* ***Journal of Energy Procedia 137 (2017) 162-176*** *as part of the proceedings of* ***14th Deep Sea Offshore Wind R&D Conference, EERA DeepWind'2017, 18-20 January 2017, Trondheim, Norway****.*

Amin Ghadirian[1], Henrik Bredmose[1], Signe Schløer[1]
[1] DTU Wind Energy, Nils Koppels Alle Building 403, DK-2800 Kgs. Lyngby, Denmark
E-mail: amgh@dtu.dk

abstract

In design of substructures for offshore wind turbines, the extreme wave loads which are of interest in Ultimate Limit States are often estimated by choosing extreme events from linear random sea states and replacing them by either stream function wave theory or the NewWave theory of a certain design wave height. As these wave theories suffer from limitations such as symmetry around the crest, other methods to estimate the wave loads are needed. In the present paper, the First Order Reliability Method, FORM, is used systematically to estimate the most likely extreme wave shapes. Two parameters of maximum crest height and maximum inline force are used to define the extreme events. FORM is applied to first and second-order irregular waves in both 2D and 3D. The application is validated against the NewWave model and also the NewForce model, which is introduced as the force equivalent of NewWave theory, that is, the most likely time history of inline force around a force peak of given value. The results of FORM and NewForce are linearly identical and show only minor deviations at second order. The FORM results are then compared to wave averaged measurements of the same criteria for crest height and peak force value. Relatively good agreement between the FORM results of free surface elevation including the second order effects, and the wave averaged measurements is observed. However, the inline force

time series reproduced using the numerical method are not as consistent with the measurements as the free surface elevation time series. The discrepancies between the FORM results and the measurements is found to be a result of more nonlinearity in the selected events than second order and negligence of the drag forces above still water level in the present analysis. This paper is one step toward more precise prediction of extreme wave shape and loads. Ultimately such waves can be used in the design process of offshore structures. The approach can be generalized to fully nonlinear models.

Introduction

In the design process of offshore substructures, including but not limited to wind turbine monopiles, Ultimate Limit States (ULS) are significantly important. Given a design wave height, the extreme wave loads are often estimated by choosing extreme events from linear random sea states and replacing them by either non-linear regular waves (stream function wave theory Dean 1965) or the NewWave theory (Tromans, Anatruk, and Hagemeijer 1991) combined with a stretching method as suggested in the design codes (*IEC 61400-3* 2009). Both of these theories are associated with limitations, the most important of which is the symmetry of these waves around the wave crest.

To avoid such shortcomings and to estimate a more realistic extreme wave, other theories and methods are suggested. One such method the "designer" wave approach by Grice, Taylor, and Taylor 2014. This wave is the average shape of waves that can create an extreme event of choice. Another approach to find an extreme wave event is using the First Order Reliability Method (FORM) to calculate the shape of the most probable extreme waves which exceeds a certain maximum crest height or inline force.

FORM and its inverse process IFORM is used extensively in probabilistic design. In the Wind Energy industry IFORM is used as an extrapolation technique for extreme waves with 50 years return period. This is described in the Annex G of the design code of offshore wind turbines, *IEC 61400-3* 2009. Based on such method Agarwal and Manuel 2008 used IFORM to extrapolate and estimate the failure bending moment in a random space of three variables wind speed, significant wave height and the load on the wind turbine. Similar methods have been used to find the responses of offshore structures and their probabilities based on the significant wave height, peak period, depth and wind velocity (Eckert-gallup et al. 2014; Valamanesh, Myers, and Arwade 2015; Ewans and Jonathan 2014). However, use of FORM to estimate the extreme event in a given sea state is more limited. One example is the work of Jensen 2008 in which FORM was used to calculate the most probable wave sequence for extreme loads on a jack-up structure, the roll response of a ship and the motion of a TLP floater. Validation of these responses with experiments, however, was not included in this study.

In the present work, FORM is used systematically to estimate extreme wave events that produces large crest heights and large peaks of the inline

force, respectively. Strict first- and second-order formulations for wave kinematics and slender body force are applied in 2D and 3D sea states. The NewForce is defined as the force equivalent of the NewWave and the FORM implementation is validated against these theories. The results of FORM are also compared to the designer wave (wave averaged measurements) of the same criteria (same maximum crest height or maximum inline force). The work enables prediction of extreme wave episodes for given free surface and inline force level. The effect of directional spreading can be investigated using results of FORM with a second-order failure function and compared with the measurements. The approach can be generalized to fully nonlinear models.

The experiments were conducted as part of the DeRisk project (Bredmose et al. 2016). Experimentally based analysis of probability curves for crest heights and inline peak force is presented in Schløer, Bredmose, and Ghadirian 2017 along with averaged time histories of the corresponding η and force variation. In the last section the results are discussed in a broader view.

First Order Reliability Method

Reliability is defined as the probability of a failure function, $g(\mathbf{X})$, being larger than zero where $\mathbf{X}$ is a vector of stochastic input variables. The First Order Reliability Method (FORM) uses a first order Taylor expansion to find the shortest distance between the failure surface (where $g(\mathbf{X})$ is zero) and center of the joint probability distribution of the input variables, mapped to a normalized Gaussian distribution. In other words, FORM provides the most probable combination of the stochastic inputs that lead to failure and the associated probability of its occurrence. The method can be used for structural reliability analysis and for extreme value prediction (Jensen 2008).

In the current paper, four different failure functions are used to predict realization of the most probable time histories for a given peak value of free surface elevation and inline force, for linear and second-order slender body wave loads on a pile.

In equations 1 to 4 the four failure functions and their representation in the next sections are shown.

$$\begin{array}{lcl} \eta^{(1)} & = & \sum_{j=1}^{N_{freq}} \sum_{i=1}^{N_{dir}} (a_{ij}\cos(\omega_j t) + b_{ij}\sin(\omega_j t)) \\ g & = & \eta_{target} - \eta^{(1)} \\ \text{Represented by} & : & FORM(\eta_1) \end{array} \tag{1}$$

$$\begin{aligned} \eta^{(2)} &= \tfrac{1}{4}\sum_{i=1}^{N_{freq}}\sum_{j=1}^{N_{freq}}\dots \\ &\quad \sum_{k=1}^{N_{dir}}\sum_{l=1}^{N_{dir}}\dots \\ &\quad (a_{ik}+ib_{ik})(a_{jl}+ib_{jl})\{\{C^{-}_{ijkl}\}\cos(\omega_i t-\omega_j t) \\ &\quad +\{C^{+}_{ijkl}\}\cos(\omega_i t+\omega_j t)\} \\ g &= \eta_{target}-(\eta^{(1)}+\eta^{(2)}) \\ \text{Represented by} &: FORM(\eta_1+\eta_2) \end{aligned} \tag{2}$$

$$\begin{aligned} F^{(1)} &= \rho A C_M \int_{-h}^{0} u_t^{(1)} dz \\ g &= F_{target}-F^{(1)} \\ \text{Represented by} &: FORM(F_1) \end{aligned} \tag{3}$$

$$\begin{aligned} F^{(2)} &= \rho A C_M \int_{-h}^{0} u_t^{(2)}+u^{(1)}u_x^{(1)}+w^{(1)}u_z^{(1)}dz+ \\ &\quad \rho A C_m \int_{-h}^{0} u^{(1)}w_z^{(1)}dz+ \\ &\quad 0.5\rho D C_D \int_{-h}^{0} u^{(1)}|u^{(1)}|dz+ \\ &\quad \rho A C_M \eta u_t^{(1)}|_{z=0} \\ g &= F_{target}-(F^{(1)}+F^{(2)}) \\ \text{Represented by} &: FORM(F_1+F_2) \end{aligned} \tag{4}$$

where Jensen 2008:

$$(a_{i,j},b_{i,j}) \in \mathcal{N}(0,\sqrt{S\Delta f\Delta\theta}) \tag{5}$$

Further S is the power spectrum of the free surface elevation as a function of frequency and direction. The frequency range was chosen from zero to 2.5 Hz for the present analysis in lab scale, corresponding to 0.35 Hz in full scale. The horizontal particle velocity is denoted by u and u_t is its Eulerian time derivative. The first-order contribution, $u^{(1)}$, is carried out with the Airy Wave theory (1895) while the second-order contribution, $u^{(2)}$, is calculated as by Sharma and Dean Sharma and Dean 1981. The transfer functions $C^{\pm}$ can be found in the same paper. The force model chosen is the Rainey force model (Rainey 1995) which includes the convective terms of the horizontal particle acceleration and the axial divergence force, as represented in the integrals of (4). In the current implementation of FORM the results of the application are the random variables $a_{i,j}$ and $b_{i,j}$. These known amplitude variables can later be used to reproduce the free surface elevation and inline force time series. We have here chosen to formulate $\eta^{(1)}$ and $F^{(1)}$ as strictly linear and $\eta^{(2)}$ and $F^{(2)}$ as strictly second order. Inclusion of higher-order terms is indeed possible, for example by application of fully nonlinear kinematics which is our next step.

The target values of η_{target} and F_{target} were chosen such that the result could be compared to averaged results of the experiments. However, for a

few cases where the effect of slamming was clearly visible in the averaged experimental data, F_{target} was chosen as an estimated non-slamming value, since slamming is beyond the scope of second-order theory.

The Matlab toolbox CODES (Lacaze and Missoum 2015) was used to apply FORM on the chosen failure functions. The sequential quadratic programming (SQP) method was used to find the most probable point on the failure surface. A tolerance value of 10^{-4} was chosen as the convergence criteria. Vectors of zero were used as the initial values for the parameters while it was observed that the results do not depend on the initial values. The code needed approximately 1800 iterations for the most complicated case with directional spreading and second-order effects to converge.

NewWave and NewForce theories

The NewWave theory (Tromans, Anatruk, and Hagemeijer 1991) expresses the expected and most likely time history for the linearized free surface elevation around a given crest value, based on its power spectrum $S_\eta(\omega, \theta)$ and the crest height α_η. Application of FORM to a linear description of the free surface elevation answers the exact same question, and the results of FORM(η_1) must therefore be identical to a NewWave time history. This serves as a check of the FORM application. We here further introduce the NewForce model (see also Schløer et al Schløer, Bredmose, and Ghadirian 2017) as the equivalent theory for the inline force, to express the most likely linear wave episode that produces a specified force peak.

The NewWave free surface elevation for a crest of height α_η in a directionally spread sea state can be written as

$$\eta_{\text{NewWave}}(\mathbf{X}, \boldsymbol{\omega}) = \frac{\alpha_\eta}{\sigma_\eta^2} \sum_n \sum_m \text{Re}\left\{ d_{n,m} \exp\left(\text{i}(\mathbf{k}_{n,m} \cdot \mathbf{X} - \omega_n \tau)\right)\right\} \tag{6}$$

where

$$d_{n,m} = S_\eta(\omega_n) \Delta\omega_n \Delta\theta_m \tag{7}$$

and $\mathbf{k}_{n,m}$ is the linear wave number vector. Further,

$$\mathbf{X} \;=\; \mathbf{x} - \mathbf{x}_0 \tag{8}$$

where $\mathbf{x}_0$ is the focus location and

$$\sigma_\eta^2 \;=\; \overline{\eta^2} = \int_{\theta=0}^{2\pi} \int_{\omega=0}^{\infty} S_\eta(\omega_n, \theta_m) \mathrm{d}\omega \; \mathrm{d}\theta. \tag{9}$$

The corresponding linear force time history for an inertia-driven structure can be obtained by application of the Morison equation and integration from the sea bed to the still water level. We may express this through the force

transfer function $\Gamma(\omega, \theta)$

$$\Gamma(\omega, \theta) = \mathrm{i}\rho\pi R^2 C_M \cos(\theta)\omega^2/k \tag{10}$$

where k is the wave number, such that

$$F_{\mathrm{NewWave}}(\mathbf{X}, \boldsymbol{\text{ø}}) = \frac{\alpha_\eta}{\sigma_\eta^2} \sum_n \sum_m \mathrm{Re}\left\{d_{n,m}\Gamma(\omega_n, \theta_m) \exp\left(\mathrm{i}(\mathbf{k}_{n,m} \cdot \mathbf{X} - \omega_{n,m}\tau)\right)\right\} \tag{11}$$

Note that the drag force has here been omitted due to its second-order magnitude.

The NewForce theory, introduced in Schløer, Bredmose, and Ghadirian 2017, uses the same approach to provide the expected force history around a specified target peak value, given the background spectrum. First, the spectrum for the force in the main wave direction is established as

$$S_F(\omega, \theta) = |\Gamma(\omega_n, \theta_m)|^2 S_\eta \tag{12}$$

and next the NewWave approach is applied to express the expected force time history as the corresponding auto-correlation function

$$F_{\mathrm{NewForce}}(\mathbf{X}, \tau) = \frac{\alpha_F}{\sigma_F^2} \sum_m \sum_n \mathrm{Re}\left\{S_F \Delta\omega\Delta\theta \exp\left(\mathrm{i}\left(\mathbf{k}_{n,m} \cdot \mathbf{X} - \omega_n\tau\right)\right)\right\} \tag{13}$$

The corresponding free surface elevation can be obtained by division of the force transfer function

$$\eta_{\mathrm{NewForce}}(\mathbf{X}, \tau) = \frac{\alpha_F}{\sigma_F^2} \sum_m \sum_n \mathrm{Re}\left\{\Gamma^*(\omega_n, \theta_m) S_\eta \Delta\omega\Delta\theta \right. \tag{14}$$

$$\left. \exp\left(\mathrm{i}\left(\mathbf{k}_{n,m} \cdot \mathbf{X} - \omega_n\tau\right)\right)\right\} \tag{15}$$

where $*$ denotes the complex conjugate. Results of the FORM analysis is compared to the NewWave and NewForce theories in the following. For the linear predictions $FORM(\eta_1)$ and $FORM(F_1)$, the results must be identical to those of the linear NewWave and NewForce theories. The comparison thus serves as a cross-validation of the two approaches. For the nonlinear results of $FORM(\eta_1 + \eta_2)$ and $FORM(F_1 + F_2)$ a comparison was made to the linear NewWave and NewForce results with the the second order terms added. It is part of the papers research to investigate how close these results are to each other.

Experiments

The experiments were conducted in the shallow water basin at DHI Denmark at a scale of 1:50 as part of the DeRisk project (Bredmose et al. 2016). The full scale diameter of the monopile was 7 m with water depths of 33 m and 20 m. The monopile was mounted on two force transducers — one at the top and one at the bottom — to measure the in-line force and the bending moment.

TABLE 1: Characteristics of the investigated sea states (full scale values).

Case	h [m]	Hs [m]	Tp [s]	Spread [°]	$\frac{h}{gT_P^2}$	$\frac{H_s}{gT_P^2}$
6	33	9.5	12	22	0.023	0.0067
11	33	9.5	12	0	0.023	0.0067
16	20	6.8	12	22	0.014	0.0048
20	20	5.8	12	0	0.014	0.0041

Wave gauges were installed to measure the free surface elevation of the wave propagation towards the cylinder and around it. The monopile was placed 7.3 m from the wave makers (lab scale). The wave generator consisted of 36 piston wave maker driven with linear wave generation theory (Dean 2013).

Several distinct random sea states were tested for a duration of between 6 and 70 hours (in full scale) from which four were selected for analysis in the current paper. The four sea states were tested both with and without 3D spreading. The cos^{2s} spreading function was used for this purpose. The same was implemented in the failure functions to define the correct spreading in the case of 3D sea states. Table 1 shows the characteristics of these four tests in full scale measures. The spreading angle is the standard deviation of direction at the peak wave frequency.

The chosen tests where repeated twice with and without the structure in the basin. In the 3D cases the free surface elevation measurements from the wave gauge at the location of the monopile in the no-structure tests was used to find the zero down-crossings of the free surface elevation. In the 2D cases, the zero down-crossings of the free surface elevation was found using measurements from a wave gauge in the same distance from the wave paddles as the monopile placed 0.4 m laterally from the pile center. Then for each wave, the maximum and minimum inline force and crest height were identified. After sorting them based on each parameter the corresponding exceedance probabilities were calculated.

The curves for exceedance probability of free surface elevation were next used to choose four crest height values within each test, see figure 4. At each level, the 9 wave events closest to that level were chosen to produce an averaged time history after normalization with the peak value and centering around the peak. The corresponding force histories were also averaged, using the same time shifts as applied for free surface elevation. Figure 5a shows such averaged time histories of η and force, with the error bars showing the standard deviation from the set of 9 waves. As the averaged time histories are conditioned on a certain crest level, they represent the expected wave and force episodes around a certain crest value and can thus be compared to FORM(η). Next, the procedure was repeated, this time by selection of events after force level. An example of exceedance probability and average time histories can be seen in figures 4 and 5a, respectively. The resulting averaged time series can be compared to FORM(F).

It should be mentioned that the force time series from the experiments were low pass filtered so the effect of the resonance of the force transducers

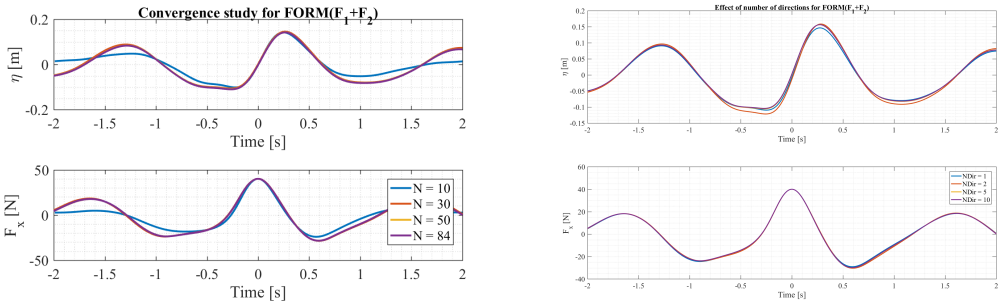

(A) Convergence study of $FORM(F_1 + F_2)$ for increasing number of frequency components from 10 to 84.

(B) Convergence study of $FORM(F_1 + F_2)$ for increasing number of directions from 1 to 10.

FIGURE 1: Convergence study of $FORM(F_1 + F_2)$ for increasing number of frequency components and wave directions.

are removed from the time series. The natural frequency of the force transducers was about 3 Hz in lab scale Schløer, Bredmose, and Ghadirian 2017.

Initial FORM results

To initially validate the model before comparing to the measured wave averaged results, a few validation studies were done. This included a convergence study, comparison to the NewWave Tromans, Anatruk, and Hagemeijer 1991 and NewForce Schløer, Bredmose, and Ghadirian 2017 theories and an investigation of the effect of 3D spreading of the waves.

Convergence study

In calculation of the second order wave quantities, the computation time is directly proportional to $N_{freq}^2 N_{dir}^2$. Because of this, a convergence study was performed to estimate the minimum number of frequency components that was needed to approach to an acceptable error level.

In Fig. 1a the results from this study is shown for the case when FORM is minimizing a failure function of first and second order inline force. Based on this figure, the the cases with $N = 30$ frequency components was found to be only marginally different from the highly resolved cases of N = 50 and N = 84. The difference does not exceed 2%. The same behavior was observed for $FORM(\eta_1)$, $FORM(\eta_1 + \eta_2)$ and $FORM(F_1)$. Hence, 30 frequency components were used for all the cases in the current paper. It is expected that a higher number of frequency components is needed for cases that exceed second order-nonlinear effects.

Since, two of the investigated tests in this paper included 3D wave spreading another convergence study was performed to determine the minimum number of directions.

Figure 1b shows the result for this study. It is seen that for a number of directions larger than 5 the difference between the results is marginal and

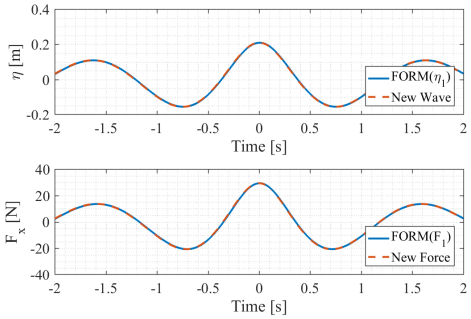

(A) Top: Comparison of free surface elevation time series of NewWave theory and $FORM(\eta_1)$. Bottom: Comparison of inline force time series of NewForce theory and $FORM(F_1)$.

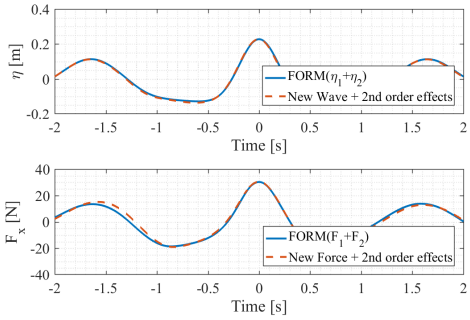

(B) Top: Comparison of free surface elevation time series of NewWave theory including the second order effects and $FORM(\eta_1 + \eta_2)$. Bottom: Comparison of inline force time series of NewForce theory including the second order effects and $FORM(F_1 + F_2)$.

FIGURE 2: Comparison of free surface elevation and inline force time series of NewWave and NewForce theory with and without the second order effects.

does not exceed 1%. It should be noted that Hence, 5 number of directions was used in the cases that includes directional wave spreading in the experiments.

Comparison to the NewWave and NewForce theories

The NewWave episode is defined as the most probable and expected shape of an extreme event (in terms of maximum crest height) in a linear random sea state (Tromans, Anatruk, and Hagemeijer 1991). In addition, the NewForce theory is the equivalent most probable force time series of an extreme event (in terms of maximum inline force) in a linear random sea state (Schløer, Bredmose, and Ghadirian 2017). Both of these definitions agree with the definition of the reliability method if used on the respective linear failure functions, see (1) and (3).

To validate the FORM implementation, the result of $FORM(\eta_1)$ and $FORM(F_1)$ are compared with the NewWave and NewForce theories in figure 2a. It can be seen that the shape, amplitude and phases of the time series of free surface elevation and inline force are identical for the results of FORM and the NewWave and NewForce theories. Hereby the FORM implementation is validated.

In figure 2b the result of $FORM(\eta_1 + \eta_2)$ and $FORM(F_1 + F_2)$ are shown in comparison to the time series of NewWave and NewForce including second-order effects. In these figures it can be seen that there are some deviations between the results of FORM and the analytical solutions. This is, however, expected since in the results from both the NewWave and NewForce theories, the theory itself is in the linear domain with subsequent addition of the second order effects, while FORM calculates the most probable combination of

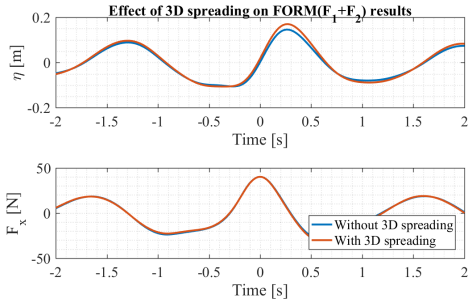

FIGURE 3: Free surface elevation and inline force time series comparison of $FORM(F_1 + F_2)$ for cases with and without directional spreading.

frequency components that generate the target extreme value including the second-order contributions. In other words FORM optimizes the combined first- and second-order contributions to free surface elevation or inline force, while NewWave provides the solution for an optimization at the linear level.

Effect of 3D spreading

It is interesting to investigate the difference between a uni-directional and multi-directional random sea state when creating a certain value of inline force. Figure 3 shows this effect through the results of $FORM(F_1 + F_2)$ for a certain target peak inline force with and without directional spreading. The sea state characteristics of cases 006 and 011, from Table 1, are used.

It is seen that the inline force time series is hardly different between the two cases while the corresponding free surface elevation time series show different crest and trough elevations. The wave with the directional spreading has a larger maximum crest height. This is expected because in the calculation of the inline forces the local accelerations should be multiplied by the cosine of the direction of each wave component. Hence to get an equal inline force, the case with directional spreading should contain larger wave amplitudes.

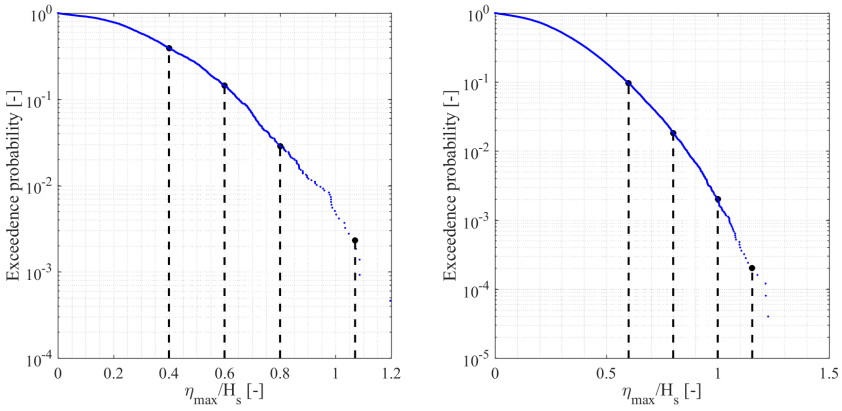

FIGURE 4: The exceedance probabilities of maximum crest heights of each wave two sea states. Left: Case 011. Right: Case 006.

Results

In this section the non-dimensional surface elevation and inline force of the selected waves are shown in exceedance probability plots and the wave averaged measurements are compared with the FORM results for selected cases.

FORM(η) in 33 m water depth

Figure 4 shows the exceedance probability plots of non-dimensional crest heights for sea state cases 011 and 006 which are both in 33 m water depth. The only difference between these two sea states is the directional spreading. This can explain the different maximum crest heights with the same exceedance probability. Since the tests without directional spreading were 6 h long and the ones with directional spreading were 70 h long in full scale, the minimum exceedance probability is one order of magnitude smaller in case 006. The comparison, however, was based on an equal fixed value of non-dimensional crest height ($\eta_{\max}/H_s = 0.6$) so that the directional spreading effect in the experiments and the reproduction of them could be investigated. Four crest heights from extreme to moderate values were chosen for reproduction of the wave shape using FORM.

Figure 5a shows the wave averaged measurements of free surface elevation and the corresponding inline force time series for case 011 in gray colored curves. The standard deviation of η and force between the nine waves is shown with error bars. In the top plot, it can be seen that the error bars are relatively small compared to the amplitude of the main wave itself from the preceding trough to the following one. The same can be seen in the bottom plot for inline force. Third harmonic reflections of the waves from the monopile can be seen in the wave averaged time series of free surface elevation as shown and explained in Ghadirian, Bredmose, and Dixen 2016 (Figure 3).

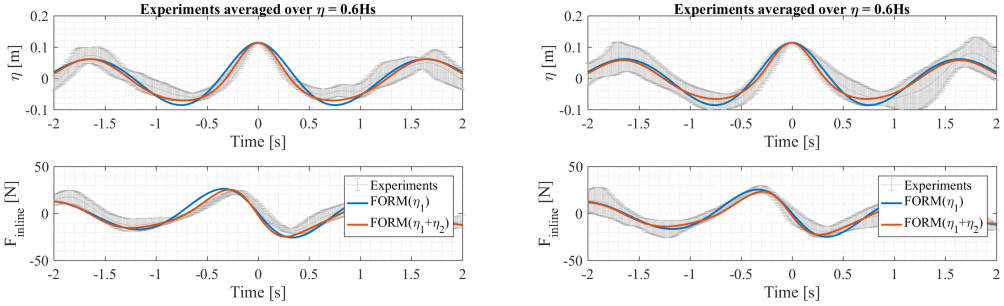

(A) Case 011. (B) Case 006.

FIGURE 5: Wave averaged time series of free surface elevation and inline force between 9 waves from case 011 and case 006 with maximum crest height close to $0.6Hs$, in addition to corresponding results from $FORM(\eta_1)$ and $FORM(\eta_1+\eta_2)$ given $\eta_{target} = 0.6Hs$.

In the same figure the results of $FORM(\eta_1)$ and $FORM(\eta_1+\eta_2)$ and the corresponding calculated inline forces are shown. The linear optimized wave shape, $FORM(\eta_1)$, can hardly predict the general shape of the wave and the inline force time series. While the crest value of η is matched by FORM(η_1) and FORM($\eta_1+\eta_2$), the amplitude of the linear result is larger than the wave averaged experiments both in free surface elevation and inline force. The result of $FORM(\eta_1+\eta_2)$ is, however, more in agreement with the experiments. The troughs of the second-order waves are much closer to the experiments compared to the linear FORM results. However, the second-order wave has a wider crest than the measurements with trough amplitude larger than the wave averaged measurements. This shows that the experimental averaged results are more nonlinear than first and second order theories. From the inline force time series, the general shape of the second-order solution is closer to the measurements than for the first order solution. However, marginal differences is seen in the peak and trough amplitude. From the free surface elevation, the FORM results down and up zero crossings have higher slopes than the experiments. Since the free surface elevation and particle acceleration are in phase at least at first order, the larger amplitude of peak and trough of inline force is expected. In the bottom plot also a phase shift between the numerical and experimental results can be seen.

Since the second order numerically reproduced results are in significantly better agreement with the measurements than the first order results the focus will be on the second order results in the following analysis.

To investigate the effect of directional spreading on the expected wave shape of averaged measurements and results of FORM, the similar analysis is shown for case 006 in figure 5b which includes directional spreading.

Based on the free surface elevation comparison of $FORM(\eta_1+\eta_2)$ to the experiments, the FORM prediction for the shape of the wave is relatively consistent with the measurements. The only significant difference is the asymmetry of η in the measurements which is not captured by the FORM simulations. The same consistency can be seen in the inline force time series. Only

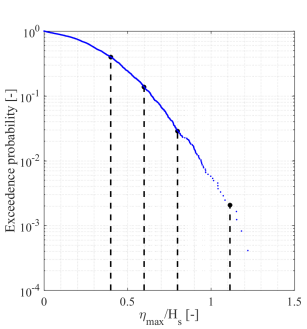

(A) The exceedance probabilities of maximum crest heights of each wave in sea state case 020.

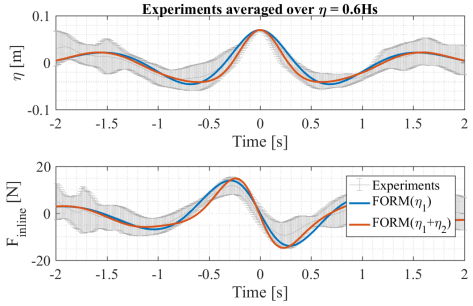

(B) Wave averaged time series of free surface elevation and inline force between 9 waves from case 020 with maximum crest height close to $0.6Hs$, in addition to corresponding results from $FORM(\eta_1)$ and $FORM(\eta_1 + \eta_2)$ given $\eta_{target} = 0.6Hs$.

FIGURE 6: The exceedance probabilities of maximum crest height and the wave averaged time series of free surface elevation and inline force.

marginal differences occur between the measurements and $FORM(\eta_1 + \eta_2)$.

The effect of directional spreading on the measurements of the two presented events, in cases 011 and 006, is investigated. As concluded in section 3 with the same inline force the case with directional spreading (here case 006) should have higher maximum free surface elevation than the case without spreading. In other words, waves with the same height in a directional sea state should induce smaller inline force on the monopile. This, however, is not observed in the experiments from figure 5a and 5b. The reason for this inconsistency is part of current research.

FORM(η) in 20 m water depth

Results for an uni-directional event in 20 m, case 020 are shown in figure 6a. The wave averaged free surface elevation and inline force measurements are shown in gray color curves with error bars presenting the standard deviation between the waves for case 020. The free surface elevation of FORM and corresponding inline force are also shown.

The shape of the free surface elevation of $FORM(\eta_1 + \eta_2)$ compare generally well with the averaged η shape from the measurements. The only significant difference between them is seen in the amplitude of the preceding trough and the slope of the wave from this trough to the main crest. Again $FORM(\eta_1 + \eta_2)$ matches the experimental results better than $FORM(\eta_1)$.

From the bottom plot, the corresponding inline force time series of $FORM(\eta_1 + \eta_2)$ has higher amplitude than the wave averaged measurements. The inline force time series based on $FORM(\eta_1 + \eta_2)$, is inside one standard deviation range of wave averaged experiments. Since H_s is different between the depths of 20 m and 33 m, no direct comparison of the events of figure 6b

and 5a is made. From the shape of the curves, however, the force peak at 20 m can be seen to be more compact than at 33 m.

FORM(F) in 33 m water depth

We now turn to the expected shape of inline force time history, conditional to the force peak value. Figure 7 shows the exceedance probability plots of the non-dimensional inline force peaks for cases 011 and 006. Four target inline force values from extreme to moderate were chosen for each case, to reproduce their wave shape using FORM. Similarly to the expected shape of η, pair-wise common peak force values were also chosen to investigate the spreading effect on the results, in this case $F/\rho g h R^2 = \{1.2, 1.7\}$.

Figure 8a shows the wave averaged measurements of free surface elevation and inline force time series of case 011 together with the FORM results. For the selected force level, the wave events were found to contain slamming, resulting in a relatively sharp peak on top of the smoother underlying force curve. As another indicator of strong nonlinearity, a secondary load cycle can be observed in the trough following the maximum inline force. Since the effect of slamming is beyond the second-order wave and force model, the target peak force in the FORM optimization was chosen to be lower than the maximum of the wave averaged signal. For this reason the resulting inline force time series of $FORM(F_1 + F_2)$ has a peak value smaller than the peak of the averaged force.

Based on comparison of the inline force result of $FORM(F_1 + F_2)$ with the experiments in the lower plot, the amplitude of the inline force is predicted relatively consistently. However, the FORM results inline force time series has a higher preceding slope and lower following slope around the main peak.

In the top plot a phase shift is seen between the numerical and experimental results, similarly to the previous cases. This phase shift was investigated more thoroughly by comparing the results from all of analyzed events and it is presented in section 3. It was observed that the magnitude of this time shift is directly proportional to the target maximum crest height and target peak inline force. The time shift can be linked to the overturning behaviour of near-breaking waves which leads to temporal asymmetry of the crest. The second-order FORM model is able to reproduce some of this asymmetry. In the same plot it is seen that the preceding and the following slope of the free surface elevation generated by $FORM(F_1 + F_2)$ are consistent with the wave averaged experiments. However, the maximum crest height is not captured by the results of $FORM(F_1 + F_2)$. In addition, from the preceding trough of the main peak in the second order free surface elevation time series, it is seen that a small crest is visible in the trough. This indicates the second order theory is not valid to include all the nonlinearity in this case. Hence it can be concluded that the experimental wave includes more nonlinearity than the second order theory. Based on comparison of the exceedance probability of this wave with the one presented in section 3 it can be seen that the exceedance probability of the current wave is about 1.5% compared to about

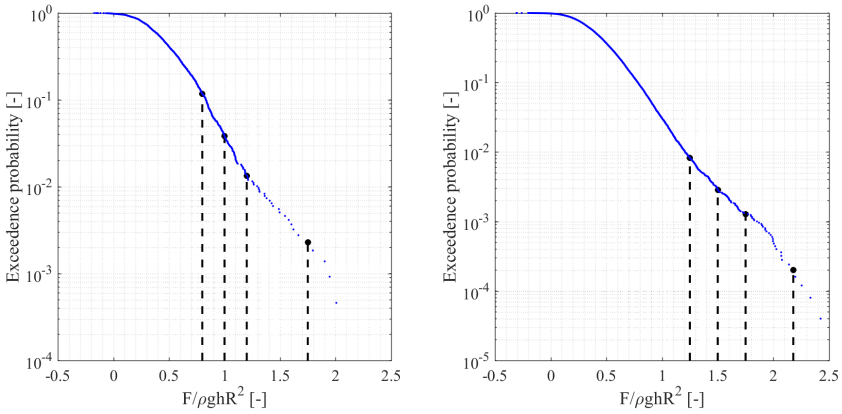

FIGURE 7: The exceedance probabilities of maximum inline force of each wave in one sea state cases 011 (left plot) and case 006 (right plot).

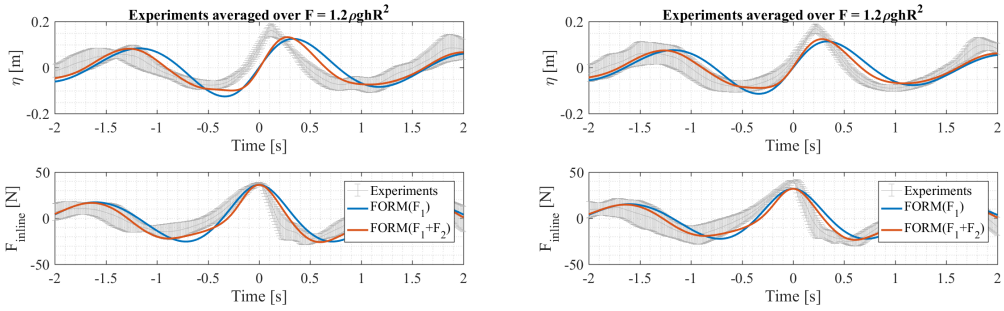

(A) Case 011. (B) Case 006.

FIGURE 8: Wave averaged time series of free surface elevation and inline force between 9 waves from case 011 and case 006 with maximum inline force close to $1.2\rho ghR^2$, in addition to corresponding results from $FORM(F_1)$ and $FORM(F_1 + F_2)$ given $F_{target} = 1.2\rho ghR^2$

15% in the previous case (case 11, $\eta = 0.6H_s$). Hence the large nonlinearity is expected. Despite higher nonlinearity effects, the reproduced wave by $FORM(F_1 + F_2)$ is in the range of one standard deviation of the wave averaged experiments most of the times.

To investigate the directional spreading effect on the measurements and FORM results of the same wave, results of case 006 is analyzed in the following. In figure 8b, in the bottom plot, the wave averaged inline force time series is seen in gray. Similarly to the 2D case, the effect of slamming is seen at the peak of the time series. Based on comparison of the $FORM(F_1 + F_2)$ inline force time series with the experiments, the amplitude of the time series compares well neglecting the effect of slamming in the crest of the time series around the main peak.

Further, from the top plot, the free surface elevation time series resulting from $FORM(F_1 + F_2)$ have a generally good agreement with the measurements, however, with lower amplitude. Similarly to the equivalent 2D event,

the experiments results look more nonlinear than the FORM results.

In figure 8a and 8b similar slamming effect is observed. As concluded in section 3 with the same inline force the case with directional spreading (here case 006) should have higher maximum free surface elevation than the case without spreading. This, however, is not observed in the experiments similarly to the previous comparison of the experiments with and without directional spreading in section 3.

From figure 8b and figure 5b, the former plots of the wave averaged experiments look more nonlinear. From the corresponding exceedance probability plots, figure 4 and figure 7 it is seen that the exceedance probability of the waves investigated in figure 8b is about 0.8% while it is around 10% for the waves investigated in figure 5b. This explains the larger nonlinearity in the latter case, figure 5b.

FORM(F) in 20 m water depth

To investigate the effect of water depth, in this section, similar results for an event in 20 m depth are investigated. Figure 9a shows the exceedance probability plot of the non-dimensional inline force peaks of case 016, in 20 m water depth including directional spreading.

In figure 9b, in the bottom plot the inline force time series of case 016 is shown similar to the previous cases. The corresponding free surface elevation is seen in the top plot.

The amplitude of the inline force time series of $FORM(F_1 + F_2)$ is consistent with the wave averaged experiments. However, the preceding slope is slightly larger than the one from the experiments.

From the top plot it can be seen that apart from the time shift between the numerical results and the experiments, the slopes and the amplitude of the waves are consistent. It is seen that the wave of $FORM(F_1 + F_2)$ is beyond the limit of second order theory demonstrated by the small crest inside the preceding trough of the free surface elevation. Also the maximum crest height of the wave averaged measurements is larger than the free surface elevation based on $FORM(F_1 + F_2)$, similar to the previously investigated events.

Based on figure 8b and figure 9b, the event in case 016, with smaller water depth is more nonlinear.

Quantification of FORM agreement

Based on the full set of results, more analysis was conducted over the agreement of the model results with the wave averaged measurements in terms of amplitude and phase shift. The analysis also included the standard deviation of the wave averaged measurements. The results are categorized into two groups where in the first group the objective was to find the most probable wave shape given η_{target} while in the second group F_{target} was given.

To quantify the FORM agreement with the measurements, the following definition of relative error measure was applied after shifting the time series to remove the time offset between them

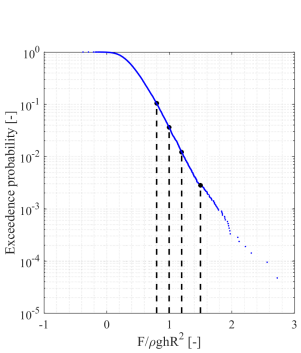

(A) The exceedance probabilities of maximum inline force of each wave in one sea state cases 016.

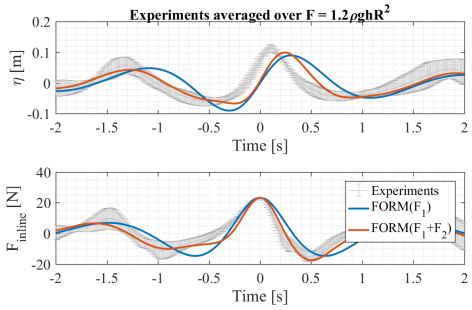

(B) Wave averaged time series of free surface elevation and inline force between 9 waves from case 016 with maximum inline force close to $1.2\rho ghR^2$, in addition to corresponding results from $FORM(F_1)$ and $FORM(F_1 + F_2)$ given $F_{target} = 1.2\rho ghR^2$.

FIGURE 9: The exceedance probabilities of maximum inline force and the wave averaged time series of free surface elevation and inline force.

$$E = \frac{\sqrt{\overline{(\mathbf{X} - \mathbf{X_{measured}})^2}}}{\max(\mathbf{X_{measured}})} \tag{16}$$

First group with given η_{target}

Figure 10a shows the relative mean error, E, of four test cases, for first and second order free surface elevation and inline force, in relation to the wave averaged measurements. For the free surface elevation of second order FORM results, E is between 6% and 18% in all analyzed events. The average error between the inline force signals of second order FORM results and the measurements, however, was larger and up to 32%. The average error of the first-order results was about twice as large. The smallest agreement was observed between the inline force time series of $FORM(\eta_1)$ and the measurements. The errors for this comparison went up to 44%. The best agreement was seen in free surface elevation comparisons of FORM results $FORM(\eta_1 + \eta_2)$ and the measurements.

No clear relation between the directional spreading and the standard deviation of the measurements was seen when events with the same exceedance probability were chosen with and without spreading.

The time shift between the results from the models and the wave averaged measurements was observed to be directly proportional to the target maximum crest height. Figure 10b shows this effect clearly. The phase shifts between the FORM results and the measurements vary from zero to one radian. The phase shifts of the first order FORM results are about 0.3 radian higher than the second order included results. This could be related to the

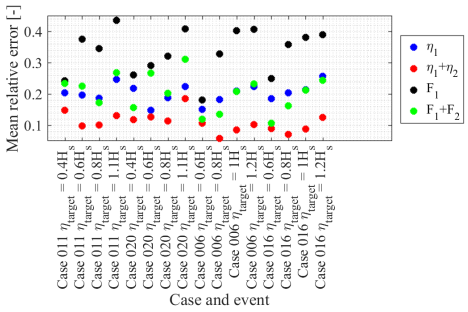

(A) The mean relative error of free surface elevation and inline force time series including first and second order for the cases with known η_{target}.

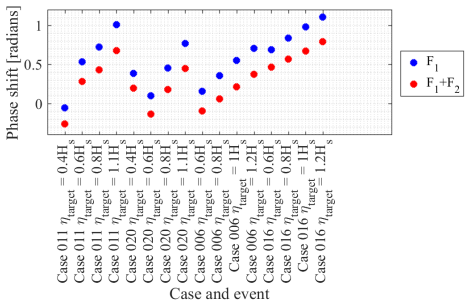

(B) The phase shift of inline force time series including first and second order for the cases with known η_{target}.

FIGURE 10: The mean relative error of $FORM(\eta)$ results and the phase shift of the force time series.

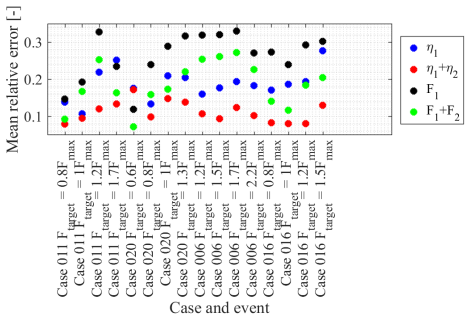

FIGURE 11: The mean relative error of free surface elevation and inline force time series including first and second order for the cases with known F_{target}.

fact that to keep the inline force calculation strictly second order, the drag term in the Morison equation was only calculated up the still water level. This means that for the times that the waves are at the highest elevation, with highest horizontal velocity, a large drag contribution to the inline force is neglected.

Second group with given F_{target}

Figure 11 shows E of the same four time series, as in figure 10a, with given F_{target}. Similarly to the results given η_{target}, in general the agreement of FORM results and the wave averaged measurements for free surface elevation time series are in better agreement than the inline force time series. The relative mean error for free surface elevation of second order FORM is less than 11%. The error for the first order FORM is about 1.5 times as big as the second order included FORM for both free surface elevation and inline force time series.

Similarly to the previous group of results, the best agreement is in free surface elevation comparisons of FORM results and the measurements.

The same magnitude and behavior of the phase shifts as for the first group was observed for the second group of results.

Summary and discussion

FORM was used to predict the extreme wave episodes defined by maximum crest height and maximum inline force in 2D and 3D sea states. The NewForce model was defined as the force equivalent of the NewWave and the FORM implementation was validated against both theories. The results were linearly consistent. Further the results of FORM for a second-order target was found to have only minor deviations to the curves obtained as first-order NewForce with the second-order terms added. The results of FORM were also compared to the wave averaged measurements of the same target crest height or inline force.

In summary, it was observed that the events with larger target crest height or peak inline force values, had smaller deviations relative to the averaged signal of 9 waves. This is in agreement with the NewWave theory.

Generally, a relatively good agreement between the First Order Reliability Method results and the wave averaged measurements was observed. The agreement was further increased by adding the second-order terms into the target of the FORM analysis, leading to a better reproduction of the asymmetry around the force peak value. In addition, it was seen that the relative error between the reproduced second-order free surface elevation and the measurements was larger for larger (more nonlinear) target values with lower exceedance probability. It is expected that with a more nonlinear model a better agreement between the FORM results and the measurements is possible.

Larger deviations were observed between FORM and measurements where seen for the inline force than for the free surface elevation. This can be explained by the omission of the drag terms above still water level. Here a more nonlinear force model, can expectedly reduce this discrepancy. The inclusion of the drag term above still water level and higher-order nonlinearity can also reduce the phase errors between the FORM results and the measurements. This is part of current research to use FORM together with the fully nonlinear potential flow solver, OceanWave3D Engsig-Karup, Bingham, and Lindberg 2009, so that all the nonlinear effects are included up to the free surface level.

It was observed that FORM predicts larger crest height for the same target inline force peak value in the multi-directional sea than in the unidirectional sea. This was not observed in the measurements. This inconsistency may be explained by presence of slamming inline forces and effects beyond the second-order model accuracy. This aspect is subject to further work. It is envisaged that such further imporovements will lead to more accurate design waves for offshore wind turbine substructures.

Acknowledgement

The present research was partly funded by the DeRisk project of Innovation Fund Denmark, grant number 4106-00038B. Further funding was provided by Statoil and the participating partners. All funding is gratefully acknowledged. Prof. Paul H. Taylor, Dr. Thomas A. A. Adcock and Dr. Dripta Sarkar, University of Oxford, are gratefully thanked for stimulating discussions.

References

Agarwal, Puneet and Lance Manuel (2008). "Wave Models for Offshore Wind Turbines". In: *46th AIAA Aerospace Sciences Meeting and Exhibit* January, p. 15.

Bredmose, H. et al. (2016). "DeRisk - Accurate prediction of ULS wave loads. Outlook and first results". In: *Energy Procedia*. Vol. 94. Elsevier, pp. 379–387.

Dean, Robert (2013). *Water wave mechanics for engineers and scientists*. Vol. 53. 9, pp. 1689–1699. arXiv: arXiv:1011.1669v3.

Dean, Robert G. (1965). "Stream function representation of nonlinear ocean waves". In: *Journal of Geophysical Research* 70.18, pp. 4561–4572.

Eckert-gallup, Aubrey C et al. (2014). "Modified Inverse First Order Reliability Method (I-FORM) for Predicting Extreme Sea States". In: *Sandia National Laboratories Report* September, p. 41.

Engsig-Karup, A. P., H. B. Bingham, and O. Lindberg (2009). "An efficient flexible-order model for 3D nonlinear water waves". In: *Journal of Computational Physics* 228.6, pp. 2100–2118.

Ewans, Kevin and Philip Jonathan (2014). "Evaluating environmental joint extremes for the offshore industry using the conditional extremes model". In: *Journal of Marine Systems* 130.November 2012, pp. 124–130. arXiv: arXiv:1211.1365v1.

Ghadirian, A., H. Bredmose, and M. Dixen (2016). "Breaking phase focused wave group loads on offshore wind turbine monopiles". In: *Journal of Physics: Conference Series* 753.9, p. 092004.

Grice, J R, P H Taylor, and R Eatock Taylor (2014). "Second-order statistics and ' designer ' waves for violent free-surface motion around multi-column structures Subject Areas :" in:

IEC 61400-3 (2009).

Jensen, J. Juncher (2008). "Extreme value predictions and critical wave episodes for marine structures by FORM". In: *Ships and Offshore Structures* 3.4, pp. 325–333.

Lacaze, Sylvain and Samy Missoum (2015). *No Title*.

Rainey, R. C. T. (1995). "Slender-body expressions for the wave load on offshore structures". In: *Proceedings of the Royal Society of London* 450.1939, pp. 391–416.

Schløer, Signe, Henrik Bredmose, and Amin Ghadirian (2017). "Analysis of experimental data: The average shape of extreme wave forces on monopile foundations". In: *DeepWind*. Vol. 137. Elsevier, pp. 223–237.

Sharma, Jagat N. and Robert G. Dean (1981). "Second-Order Directional Seas and Associated Wave Forces." In: *Society of Petroleum Engineers journal* 21.1, pp. 129–140.

Tromans, Peter S, A R Anatruk, and Paul Hagemeijer (1991). "A New Model for the Kinematics of Large Ocean Waves Application as a Design Wave". In: *Proceedings of the First International Offshore and Polar Engineering Conference* 8.August, pp. 64–71.

Valamanesh, V, A T Myers, and S R Arwade (2015). "Multivariate analysis of extreme metocean conditions for offshore wind turbines". In: 55, pp. 60–69.

Paper 4

Investigation of the effect of the bed slope on extreme waves using First Order Reliability Method

* *This paper is submitted to the* ***Journal of Marine Structures****.*

Amin Ghadirian[1], Henrik Bredmose[1]
[1] DTU Wind Energy, Nils Koppels Alle Building 403, DK-2800 Kgs. Lyngby, Denmark
E-mail: amgh@dtu.dk

Abstract

The effect of bed slope for the force statistics and shape of the force time history around the force peak is investigated numerically with a fully nonlinear wave model and FORM analysis. The numerical model setup is validated by comparison of averaged experimental force and free surface elevation time series and the FORM results for the given force levels. The fully nonlinear FORM solution shows a good improvement over first-order and second-order results by increasing the asymmetry of the force history through the peak. The average deviation between FORM and the experimental curve is found to be at the level of 10% of the maximum force value. Next, the order statistics for force peaks from an experimental and numerical 3 h realization are compared. Bootstrapping is applied to estimate the expected mean value of the inline forces for a given exceedance probability and a good match between the numerical and experimental order statistics is found.

FORM predictions of the force peak histories for a cylinder on flat or sloping bed are next compared. The diameter, depth at the structure and significant wave height is kept identical between the two cases. It is found that the force histories are not changed significantly by the presence of the slope in the sea states with lower Ursell number. For the larger Ursell number sea states, the corresponding time histories of the free surface elevation, however, show a larger skewness for the flat bed case. Further, from the FORM analysis, the exceedance probabilities for a given force level at sloped bed is

found to be larger than for flat bed. The ratio of exceedance probability is found to increase with force level except for the sea states with larger Ursell number where the numerical results are affected by strong nonlinearity.

The higher-harmonic content of the force histories is further analyzed by the four-phase separation method of Fitzgerald et al (2014). The analysis confirms that the relative contribution from the higher-harmonic force components increase with the force peak level and further shows that the contribution from the first, second and third harmonics are very similar between flat bed and sloped bed. The analysis further highlights the presence of spurious second-harmonic waves from the linear wave generation method and shows that these are stronger for the flat bed case. The phase shift between the different harmonics of free surface elevation and inline force time series is observed to be constant for different sea states and target forces irrespective of the bed slope.

Besides the direct findings of the study, the paper demonstrates the applicability of the FORM method for determination of design waves based on certain load effects. Although difficulties may occur for breaking waves or very strong nonlinearity, the combination of FORM and a fully nonlinear wave model enables average probability levels and time histories for extreme events to be determined and applied as design waves specific to a given load level or response level.

Introduction

The calculation of the Ultimate Limit State (ULS) load cases is an important step in the design process of substructures for offshore wind turbines. For such cases, normally, a set of sea state characteristics are chosen from the long term data or hind cast simulations based on a target return period. Irregular time series of free surface elevation are then made using linear wave theory. Afterwards the extreme waves are selected and replaced by either linear New Wave (Tromans, Anatruk, and Hagemeijer 1991) or the stream function wave theory (Fenton 1988) to calculate the kinematics and the distributed force on the structures (*IEC 61400-3* 2009). In both methods the bed is assumed to be flat which is usually not the case in the open sea, especially close to the coast. The current study aims to investigate the effect of the presence of a sloped bed on the exceedance probability, frequency content and shape of waves that create extreme force episodes.

Although several studies on the effect of bed slope exist in the literature, only one study of the effect on the load on the structure exists to the authors knowledge. Nelson 1982 investigated characteristics of regular waves on various slopes. These characteristics included wave profile, celerity and ratio of crest height to wave height among many others. He found out that the effect is minimal on wave celerity and potential energy but significant on crest and trough skewness and the asymmetry of the wave. Nevertheless, linked to the limitation of regular waves, he did not investigate the time series, power spectral density or the statistical distribution of the free surface elevation of the waves on different bed slopes. Elgar and Guza 1985, Freilich

and Guza 1984 and Freilich, Guza, and Elgar 1990 used field measurements to investigate the effect of shoaling of gravity waves and compared these results to linear shoaling theory and a nonlinear model. The nonlinear model was based on Boussinesq-type equations for a sloping bottom. The change in power spectral density of the free surface elevation of different sea states due to the slope was the focus of these studies. Hence, the time series and statistical distribution of the free surface elevation were not investigated. Nwogu 1993 developed a new form of Boussinesq-type equations with the velocity variable in an arbitrary depth. These equations were then implemented and used to investigate the propagation of regular and irregular waves on a constant slope beach. Time series of the surface elevation and the power spectral density of them were investigated and the results were compared to experiments. The results demonstrated that the developed form of the equations could reasonably simulate several nonlinear effects that occur in the shoaling of surface waves from deep to shallow water. He reported that the forced lower- and higher-frequency wave harmonics amplify during shoaling and the horizontal and vertical asymmetry of the waves increases. In none of these studies the statistical distribution of the wave height and the maximum inline force were investigated.

Schløer, Bredmose, and Bingham 2011 investigated the statistical distribution of the maximum inline forces numerically on two bed slopes of 1:25 and 1:100. They used the same linear wave time series based on the JONSWAP spectrum at the wave generation zone, at equal depth in the two domains. The study concluded that a larger bed slope results in largest maximum crest height, inline force and bending moment. The work included numerical simulation of just one sea state. Katsardi, Lutio, and Swan 2013 used a systematic campaign of experiments to investigate the role of local water depth, peak period, significant wave height, spectral band width and the bed slope on the statistical distribution of the wave heights and the crest heights. Two different bed slopes of 1:100 and 1:250 were used. The dependence of the statistical distribution to the local effective water depth ($k_p d$) and the local sea state steepness ($\frac{1}{2} H_s k_p$) was shown and it was found that the two different mild bed slopes analyzed did not change the wave height or crest height statistical distributions. However, in this study the statistical distribution of the inline force was not investigated.

The main difference between the current work and previous literature is the focus on the extreme waves in term of maximum inline force in the present work. In this paper we present a detailed study on the effect of the bed slope on the inline force peak statistical distribution, power spectral density and the time series of the free surface elevation and inline force on two bed slopes and six sea states. Another important feature of the present study is that the sea state parameters are kept identical where results at a slope and flat bed are compared. This study includes measurements of the inline force and free surface elevation which will be described in Section 4. The process used to analyze the data is also explained in Section 4. In Section 4 the numerical model used to simulate the fully nonlinear waves and the reliability problem which was solved to calculate the most probable shape of the waves

with certain maximum inline force and their probabilities are described. The measurements and the comparison to the numerical model used on a flat and a sloped bed can be found in Section 4. The effect of the bed slope is investigated using the proposed method in Section 4 and finally more discussions and some suggestions for the future work are presented in Section 4.

Experiments and the data analysis methods

Data from two sets of experiments are used in the present study. These two data sets are related to the experiments performed as part of the DeRisk project (Bredmose et al. 2016) and the Wave Loads project (Bredmose et al. 2013). In both test campaigns several different sea states were tested with duration of 3 hours in full scale.

DeRisk data set: flat bed

The flat bed experiments of the DeRisk project were conducted at DHI Denmark in 2015 with a scale of 1:50. A monopile was installed on two force transducers at the top and the bottom, 7.3 m from the wave makers. Wave gauges were installed in the basin to measure the free surface elevation approaching and passing the monopile. In the present study only unidirectional wave sea states were investigated, even though the experiments in the project included several directionally spread sea states. The diameter of the monopile was 7 m and the water depth was 33 m in full scale. The wave makers were of piston type and waves were generated by linear wave generation theory (Dean 2013).

A schematic drawing of the wave basin layout is given in figure 1.

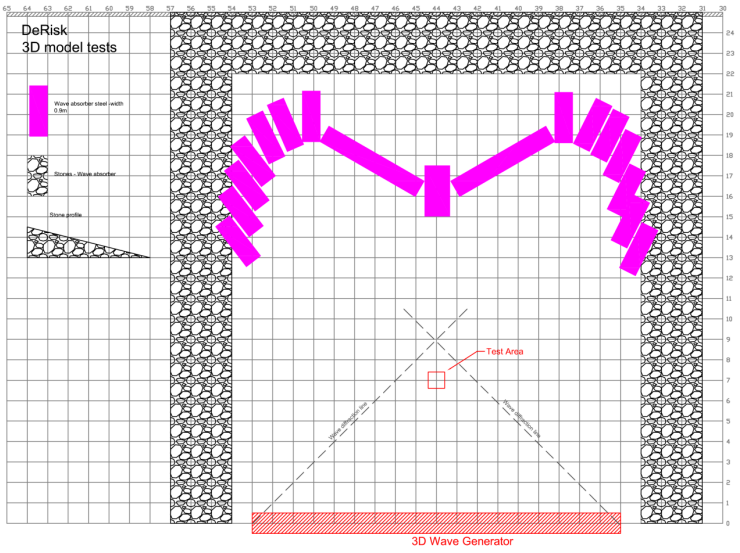

FIGURE 1: Schematic drawing of the test layout of the DeRisk DHI tests on flat bed Vindenergi 2015.

Wave Loads data set: sloped bed

The Wave Loads project (Bredmose et al. 2013; Bredmose 2013), included experiments of irregular waves on a 1:25 sloped bed in scale 1:80. The diameter of the monopile, installed on the slope was 6 m and the water depth at the location of the monopile varied between 40.8 m, 30.8 m and 20.8 m in full scale. The monopile was mounted on a force transducer at the bottom, 7.75 m from the wave makers and 6.75 m from the beginning of the slope. The investigated sea states from this data set were also unidirectional. Linear wave generation theory was used to form the paddle movement signal for the piston type wave makers.

A schematic drawing of the test layout is shown in figure 2.

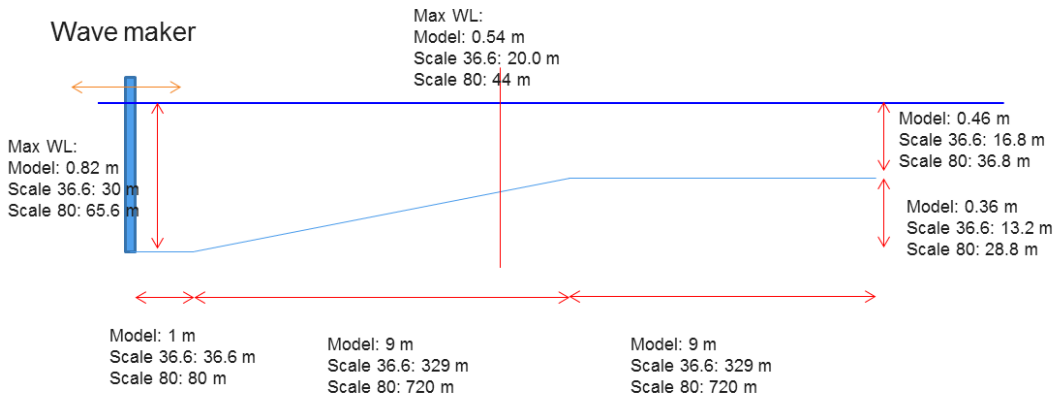

FIGURE 2: Side view of the test layout used in the Wave Loads project, sloped bed Bredmose et al. 2013.

Data analysis

The parameters of the selected sea states are shown in table 1. Sea states 1 and 2 were conducted in the DeRisk project on a flat bed while the sea states 3 to 8 were tests conducted in the Wave Loads project on a sloped bed. From the table, one can see that the sea states cover a range of water depth, significant wave height and peak periods which is suitable for validation of the numerical methods. The Ursell number (Ursell 1953) was calculated for each sea state to give a measure of nonlinearity of each sea state and is presented in table 1.

$$Ursell = \frac{H_s L_p^2}{h^3} \tag{1}$$

Here L_p is the wave length calculated from the linear wave dispersion relation for the peak frequency.

In the analysis of the experimental data, reflections from the artificial beach was observed. Hence, reflection analysis was performed to choose only the sea states with the least reflection affecting the data. The free surface elevation time series from 4 different wave gauges in different distances from

the wave maker were used to calculate the incident wave and the reflected wave using least square method based on the work of Goda and Suzuki 1976 and Bredmose et al. 2010. The calculated reflection coefficients based on equation 2 are shown in table 1.

$$\text{Reflection coefficient} = \frac{\sigma(\eta_{incident})}{\sigma(\eta_{reflected})} \tag{2}$$

where σ is the standard deviation of the time series. The reflection coefficients vary from 7% to 18% which might effect the quality of the measured η and force. While this may thus affect the validation of the numerical setup, the main part of the paper results is based on pure numerical calculations and is thus not affected.

The equivalent flat bed paddle signal coefficient is also presented for the cases that were used in the investigation of the effect of the bed slope. This parameter is further explained in Section 4. Due to the difference in parameters, the tests in the two test campaigns could not be compared directly. Hence, these sea states are used only for validation of the numerical method. Figure 3 shows the wave diagram for the selected sea states in addition to the breaking criterion proposed by Goda 2010. The sea states were selected in a way that are as nonlinear as possible but still small enough for a good part of the wave population to be non-breaking. This is beneficial because the numerical model used in this study is a potential flow model as explained in the next section and does not include a physics based breaking model.

TABLE 1: Characteristics of the investigated sea states (Full scale values). Water depth is given at the location of the monopile (MP) and the wave makers (WM).

Sea state	h [m] MP	h [m] WM	H_s [m]	T_p [s]	D [m]	Slp.	Scl.	Ur	Rfl.	Eqv. flat coef.
1	33	33	7.5	15	7	0	50	12.3	8%	-
2	20	20	5.8	9	7	0	50	8.0	7%	-
3	40.8	62.4	8.3	12.6	6	1:25	80	5.9	8%	0.9788
4	40.8	62.4	11	14	6	1:25	80	10.9	8%	0.9967
5	30.8	52.4	8.3	12.6	6	1:25	80	11.6	9%	0.9978
6	30.8	52.4	11	14	6	1:25	80	18.4	10%	0.9840
7	20.8	42.4	8.3	12.4	6	1:25	80	22.8	18%	0.9840
8	20.8	42.4	11	14	6	1:25	80	30.8	15%	1.3550

The individual waves were separated in the measured time series of the free surface elevation (η) with the zero up-crossing technique. The wave height and maximum inline force for each wave was then stored. These data were used to calculate the exceedance probability for each wave based on peak inline force and the crest height based on the individual wave events. For a given maximum inline force, 9 waves with the closest maximum inline force were selected and ensemble averaged to obtain the expected shape of the wave in the specific sea state with the given maximum inline force. This

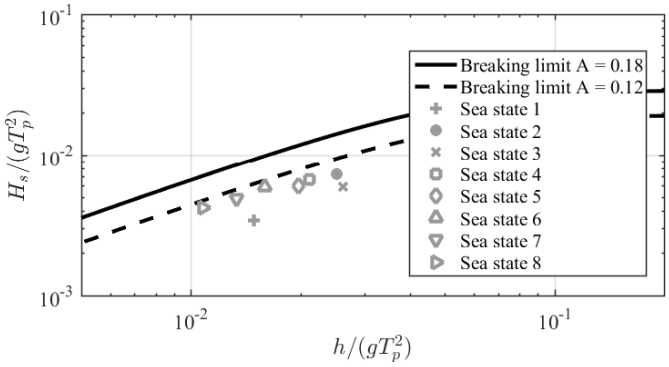

FIGURE 3: Wave diagram for the investigated sea states.

method was initially proposed by Grice, Taylor, and Taylor 2014 for use with free surface elevations and coined as the "designer wave". Later this method was used for inline force time series by Schløer, Bredmose, and Ghadirian 2017 and Ghadirian, Bredmose, and Schløer 2017. Although more than nine wave episodes for the averaged events is desirable, the nature of the extreme events, especially towards the tail of the distribution makes the number of observed peaks close to the largest forces limited. An example of such waves can be seen in figure 5 as gray lines with error bars.

Wave model and FORM problem

In this section the numerical methods which were used to reproduce the experiments, to estimate the most probable wave which gives a certain maximum inline force and to calculate the probability of such waves are explained.

The numerical flow solver: OceanWave3D

OceanWave3D (Engsig-Karup, Bingham, and Lindberg 2009) is a finite difference potential flow solver that solves the Laplace equation in three dimensions with kinematic and dynamic free surface boundary conditions and kinematic boundary conditions on varying topography. A flux boundary condition on one of the side walls can be used similarly to the wave makers in experiments. This method is linearly consistent with the piston type wave makers to replicate the wave maker motion of the experiments and has been used successfully in previous studies for reproduction of wave tank experiments (Paulsen, Bredmose, and Bingham 2014; Paulsen et al. 2014). A sixth order discretization scheme in space was used for all simulations while the classical explicit four-stage, fourth-order Runge-Kutta scheme was used for time stepping.

A convergence study was performed to make sure all the waves in each sea state, even with the highest frequency and smallest wave length are well resolved. In all the cases the size of the cells in the wave propagation direction was 2 cm, that is between 120 to 240 points per wave length, while

15 points were used in the vertical direction with clustering of the points towards the free surface. A relaxation zone was used in the OceanWave3D domain to damp the waves at the end of the numerical flume. The length of this zone was tested to ensure proper damping of the longest waves in all the investigated sea states. The OceanWave3D domain is shown in Figure 4.

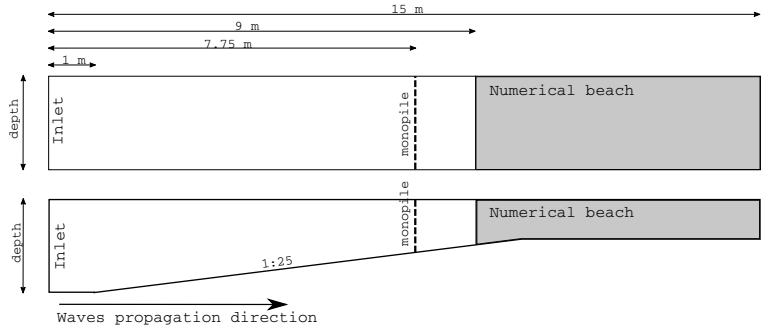

FIGURE 4: OceanWave3D domain to reproduce the flat bed (top) and sloped bed (bottom) cases.

To calculate the forces from the kinematics the drag and inertia coefficient must be known. To find the optimum C_d and C_M for all the sea states mentioned in table 1 the following method was used. Firstly the measured free surface elevation was used to calculate wave kinematics time series at the location of the monopile. Linear wave theory and Wheeler stretching were used for the calculation of the wave kinematics from the free surface elevation. Afterwards the linear least square method was used to calculate the optimum C_d and C_M which would result in a computed inline force time series closest to the measured force time series. We could not use OceanWave3D simulations for this process because the paddle signal from the experiments were not available and thus did not allow a complete deterministic reproduction of the measured wave field.

First Order Reliability Method

The First Order Reliability Method was used to calculate the most probable wave generation signal to make a wave that creates a target value of maximum inline force (F_{target}). The linear wave generation theory (Dean 2013) was used to create the wave generation signal as denoted in the following equations

$$\begin{aligned}
\sigma_j &= \sqrt{S_j \cdot df} \\
A_j &= \sigma_j \sqrt{a_j^2 + b_j^2} \\
C_j &= \frac{-2+2cosh(2k_jh)}{2k_jh+sinh(2k_jh)} \\
ap_j &= \frac{A_j}{C_j} \\
\phi_j &= arctan(\frac{-b_j}{a_j}) \\
u_{paddle}(t) &= \textstyle\sum_j ap_j \omega_j cos(\omega_j t + \phi_j).
\end{aligned} \tag{3}$$

Here index j indicates the element number of the vectors for each frequency. The JONSWAP power spectral density of the free surface elevation is shown by S, calculated for a given sea state in Table 1. The frequency increment is given by df. Angular velocity is shown by ω and the wave number by k. The wave generation signal is shown by $u_{paddle}(t)$ which is the velocity time series of the wave maker paddles, used as a flux boundary condition in the OceanWave3D simulation. Finally a_j and b_j are normal distributed variables denoted in

$$(a_j, b_j) \quad \in \quad \mathcal{N}(0, \sqrt{S_j \Delta f}). \tag{4}$$

From the OceanWave3D simulation, the kinematics in the location of the cylinder is obtained. The Rainey formulation of the Morison equations (Rainey 1995) was used to calculate the inline force on the monopile from the kinematics by

$$\begin{aligned} F_{OCW3D} \quad = \quad & \int_{-h}^{\eta} (\rho A C_m \tfrac{Du}{Dt} + \tfrac{1}{2}\rho D C_D u|u| + \rho A \tfrac{\partial u}{\partial t}) dz \\ & - \tfrac{1}{2}\rho A C_m \tfrac{\partial \eta}{\partial x} u^2. \end{aligned} \tag{5}$$

Here $\frac{Du}{Dt} = \frac{\partial u}{\partial t} + u\frac{\partial u}{\partial x} + w\frac{\partial u}{\partial z}$ is the material time derivative of the velocity in the wave propagation direction. In (5), ρ is the water density, A is the cross section area of the cylinder, C_m is the inertia coefficient, D is the cylinder diameter and C_D is the drag coefficient.

To calculate the most probable wave generation signal is to find the most probable combination of the random set of numbers $\underline{\alpha} = (\underline{a}, \underline{b})$. Since the random numbers in $\underline{\alpha}$ belong to independent normal distributions, the FORM problem can be rewritten as an optimization problem to minimize the summation of square of the random variables, $\underline{\alpha} \cdot \underline{\alpha}^T$, when the calculated inline force from the set of random numbers is equal to a target force.

$$\begin{aligned} & \min \ \underline{\alpha} \cdot \underline{\alpha}^T \\ & \text{subject to } F_{target} - F_{OCW3D} = 0 \\ & \\ & \text{where } \underline{\alpha} = \{\underline{a}, \underline{b}\} \end{aligned} \tag{6}$$

The optimization problem in (6) was solved using the Sequential Quadratic Programming method (Lacaze and Missoum 2014). In the current study, four different values of F_{target} are chosen in each sea state, ranging from $0.6 \cdot \rho g h R^2$ to $1.7 \cdot \rho g h R^2$, where g is the gravitational acceleration, h is the local water depth and R is the radius of the monopile. The chosen values of the target forces are in the higher range of the maximum inline forces in the sea states because the focus of the study is the extreme waves.

For any set of $\{\underline{a}, \underline{b}\}$ during the optimization, a wave paddle signal for OCW3D was computed. Then an OceanWave3D simulation was run to obtain the free surface elevation and kinematics at the location of the structure.

The final result of the FORM optimization is represented by $FORM(OCW3D)$. Because the variables $\{\underline{a}, \underline{b}\}$ are standard normally distributed around zero, the exceedance probability of the found realization with the given maximum inline force, F_{target}, is given by

$$\begin{aligned} \Phi &= e^{(\frac{-\beta^2}{2})} \\ \beta^2 &= \underline{\alpha} \cdot \underline{\alpha}^T \end{aligned} . \tag{7}$$

This follows from the result that the peaks of a Gaussian process are Rayleigh distributed (Longuet-Higgins 1952). Similar method was previously used by Gibson, Swan, and Tromans 2007 and Jensen 2007.

Validation of the model with measurements

In this section we present the results for the flat and sloped bed cases and show the comparison between these cases. Time series of the free surface elevation and inline force is presented. The mean relative errors are also presented for each case. The calculated exceedance probabilities are also presented in the following sections.

Flat bed

The time series and the relative errors

The time series of the ensemble averaged measured free surface elevation and inline force are presented in figure 5 for 9 events with maximum inline force equal to $1 \cdot \rho g h R^2$ in sea state 1. The 9 events are synchronized around the peak force time. The error bars in this plot show the standard error of the mean, $\sigma_M = \frac{\sigma}{\sqrt{N}}$, where σ is the standard deviation and N is the sample size (here 9). The wave appears nonlinear with symmetric trough heights and asymmetric slopes on two sides of its crest. The wave reflection from the monopile is visible as a small wriggle in the following trough of the main wave in the free surface elevation time series. The inline force time series is asymmetric and backwards leaning. A small wriggle in the trough of the inline force time series is noticeable in the measured data which is an indicator of the secondary load cycle (Paulsen, Bredmose, and Bingham 2014; Paulsen et al. 2014; Grue and Huseby 2002).

In the same figure the FORM(OCW3D) results are presented in blue color. The general behavior is consistent with the measurements. The shape of the wave and the backward leaning of the inline force time series are captured in these numerical results. However, there is a small phase shift between the free surface elevation time series of the measurements and FORM(OCW3D). The small phase shift might come from the inaccuracies in the estimated C_D and C_M. A larger C_D value will shift the peak force for large waves to a time instant closer to the wave crest. Another reason for the phase shift might be the higher-order diffraction waves which are not considered in the model. In

addition, the secondary load cycle is not visible in FORM(OCW3D) which is expected since, as explained in the previous section, the structure is not present in the numerical domain and the forces are only calculated using the Morison equation and the Rainey correction.

The results from FORM application to linear wave theory and second order (Dean 2013) are also presented in this plot denoted by FORM(F1) and FORM(F2) respectively. Similar results and the theory were previously presented in the work by Ghadirian, Bredmose, and Schløer 2017. The generated linear wave presented in dashed black line is more asymmetric in trough height and in the slopes leading and proceeding the main crest than the measured wave. Moreover, there is a large phase shift between its crest and the crest of the measured wave. The inline force time series of FORM(F1) is symmetric, peaking at the peak time of the measured ensemble averaged time series. It should be noted that the FORM(F1) result is identical to the analytical New Force model introduced by **Schloer2017** Comparison of FORM(F1) results to the New Force model was previously presented by Ghadirian, Bredmose, and Schløer 2017. The FORM(F2) free surface elevation result is more consistent with the measurements than the New Force model wave. There is also a phase shift between the second order wave crest and the measured wave crest time. The shape of the second order wave is asymmetric in trough height and in wave slope but generally in better consistency with the measured η than FORM(F1). The second order force time series shows different slopes before and after the peak only slightly better than the New Force results. The local events such as the wave scattering of the monopile and the secondary load cycle are not visible in the FORM(F1) and FORM(F2) results.

Similarly the time series of the ensemble averaged measured free surface elevation and inline force are presented in figure 6 for 9 events with maximum inline force equal to $1.2 \cdot \rho g h R^2$ in sea state 2. The wave appears nonlinear with symmetric trough heights and asymmetric slopes on two sides of its crest. Even though the absolute crest height is smaller than the crest height of the case shown in figure 5 it is larger relative to the water depth and the wave is more nonlinear. The general behavior of the FORM(OCW3D) free surface elevation is consistent with the measurements. However, the phase shift between the free surface elevation time series of the measurements and FORM(OCW3D) is larger in this case compared to the case shown in figure 5. The consistency between the FORM(F1) and FORM(F2) results is similar to the previous case. From the simulation log files in this case it was observed that the breaking filter in the numerical domain has been activated and smoothened some of the wave at the location of breaking. Probably because of the activation of the breaking filter the time series of FORM(OCW3D) are not as consistent with the measurements as in figure 5. The case shown in figure 6 was the largest target force in sea state 2. The third target force in the same sea state is shown in figure 7 which displays a better consistency between the FORM(OCW3D) results and the wave averaged measurements.

Figure 8 shows the mean relative errors of the inline force and free surface

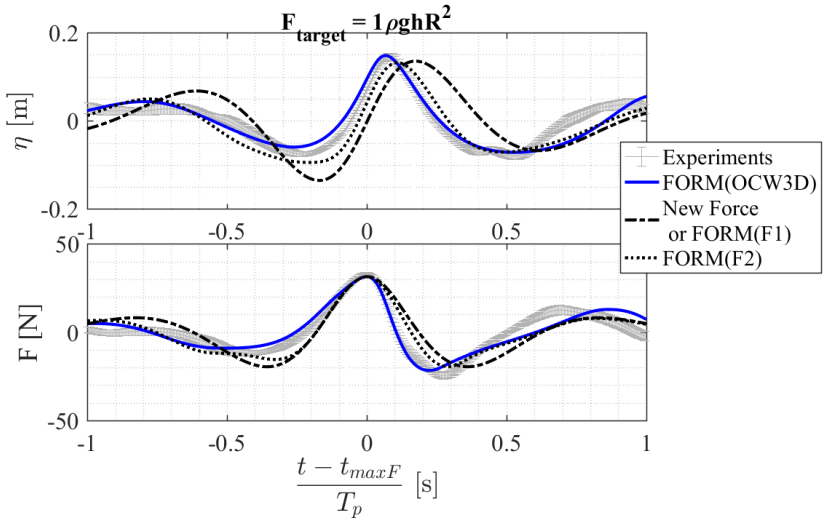

FIGURE 5: Free surface elevation and inline force time series of the sea state 1, $F_{target} = 1 \cdot \rho g h R^2$, on a flat bed.

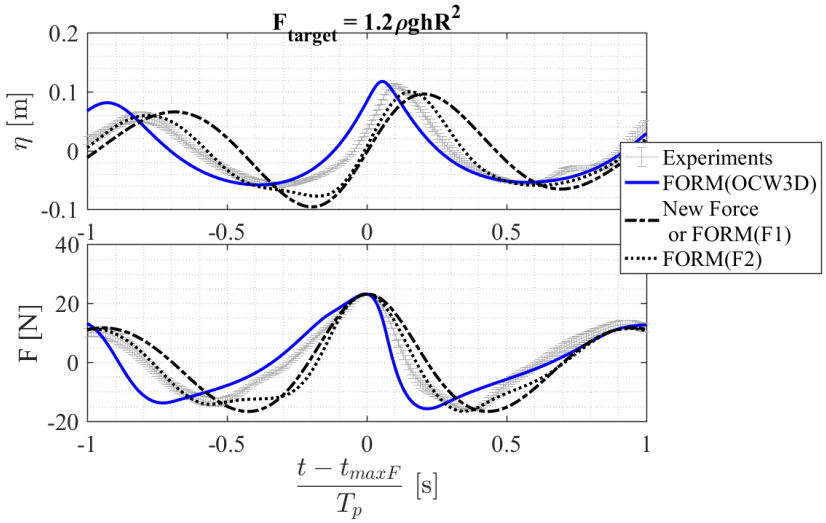

FIGURE 6: Free surface elevation and inline force time series of the sea state 2, $F_{target} = 1.2 \cdot \rho g h R^2$, on a flat bed.

elevation time series between the ensemble averaged measurements and the numerical results namely FORM(F1), FORM(F2) and FORM(OCW3D). The absolute relative phase shift between the free surface elevation time series of the measurements and the numerical results is also presented in this figure relative to the peak period of each sea state. The relative error from $-1.5 \cdot T_p$ to $1.5 \cdot T_p$ around the peak force time is calculated by

$$E = \frac{\sqrt{\overline{(\mathbf{X} - \mathbf{X_{measured}})^2}}}{\max(\mathbf{X_{measured}})}, \tag{8}$$

where $\mathbf{X}$ can be the inline force or free surface elevation for each time step. It is observed that the relative errors of the free surface elevation of

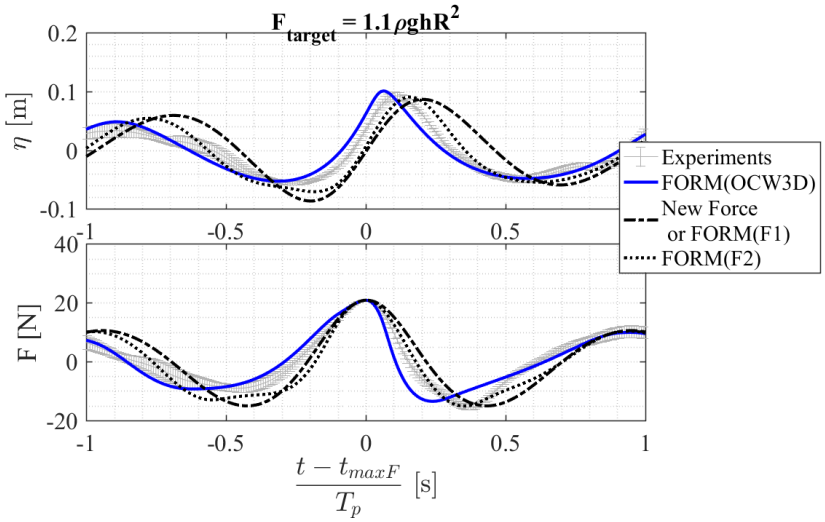

FIGURE 7: Free surface elevation and inline force time series of the sea state 2, $F_{target} = 1.1 \cdot \rho g h R^2$, on a flat bed.

FORM(OCW3D) from $-1.5 \cdot T_p$ to $1.5 \cdot T_p$ non-dimensional time does not exceed 16%. The average is around 12% and the mean relative error for the inline force of FORM(OCW3D) time series is smaller than 19% with an average around 10% for all the cases. One probable reason for the inconsistencies might be the fact that the model does not include higher-order diffraction. Another linked to this limitation, probable reason is the secondary load cycles in the wave averaged measured inline force history do not appear in the numerical results. Non-converged mean of the ensemble averaging of the measurements can also contribute to the errors. We expect these errors to be reduced by increasing the number of wave samples of ensemble averaging. The relative phase shift between the η time series of FORM(OCW3D) and the measurements is smaller than 6% for all the cases as shown in the bottom plot of this figure.

The relative errors for η and F for FORM(F1) and FORM(F2) are also shown in figure 8. The relative errors of FORM(F1) results are significantly larger than the ones from FORM(OCW3D). The relative errors of FORM(F2) results are always smaller than FORM(F1) as expected. The errors of FORM(F2) are larger than the FORM(OCW3D) results for all cases except the largest target force $1.2 \cdot \rho g h R^2$ in sea state 2. The reason might be activation of the breaking filter in the OceanWave3D model in this case. The average of the mean relative error of the free surface elevation is around 27% and 15% for FORM(F1) and FORM(F2) respectively. The average of the mean relative error of the inline force for FORM(F1) and FORM(F2) is 18% and 14% respectively. From figure 8, it is observed that implementing the FORM(OCW3D) model has reduced the errors around 40% compared to η of FORM(F2) and 80% compared to F of FORM(F2).

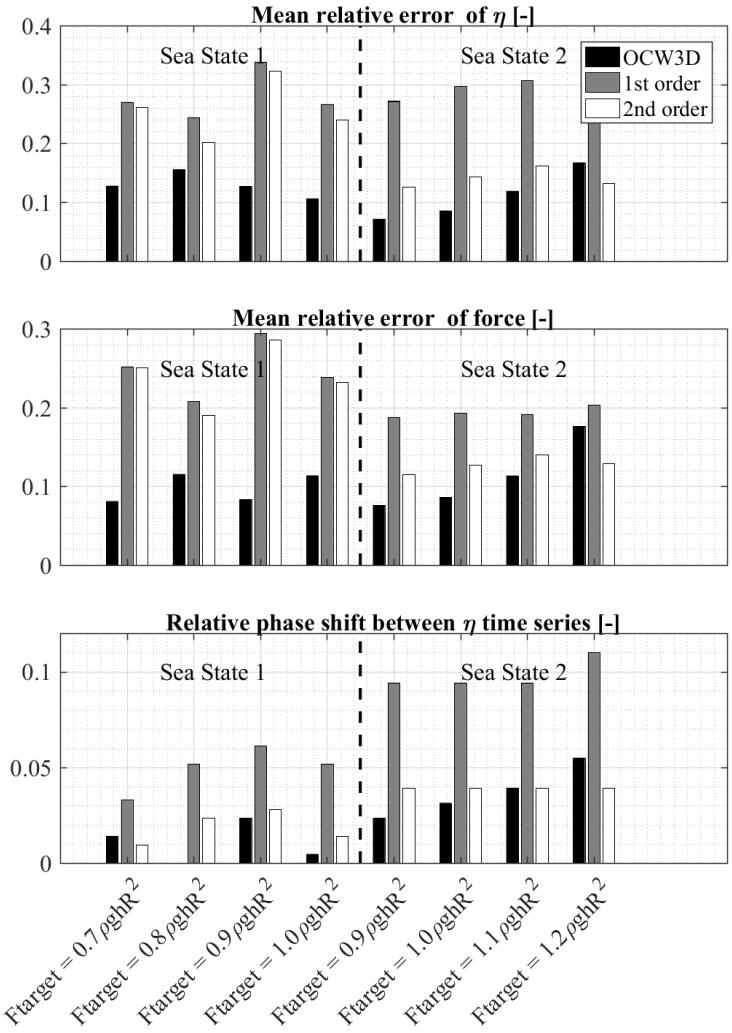

FIGURE 8: Mean relative error of the free surface elevation and inline force time series between the ensemble averaged measurements and the numerical results for sea states 1 and 2 on flat bed.

The probability plots

Figure 9 shows exceedance probability plots of the force peaks and crest heights of random realizations from sea state 1 and 2. The measurements are shown in gray lines with error bars. These data were extracted from 3 hour (full scale) random realizations for each sea state. After the waves were separated using zero up-crossing 20 sets of wave event collections were randomly selected from them with the same size as the original set of waves. Same size of the samples means that in each of the 20 sets there might be repeated wave events. This process is called bootstrapping with replacement (Efron 1993) and serves to estimate the stochastic variability for the obtained exceedance probability curve of a single realization. The advantage of this method is to avoid performing 20 random realization simulations or experiments for the same sea state.

A random realization, with an independent stochastic seed, of each sea

state was also simulated in OceanWave3D and the results are shown in black curves in the plots in figure 9. The random realization time series of the OceanWave3D simulations were not comparable with the experiments because neither the stochastic seed nor paddle signal from the experiments were available. For both sea states the OceanWave3D statistical distributions of maximum inline force and maximum crest heights are in relative good agreement with the measurements for high probabilities of exceedance but they deviate in the lower exceedance probabilities. This can be explained by stochastic variability and also to a lesser extent the limits of OceanWave3D which does not include a physics based breaking model.

The estimation of the exceedance probability from the FORM problem is also presented in the exceedance probability plots of inline force with blue filled circles. We expect these results to be in the range of the variations of the random realizations of the OceanWave3D simulations. A good consistency between the FORM results and the random realizations is thus observed except for the largest FORM force of sea state 2. It is worth mentioning that the case with the largest target inline force in the second sea state, the right side plot, seems to be in-converged, since the calculated exceedance probability of this case from the FORM problem is much lower than the random realization from the OceanWave3D simulations. However, since these cases are only for validation the re-computation of this case is omitted.

Sloped bed

The time series and the relative errors

The time series of the ensemble averaged measured free surface elevation and inline force are presented in figure 10 for 9 waves with maximum inline force as large as $1 \cdot \rho g h R^2$ in sea state 3. The wave is nonlinear with an asymmetric shape. The results from the FORM analysis is presented in blue color. The general behavior is very close to the ensemble averaged measurements of the free surface elevation and inline force time series. The shape of the wave and the backward leaning of the inline force time series are captured in the numerical results. The local effects on the ensemble averaged free surface elevation and inline force time series, the wave reflection and the secondary load cycle, are not captured in the numerical results as expected. The initial measured water level could not be determined accurately. For this reason in the comparison of the free surface elevations a zero mean has been imposed in both experiments and numerical results. After this correction, a good consistency between the measurements and the numerical results can be observed in this figure.

Similar time series of the ensemble averaged measured free surface elevation and inline force are presented in figure 11 to 15 for sea states 4 to 8 with largest maximum inline force in each case. Similar consistency between the FORM results and the wave averaged measurements is observed for all the cases. However, in sea states 6 to 8 a larger preceeding slope is observed

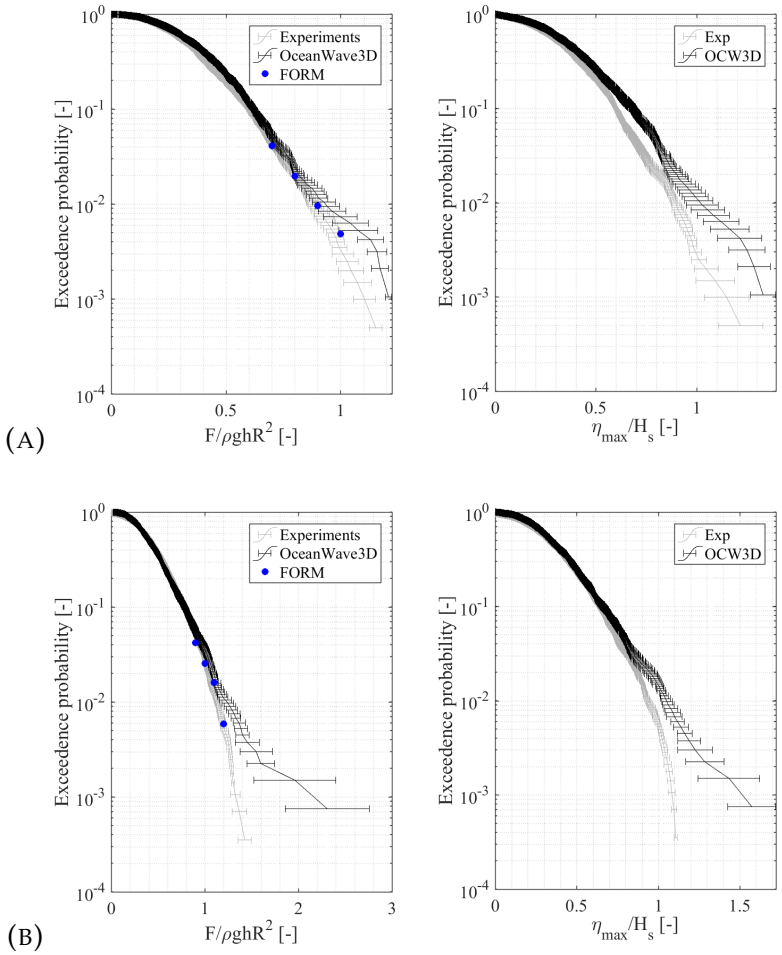

FIGURE 9: Exceedance probabilities relative to maximum inline force and maximum crest height from random realization tests, numerical simulations in OceanWave3D and numerical results from FORM problem for two sea states. (a) sea state 1 and (b) seat state 2.

in the free surface elevation time series of the FORM results. In general the FORM results are more skewed in these cases than the measurements.

Figure 16 shows the mean relative errors of the inline force and free surface elevation time series between the ensemble averaged measurements and numerical results for all the cases on a sloped bed, sea states 3 to 8. The absolute relative phase shift between the free surface elevation time series of the measurements and numerical results is also presented in this plot relative to the peak period of each sea state. It is observed that the average of the mean relative error for the inline force time series is around 8% for all the cases. The relative errors of the free surface elevation from the leading zero up crossing to the following zero up-crossing does not exceed 12% in all cases with average mean relative error around 8.6%. The phase shift between the free surface elevation time series does not exceed 3%. In general, a good consistency between the numerical results and the measurements is observed in the cases on sloped bed.

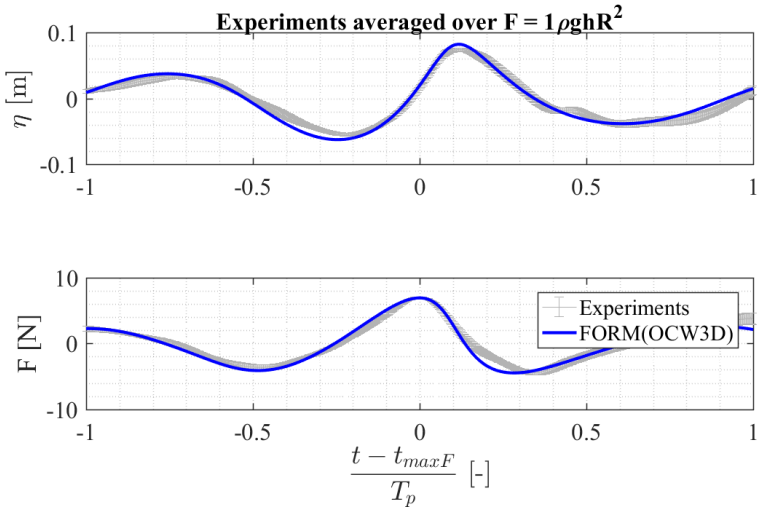

FIGURE 10: Free surface elevation and inline force time series of the sea state 3, $F_{target} = 1 \cdot \rho g h R^2$, on a sloped bed.

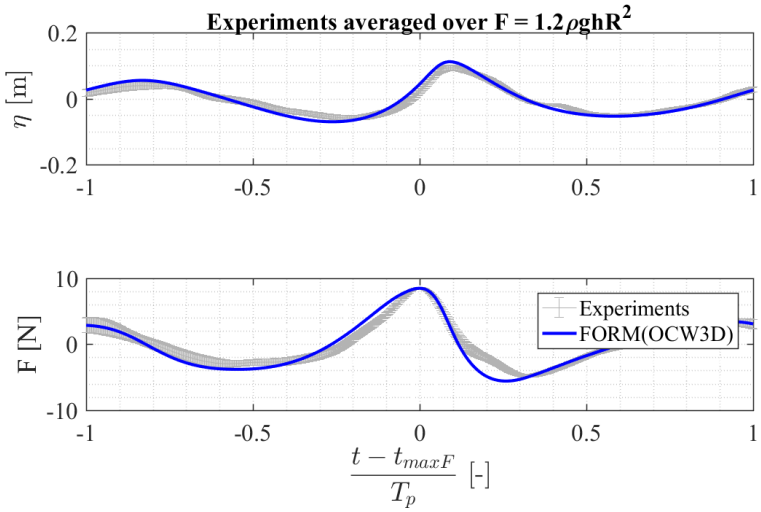

FIGURE 11: Free surface elevation and inline force time series of the sea state 4, $F_{target} = 1.2 \cdot \rho g h R^2$, on a sloped bed.

The probability plots

Figure 17 to 21 show the exceedance probabilities of maximum inline forces and maximum crest heights for sea states 3 to 8. The measurements are shown in gray lines with error bars. As the maximum inline force increases the probability of the exceedance decreases. The black curves show the same general behavior for the results from a three hour (full scale) random realization of each sea state simulated in OceanWave3D. In this figure we can see that the statistical distribution of the maximum inline forces are generally consistent between the measurements and the OceanWave3D simulations.

The estimation of the exceedance probability from the FORM problem is presented with filled blue circles. It is expected that these results lie in the range of the variations of the random realization of the OceanWave3D simulations and so in the range of the variation of the measurements. A

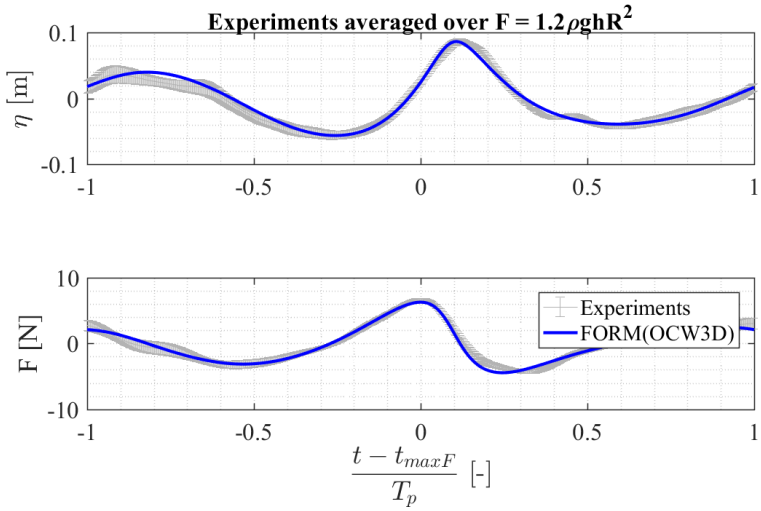

FIGURE 12: Free surface elevation and inline force time series of the sea state 5, $F_{target} = 1.2 \cdot \rho g h R^2$, on a sloped bed.

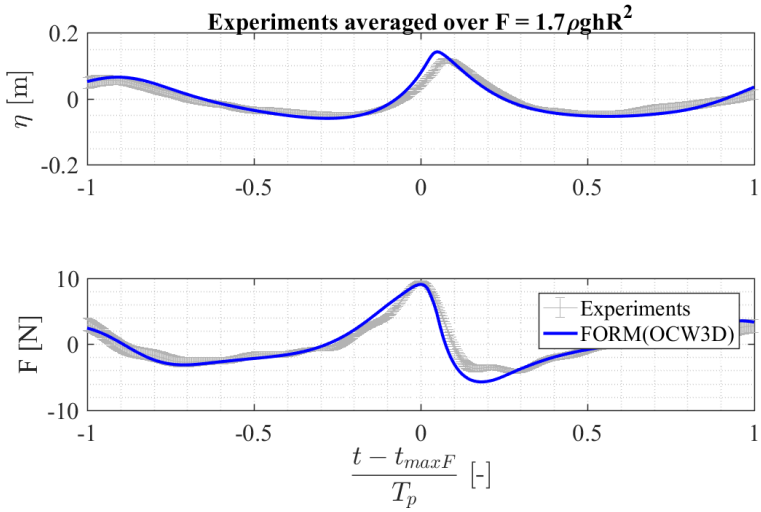

FIGURE 13: Free surface elevation and inline force time series of the sea state 6, $F_{target} = 1.7 \cdot \rho g h R^2$, on a sloped bed.

good consistency between the FORM results and the random realizations is observed for all the 6 sea states.

The results in this section show that the method is valid to use for similar cases on a sloped bed. In the next section the application of the method for investigation of the effect of the bed slope is presented.

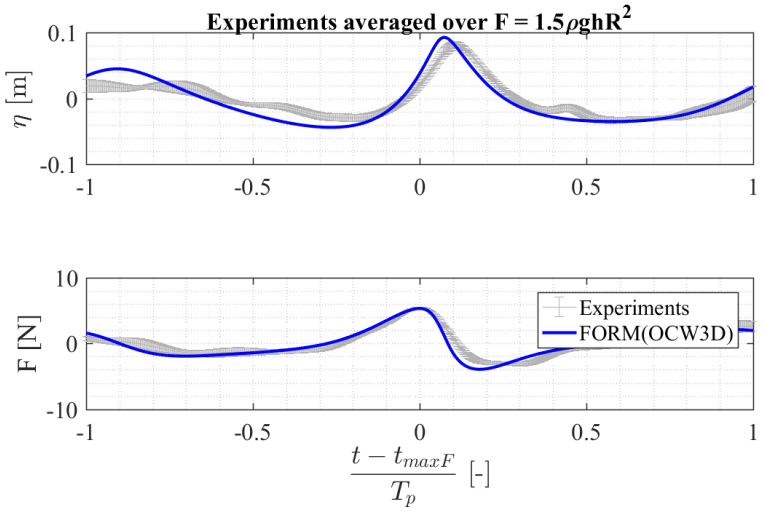

FIGURE 14: Free surface elevation and inline force time series of the sea state 7, $F_{target} = 1.5 \cdot \rho g h R^2$, on a sloped bed.

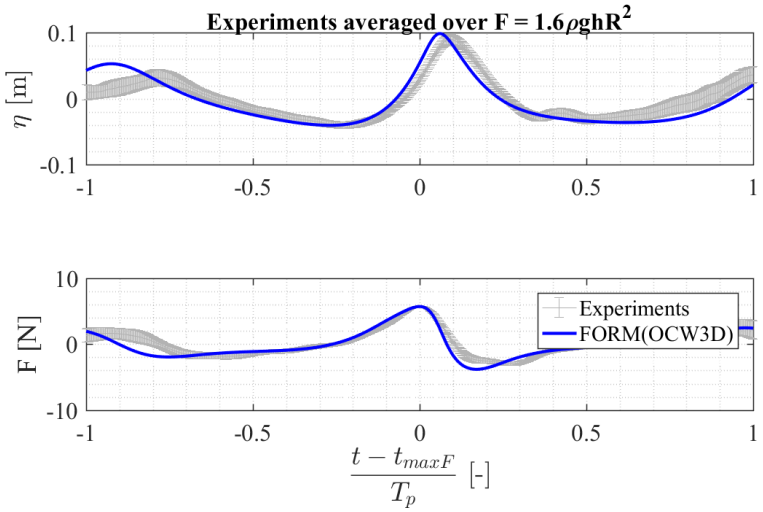

FIGURE 15: Free surface elevation and inline force time series of the sea state 8, $F_{target} = 1.6 \cdot \rho g h R^2$, on a sloped bed.

The effect of the bed slope

The main aim of the current study is to investigate the effect of the bed slope on the force statistical distribution and time history. Here an equivalent numerical domain with flat bed and the same depth at the location of the cylinder in tests 3 to 8 was created. A series of calibration simulations were performed to obtain the same sea state parameters and

$$H_s \quad \text{and} \quad T_1 = \frac{\int Sdf}{\int fSdf}$$

for these simulations on the equivalent flat bed at the location of the cylinder as on the sloped bed simulations. The time scale T_1, however, is hardly

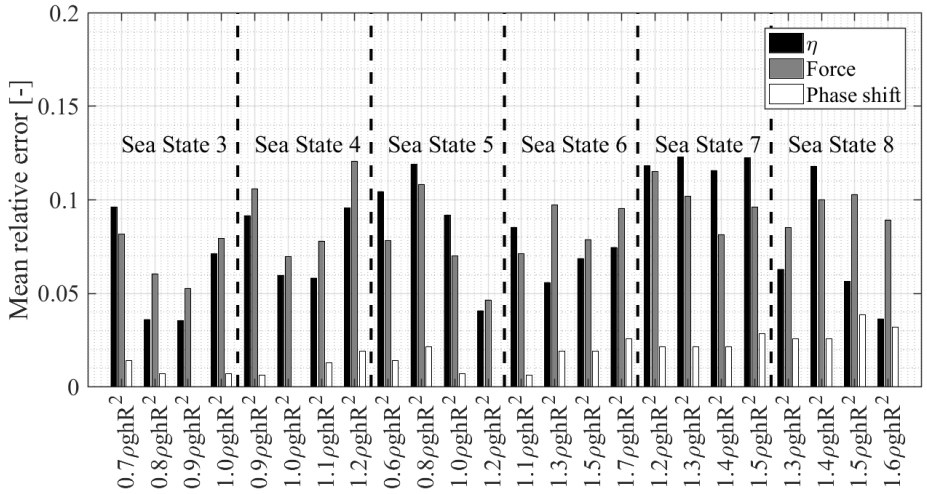

FIGURE 16: Mean relative error of the free surface elevation and inline force time series between the ensemble averaged measurements and the numerical results for sea states 3 to 8 on sloped bed.

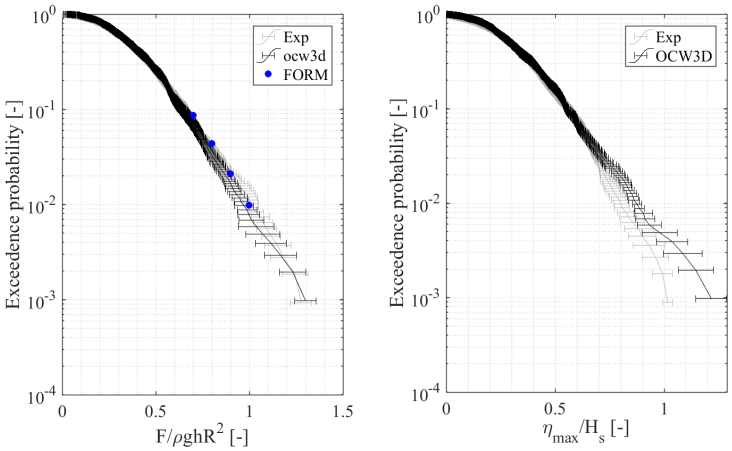

FIGURE 17: Exceedance probabilities relative to maximum inline force from random realization tests, numerical simulations in OceanWave3D and numerical results from FORM probem for sea states of 3 on sloped bed.

changed over the slope. Then the same target force levels were used for the FORM analysis in both setups. The FORM problem was solved this time around the new OceanWave3D domain for all the cases in the equivalent sea states.

It should be mentioned that the sea states 7 and 8 mentioned in Table 1 could not be simulated on the equivalent flat bed in the OceanWave3D domain, therefore the H_s was decreased in these two cases by 10% and 30% respectively to be able to have random long time realizations of the same sea states on sloped and equivalent flat bed. The equivalent flat bed paddle signal coefficient was then calculated for the sea states on a flat equivalent bed similarly to the other sea states in Table 1.

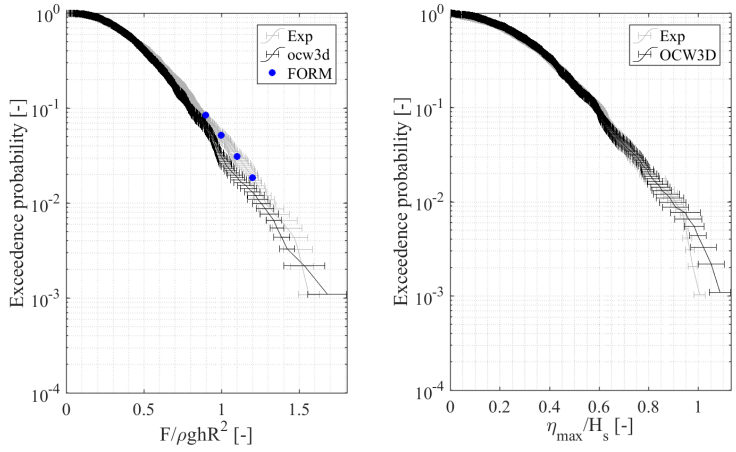

(A)

FIGURE 18: Exceedance probabilities relative to maximum in-line force from random realization tests, numerical simulations in OceanWave3D and numerical results from FORM probem for sea states of 4 on sloped bed.

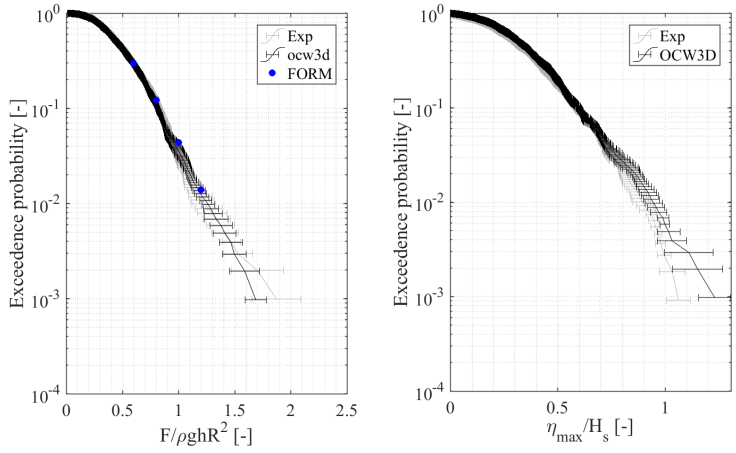

(A)

FIGURE 19: Exceedance probabilities relative to maximum in-line force from random realization tests, numerical simulations in OceanWave3D and numerical results from FORM probem for sea states of 5 on sloped bed.

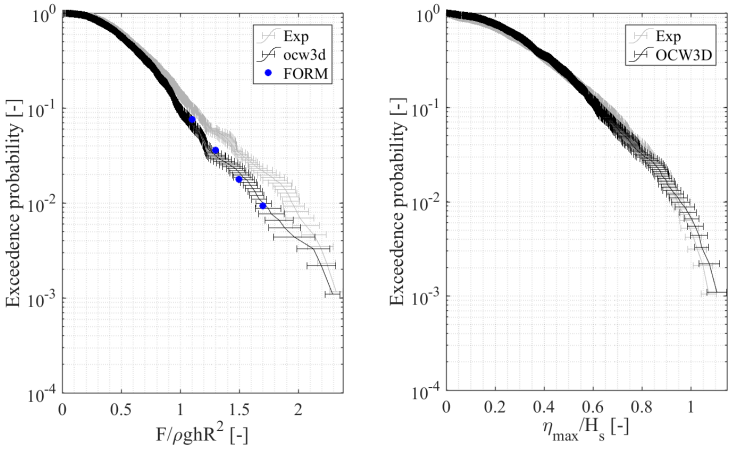

(A)

FIGURE 20: Exceedance probabilities relative to maximum in-line force from random realization tests, numerical simulations in OceanWave3D and numerical results from FORM probem for sea states of 6 on sloped bed.

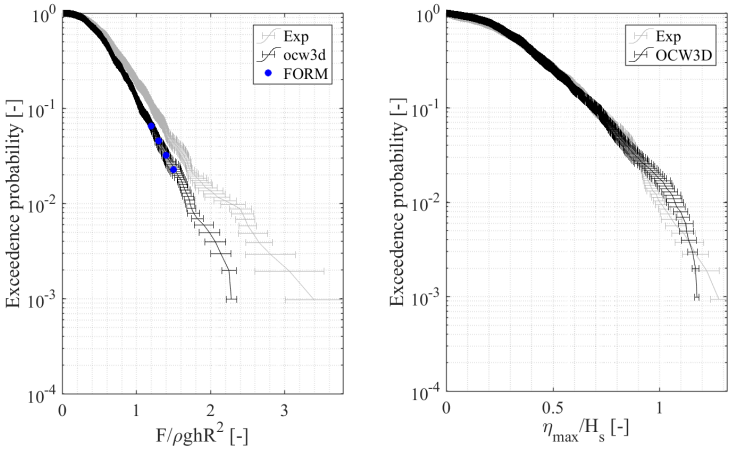

(A)

FIGURE 21: Exceedance probabilities relative to maximum in-line force from random realization tests, numerical simulations in OceanWave3D and numerical results from FORM probem for sea states of 7 on sloped bed.

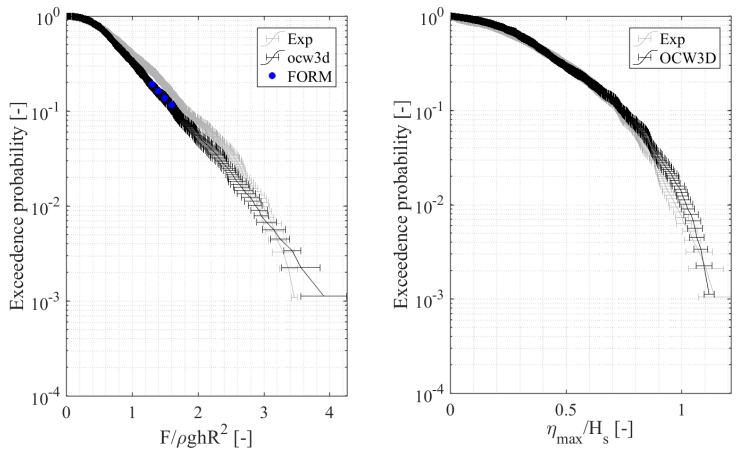

(A)

FIGURE 22: Exceedance probabilities relative to maximum inline force from random realization tests, numerical simulations in OceanWave3D and numerical results from FORM probem for sea states of 8 on sloped bed.

Comparison of the sloped bed with the equivalent flat bed: the time series and their frequency content

The free surface and inline force time series and their frequency content are presented in figure 24 to 28 for sloped and equivalent flat bed for sea state 3 to 8 with the largest target forces. The results for the sloped bed are shown in gray color. The consistency of these results with the measurements are previously shown in section 4. The black curves show the results from the equivalent flat bed numerical domain. It is observed that the force time series are very similar in sea states 3, 4 and 5 but they do show larger differences in sea states 6, 7 and 8. The same similarity is visible in the free surface elevation time series. Larger differences around the peak and second harmonic frequencies are observed in the PSD of these time series. With more investigation in all the cases it was observed that the energy content around the double peak frequency is larger in the equivalent flat bed cases. More investigation for the nature of this difference was performed and the results are shown in section 4.

In the cases from sea states 6, 7 and 8 the wave episodes have more skewness on the flat bed than on the sloped bed while the wave heights are smaller on a flat bed. The differences between the force time series are smaller than the differences between the η time series. This similarity of the inline force times series between the flat and sloped bed cases is specially clear from trough to trough. The frequency content around the peak frequency is always higher in the sloped bed cases than in the flat bed cases.

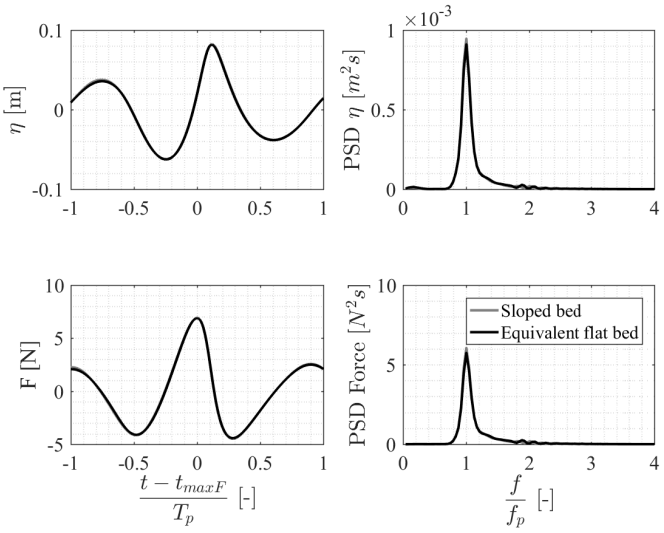

FIGURE 23: Free surface elevation and inline force time series and power spectral density for numerical results of a case in sea state 3 with $F_{target} = 1 \cdot \rho g h R^2$ with sloped bed and the equivalent flat bed.

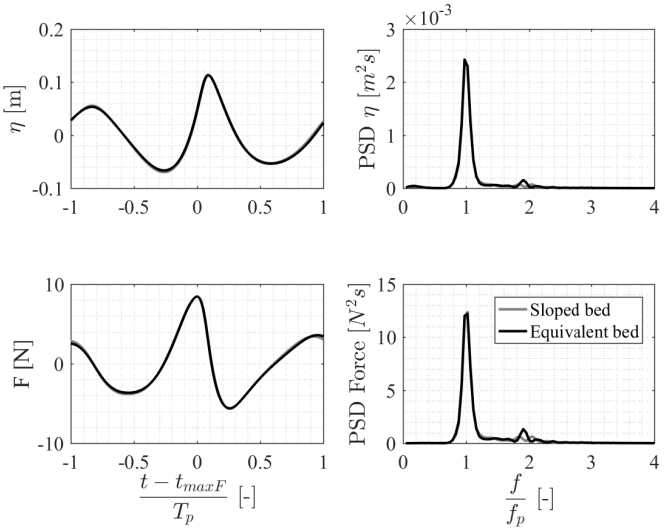

FIGURE 24: Free surface elevation and inline force time series and power spectral density for numerical results of a case in sea state 4 with $F_{target} = 1.2 \cdot \rho g h R^2$ with sloped bed and the equivalent flat bed.

Exceedance probabilities of maximum inline force and crest height

Figures 29 to 34 show the exceedance probabilities relative to the non-dimensional inline force peaks (left hand side plot) and crest heights (right hand side plot) for sea states 3 to 8. The plots on the right hand side show the agreement of the two sea states with and without a sloped bed. Similarly to figure 9 and figure 17 the curves with error bars are obtained from only one

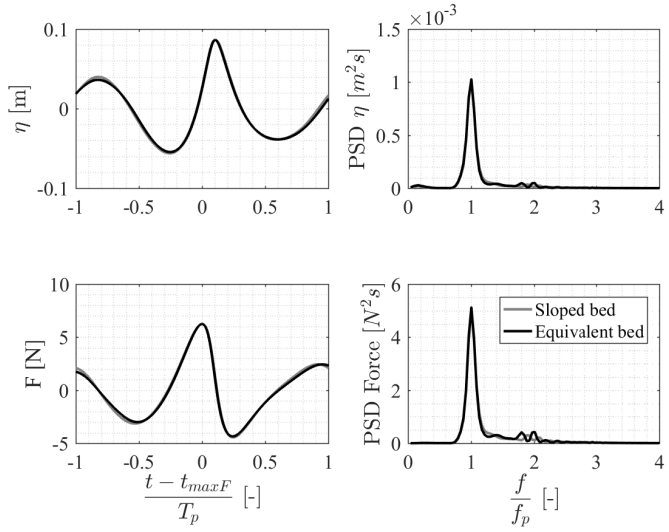

FIGURE 25: Free surface elevation and inline force time series and power spectral density for numerical results of a case in sea state 5 with $F_{target} = 1.2 \cdot \rho g h R^2$ with sloped bed and the equivalent flat bed.

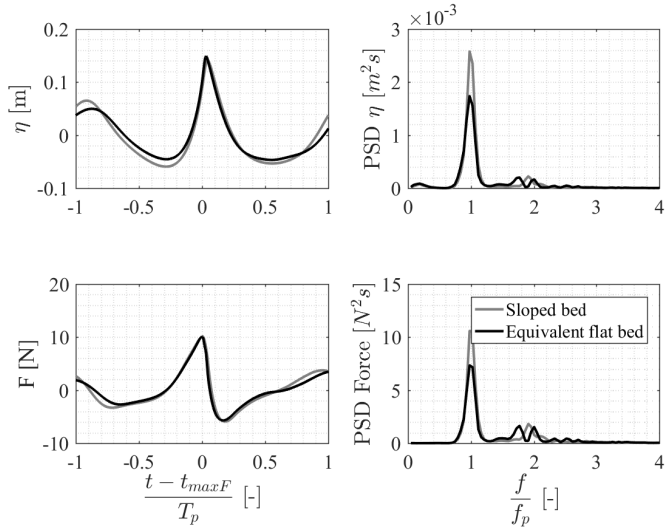

FIGURE 26: Free surface elevation and inline force time series and power spectral density for numerical results of a case in sea state 6 with $F_{target} = 1.7 \cdot \rho g h R^2$ with sloped bed and the equivalent flat bed.

realization of the random phase sea state time series with bootstrapping.

On the left hand side plots in addition to the results from the random phase realization the results from FORM simulations are shown for four different target maximum inline force. The differences between the curves with error bars and the FORM results are due to the stochastic uncertainty of the random phase realizations. From these plots, the exceedance probability is always higher for the cases on a sloped bed in all the sea states. This observation is generally in agreement with the full probability curves from the

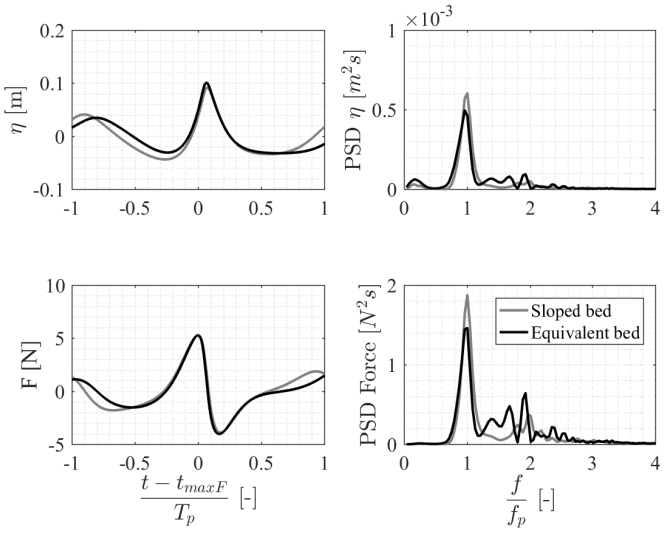

FIGURE 27: Free surface elevation and inline force time series and power spectral density for numerical results of a case in sea state 7 with $F_{target} = 1.5 \cdot \rho g h R^2$ with sloped bed and the equivalent flat bed.

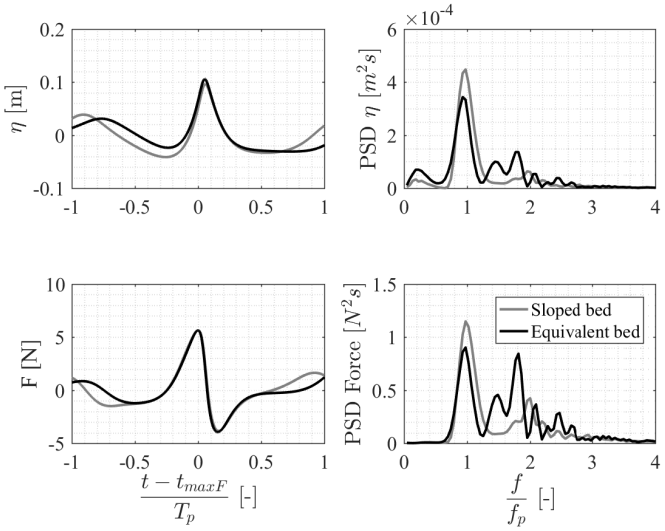

FIGURE 28: Free surface elevation and inline force time series and power spectral density for numerical results of a case in sea state 8 with $F_{target} = 1.6 \cdot \rho g h R^2$ with sloped bed and the equivalent flat bed.

random realizations. The increase of the exceedance probability on a sloped bed is more significant in sea state 7 and 8, shown in figure 33 and figure 34. It is worth mentioning that the different exceedance probabilities for the same target forces on sloped bed versus the equivalent flat bed means that the linear combination of the parameters, $\{\underline{a}, \underline{b}\}$, is different at location of the wave paddles in the cases on different slopes.

The ratio between the exceedance probabilities for fixed non-dimensional force value on the sloped bed and flat bed are shown in figure 35. For sea

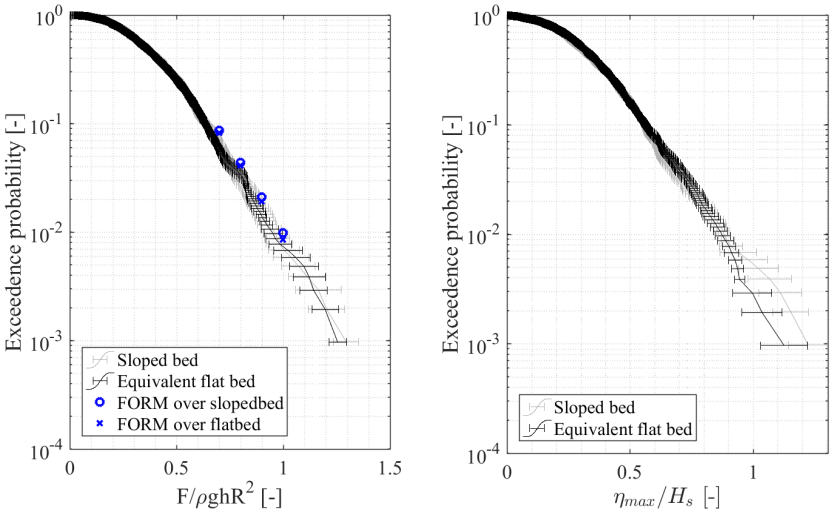

FIGURE 29: Exceedance probabilities relative to the non-dimensional maximum in-line force (left hand side plot) and maximum crest height (right hand side plot) for sea state 3. The results from FORM calculations are also included in the left hand side plot for sloped bed and equivalent flat sea bed.

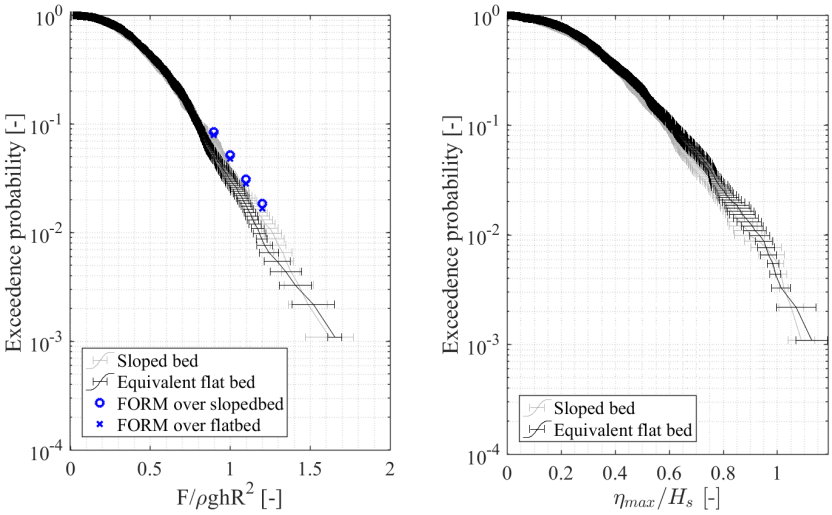

FIGURE 30: Exceedance probabilities relative to the non-dimensional maximum in-line force (left hand side plot) and maximum crest height (right hand side plot) for sea state 4. The results from FORM calculations are also included in the left hand side plot for sloped bed and equivalent flat sea bed.

states 3, 4 and 5 an increase in the ratio is observed as the target inline force is increased in each sea state. The ratio changes from 1.05 for a small target force $0.6\rho ghR^2$ in sea state 5 to 1.25 for the largest target force of $1.2\rho ghR^2$ in sea state 5. The increase in the ratio in each sea state might be explained by the increase of contribution of the longer waves which are effected by the shoaling effect more significantly. The nonlinear content of the force time series are analyzed in the next section.

The ratio of exceedance probabilities in sea state 6 , 7 and 8 in figure 35

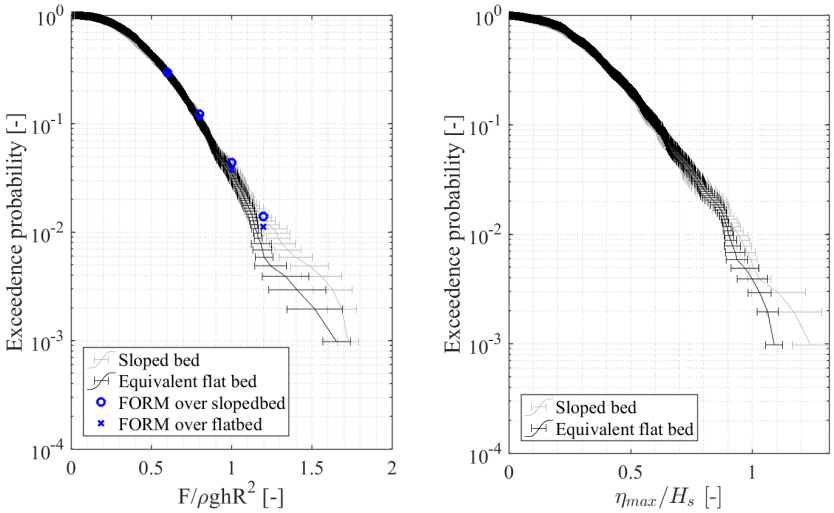

FIGURE 31: Exceedance probabilities relative to the non-dimensional maximum in-line force (left hand side plot) and maximum crest height (right hand side plot) for sea state 5. The results from FORM calculations are also included in the left hand side plot for sloped bed and equivalent flat sea bed.

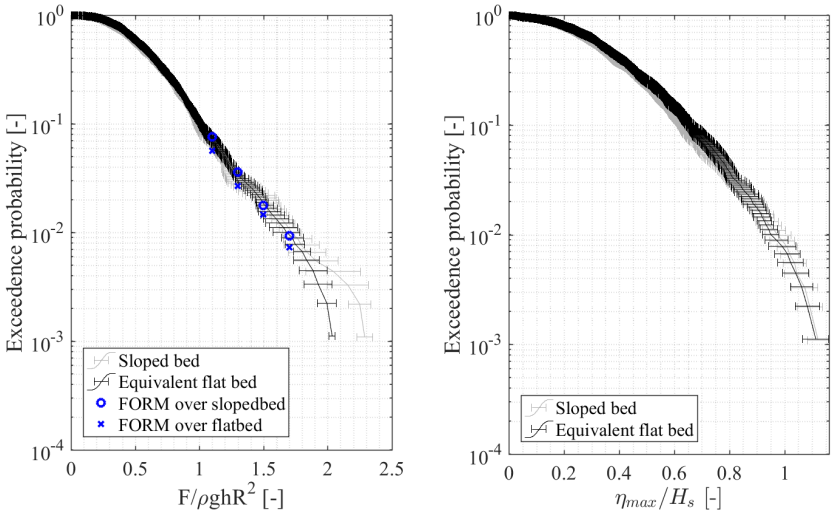

FIGURE 32: Exceedance probabilities relative to the non-dimensional maximum in-line force (left hand side plot) and maximum crest height (right hand side plot) for sea state 6. The results from FORM calculations are also included in the left hand side plot for sloped bed and equivalent flat sea bed.

have a different and non-monotonic trend unlike in sea states 3, 4 and 5. The ratio is significantly larger and reaches about 2 for these conditions. From Table 1 it is visible that the three sea states 6, 7 and 8 have much larger Ursell numbers and this increased nonlinearity is expected to cause this dramatic increase in exceedance probability for the sloped cases. The implication for design is dramatic and should be noted.

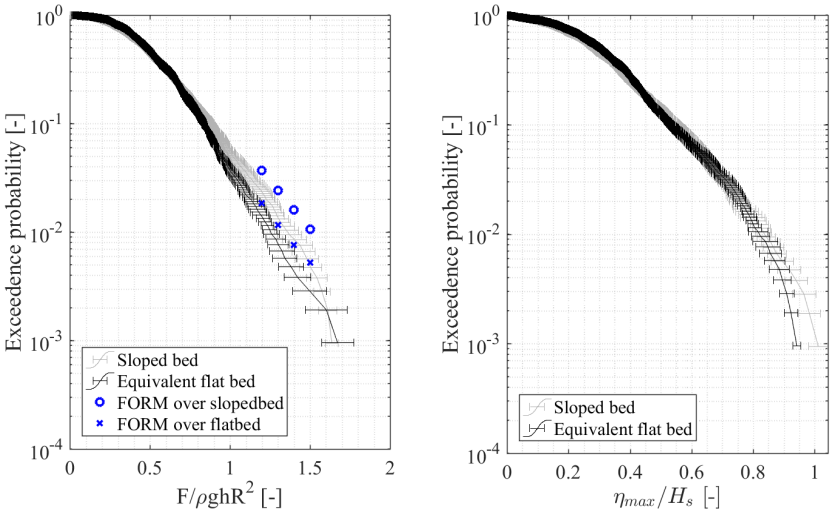

FIGURE 33: Exceedance probabilities relative to the non-dimensional maximum in-line force (left hand side plot) and maximum crest height (right hand side plot) for sea state 7. The results from FORM calculations are also included in the left hand side plot for sloped bed and equivalent flat sea bed.

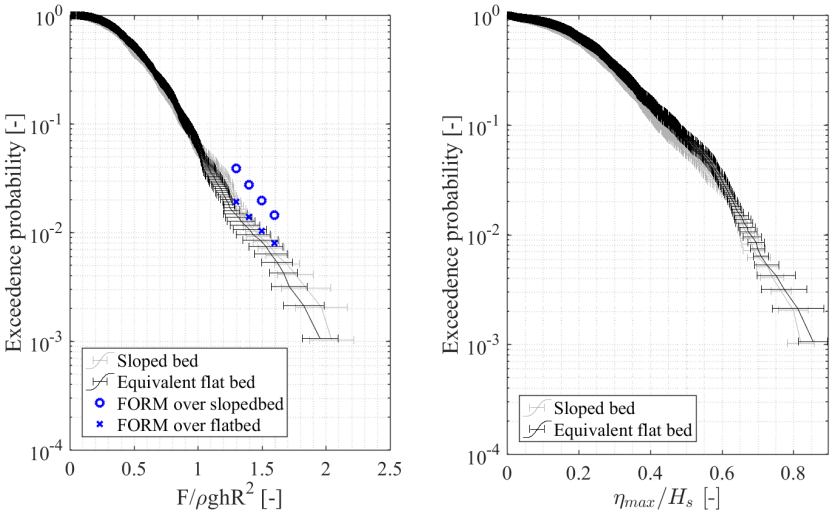

FIGURE 34: Exceedance probabilities relative to the non-dimensional maximum in-line force (left hand side plot) and maximum crest height (right hand side plot) for sea state 8. The results from FORM calculations are also included in the left hand side plot for sloped bed and equivalent flat sea bed.

Harmonic analysis of force components

To investigate the effect of the bed slope on the produced force episodes in details, the harmonic separation technique was used to separate the harmonics based on the work by Fitzgerald et al. Fitzgerald et al. 2014. The method is built up on the assumption that the viscous effects are negligible relative to the potential flow effects. In addition, the classic Stokes perturbation expansion is used to describe the higher-harmonic nonlinear force structure and

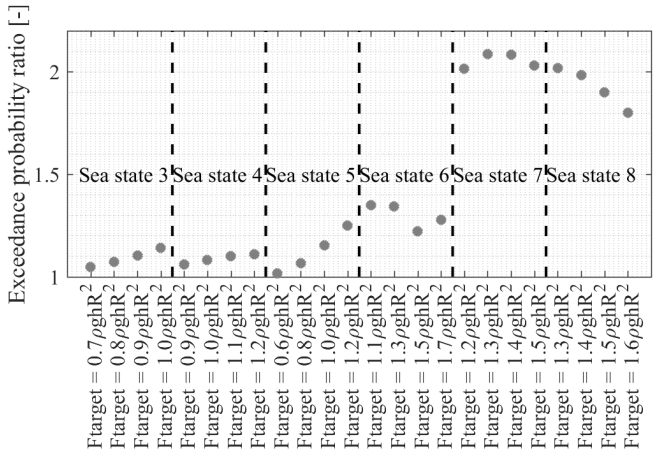

FIGURE 35: The ratio between the exceedance probabilities of the same load in sloped sea bed and equivalent flat bed.

devise its decomposition from phase shifted input signals. Thus for a linear force signal of amplitude A, frequency ω and wave number k, the following harmonic structure will emerge

$$\begin{aligned} F =& Af_{11}cos\phi + A^2(f_{20} + f_{22}cos2\phi) + \\ & A^3(f_{31}cos\phi + f_{33}cos3\phi) + A^4(f_{42}cos2\phi + f_{44}cos4\phi). \end{aligned} \tag{9}$$

Here the coefficients f_{mn} represent the wave-to-force transfer functions and ϕ is the phase of the linear component of the incident wave. Fitzgerald et al. Fitzgerald et al. 2014 suggested that the harmonic hierarchy of regular Stokes waves can also be used to approximate the phase focused wave groups. In such cases the Stokes terms are replaced with summation of products of frequency components. In the present work we can assume that the solutions to the FORM problem is a highly nonlinear focused wave group. The solutions of the FORM problems can then be used to create paddle signals with $\frac{1}{2}\pi$, π and $\frac{3}{2}\pi$ phase shifts relative to each other. The original force time series are noted by F_0 and the force time series resulting from the phase shifted paddle signals are denoted by F_{90}, F_{180} and F_{270} respectively. Therefore, different harmonics of the force time series can be divided using the following equations as provided by Fitzgerald et al. Fitzgerald et al. 2014.

$$\frac{(F_0 - F_{90}^H - F_{180} + F_{270}^H)}{4} = Af_{11}cos\phi + A^3 f_{31}cos\phi + O(A^5) \tag{10}$$

$$\frac{(F_0 - F_{90} + F_{180} - F_{270})}{4} = A^2 f_{22}cos2\phi + A^4 f_{42}cos2\phi + O(A^6) \tag{11}$$

$$\frac{(F_0 + F_{90}^H - F_{180} - F_{270}^H)}{4} = A^3 f_{33}cos3\phi + O(A^5) \tag{12}$$

$$\frac{(F_0 + F_{90} + F_{180} + F_{270})}{4} = A^2 f_{20} + A^4 f_{44}cos4\phi + O(A^6). \tag{13}$$

Here the superscript H shows the harmonic conjugate of the signal, obtained by Hilbert transformation. Equations (10) to (12) separate the first three harmonics of the signal while equation (13) includes the second-order difference long-wave force signal and the fourth-order summation harmonic force signal which are easily distinguished in the frequency domain.

The time series of different harmonics were separated and plotted on a sloped bed versus the equivalent flat bed for all sea states and each target force. The results for sea state 4 with the largest target force are presented in figure 36. In this figure it is visible that the differences between the time series on a sloped bed versus the flat bed are negligible in the main wave group envelope. However, deviations are observed between the time series of the second and third order free surface elevation and inline force on a sloped bed versus a flat bed. The differences in the second packet of the waves in higher orders is related to the free spurious waves caused by the linear boundary condition. In the cases on a sloped bed this linear boundary condition is closer to the actual physics of the problem because of the larger depth at the location of the wave makers. Hence, smaller spurious waves are created. The same consistency between the results from the flat bed and the sloped bed around the inline force peak time are also observed in other cases in sea states 3 to 8. In the time series of harmonics of free surface elevation and inline force, differences between the cases on flat and sloped bed are visible further away from the peak time of the total inline force in the sea states 6, 7 and 8 which have larger Ursell numbers. In all of the cases on different sea states the waves on a flat bed contained larger packets of spurious waves than the counterpart waves on the sloped bed. This observation is in consistency with the comparisons of the PSDs of these cases, where the frequency content of the cases on a flat bed was larger than the cases on a sloped bed around the second harmonic frequency range.

In figure 37 the same time series as in the figure 36 are shown but zoomed in around the time for the main force peak. The plots show that the different harmonics of the free surface elevation reach their peak at the same time relative to each other. The peak time, however, changes relative to the x axis zero as a function of target forces and sea states. Further, the different harmonics of the inline force time series have time shifts relative to each other which are fixed among all target forces and sea states. The peak times, similarly to the free surface elevation, do shift in relation to the total inline force time series peak time for different target forces. There is a phase shift between the η peaks and F peaks which is around 90 deg in the linear contributions, as expected from the linear theory, but becomes smaller for higher harmonics as the drag term contribution increases. These unique observations, which are irrespective of the bed slope, can help to develop an analytical force model similar to the model developed by Sarkar et al. Sarkar et al. 2017.

In order to investigate the change of the magnitude of different harmonics in different sea states and with different target forces, the relative contribution of the inline force value from the different harmonics at the peak time of the total inline force time series to the target inline force was calculated. This was quantified as

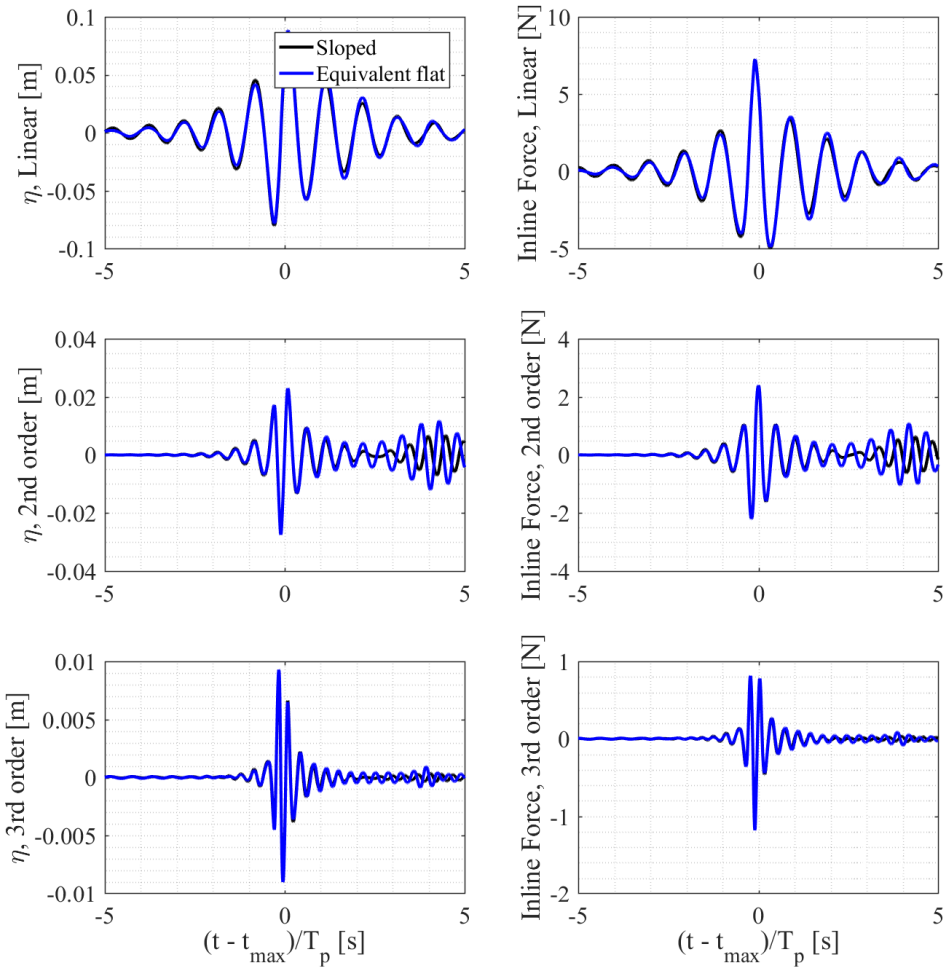

FIGURE 36: Time series of free surface elevation and inline force of different harmonics for sea state 4 with target inline force $1.2\rho ghR^2$

$$\text{Relative contribution of n'th harmonic} = \frac{F_n(t_{max})}{F_{total}(t_{max})} \tag{14}$$

where n is harmonic number and t_{max} is the time when the total force peaks.

Table 2 to 4 show these ratios for three different sea states, 4, 6 and 8, on flat and sloped bed, for different target force values. In table 2 these results are shown for sea state 4. It can be seen that the relative linear contribution decreases as the target force in that sea state increases. As the relative linear contribution decreases the relative contribution of the 2nd and 3rd order superharmonic increase. The 2nd order subharmonic contribution has the smallest effect while the 2nd order superharmonic has the largest effect on the final inline force after the linear.

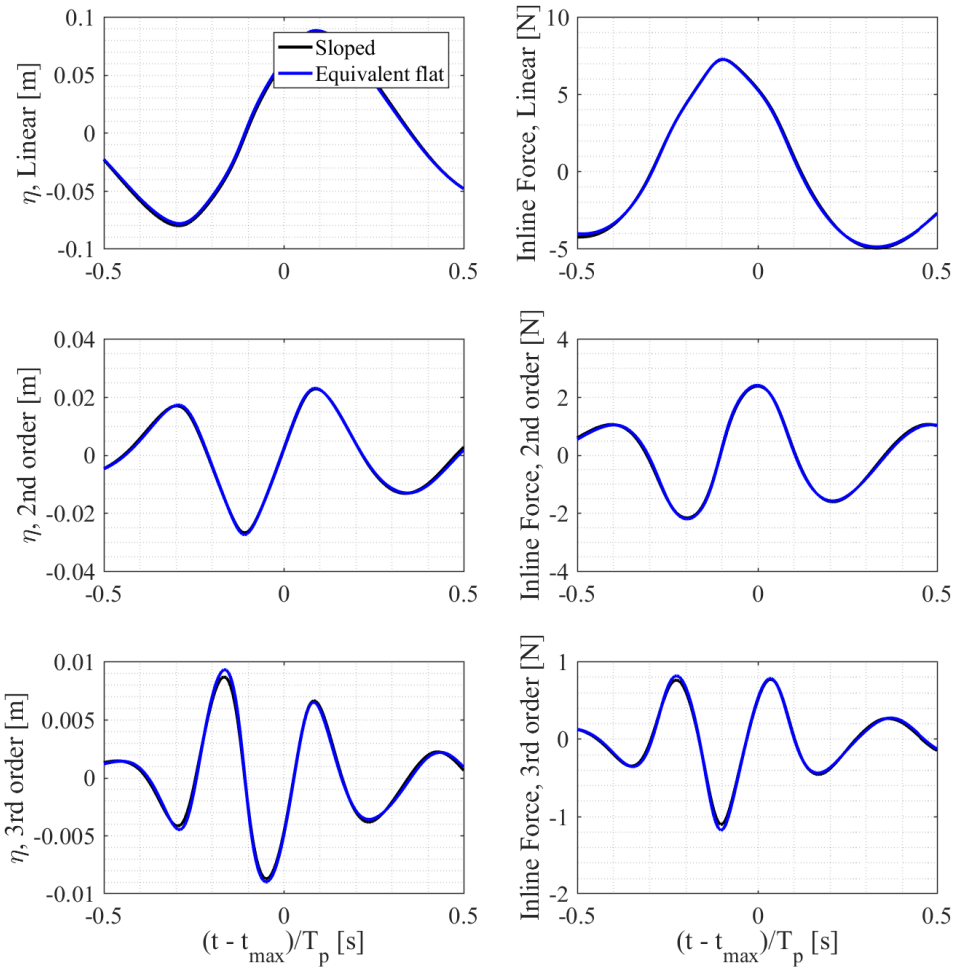

FIGURE 37: Time series of free surface elevation and inline force of different harmonics for sea state 4 with target inline force $1.2\rho g h R^2$ with limited x axis.

Further, the results show that the differences between the linear and non-linear contributions on a sloped and equivalent flat bed are negligible. This observation is true despite the fact that the probability of exceedance is different for each target value in this sea state, see figure 30.

In table 3 the relative contribution of the different harmonics is presented for sea state 6 on a sloped and equivalent flat bed. The contribution of the different harmonics follow the same pattern as sea state 4. The relative linear contribution decreases by increased target force while the relative contribution of the higher harmonics increase. The different harmonic contributions between the two bed slopes is very similar. The largest difference between the contributions of different harmonics is observed between the linear contribution for the largest target force in which the linear contribution is 6% smaller on the flat bed. The breaking filter was activated close to the structure and at the peak time of the inline force which might explain the smaller

TABLE 2: Ratio of the relative contribution of different harmonics on the inline force at the target time in sea state 4 on sloped and equivalent flat bed.

Target force $[\rho g h R^2]$	Bed slope	Linear	2nd order super-	2nd order sub-	3rd order	4th order	Total
0.9	sloped	0.8	0.22	0.01	-0.01	-0.02	1
	flat	0.82	0.22	0	-0.01	-0.02	1.01
1.0	sloped	0.77	0.24	0.01	0.01	-0.02	1.01
	flat	0.76	0.25	0.01	0	-0.02	1
1.1	sloped	0.72	0.27	0.01	0.03	-0.02	1.01
	flat	0.71	0.27	0.01	0.03	-0.02	1
1.2	sloped	0.66	0.28	0.02	0.05	0	1.01
	flat	0.65	0.28	0.02	0.05	0	1

contribution from the linear harmonic in this case.

TABLE 3: Ratio of the relative effect of different harmonics on the inline force at the target time. sea state 6 sloped and equivalent flat bed.

Target force $[\rho g h R^2]$	Bed slope	Linear	2nd order super-	2nd order sub-	3rd order	4th order	Total
1.1	slope	0.64	0.32	0	0.06	-0.01	1.01
	flat	0.62	0.32	0	0.07	-0.01	1
1.3	slope	0.55	0.33	0	0.1	0.01	0.99
	flat	0.54	0.33	0	0.11	0.02	1
1.5	slope	0.48	0.33	0.01	0.13	0.05	1
	flat	0.49	0.33	-0.01	0.13	0.05	0.99
1.7	slope	0.44	0.32	0.01	0.15	0.08	1
	flat	0.41	0.32	0	0.16	0.11	1

In table 4 the relative contribution of different harmonics is presented for sea state 8 on a sloped and equivalent flat bed. Similarly to the previous cases the contribution of the first harmonic decreases by the increase of the target force while the contribution of the higher harmonics increases. However, the contribution of the second harmonic seems to be constant in all the target forces on flat or sloped bed.

In this section it was shown that the different harmonics of the produced force episodes are consistent between the flat and sloped bed cases around the inline force peak time. The time series, however, diverge away from the force peak time between the cases on flat and sloped bed. The higher harmonic spurious waves were found to be more significant for the cases on flat bed. In addition, it was found that the phases of the harmonics are locked to each other and constant irrespective of the bed slope. In addition, the relative contribution of the higher harmonics in each sea state increases as the target force is increased while the relative linear contribution decreases. Moreover,

TABLE 4: Ratio of the relative effect of different harmonics on the inline force at the target time. sea state 8 sloped and equivalent flat bed.

Target force $[\rho g h R^2]$	Bed slope	Linear	2nd order super-	2nd order sub-	3rd order	4th order	Total
1.3	slope	0.48	0.36	-0.02	0.15	0.03	1
	flat	0.49	0.36	-0.03	0.15	0.03	1
1.4	slope	0.45	0.35	-0.02	0.17	0.05	1
	flat	0.47	0.36	-0.03	0.16	0.04	1
1.5	slope	0.43	0.35	-0.02	0.18	0.06	1
	flat	0.46	0.36	-0.04	0.17	0.05	1
1.6	slope	0.41	0.34	-0.02	0.19	0.08	1
	flat	0.44	0.35	-0.04	0.18	0.06	0.99

it was shown that the relative contributions of the higher harmonics to the maximum inline force of the waves are not influenced significantly by the bed slope.

Discussion and future work

We have investigated the effect of sea bed slope on the force statistics and the shapes of the force time series numerically using a nonlinear wave model, OceanWave3D, and FORM analysis. The wave and FORM model were initially validated against two sets of measured data. The validations were also compared with previously published results in which first and second order wave theories were used instead of the fully nonlinear flow solver and it was shown that a significant improvement is obtained using the new method.

In section 4 it was shown that the First Order Reliability Method in combination with the OceanWave3D potential flow solver can be used to estimate the most probable wave that creates a predefined target inline force. The comparisons with the ensemble averaged measurements showed the validity of this method. The exceedance probability calculated from this method was compared to random realizations of the same sea states and good consistency between the numerical probabilistic approach, the random deterministic approach and the measurements was observed.

The validated wave model and FORM setup was next used to compare the extreme force episodes of the two bed slopes. Except for sea state 7 and 8 for which their significant wave heights were reduced, the same sea states which were validated against measurements on a sloped bed were used on an equivalent flat bed to estimate the most probable waves that give the target forces. The time series and power spectral density of these force episodes were compared between flat bed and sloped bed. It was shown that the frequency contents in the linear range are very similar for low Ursell number while the differences are larger when the Ursell number is larger. The frequency contents in the range of the second-harmonic peak was always larger

on the equivalent flat beds and can be linked to the larger occurance of spurious second-order waves at flat bed due to the linear wave generation technique. The exceedance probability of the cases on flat and sloped beds were also compared for all the target maximum inline forces in all the 6 sea states. It was observed that in the same sea state, on a sloped bed the probability of exceedance for a given maximum inline force is larger. The ratio of the exceedance probability between the sloped and flat bed was calculated and it was observed that in all the sea states with lower Ursell number the ratio increases with force level while in the sea states with larger Ursell number the trend is not as uniform because of larger nonlinearities but it can be larger than 2.

From the harmonic separation method it was observed that the phases of the different harmonics of the inline force and free surface elevation histories are locked to each other with constant phase shifts irrespective of the bed slope. The free surface elevation time series of different harmonics all peaked simultaneously in all cases. Moreover, it was shown that the relative contributions of the higher harmonics to the maximum inline force of the waves are not influenced by the bed slope. The relative contribution of the higher harmonics in each sea state increases as the target force is increased while the relative linear contribution decreases in all cases.

It should be noted that the suggested method in this paper is an alternation to the use of Monte Carlo simulations. Even though the suggested method is not computationally cheap it is cheaper than using Monte Carlo method to investigate the effect of the bed slope on the extreme waves.

The current method can thus be used in the design process to provide the designer with extreme nonlinear waves that create a certain inline force or bending moment with a given exceedance probability. The method could also be used for response of the structures. Based on the current study the slope effect on exceedance probability is significant and calls for care in the analysis of lab test results. To extend the research a wider range of sea states, with different water depths and different bed slopes can be investigated. In addition, the method can be used for sea states with larger shoaling coefficient where the frequency change from the paddle position to the location of the structure is also of interest. The fixed phases between the different harmonics in the inline force time series can be calculated and used to formulate new analytical wave force models based on the model suggested by Sarkar et al. 2017.

Acknowledgement

This work was funded by the Innovation Fund Denmark and other partners as part of DeRisk project with grant number 4106-00038B. This support is gratefully acknowledged by the authors. The authors are also grateful to professor Paul Taylor, the university of Western Australia , associate professor Thomas Adcock, the university of Oxford , professor emeritus Jørgen Juncher Jensen, Denmark Technical University and Ju Hyuck Choi, Denmark Technical University for helpful discussions.

References

Bredmose, H. (2013). "Dynamic excitation of monopiles by steep and breaking waves. Experimental and numerical study." In: *OMAE2010: Proceedings of the ASME 29th 2010 International Conference on Ocean, Offshore and Arctic Engineering*. 2011.

Bredmose, Henrik et al. (2013). *The Wave Loads project*, p. 119.

Bredmose, H. et al. (2010). "The ideal flip-through impact: Experimental and numerical investigation". In: *Journal of Engineering Mathematics* 67.1, pp. 115–136.

Bredmose, H. et al. (2016). "DeRisk - Accurate prediction of ULS wave loads. Outlook and first results". In: *Energy Procedia*. Vol. 94. Elsevier, pp. 379–387.

Dean, Robert (2013). *Water wave mechanics for engineers and scientists*. Vol. 53. 9, pp. 1689–1699. arXiv: arXiv:1011.1669v3.

Efron, Bradley (1993). "An introduction to the Bootstrap". In:

Elgar, Steve and R. T. Guza (1985). *Shoaling gravity waves: comparisons between field observations, linear theory, and a nonlinear model*.

Engsig-Karup, A. P., H. B. Bingham, and O. Lindberg (2009). "An efficient flexible-order model for 3D nonlinear water waves". In: *Journal of Computational Physics* 228.6, pp. 2100–2118.

Fenton, J.D. (1988). "The numerical solution of steady water wave problems". In: *Computers & Geosciences* 14.3, pp. 357–368.

Fitzgerald, C. et al. (2014). "Phase manipulation and the harmonic components of ringing forces on a surface piercing column". In: *Proceedings of the Royal Society of London A: Mathematical, Physical and Engineering Sciences* 470.2168, p. 20130847.

Freilich, M H and R. T. Guza (1984). "Nonlinear Effects on Shoaling Surface Gravity Waves". In: 41, pp. 1–41.

Freilich, M H, R T Guza, and S L Elgar (1990). "Observations of Nonlinear Effects in Directional Spectra of Shoaling Gravity Waves". In: *J. Geophysical Res.* 95.C6, pp. 9645–9656.

Ghadirian, Amin, Henrik Bredmose, and Signe Schløer (2017). "Prediction of the shape of inline wave force and free surface elevation using First Order Reliability Method (FORM)". In: *Energy Procedia* 00.January, pp. 18–20.

Gibson, R. S., C. Swan, and P. S. Tromans (2007). "Fully Nonlinear Statistics of Wave Crest Elevation Calculated Using a Spectral Response Surface Method: Applications to Unidirectional Sea States". In: *Journal of Physical Oceanography* 37.2000, pp. 3–15.

Goda, Yoshimi (2010). "Reanalysis of Regular and Random Breaking Wave Statistics". In: *Coastal Engineering Journal* 52.01, pp. 71–106.

Goda, Yoshimi and Yasumasa Suzuki (1976). "Estimation of Incident and Reflected Waves in Random Wave Experiments". In: *Proc. of 15th Int. Conference on Coastal Engineering, ASCE*, pp. 828–845.

Grice, J R, P H Taylor, and R Eatock Taylor (2014). "Second-order statistics and ' designer ' waves for violent free-surface motion around multi-column structures Subject Areas :" in:

Grue, John and Morten Huseby (2002). "Higher harmonic wave forces and ringing of vertical cylinders". In: *Applied Ocean Research* 24.4, pp. 203–214.
IEC 61400-3 (2009).
Jensen, Jørgen Juncher (2007). "Efficient estimation of extreme non-linear roll motions using the first-order reliability method (FORM)". In: *Journal of Marine Science and Technology* 12.4, pp. 191–202.
Katsardi, V., L. de Lutio, and C. Swan (2013). "An experimental study of large waves in intermediate and shallow water depths. Part I: Wave height and crest height statistics". In: *Coastal Engineering* 73, pp. 43–57.
Lacaze, Sylvain and Samy Missoum (2014). "A generalized "max-min" sample for surrogate update". In: *Structural and Multidisciplinary Optimization* 49.4, pp. 683–687.
Longuet-Higgins, H.C. (1952). "On the statistical distribution of the height of sea waves". In: *The Journal of Japan Institute of Navigation* 11, pp. 245–266.
Nelson, R. C. (1982). "The Effect of Bed Slope on Wave Characteristics". In: pp. 555–572.
Nwogu, Okey (1993). "Alternative Form of Boussinesq Equations for Nearshore Wave Propagation". In: *Journal of Waterway, Port, Coastal, and Ocean Engineering* 119.6, pp. 618–638.
Paulsen, Bo Terp, Henrik Bredmose, and Harry B. Bingham (2014). "An efficient domain decomposition strategy for wave loads on surface piercing circular cylinders". In: *Coastal Engineering* 86, pp. 57–76.
Paulsen, Bo T. et al. (2014). "Forcing of a bottom-mounted circular cylinder by steep regular water waves at finite depth". In: *Journal of Fluid Mechanics* 755, pp. 1–34.
Rainey, R. C. T. (1995). "Slender-body expressions for the wave load on offshore structures". In: *Proceedings of the Royal Society of London* 450.1939, pp. 391–416.
Sarkar, Dripta et al. (2017). "The extraction of nonlinear harmonics of extreme wave load on a surface piercing column in random waves". In: *Journal of Fluid Mechanics* Submited for publication.
Schløer, S., H. Bredmose, and H. B. Bingham (2011). "Irregular Wave Forces on Monopile Foundations: Effect of Full Nonlinearity and Bed Slope". In: *International Conference on Ocean, Offshore and Arctic Engineering*.
Schløer, Signe, Henrik Bredmose, and Amin Ghadirian (2017). "Analysis of experimental data: The average shape of extreme wave forces on monopile foundations". In: *DeepWind*. Vol. 137. Elsevier, pp. 223–237.
Tromans, Peter S, A R Anatruk, and Paul Hagemeijer (1991). "A New Model for the Kinematics of Large Ocean Waves Application as a Design Wave". In: *Proceedings of the First International Offshore and Polar Engineering Conference* 8.August, pp. 64–71.
Ursell, F. (1953). "The long-wave paradox in the theory of gravity waves". In: *Mathematical Proceedings of the Cambridge Philosophical Society* 49.04, p. 685.
Vindenergi, D T U (2015). "DeRisk - WP2 Proposal for DeRisk 3D Physical Model Tests DTU Vindenergi". In: October.

Paper 5

Detailed force modelling of the secondary load cycle

* *This paper is submitted to the* ***Journal of Fluid Mechanics****.*

Amin Ghadirian[1], Henrik Bredmose[1]
[1] DTU Wind Energy, Nils Koppels Alle Building 403, DK-2800 Kgs. Lyngby, Denmark
E-mail: amgh@dtu.dk

Abstract

Steep wave impacts on vertical cylinders are associated with an additional force peak placed after the main peak: the secondary load cycle. We investigate the secondary load cycle for a focused wave group impact typical of offshore wind turbine foundations. Ensemble averaged experimental results for depth integrated force, front face pressures and free surface elevation are used as basis for the investigation. A two-phase free-surface RANS solver is set up and validated against generic cases of turbulent flow over a wall, wave-boundary layer flow for $1 \cdot 10^4 < Re < 1 \cdot 10^7$, 2D drag on a cylinder for $1 \cdot 10^2 < Re < 2.5 \cdot 10^5$ and 2D oscillatory flow for three sets of flow parameters $Re = \{5.8 \cdot 10^4, 9 \cdot 10^4, 1.7 \cdot 10^5\}$ and $KC = \{6, 12, 18\}$. The solver is next applied to reproduce the ensemble-averaged experimental results for the focused wave group impact and an excellent match for the inline force and free surface elevation is found along with a good match for the measured front face pressures.

The numerical solution is next analyzed in detail to explain the cause of the secondary load cycle. We find that the secondary load cycle is confined to an upper region ranging from just above the still water level and 1.5 diameter down. By a further break down of the pressure field into contributions from the individual terms of the vertical Euler equation we find that the local force peak in the secondary load cycle is mainly caused from suction effects around the still water level on the back side, contributed through the $\frac{D\rho u_z}{Dt}$ term. The suction occur due to the rapid decrease of water level below the generated water column at the back of the cylinder, which at this time has only just begun its downward motion. The preceding force dip is aided by

the hydrostatic pressure from the water column while the succeeding dip is aided by wash-down effects on the front side.

Finally, the role of the observed vortices behind the cylinder is discussed and compared to a reference computation with slip conditions. Vortices give rise to a slight force increase, occurring over the whole span of the secondary load cycle. They are thus not correlated to the secondary load cycle. Results confirm findings from earlier slip studies that the global force history is not strongly affected by boundary layer. The paper gives a detailed study of the secondary load cycle, puts more light on the physics and provides a clear explanation of its cause.

Introduction

In the design process of substructures for offshore wind turbines loads from the extreme and near breaking waves are of crucial importance. Such extreme wave loads are created by steep waves in the sea states which might have cumulative effect on the fatigue loads of the wind turbines too. Particularly, local events might excite the natural frequency of the structures of the wind turbines. The secondary load cycle in the force time history is one of the local events which has been claimed to be imposing ringing on the structure (Chaplin, Rainey, and Yemm 1997). Several explanations have been made for the reason of appearance of the secondary load cycle. However, there is not an agreement about the physical process which drives the secondary load cycle. The current paper investigates the physical process of its creation using measurements and numerical results. We further quantify the influence of flow separation and vortices behind the cylinder by comparison of computational results with and without the structural boundary layer.

Grue, Bjørshol, and Strand 1994 were the first to report the existence of what was initially called a secondary oscillation in the force-recordings. They characterized the starting time, period and amplitude of the oscillation in detail. Grue, Bjørshol, and Strand 1994 reported that these oscillations occur about one quarter wave period after the main peak in the loading and has a period of as long as 15% of the wave period, with 11% of the magnitude of the total force. A criterion, $Fr = U/(gd)^{1/2} > 0.4$, was suggested for appearance of the secondary load cycle, where U is the particle velocity below the crest, g is the gravitational acceleration and d is the water depth. They attributed the local event to a suction region one diameter below the still water level. They claimed that a resonance between the free surface and the body may occur which creates this suction and ultimately the secondary oscillation. In addition, the authors suggested that since the secondary oscillation happens one fourth of the wave period after the main peak of the inline force, the marine structure might experience a build-up of resonant responses.

Chaplin, Rainey, and Yemm 1997 conducted a set of experiments concerned with the response of a single vertical cylinder in the inertia regime in steep non-breaking waves with emphasis on the secondary load cycle. They used spring-supports to adjust the stiffness of the cylinder, to get its natural frequencies in the range from 3 to 11 times the dominant wave frequency. The

experiments were performed with three different cylinder diameters. It was shown that the secondary load cycle has significant effect on the response of the structures mounted on more flexible supports. The magnitude and period of the cycle was comparable to the results from Grue, Bjørshol, and Strand 1994, with magnitude between 8%-12% of the total force for smallest and largest diameter cylinder respectively and period of 15% of the main force cycle period. They suggested that the secondary load cycle only appears significantly when, $Fr = U/(2gc)^{1/2} > 0.6$, where c is the cylinder diameter. They further suggested that the Froude number is neither the sole influential parameter on the magnitude of the secondary load cycle nor the most important one. Instead they suggested that the wave steepness is more influential in the magnitude of the secondary load cycle and for the largest waves the secondary load cycle magnitude decreases with increasing steepness while it is proportional to the cylinder diameter. They suggested that there is a direct relation between the diameter cubed and the magnitude of the secondary load cycle. The importance of the secondary load cycle in ringing of the response cylinder was emphasized in the paper.

Later on, Grue 2002 extended the analysis by PIV measurements and while they reported the same approximations for the relative magnitude and period of the secondary load cycle as in the initial investigation (Grue, Bjørshol, and Strand 1994) they mentioned that appearance of the secondary load cycle depends both on th relative cylinder radius and the wave amplitude. They reported that the secondary load cycle happens when the wave length is more than approximately 10 times longer than the cylinder diameter. Grue 2002 stated that the secondary load cycle does not happen in the lab when the scale is too small and explained this phenomena by presence of flow separation. Finally they speculated that the secondary load cycle is due to a particular resonance between the cylinder and the induced local flow. Grue and Huseby 2002 investigated in more details the effects of the scale factor. They concluded that in the small scale the secondary load cycle happens when the wave slope, $k\eta_m$, exceeds 0.3 and for wave numbers, kR, smaller than 0.33 where R is the cylinder radius. In the moderate scale the secondary load cycle is more visible for waves with smaller slope. The difference between the experiments in small and moderate scale was explained by the effect of flow separation. Based on this work the secondary load cycle gives an important contribution to build-up of resonant body responses for a natural frequency of the structure about four times the local wave frequency.

Rainey 2007 associated the secondary load cycle with the violent motion of the water surface. A cavity bubble is formed behind the cylinder which then collapses to give the secondary load cycle. They reported no connection between the secondary load cycle and the 3rd harmonic of the wave frequency.

Paulsen et al. 2014 also stated by visual observation and a simplified analytical model that the secondary load cycle was caused by the free surface which drives a return flow from the back of the cylinder towards the front side after the passage of the wave crest. A distinct vortex pair at the downstream side of the cylinder was shown to appear during the presence of a

secondary load cycle. A simple potential flow model was used, to deduce that the force contribution from the secondary load cycle may be caused by the upstream propagating flow towards the front side of the cylinder and the associated downstream vortex. The investigations were based on regular stream function waves. The numerical computations were analyzed in the frequency domain and it was concluded that in the analyzed cases, the secondary load cycle was associated with frequencies above the fifth- and sixth-harmonic force component. They also found that the magnitude of the secondary load cycle increases for decreasing values of kR in agreement with observations of Grue 2002. The magnitude and period of the secondary load cycle was shown to depend largely on H/H_{max} and to a lesser extent to kh for the analyzed cases.

Jose et al. 2017 explained the secondary load cycle shortly by the blockage of the flow by the cylinder being filled by the diffracted waves and the resulting hump of water piled up at the back of the cylinder. This hump of water would create high pressure which would act in the opposite direction to that of the flow and exert a negative force on the back of the cylinder. Jose et al. 2017 also stated that the correct turbulence modelling would contribute to an accurate estimation of the secondary load cycle. They did not, however, explain the reason for assuming the importance of the turbulence in the characteristics of the secondary load cycle.

Kristiansen and Faltinsen 2017 speculated that the flow separation contributes to the local run-up and creation of the water column behind the cylinder, which in turn contributes to the high-frequency forces including the secondary load cycle. They stated that the flow separation is governed by the dimensionless Keulegan-Carpenter number (KC) and its ratio to Reynolds number (Re).

Riise et al. 2018 investigated 2166 individual waves and separated the harmonics larger than $3.5\omega_{TT}$ from the force time series , where ω_{TT} is the trough to trough angular frequency of the wave. They used regression methods to investigate the effect of the Keulegan-Carpenter number (KC), governing flow separation, and Froude number (Fr), governing free surface gravity wave effects, on the magnitude of the secondary load cycle. They concluded that both parameters are important while the best correlation was found between the secondary load cycle magnitude and Fr. They showed a limiting threshold of $KC \approx 4-5$ or $Fr \approx 0.3-0.4$ which indicates a change in the physical mechanisms that govern the high-frequency force.

Other authors (Ghadirian, Bredmose, and Dixen 2016; Ghadirian, Bredmose, and Schløer 2017) reported the presence of the secondary load cycles in lab measurements and in numerical computations without explaining the source of the phenomena. From the literature review it is observed that although the secondary load cycle is clearly a result of the wave-structure interaction and often linked to the flow at the back side of the cylinder, no precise account of the detailed flow mechanics causing it has been provided. The main goal of the present paper is to explain the physical process in which the secondary load cycle is created. Experimental and simulations results are

extensively used for one sea state and deep analysis is performed to separate the flow in different terms and identify the source of the secondary load cycle.

In section 5 the experimental setup and the numerical model are described thoroughly. The models used and the numerical schemes with modified turbulence models implemented in OpenFOAM are described. To increase the trust in the numerical model an extensive validation for basic cases is performed and presented in section 5. The cases include single phase steady and oscillating flow around a cylinder which are close to the flow regimes of the investigated focused wave group case. A focused wave group is a wave episode based on superposition of all the wave components in a sea state at the same time and place. Afterwards, in section 5 the numerical results are validated in terms of free surface elevation, inline force and local pressure in detail against measurements. Section 5 includes detailed investigation of the flow by dividing the flow into horizontal disks and by calculating the pressure contribution from separate terms of the vertical Navier-Stokes equations. The role of the structural boundary layer and the force contribution from the vortices at the back of the cylinder are investigated in section 5 by comparison to a force computation with slip condition. At last concluding remarks and suggested future work is presented in the last section 5.

Methodology

Experiments

The experiments were conducted at DHI Denmark in scale 1:50 as part of the DeRisk project (Bredmose et al. 2016). The full scale significant wave height of the investigated sea state in the current paper was 7.5 m while the peak period was 15 s and the water depth 33 m. The investigated test did not include directional spreading. The monopile was installed on two force transducers on top and bottom of the cylinder with full scale diameter of 7 m. In addition, 5 pressure sensors were installed on the front side of the cylinder facing the wave makers. The reproduced test consists of a focused wave group generated based on New Wave theory (Tromans, Anatruk, and Hagemeijer 1991). The test was repeated 8 times and the used measurements are ensemble averaged of them. The linear wave generation theory (Dean 2013) was used to calculate the piston type wave makers position signal in the lab.

Reflection analysis was performed on the measured free surface elevation and it was observed that there was less than 5% reflection from the artificial beach in the test studied.

Several methods were used to estimate the Kaulegan-Carpenter and Reynolds numbers in the studied focused wave packet. In (1) and (2) the equations for calculating these number are given.

$$KC = \frac{U_m}{f_p D} \tag{1}$$

$$Re = \frac{U_m D}{\nu} \tag{2}$$

Here U_m is either maximum or standard deviation of velocity in equivalent depth of the flow, D is the diameter of the cylinder, f_p is the peak frequency of the flow and ν is the kinematic viscosity of the fluid. The calculated non-dimensional numbers depend on choosing maximum or standard deviation of the velocity and the depth in which the velocity is sampled. In the experiments used the velocity was not measured, however from the fully nonlinear potential flow solver (OceanWave3D) results we could get the velocity time series in any height. Following Sumer and Fredsoe 2006 *KC* and *Re* were calculated using the standard deviation of the velocity at the still water level and were equal to 6 and to $1 \cdot 10^4$ respectively. Choosing the maximum velocity value at the maximum crest height (Yang and Rockwell 2002) leads to KC value of 18 and Re value of $1.7 \cdot 10^5$ and at the half depth (Yang and Rockwell 2002) leads to KC and Re values of 6.4 and 5.8e4 respectively. The estimation of the KC and Re number are important for recognition of the flow regime around the cylinder.

Numerical model

The coupled solver OceanWave3D-OpenFOAM (Waves2Foam) (Paulsen 2013; Paulsen, Bredmose, and Bingham 2014) was used to reproduce the experiment. Waves2Foam is an extension to the InterFoam solver of OpenFOAM which uses relaxation zones to induce incident gravity waves (Jacobsen, Fuhrman, and Fredsøe 2012) in the domain. InterFoam uses a volume of fluid (VOF) method to treat the free surface flows (Hirt and Nichols 1981). It solves the continuity equation and the momentum conservation equations

$$\frac{\partial u_i}{\partial x_i} = 0 \tag{3}$$

$$\frac{\partial \rho u_i}{\partial t} + u_j \frac{\partial \rho u_i}{\partial x_j} = -\frac{\partial p^*}{\partial x_i} - g_j x_j \frac{\partial \rho}{\partial x_i} + \frac{\partial}{\partial x_j}\left(2\mu_{\text{eff}} S_{ij}\right) + \sigma_T \kappa \frac{\partial \alpha}{\partial x_i} \tag{4}$$

$$S_{ij} = \frac{1}{2}\left(\frac{\partial u_i}{\partial x_j} + \frac{\partial u_j}{\partial x_i}\right). \tag{5}$$

where u_i are the velocities in the different directions, x_i are the coordinate directions, ρ is the local fluid density, p^* is the pressure minus the hydrostatic potential $\rho g_j x_j$, g_j is the gravitational acceleration, μ_{eff} is the local dynamic viscosity and S_{ij} is the mean strain rate tensor. The only difference in this formulation between a laminar and a turbulent flow is the calculated viscosity $\mu_{\text{eff}} = \mu + \mu_t$. For the laminar case μ_t is equal to zero

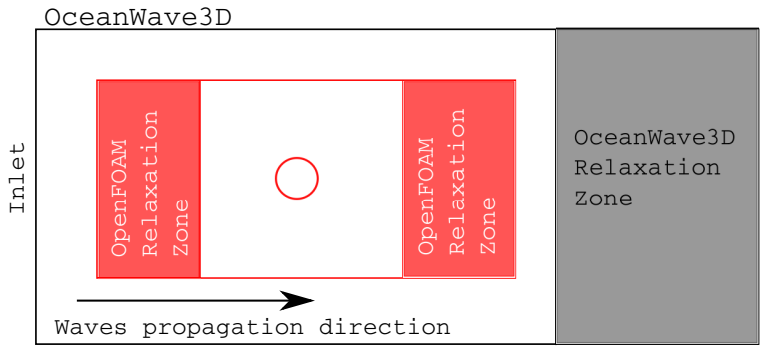

FIGURE 1: The numerical domain including the potential flow fully nonlinear solver OceanWave3D and the Navier-Stokes solver OpenFOAM.

while for the turbulent case it is calculated using a turbulence model. The fluid fraction is denoted by α which can take values between 0 and 1 for full air and water occupation of the cells respectively. Local fluid properties are calculated by linear weighting between the water and air properties, e.g. $\Phi = \alpha\Phi_{water} + (1-\alpha)\Phi_{air}$. Hence $\mu_{eff} = \alpha\mu_{\text{water}} + (1-\alpha)\mu_{\text{air}} + \mu_t$ in each cell. The last term in (4) takes the surface tension, σ_T, into account by considering the surface curvature, κ, in the border of the two phases where the gradient of α is non-zero. In our calculations this term is dismissed.

The transport equation of α is

$$\frac{\partial \alpha}{\partial t} + \frac{\partial \alpha u_j}{\partial x_j} + \frac{\partial}{\partial x_j}\left(\alpha(1-\alpha)u_j^r\right) = 0 \tag{6}$$

where u_j^r has the unit of velocity and is in the normal direction to the air-water interface with no physical meaning (**Berberovic2009a**). The last term compresses the region where α is between 0 and 1. More information on the performance of this term can be found in Deshpande, Anumolu, and Trujillo 2012.

To reproduce the measurements, the wave paddle signals were created from the first order wave generation similarly to the experiments (Dean 2013) and the velocity of the paddles were used as flux boundary condition in the nonelinear solver OceanWave3D. This method of generation is linearly consistent with the piston wave generation in the lab. Differences at higher order are expected because no piston or boundary movement is included in the numerical model. However, good consistency with experiments using this approach, has been presented in earlier work Paulsen, Bredmose, and Bingham 2014 and as part of DeRisk project Bredmose et al. 2016; Ghadirian, Bredmose, and Dixen 2016; Ghadirian, Bredmose, and Schløer 2017. A top view of the computational domains are shown in figure 1. The embedded OpenFOAM domain was driven with waves generated in OceanWave3D through a relaxation zone (Jacobsen, Fuhrman, and Fredsøe 2012).

Convergence studies was performed to verify that all the significant waves in the sea state, even with the highest frequency were resolved. From these studies it was observed that in the OceanWave3D domain a discretization by

$501 \times 1 \times 15$ cells with constant $\delta t = 0.01\ s$ was numerically converged more than 99% meaning that the results would change less than 1% by refining the mesh. The OceanWave3D results were mapped inside the OpenFOAM domain in each time step in 3 meters long relaxations zones. The OpenFOAM mesh size with dx = 0.02 m and with cell aspect ratio of close to one showed convergence with consistency of larger than 99% compared to a case doubly refined in all directions. Nevertheless, for better resolution of the vortices around the cylinder the finest mesh was used with dx = 0.01 m and 24 m cells.

For turbulence modelling, the kω–SST model implemented in OpenFOAM was used. The implementation is based on Menter, Kuntz, and Langtry 2003 without the density in the transport equations in OpenFOAM which was added following the work of Brown et al. 2014 and Devolder, Rauwoens, and Troch 2017 resulting in

$$\frac{\partial \rho k}{\partial t} + \frac{\partial \rho u_j k}{\partial x_j} - \frac{\partial}{\partial x_j}(\Gamma_k \frac{\partial k}{\partial x_j}) = \rho P_k - \beta^* \rho \omega k \tag{7}$$

$$\frac{\partial \rho \omega}{\partial t} + \frac{\partial \rho u_j \omega}{\partial x_j} - \frac{\partial}{\partial x_j}(\Gamma_\omega \frac{\partial \omega}{\partial x_j}) = \rho \frac{\gamma}{\nu_t} G - \beta \rho \omega^2 + \rho 2(1 - F_1)\frac{\sigma_{\omega 2}}{\omega}\frac{\partial k}{\partial x_j}\frac{\partial \omega}{\partial x_j} \tag{8}$$

where

$$\Gamma_k = \mu + \mu_t \sigma_k,\ \Gamma_\omega = \mu + \mu_t \sigma_\omega, \tag{9}$$

$$G = \nu_t \tau_{ij} \frac{\partial u_i}{\partial x_j},\ P_k = min(G; c_1 \beta^* k \omega), \tag{10}$$

$$\mu_t = \rho \frac{a_1 k}{max(a_1 \omega; S \cdot F_2)}. \tag{11}$$

The constants, σ_k, σ_ω, β and γ are chosen and computed according to Brown et al. 2014 among others. The resulting k and ω from solving (7) and (8) are used to calculate μ_t in (4).

Convergence simulations were performed to find the optimum combination of Courant number and the discretization schemes based on the work by Eltard, Fuhrman, and Roenby 2017. A summary of the numerical setup is presented in table 1. The upwind scheme was used for the divergence term of the turbulence quantities k and ω.

The coupling of the pressure and velocity equations were done by the PIMPLE solver. While "smoothsolver" was used for solving the α, k and ω linear equation, pressure equation was solved by GAMG and velocity by PBiCG with DILU pre-conditioner (Greenshields 2015). It was observed that the most consistent results to the measured free surface elevation was obtained when the number of outer corrections in the PIMPLE solver was set to one, which practically makes this solver the PISO solver. The residuals were observed to be smaller than 0.001 in all simulations to make sure the result is converged in each time step.

Max Courant	$\frac{\partial}{\partial t}$	$\nabla \cdot (\rho u u)$
0.15	Crank-Nicolson 0.9	Gauss SFCD
$\nabla \cdot (U\alpha)$	$\nabla \cdot (\nu_{eff} \nabla \otimes u)$	interpolation scheme
Gauss MUSCL	Gauss linear	linear

TABLE 1: The numerical discretization schemes used in the simulations.

	cylinder wall	atmosphere	inlet	outlet
U	fixedValue (0 0 0)	pressureInletOutletVelocity	waveVelocity	waveVelocity
p	zeroGradient	totalPressure 0	zeroGradient	zeroGradient
α	zeroGradient	inletOutlet	zeroGradient	zeroGradient
k	kqRWallFunction	zeroGradient	zeroGradient	zeroGradient
ω	omegaWallFunction	zeroGradient	zeroGradient	zeroGradient

TABLE 2: The boundary conditions.

The boundary conditions of the domain are shown in table 2. The boundary conditions on the sea bed and the side walls were zeroGradient for all quantities. The length of the domain was defined by the wave length and the fact that the relaxation zones in the OpenFOAM domain should be at least as large as the longest wave mapped into the domain (Jacobsen, Fuhrman, and Fredsøe 2012; Jacobsen 2017). However, since the focused wave packet contains very large waves in the spectrum of the sea state a reflection analysis was performed to find the shortest relaxation zone length for which reflected waves are smaller than 5 %. In addition, it was observed that the perfect transport of the wave depends drastically on the aspect ratio of the cells around the free surface. The aspect ratio should be as close to one as possible and even an aspect ratio of 2 diminishes the performance of the InterFoam solver (Jacobsen 2011; Paulsen 2013; Eltard, Fuhrman, and Roenby 2017). This limitation in the aspect ratio limited the ability of resolving the boundary layer of the cylinder wall. It was also observed that refining the mesh in the radial direction around the cylinder introduced artificial waves around the cylinder which affects the inline force time series on the cylinder. Hence using a uniform mesh in the domain with a wall function on the cylinder wall was found to be a more viable solution.

Model validation

The numerical setup with the same discretization as described in the previous section was validated against cases of channel flow and steady and oscillating single phase flow around a cylinder.

The simplest validation case was to investigate if the model is capable of capturing the law of the wall of a steady channel flow over a smooth wall. In

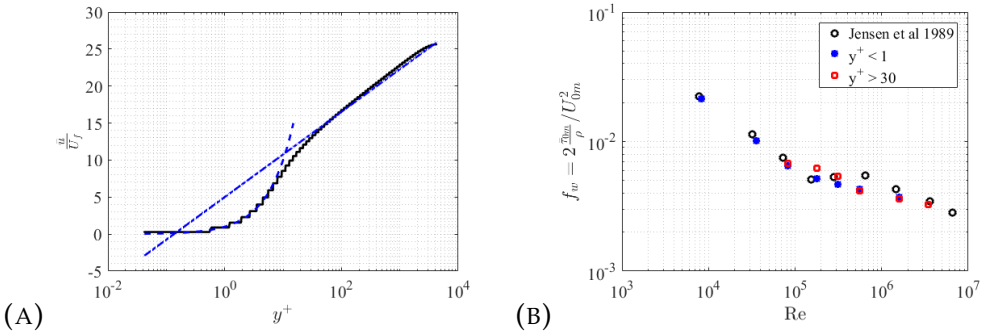

FIGURE 2: (a) The law of the wall. (b) Wave boundary layer.

plot (a) of figure 2 the validity of the model is shown in comparison to theory from Karman 1931.

The theoretical equations used in this plot are given by

$$\frac{\overline{u}}{U_f} = \begin{cases} y^+ & y^+ < 5 \\ 2.5 \ln y^+ + 5 & 30 < y^+ < 500 \end{cases}. \tag{12}$$

Here $y^+ = \frac{yU_f}{\nu}$ is the non-dimensional wall distance, U_f is the friction velocity and ν is the kinematic viscosity. The viscous sublayer, buffer layer and log-law region are resolved and predicted very well in the inner layer of the flow.

The validity of the model in comparison with the measurements conducted by Jensen, Sumer, and Fredsoe 1989 in calculation of the friction coefficient in the wave boundary layer next to a smooth wall is shown in plot (b). Two sets of simulations were performed to validate the model with and without using the wall function respectively. The first set of the simulations, carried out for a range of Reynolds numbers from $8.5 \cdot 10^3$ to $1.6 \cdot 10^6$, resolved the boundary layer with y^+ values smaller than 1 in the first cell for all cases. The results of this group are consistent with the measurements except in the transition region, $1.5 \cdot 10^5 < Re < 7 \cdot 10^5$. It should be noted that the behavior of the flow in this region is in general associated with some scatter for the friction coefficient since different experiments also obtain different friction coefficients (Jensen, Sumer, and Fredsoe 1989; Fredsøe et al. 2003). The second group of simulations was for a larger range of Reynolds numbers with y^+ values larger than 30 next to the wall. The results for this group for Reynolds numbers larger than $1 \cdot 10^5$ are also consistent with the experiments.

To validate the model in flows around bluff bodies, cases of steady flow around a cylinder with different Reynolds numbers were simulated and the drag coefficient and Strouhal number were compared with experimental results represented in Sumer and Fredsoe 2006 and simulation results from Rosetti, Vaz, and Fujarra 2012, Stringer, Zang, and Hillis 2014 and Ye and Wan 2017. It is shown in figure 3 that the results obtained using the current model and setup can give among the most consistent results with the measurements up to Reynolds number of $1 \cdot 10^5$. However, the results for

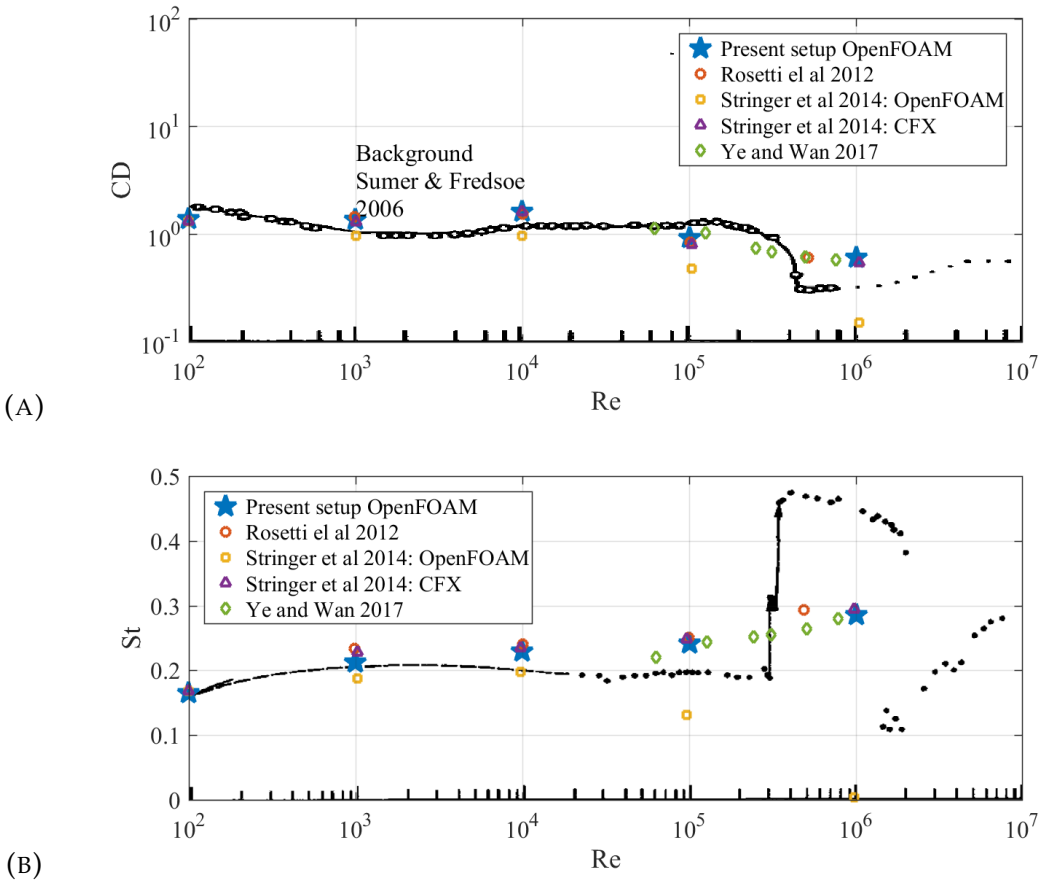

FIGURE 3: (a) Drag coefficient as a function of Reynolds number for a steady flow around cylinder. (b) Strouhal number as a function of Reynolds number for a steady flow around cylinder. Results from three studies (Rosetti, Vaz, and Fujarra 2012; Stringer, Zang, and Hillis 2014; Ye and Wan 2017) are included for comparison. The background plot shows the experiments represented in Sumer and Fredsoe 2006.

$Re \geq 1 \cdot 10^6$, in the super critical region, are not as consistent with the measurements. The inconsistency in this range is expected since the RANS simulations do not usually capture the correct behavior of the flow in the critical (Rosetti, Vaz, and Fujarra 2012; Stringer, Zang, and Hillis 2014; Ye and Wan 2017). For the cases of the present paper, Re is below $1.7 \cdot 10^5$. The solver is therefore considered sufficiently accurate for the flow regimes studied.

The next validation case is 2D oscillating flow around a circular cylinder. In figure 4 the drag and inertia coefficients for three Reynolds and KC numbers corresponding to the free surface flow at the crest, still water level and in half depth of 0.33 m are shown. In these computations the wall function was used on the cylinder wall and the boundary layer was not resolved. From plot (a) in this figure it is observed that the inertia coefficient is over predicted less than 0.05 in all cases with KC numbers 6, 12 and 18. For the drag coefficient there is an under prediction of less than 0.1 in the case of the drag coefficient shown in the plot (b) of figure 4. In general a good agreement between the simulations results and the measurements is shown in figure 4.

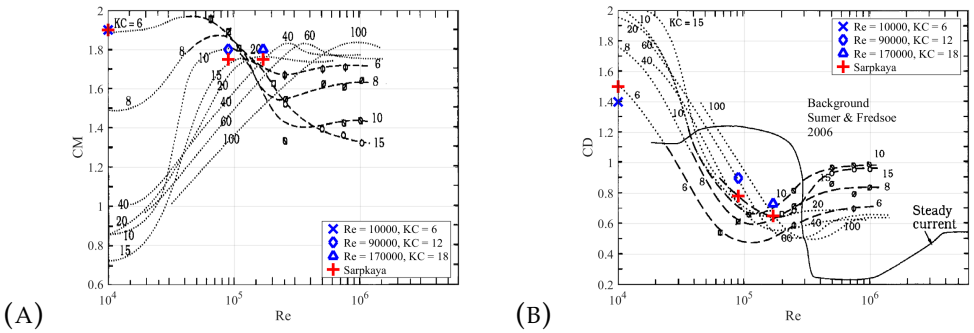

FIGURE 4: Drag and inertia coefficients of oscillating flow around the cylinder with three Reynolds and *KC* covering the flow regimes of the free surface flow at three heights. (a) Inertia Coefficient. (b) Drag Coefficient. The background plot shows the experiments represented in Sumer and Fredsoe 2006.

Validation of the numerical results with experiments

We now turn to the re-computation of the ensemble-averaged focused wave group impact. In figure 5 the measured time series of inline force is presented in the top plot. It is observed that the maximum inline force happens at 14.8 s hereafter referred to as the first peak. The horizontal axis of the plots are limited to the event of interest, the secondary load cycle. Two local minima are observed in the force time series at 15.1 s and 15.32 s with a maximum in between which hereunder are referred to as the first dip, the second dip and the second peak. The simulation results of inline force are presented from OceanWave3D and OpenFOAM in the same plot. The inline force from OceanWave3D is calculated using the Morison equation with the Rainey corrections (Rainey 2007). The inline force time series based on OceanWave3D has its maximum at 14.75 s and the decrease in the inline force also happens earlier than the measurements. The OpenFOAM results, computed from pressure integration, are in very good agreement with the measurements. OpenFOAM shows an excellent reproduction of the secondary load cycle events.

The free surface elevation at the monopile center (measured 5 diameters across from the cylinder) is shown in the middle plot. The measured time series is maximum at 14.92 s which indicates a phase shift between the inline force and the free surface elevation which is in agreement with the known characteristics of a inertia dominant flow. The free surface elevation time series of simulations are also presented in this plot. There is an excellent agreement between the numerical results and the measurements. However, the measured wave is slightly more symmetric than the numerical results. Since the wave paddles in the numerical simulations were only linearly consistent with the experiments these minor differences are expected. The agreement between the OpenFOAM results and the measurements is slightly better than the agreement for the OceanWave3D results.

In the bottom plot the run-up on the front and back side of the cylinder and the difference between them is shown from the OpenFOAM results. In addition, a free shoot and fall trajectory from the maximum run-up on both sides is presented. The water on the front side is thrown up at 14.85 s with only gravity imposing a force on it hence its trajectory is similar to the free shoot trajectory. After 15 s the run-up water falls faster than free fall. On the back side the run-up water is moved up and down slower than free shoot and fall peaking at 15.1 s. The difference in the run-up on the front and the back side is a simple representation of the possible hydrostatic force contributions to the force history from the front and back flows. From the curve though a different time scale than the secondary load cycle is visible. The secondary load cycle can thus not be explained by hydrostatic effects relate to the run-up and down flows at the front and back side.

In figure 6 the wave induced pressure time series measured at 5 different heights in the experiments is shown. The measurement height is presented in the title of each plot. The wave induced pressure is calculated as

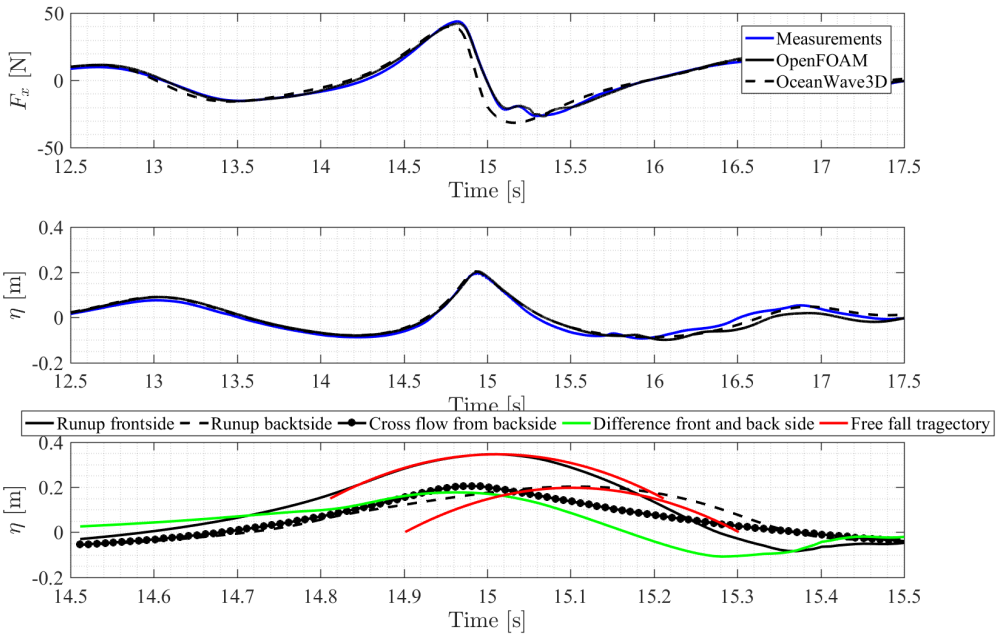

FIGURE 5: Top: Inline force time series. Middle: Free surface elevation. Bottom: Run-up from the OpenFOAM simulations.

$$p_{wave} = \begin{cases} p_{total} + \rho g z, & z < 0 \\ p_{total} & z \geq 0 \end{cases} \tag{13}$$

which represents the pressure additional to the gauge pressure in calm water conditions.

From figure 6 we can see that the pressure sensors that are always wet show positive and negative wave induced pressure similar to a sine wave, but the pressure sensors that are above the still water level and are sometimes dry show positive values only when wet during the run-up time on the front side. It is worth mentioning that the maximum wave induced pressure measured at 12 cm above the still water level is smaller than the ones measured at higher and lower heights. Small wriggles in the pressures above still water level are seen right after they become dry. This is likely to be a spurious feature of the pressure sensor or due to the aeration effects.

In the same figure wave induced pressure from computations with slip and no-slip boundary condition on the cylinder are shown. The differences between the two calculations are very small and the agreement between the computations and the measurements is good. The computations show a lower maximum pressure at 12 cm than at 16 cm similarly to the measurements. There seems to be an offset between the measurement and the sampled wave induced pressure from the simulations in all heights. After more investigation it was observed that this offset is smaller for the small-amplitude parts of the time series in the beginning of the wave packet. This difference is very likely related to slight differences in the waves that are

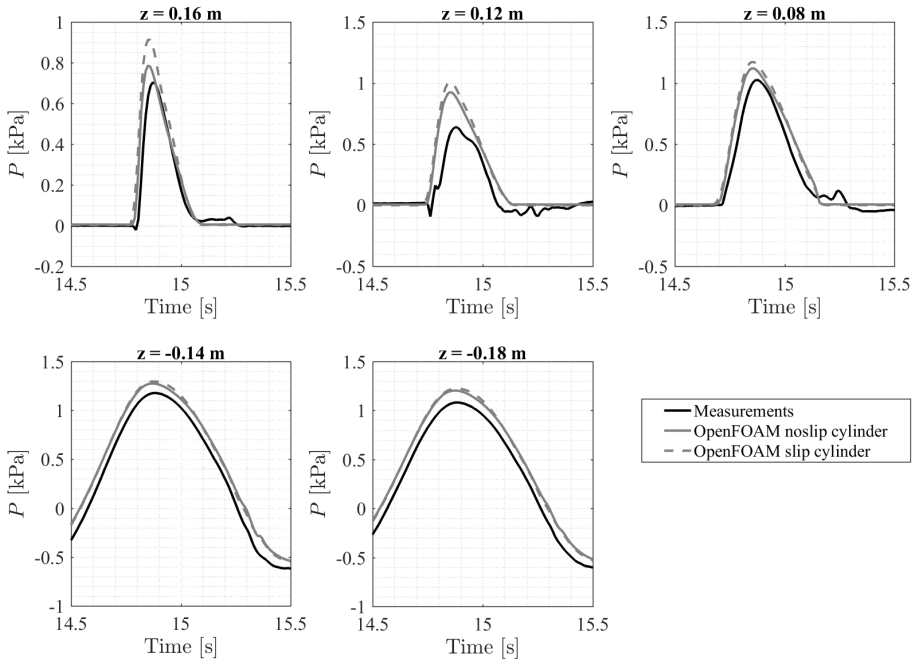

FIGURE 6: Wave induced pressure at five different heights on the front side of the cylinder.

reproduced in the computations. From the precise match of inline force, free surface elevation and front face pressures, we deduce that the present OpenFOAM computations represent an accurate reproduction of the physical wave impact. The computational results are thus used in the following for further detailed analysis of the secondary load cycle and the associated flow.

In figure 7 the free surface of the flow is shown in 6 time instants before and after the secondary load cycle. In plot (a), at 15.0 s, the run-up on the front side is maximum. The wave crest is just on the back side of the cylinder. A distinct water column (mound) has already been formed at the back and is placed in the middle of a gap in the middle of the wave crest.

In plot (b), at 15.1 s, the run-up on the back side starts to fall down. This is the same time when the first dip occurs in the inline force time series. The water column is extending in length from the back of the cylinder until the wave crest which is 1.5 diameters behind the cylinder.

At 15.2 s, plot (c), when also the second peak occurs, the water column still distinctly exists. Even though the run-up on the back side has decreased, the free surface elevation of the outer wave flow has decreased so much that the relative height of the water column is larger than before. The water column width at the base of the water column, however, has spread.

In plot (d), at 15.3 s, when the second dip occurs, there is a backwards water flow towards the front of the cylinder. The height of the water column has drastically decreased.

At 15.4 s, plot (e), two water jets created from the initial collapse of the water column have reached the front side. Two further side waves from the

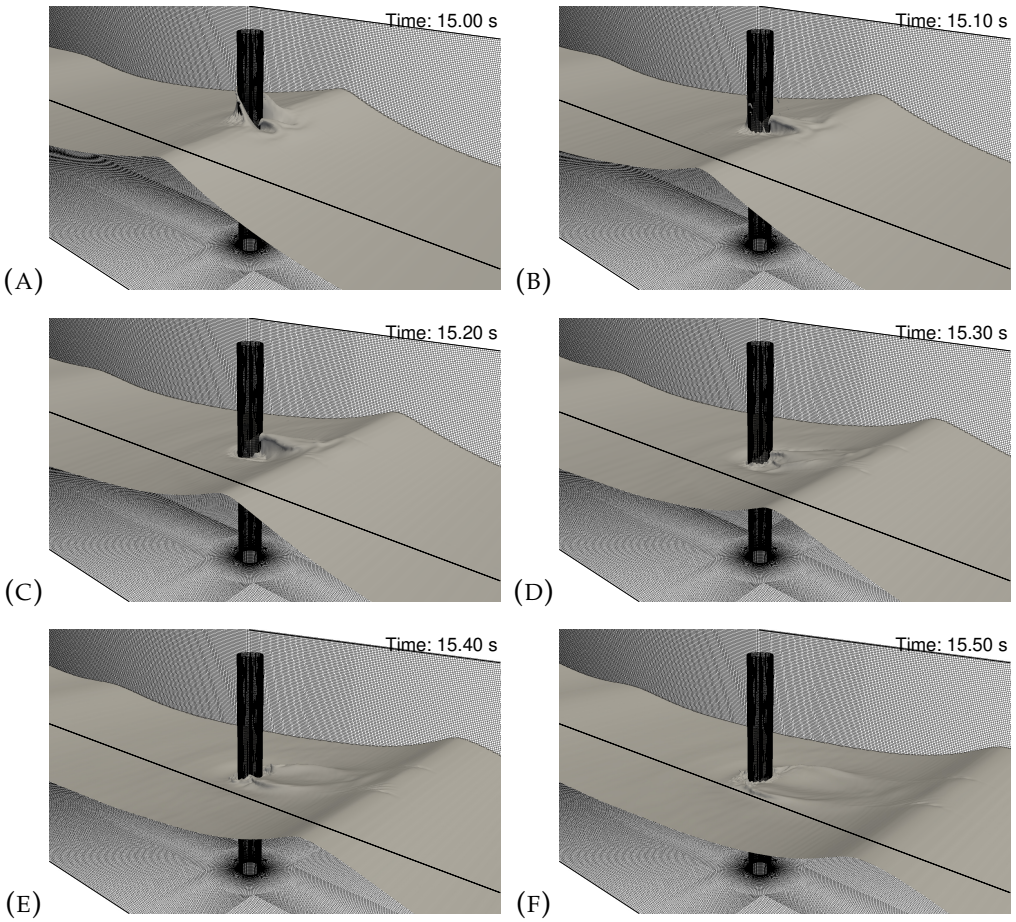

FIGURE 7: Snapshots of the free surface: (a) at the time of the wave impact, (b) when the water column is fully formed behind the cylinder (maximum run-up behind the cylinder), (c) at the beginning of the secondary load cycle (collapse of the water column), (d) at the time of the local minimum of the secondary load cycle, (e) end of the secondary load cycle, (f) at the end of the secondary load cycle

collapse of the water column have started to spread towards the outer flow.

In plot (f), time 15.5 s, the remaining part of the water column is disappearing. Also the created second pair of waves from the collapse of the water column have started to disappear. Some surface disturbance can still be seen around the cylinder.

Detailed investigations

We now turn to a more detailed investigation of the flow and forces associated with the secondary load cycle. The vertical distribution of the inline force time series is firstly visualized and then detailed into contributions from the front and back sides to isolate the secondary load cycle. Afterwards, we divide the pressure on the cylinder into different terms of the vertical momentum equation. Because we have all the variables in the numerical domain and around the cylinder, we can use these variables, pressure and velocity components, to recompute the different terms. It should be mentioned that all the results presented in this section are analysis of the numerical results and not the measurements. However, since the validity of the model is demonstrated in the previous section the results are extendibile to the details of the physical flow.

To explain the flow in more detail a few terms for describing the physical events related to vertical run-up and run-down flows are given. A throw-up event is defined as shooting the water upwards in form of a water jet. The most intuitive example of a throw-up event is when the steep wave hits the cylinder (or a flat wall) and shoots a water jet upwards. The pressure effect of the throw-up event are associated with positive acceleration of the particles in the vertical direction (i.e. $\frac{\partial \rho u_z}{\partial t} \gg 0$). A suction event on the back side of the cylinder is related to the decreasing acceleration of the water column when the water below has been moved away because of the incident wave kinematics. This suction event is associated with $\frac{\partial \rho u_z}{\partial t} \ll 0$. A wash-down event occurs when there is a high velocity flow on the cylinder wall and it is associated with $\frac{u_z \partial \rho u_z}{\partial z}$ term. Finally catch pressure effect is observed when lower layers of the fluid decelerate the falling fluid above them and it occurs when $\frac{\partial \rho u_z}{\partial t} > 0$ and $u_z < 0$. Wash-down and catching usually occur simultaneously with possibly wash-down leading the process. These terms will be used in the following.

Vertical distribution of inline force

In figure 8 the inline force is plotted in a contour plot with axis of time and height. The plot is a result of integration of the computational pressure on the cylinder wall in the azimuth direction. At 15.1 s a force minimum appear to be caused by a local low-force event close to the still water level followed by a higher force event at 15.2 s that propagates from above. Finally the second force minimum at 15.32 s is related to another local low-force event which extends down to 1.5 time the diameter. Hence, in this plot it is observed that the secondary load cycle is visible in the heights closer to the still water level from 15.1 s to 15.4 s and its effect extends down to 1.5 diameter from the still water level.

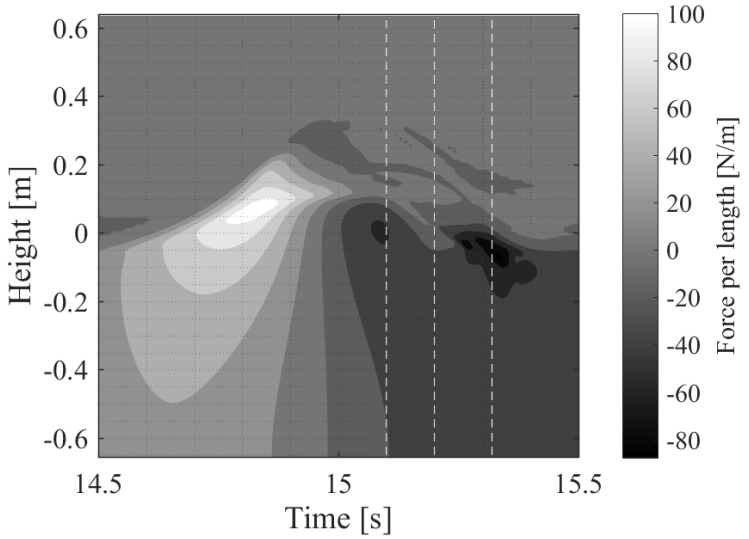

FIGURE 8: Force per length as a function of height and time. Integrating in height leads to the total inline force time series.

Azimuthal and vertical distribution of inline force

The front side and the back side forces are separately shown in figure 9 in the heights where the secondary load cycle effect was distinctly visible. The total force per unit height is shown in blue curves while, for the same heights, the front side force per unit height is shown in solid black line and the back side force per unit height is shown in black dashed lines. The force per height from the back side is multiplied by minus one so that visual comparison with the front side is easier. In these plots an event resembling the secondary load cycle can be observed in the same time period as in the total inline force time series. From $z = 0.04\ m$ to $z = -0.05\ m$ the secondary load cycle correlates to a cycle of decrease and increase from 15.2 s to 15.4 s in the absolute value of the inline force on the back side. Similar behaviour is observed from $z = -0.09\ m$ to $z = -0.21\ m$ with a smaller cycle until at $z = -0.28\ m$ where it has almost completely disappeared. The front side force time series show an abrupt decrease at around 15.2 s from $z = 0.04\ m$ to $z = -0.09\ m$ during the same period as the second peak. A small increase in the inline force from the front side can also be seen from $z = -0.01\ m$ to $z = 0.13\ m$ after the sudden decrease in the inline force. Hence, the first dip and the subsequent peak in the total inline force time series cannot be related to a distinct event at either front or back. The second dip occurs when the water from the front side is washed down and a sudden stop of force decrease occurs on the back side.

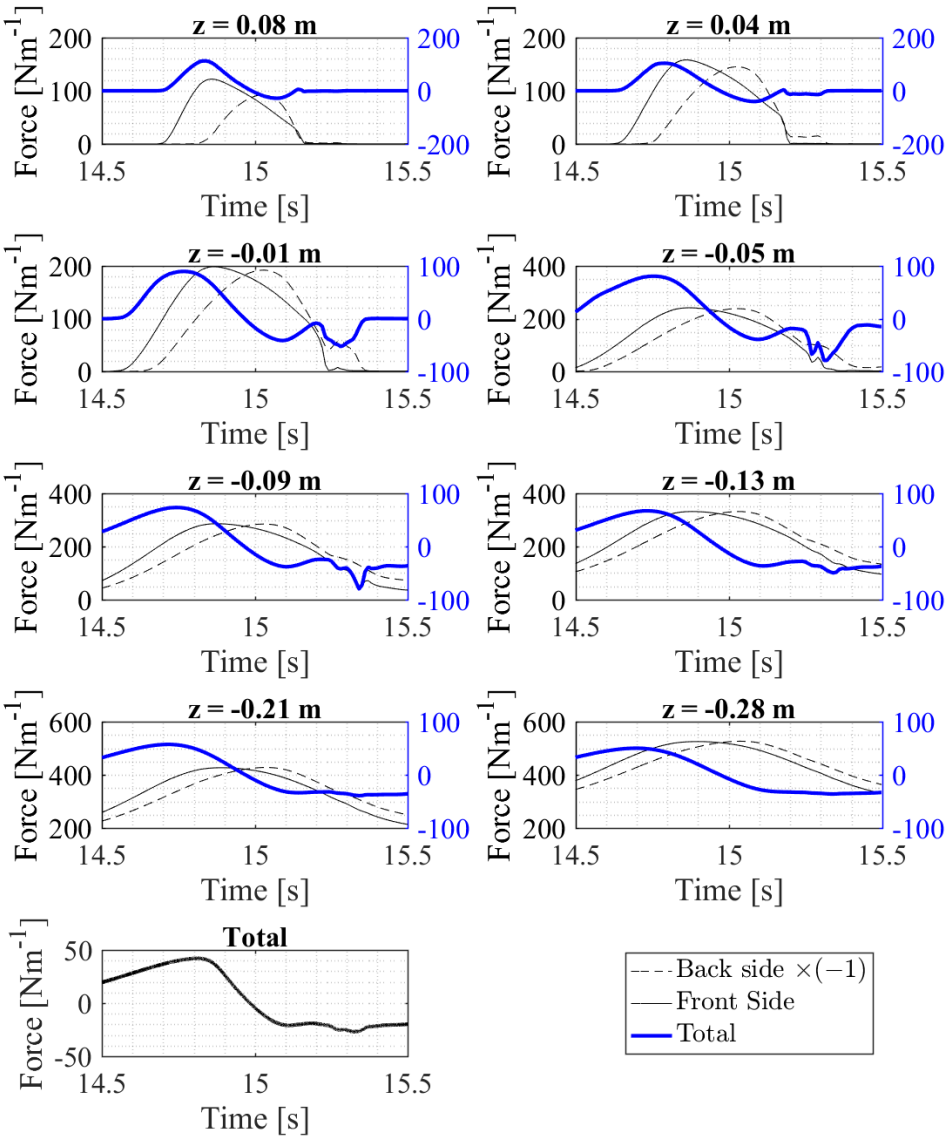

FIGURE 9: Separated front side, back side and total forces shown in the heights.

Detailed study by the vertical momentum equation

To understand the nature of the secondary load cycle, the vertical momentum conservation equation was used to separate the local pressure contribution for each term. Equation 4 can be rewritten in polar coordinates with total pressure, p, instead of p^* to be used easily around the cylinder

$$\frac{\partial \rho u_z}{\partial t} + u_r \frac{\partial \rho u_z}{\partial r} + \frac{u_\theta}{r}\frac{\partial \rho u_z}{\partial \theta} + u_z \frac{\partial \rho u_z}{\partial z} = -\frac{\partial p}{\partial z} + g_z z + \text{Viscous terms}. \quad (14)$$

The surface tension term in (4) has been dismissed since it was not included in our computations. The vertical momentum equation has the benefit that it separates the hydrostatic terms from the other terms. The values from the OpenFOAM domain in Cartesian coordinates were transferred into the polar coordinates for these analysis.

The polar momentum equation can be rewritten to separate the sources of pressure

$$\begin{aligned} p(z) = &\int_z^{atmosphere} (\rho_{local} g)\, dz \\ &+ \int_z^{atmosphere} \Bigg(\underbrace{\frac{\partial \rho u_z}{\partial t} + \frac{U_\theta}{r}\frac{\partial \rho u_z}{\partial \theta} + u_z \frac{\partial \rho u_z}{\partial z} + u_r \frac{\partial \rho u_z}{\partial r}}_{\frac{D \rho u_z}{Dt}} + \\ &\text{Viscous terms} \Bigg) dz. \end{aligned} \quad (15)$$

To calculate the pressure contribution from the first to the fourth term on the right hand side we started from the top of the numerical domain (atmosphere) where the pressure was close to zero. Hence the effect of the forces from the air on the cylinder were negligible which is expected considering the ratio of the density between water and air. The total pressure on the left hand side is known from the simulations. The pressure contribution from $u_r \frac{\partial \rho u_z}{\partial r}$ plus the viscous terms was thus calculated from the difference between the total pressure and the other calculated terms on the right hand side. This process was repeated for 170 azimuth angles to get the pressure distribution around the cylinder. The calculated total force from the cell centre pressure values were calculated and were found identical to the face value results. Therefore, it was justified to use the cell centre pressure and velocity component values to calculate the forces and to separate the forces from each term in the cell centres closest to the cylinder wall.

The inline force resulting from each term of (15) is shown in figure 10. It can be seen that the time series from the term $\frac{\partial \rho u_z}{\partial t}$ peaks at 15.2 s similar to the secondary load cycle. The hydrostatic force time series has a minimum at around 15.26 s which is close to the second dip of the secondary load cycle. However, since from figure 9 it is clear that the forces should be investigated

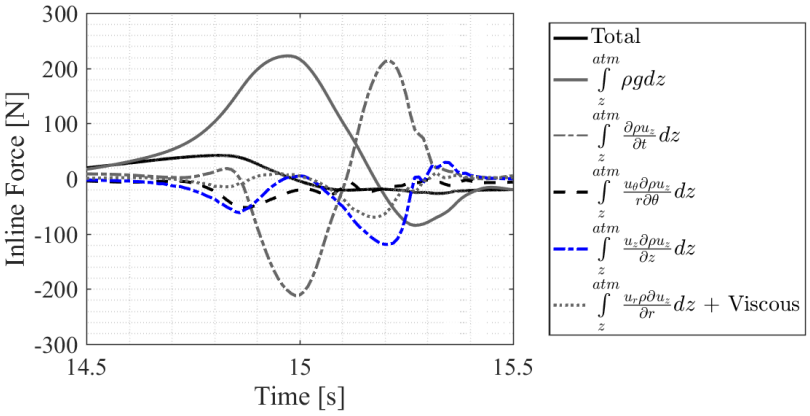

FIGURE 10: The forces originated from different terms of the Navier-Stokes equation in the vertical direction in polar coordinate system.

more locally a side and height divided analysis of these results is next carried out.

In figures 11 and 12 the force per unit height contours plots for the major sub-terms of (15) are visualized. Each row is assigned to either the total pressure or one sub-term. From left to right, each column is attributed to the contribution from both sides, front side and back side respectively. In all the contour plots the time instants 15.10 s, 15.20 s and 15.32 s are marked for reference to the secondary load cycle with vertical dashed lines. The contours of force per meter height from the total pressure is shown in the first row of figure 11. The first plot in the first row is the same contour plot presented in figure 8. The middle plot visualizes the force per height on the front side of the cylinder. This plot shows some small local events by proximity of contour lines at the same time period as the secondary load cycle. At around 15.15 s the slope of decrease in the front side force increases. The change of rate of change in the contour plot can be judged from the proximity of the contour lines. The right-most plot shows the forces only on the back side of the cylinder where a local cycle can be seen in the contour lines from 15.15 s to 15.35 s. The local cycle can be seen in the contour lines down to 1.5 diameter from just above the still water level.

The second row includes plots of forces originated from the hydrostatic pressure. In the left-hand plot the total hydrostatic force per unit height is shown as a function of time and height. It is observed that depending on the integrated effect of the run-up around the cylinder the hydrostatic force is positive until 15.1 s and afterwards, since the integrated run-up on the front side is smaller than on the back side, the inline force per unit height becomes negative. The hydrostatic forces on the front side maximizes at 15.0 s as shown in the middle plot. In addition, an increase in the hydrostatic pressure is observed after 15.32 s. This is probably best explained by the fact that the water from the collapsed water column travels towards the front side of the cylinder and because of lower elevation of the water surface on the front side at this time. At 15.3 s the water columns arrive at the front side

so the free surface elevation increases and so the hydrostatic force increases at this point. This can also be seen in the sub-plot (d) and (e) of figure 7 in which the water jets are observed to travel around the cylinder towards the front side of the cylinder. In the right-hand plot in this row the hydrostatic force per unit height from the back side is shown. The hydrostatic forces on the back side reach the minimum at 15.1 s when the run-up is maximum. This contributed tot he first dip of the secondary load cycle.

In the third row the force per-height is shown, originated from the non-hydrostatic terms. An extended negative force can be observed from 15.2 s to 15.3 s close to the free surface in the middle plot which have added a tongue to the dome shaped contours just above the still water level. In the right-most plot an extended positive force can be seen around the still water level maximizing at 15.2 s. The positive force occur right at the second peak and is thus perfectly in phase with the positive force peak of the secondary load cycle. Further, from inspection of figure 7, this moment of time is associated with a rapid decrease of water level below the water column at the back of the cylinder. Next, to investigate the sources of the non-hydrostatic forces the term $\frac{\mathrm{D}\rho u_z}{\mathrm{D}t}$ is further divided into sub-terms.

The force per height contour plots of three first sub-terms of $\frac{\mathrm{D}\rho u_z}{\mathrm{D}t}$ are shown in figure 12. In the plot of the contribution of $\frac{\partial \rho u_z}{\partial t}$ on the front side a positive force can be associated to the water jet created from the wave hitting the front side of the cylinder close to the free surface from 14.7 s to 15.0 s (throw-up effect). In addition, another region of large inline force can be seen after the run-up on the front side has started to fall down from 15.05 s to 15.32 s. The large inline force on the front side is closely correlated to the positive catch pressure of the lower layers of water. On the back side two regions of local forces can be seen. The first positive region of inline force per height is observed from around 15.10 s to 15.25 s and since it is a positive force on the back side it should be caused by a suction on this side. Linked to the rapid down-fall of the water level below the back-side water column, we deduce that the suction is caused by the removal of water below the water column base, because of change of direction of the particles in the incident wave, which should be filled by the water column. The second local inline force on the back side starts from 15.2 s and continues until 15.35 s below the free surface. Since this local force is negative there should be a relative high pressure on the back side which is associated with the catch pressure of the water on back side.

The second row of plots show the force contributions from the term $\frac{u_\theta}{r}\frac{\partial \rho u_z}{\partial \theta}$ on both sides. From these plots the scale of this term is much lower than the other terms and does not contribute significantly to the total local forces on the cylinder. In the third row of plots the force contributions from the term $\frac{u_z \partial \rho u_z}{\partial z}$ is presented. In the front side contribution plot the most significant contribution is from the wash down effect of the water on the front side. The wash down phenomena happens slightly before the catch phenomena. On the front side where the water is thrown up and little water is there to catch it,

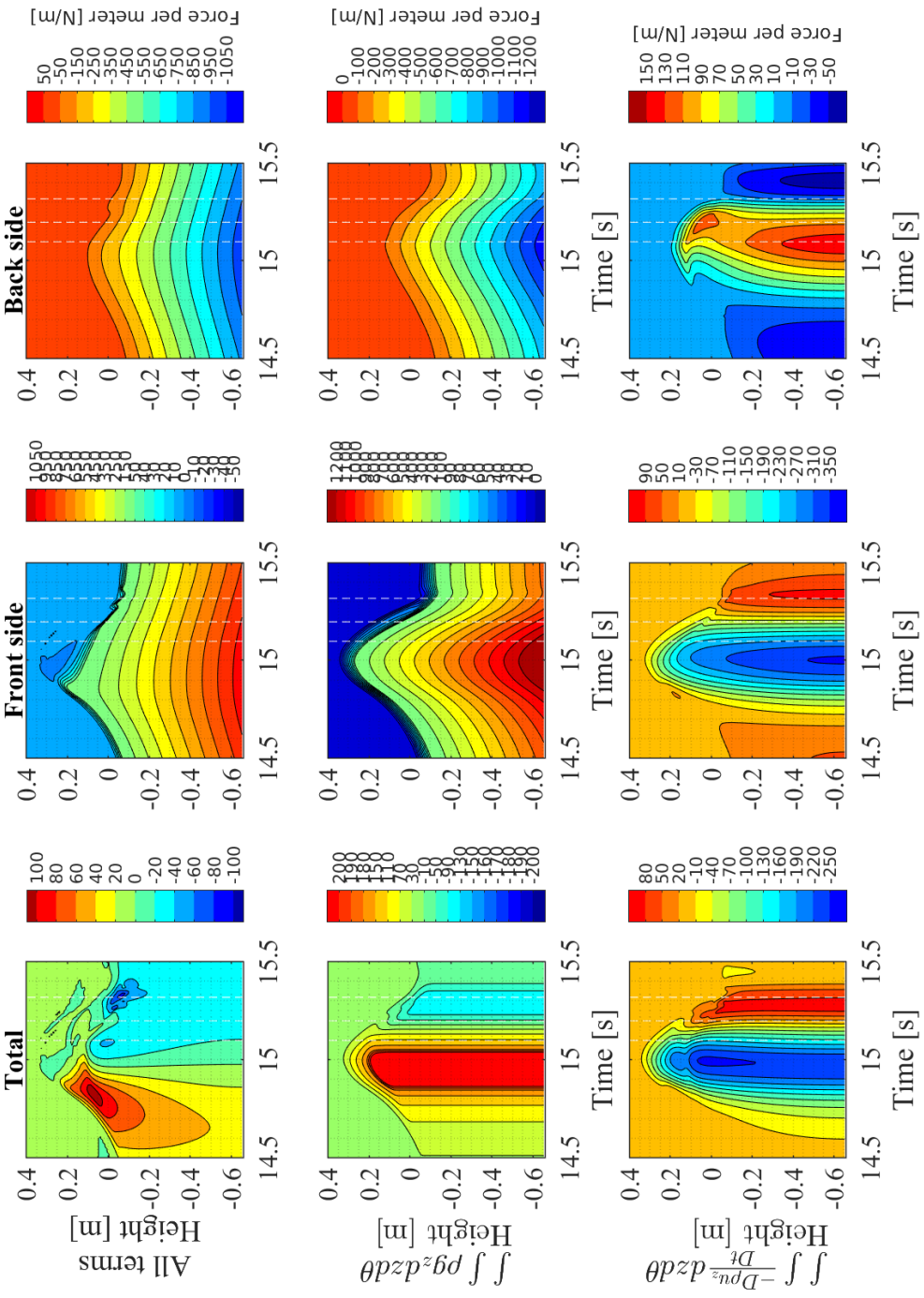

FIGURE 11: Force per meter separated for hydrostatic and non-hydrostatic terms in the vertical direction Navier-Stokes equation.

the wash down effect is larger in magnitude than the catch forces. The wash-down effect starts at around 15 s and continues until 15.32 in two almost separate bands similar to the catch pressure effect. Its effect on the force time series can be seen in figure 9 in depths 0.04 m to -0.09 m with the sudden decrease at around 15.2 s. In the right-most bottom plot in this figure the forces on the back side are shown where the two local forces are recognizable from 15.05 s until 15.35 s. These two local effects are also associated with the wash down effect of the water falling down or pulled down on the back side of the cylinder. With respect to the secondary load cycle, although the wash-down, catch and hydrostatic pressures on both sides play roles, the most important contribution is from the suction on the back side of the cylinder.

Snapshots of the total, hydrostatic and non-hydrostatic pressures on the cylinder are plotted in figure 13 for two time steps of 15.20 s and 15.25 s. In the middle plot in the first row the suction region can be distinctly observed in the base of the water column on the back side of the cylinder which is created because of the rapid decrease of the wave elevation below the water column a which leads to a low pressure region below the water column. The suction effect is maximum at around 15.2 s according to right-most bottom plot of figure 11, right-most top plot of figure 12 and the non-hydrostatic pressure contour plots. In the same plot low pressure bands can be observed on the front side of the cylinder around the free surface which correlates to the wash-down effect of the water on this side. From the middle plot in the second row and other snapshots not presented here for brevity the wash down effect on the front side continues its effect as a negative force until 15.32. The hydrostatic pressure contour plots show that from 15.2 s to 15.25 s the hydrostatic pressure has decreased more on the front side than on the back side which is consistent with the results shown in the integrated force time series of the hydrostatic forces in figure 10. In summary, from the detailed analysis, the secondary load cycle is mainly caused by the suction effect from the back of the cylinder, when the water level decreases rapidly while the water column has only just begun its downward acceleration after its maximum run-up. While this effect alone can create the second peak in the force time series, the preceding first dip is enhanced by the hydrostatic pressure from the back-side water column. The second dip is mainly a result of the second peak diminishing and the return to the global force time series related to the outer wave flow.

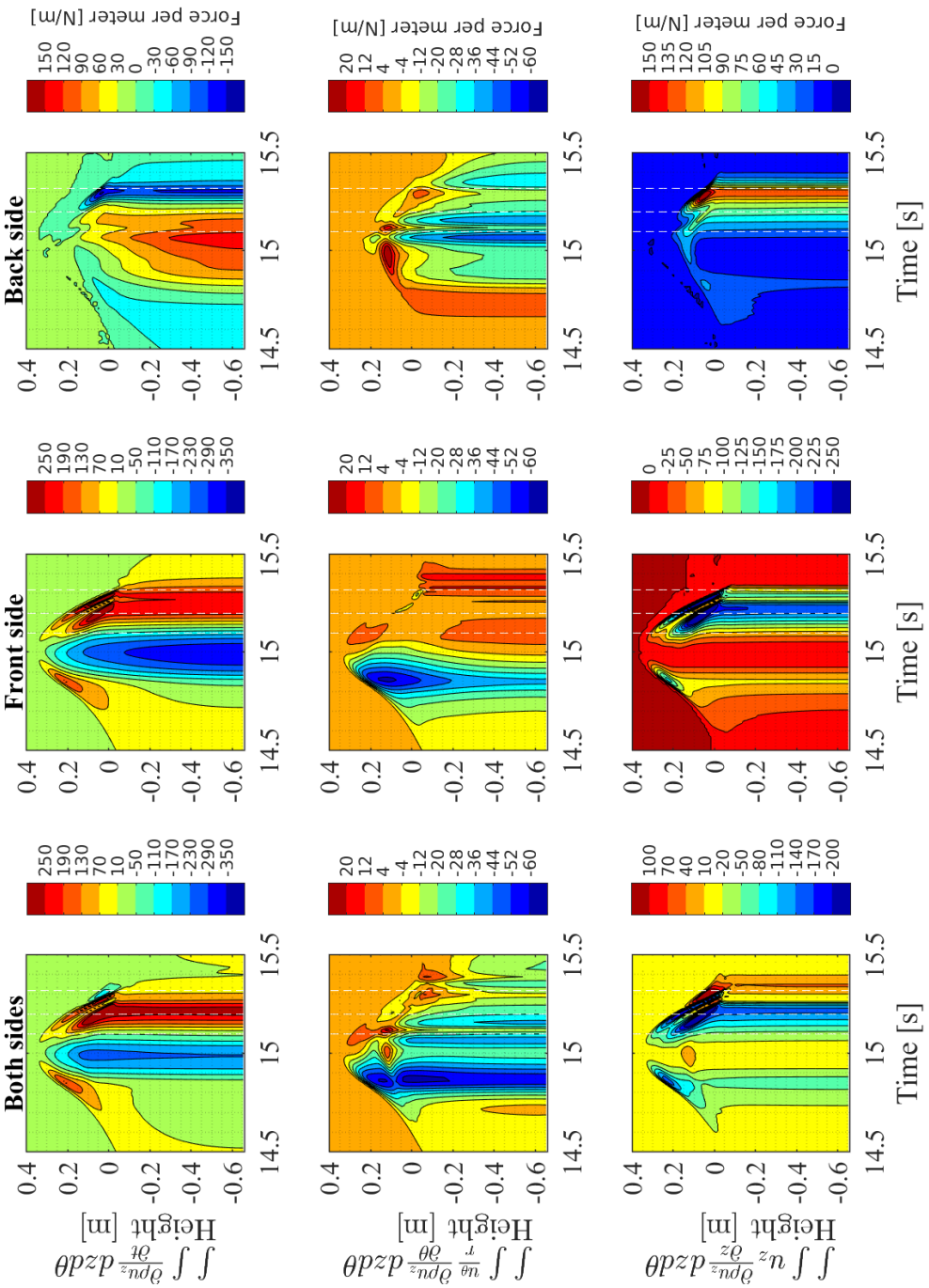

FIGURE 12: Force per meter $\frac{\partial \rho u_z}{\partial t}$, $\frac{u_\theta}{r}\frac{\partial \rho u_z}{\partial \theta}$ and $u_z\frac{\partial \rho u_z}{\partial z}$ terms.

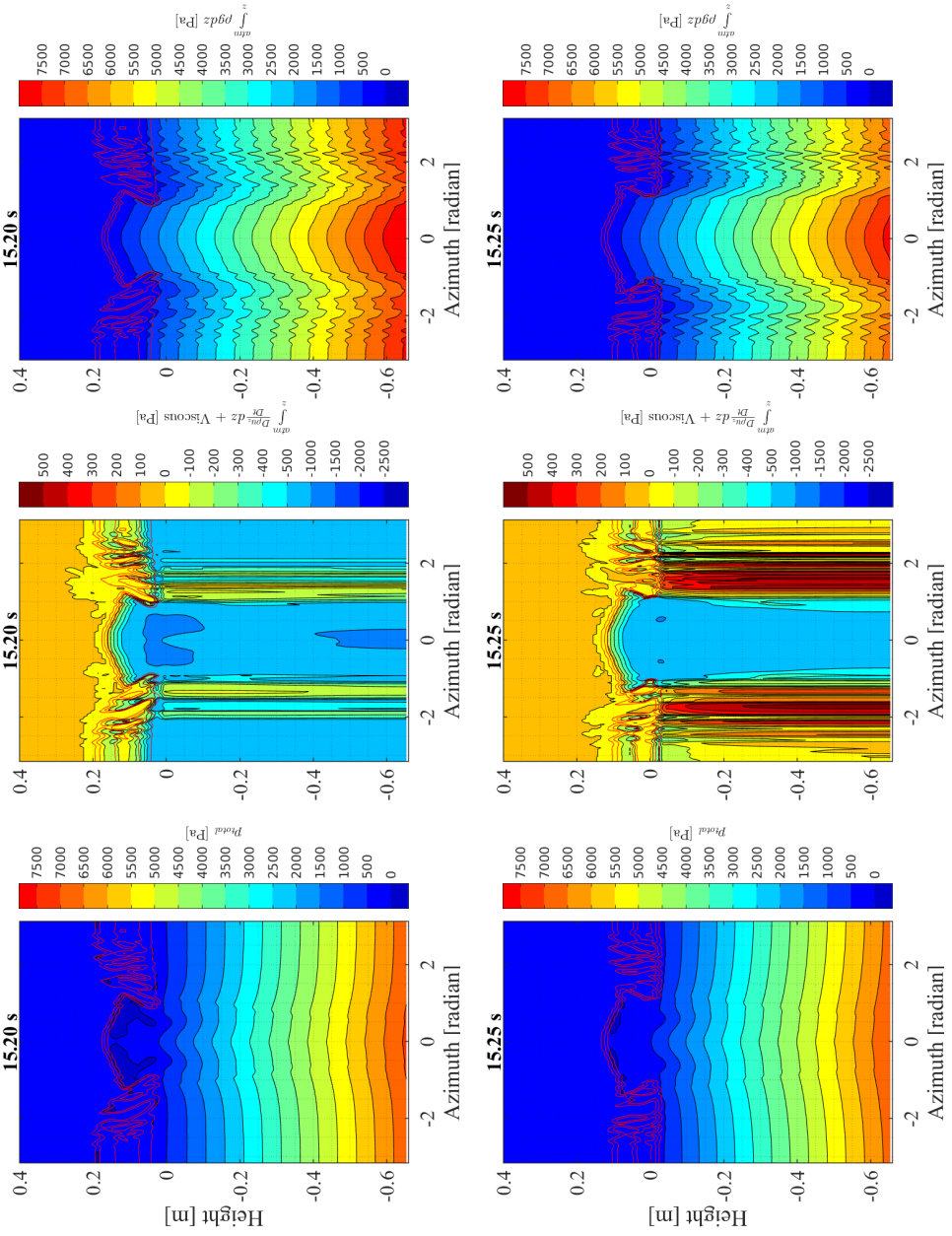

FIGURE 13: Pressure contours from total, hydrostatic and non-hydrostatic sources at times 15.20 s and 15.25 s.

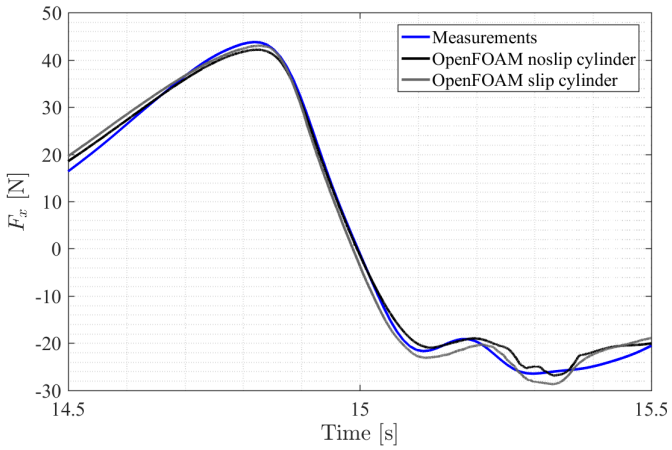

FIGURE 14: Comparison of the inline force in the simulations with no-slip boundary condition and with slip boundary condition on the cylinder.

The effect of no-slip boundary condition on the cylinder wall

To investigate the effect of the slip boundary condition, simulations with slip boundary condition and laminar flow was performed. In figure 14 the measured inline force time series are plotted with the integrated forces from the laminar and turbulent computations. Both set of numerical results are close to the measurements, however the time series from the no-slip simulations are slightly closer to the measurements during the secondary load cycle and before that. Nevertheless the secondary load cycle is observable in both sets of results during the same time period and with approximately same magnitude. Hereby, the secondary load cycle is thus seen to be only slightly affected by the wall boundary layer. At least for the present case quite good results for the total inline force time series can be obtained by laminar flow computations.

In the literature (Paulsen et al. 2014), appearance of vortices behind the cylinder were reported from laminar simulations and the secondary load cycle was associated with such vortices. Similar vortices are visible in the laminar simulations that we ran. In figure 15, contour plots of the vorticity just after the first appearance behind the cylinder are shown. The left column shows the results from the no-slip simulation and the right column shows the results of the one associated with the slip condition. As it can be seen in these plots the vortex starts to appear behind the cylinder at 14.9 s which is long before the secondary load cycle period. The vortices appear at this time irrespective of the turbulence modelling. The magnitude and spread of the vortices behind the cylinder grow up until 15.2 s when the vorticity in the fluid starts to smear out. In general, the magnitude of the vorticities is larger in the turbulent case with the no-slip boundary condition. Closer inspection of the flow suggests that the creation of the vortices behind the cylinder in this case is correlated most closely to the effect of the scattered waves behind

the cylinder. This hypothesis was reinforced by more investigation.

In figure 16 the free surface elevation is shown from a point of view behind the cylinder. The wave propagation direction in this figure is from the top left corner of each plot towards the bottom right corner. The cylinder itself is not shown in the illustrations to have an overview over the whole free surface. The two illustrations in this figure are only 0.02 s apart. In the left hand side plot the diffracted waves can be observed behind the cylinder as separate arc pairs which have not reached each other. In the right hand side illustration, only 0.02 s later the pair of arc shaped scatter waves have reached each other and started to form the water column. Creation of vortices might be linked to the emergence of the adverse pressure gradient from the collision of the two scattered waves.

Further investigation of sources of vorticity reveals that some vorticity is generated by the numerical scheme in regions where the mesh is abruptly changed, e.g. where blocks of the body fitted circular mesh around the cylinder meets the outer Cartesian mesh blocks. A further source of vorticity is the baroclinic contribution through $\nabla\rho \times \nabla\ p$. Both of these contributions though, were found to be minor relative to the main vorticity field.

The inline force from vorticities

To examine the effect of the vortices on the inline force, the Biot-Savart law was applied. To do so a few assumptions are made; the far-field pressure and velocity are assumed to be zero and the Bernoulli equation is assumed to be valid. These assumption are equivalent to taking out the vortices and placing them in a still fluid and calculating the forces they would induce on the cylinder. The effect of the rate of change of the vorticies in time on the induced velocities and forces are neglected. The calculated force with these assumptions may not be accurate in magnitude but it indicates the time scale of the force contribution from the vortices.

For this purpose we use the vorticity of the no-slipe computations up to one diameter from the cylinder wall and calculate the induced velocity on the cylinder wall using Biot-Savart law,

$$v(r) = \frac{1}{4\pi} \int_R \frac{\omega_0 \times (r_0 - r)}{|r_0 - r|^d} dR. \tag{16}$$

Here r is the position vector, ω_0 and r_0 are the vorticity, and the position vector of the vorticity, d is the number of dimensions and R denotes the domain of integration.

Afterwards with the assumption of the far field velocity and pressure equal to zero we calculate the pressure around the cylinder and integrate to obtain the total inline force for each time step.

Figure 17 shows the total force and the force induced by the vortices on the cylinder. The force induced by the presence of the vortices on the back side of the cylinder has a much larger time scale than the secondary load cycle. These vortices are created at 14.8 s before the secondary load cycle begins and their presence continues until after the water column is collapsed

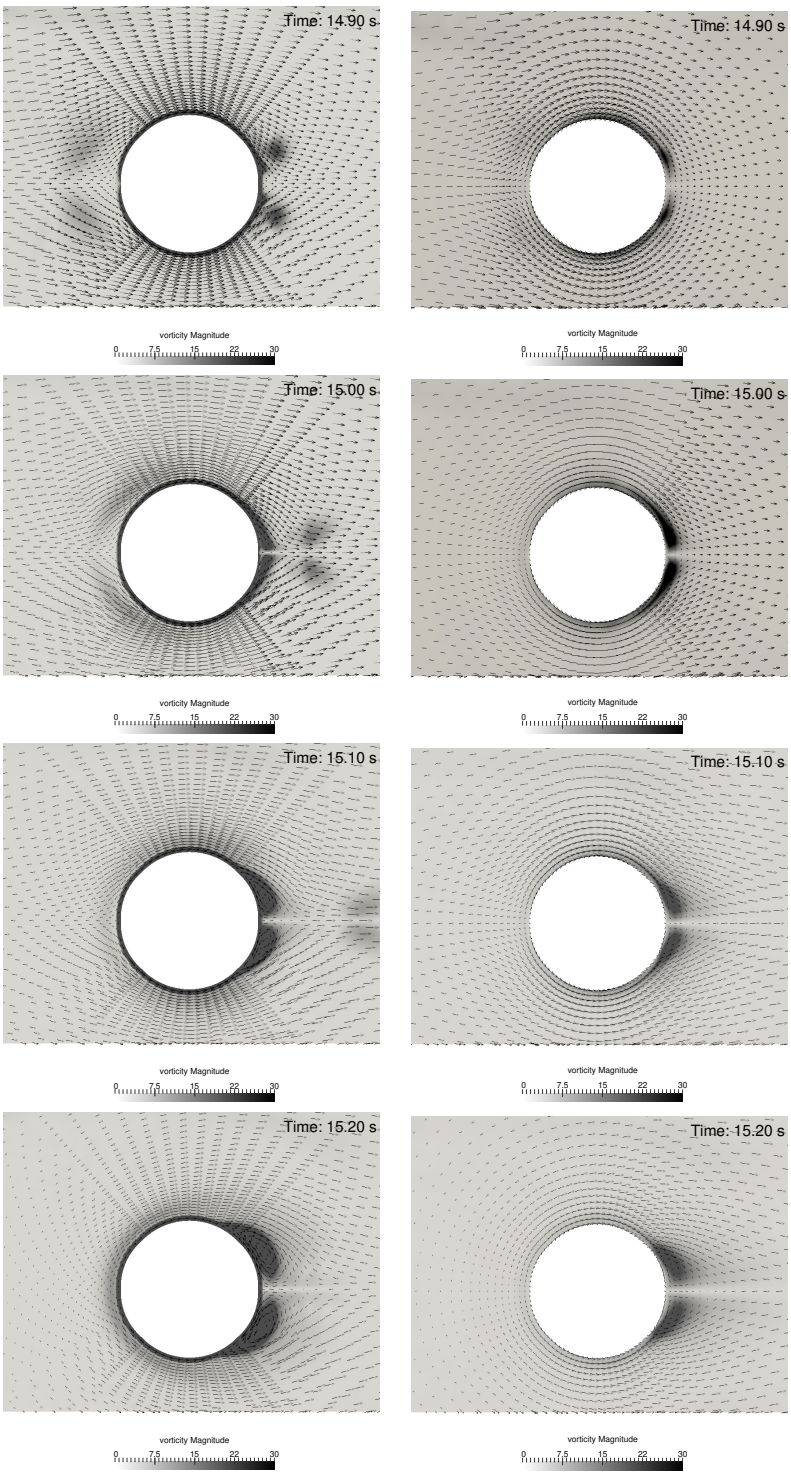

FIGURE 15: Appearance of vortices around the cylinder with passage of steep waves in diffraction zone at $h = -5cm$. Vorticity is shown with filled contours. Left column: no-slip. Right column: slip.

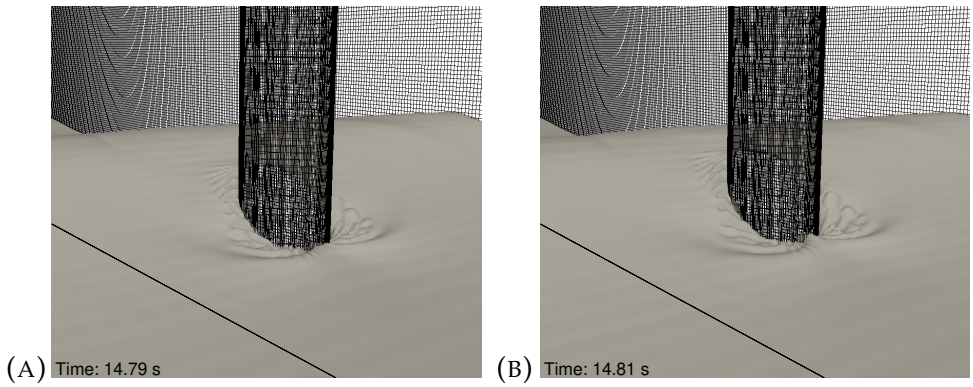

FIGURE 16: Formation of the water column behind the cylinder.

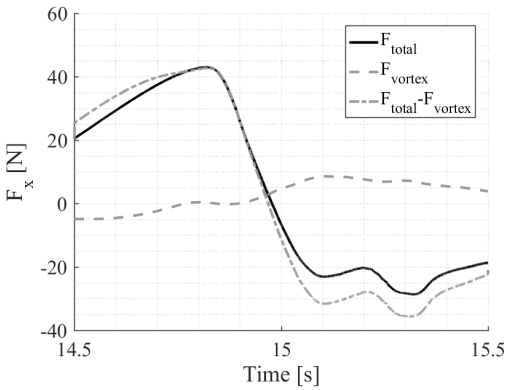

FIGURE 17: Force contribution from the vorticity in the domain.

at 15.3 s. Paulsen et al. 2014 observed the correlation between the presence of the secondary load cycle and the presence of the vorticies and suggested that the secondary load cycle is associated with back flow and vortices created behind the cylinder after the wave passage. The present analysis enables us to conclude that although the velocities induced by the velocities do create a local suction and thus a positive inline force on the cylinder, the time scale is too slow to form the rapid load variations associated with the secondary load cycle. Further, linked to the force contribution from the $\frac{u_\theta}{r}\frac{\partial \rho u_z}{d\theta}$ term of figure 10, we conclude that the main source of the rapid force oscillations from the secondary load cycle are not due to horizontal velocities caused by the back flow from the water column.

Summary and discussion

The secondary load cycle for a focused wave group impact on a vertical circular cylinder has been investigated experimentally and numerically. The experiment consisted of eight repeats of a focused wave group impact in the parameter range typical for offshore wind turbine storm conditions. A two-phase CFD model was next set up to reproduce the experiment. The numerical model was validated with satisfactory agreement for cases of turbulent

flow over a wall, oscillatory boundary layer, steady flow around a cylinder and oscillatory flow around a cylinder. The latter flow was validated for $Re = \{5.8 \cdot 10^4, 9 \cdot 10^4, 1.7 \cdot 10^5\}$ and $KC = \{6, 12, 18\}$ which is representative for the experimental flow conditions of the focused wave group impact.

Afterwards, a detailed study of the secondary load cycle was performed using the validated numerical model. By comparison of the run-up and run-down time series at the front and back of the cylinder, it was found that the time scales of these flows are too long to explain the load cycle through hydrostatic effects. Next, by inspection of the inline force distribution, we found that the secondary load cycle is associated with local events affecting the cylinder in a region from just above the still water level and 1.5 diameters down. Further division into the contributions from the front and back side reveals that the secondary load cycle is correlated with irregularities in the time series from both the front side and back side.

For further investigation, the forces from hydrostatic and non-hydrostatic terms of the vertical momentum equation were calculated and it was observed that the secondary load cycle is mostly correlated with forces from the non-hydrostatic term. More precisely, the main cause of the secondary load cycle is a suction pressure which occurs just after the maximum run-up of the water column at the back of the cylinder. At this time the free surface elevation of the outer wave flow falls rapidly. The needed downward acceleration of the water column generates the suction pressure at the root of the column which constitutes the local peak of the secondary load cycle The first dip, preceding this peak, is enhanced by the hydrostatic pressure of the water column during its maximum height, while the second dip is enhanced by wash-down effects on the front side and the total hydrostatic pressure from both sides.

Further observations during the flow includes

- A throw-up pressure at 14.85 s the on the front side which contributes to peak the total inline force at the same time.
- Free-fall conditions for the run-up at the front side. At 15.0 s this run-up is maximum. However, since the water is thrown up freely the hydrostatic pressure is cancelled out by the acceleration term $\frac{\partial \rho u_z}{\partial t}$.
- Fall down at 15.2 s on the front side with faster velocity than free fall. This leads to a low pressure region, created just below the free surface.
- A similar wash-down pressure at 15.32 s a at the back
- Generation of two sets of waves that propagates from the back to the front. The first set is associated with the initial fall-down of the water column and the second with its collapse.

In the last section emphasis was given to the effect of the wall boundary layer on the vortex formation behind the cylinder and the inline force. While vortices occur for computations with both slip and no-slip boundary conditions, we found that the time scale of vortex formation is too slow to

explain the secondary load cycle. Further, although differences between the two computations could be observed, the secondary load cycle appears to be quite similar for both slip and no-slip computations and quite accurate results for the inline force can thus be obtained with both slip and no-slip conditions for the present case.

The study demonstrates the strength of combined experimental-numerical investigations, where further and even very local details can be obtained from a numerical model after careful reproduction of a physical test. While the secondary load cycle has been known for more than two decades, and has often been associated with the flow at the cylinder back, the present investigation provides for the first time an accurate explanation of its cause. The good resemblance between the slip and no-slip results show that the flow separation, which has been observed also experimentally, is not only contributed from the wall boundary layer. It further suggests that good results for the inline force can be obtained by slip-condition calculations. Due to the lower CPU cost, this is encouraging for the application of such models in practical Engineering.

Acknowledgement

This work was funded by the Innovation Fund Denmark and other partners as part of DeRisk project with grant number 4106-00038B. This support is gratefully acknowledged by the authors.

References

Bredmose, H. et al. (2016). "DeRisk - Accurate prediction of ULS wave loads. Outlook and first results". In: *Energy Procedia*. Vol. 94. Elsevier, pp. 379–387.

Brown, S.A et al. (2014). "An Evaluation Of Rans Turbulence Closuremodels For Spilling Breakers". In: *Coastal Engineering*. 1995, pp. 1–12.

Chaplin, J.R. R, Rod C. T. Rainey, and R.W. W Yemm (1997). "Ringing of a vertical cylinder in waves". In: *Journal of Fluid Mechanics* 350, pp. 119–147.

Dean, Robert (2013). *Water wave mechanics for engineers and scientists*. Vol. 53. 9, pp. 1689–1699. arXiv: arXiv:1011.1669v3.

Deshpande, S. S., L. Anumolu, and M. F. Trujillo (2012). "Evaluating the performance of the two-phase flow solver interFoam". In: *Computational Science & Discovery* 5.1, p. 014016.

Devolder, Brecht, Pieter Rauwoens, and Peter Troch (2017). "Application of a buoyancy-modified k-ω SST turbulence model to simulate wave run-up around a monopile subjected to regular waves using OpenFOAM®". In: *Coastal Engineering* 125.June 2016, pp. 81–94.

Eltard, Bjarke, David R Fuhrman, and Johan Roenby (2017). "Performance of interFoam on progressive waves". In: *Preprint submitted to Applied Ocean Research* 2014. arXiv: 1804.01158.

Fredsøe, Jørgen et al. (2003). "Effect of externally generated turbulence on wave boundary layer". In: *Coastal Engineering* 49.3, pp. 155–183.

Ghadirian, A., H. Bredmose, and M. Dixen (2016). "Breaking phase focused wave group loads on offshore wind turbine monopiles". In: *Journal of Physics: Conference Series* 753.9, p. 092004.

Ghadirian, Amin, Henrik Bredmose, and Signe Schløer (2017). "Prediction of the shape of inline wave force and free surface elevation using First Order Reliability Method (FORM)". In: *Energy Procedia* 00.January, pp. 18–20.

Greenshields, C J (2015). "OpenFOAM-3.0.1". In: December.

Grue, John (2002). "On four highly nonlinear phenomena in wave theory and marine hydrodynamics". In: *Applied Ocean Research* 24.5, pp. 261–274.

Grue, John, Gunnhild Bjørshol, and Øivind Strand (1994). "Nonlinear wave loads which may generate "Ringing" responses of offshore structure". In: *Workshop on Water Waves and Floating Bodies*.

Grue, John and Morten Huseby (2002). "Higher harmonic wave forces and ringing of vertical cylinders". In: *Applied Ocean Research* 24.4, pp. 203–214.

Hirt, C. W and B. D Nichols (1981). "Volume of fluid (VOF) method for the dynamics of free boundaries". In: *Journal of Computational Physics* 39.1, pp. 201–225.

Jacobsen, Niels Gjøl (2011). "A Full Hydro- and Morphodynamic Description of Breaker Bar Development". PhD thesis, p. 200.

— (2017). *waves2Foam Manual*. Tech. rep. August. Deltares.

Jacobsen, Niels Gjøl, David R Fuhrman, and Jørgen Fredsøe (2012). "A wave generation toolbox for the open-source CFD library: OpenFoam". In: *International Journal for Numerical Methods in Fluids* 70.9, pp. 1073–1088.

Jensen, B L, B M Sumer, and J Fredsoe (1989). "Turbulent oscillatory boundary layers at high Reynolds numbers". In: *Journal of Luid Mechanics* 206, pp. 265–297.

Jose, Jithin et al. (2017). "A comparison of numerical simulations of breaking wave forces on a monopile structure using finite difference and finite volume models". In: *Ocean Engineering* m.1, pp. 1–26.

Karman, Th. von (1931). "Mechanical Similitude and Turbulence". In:

Kristiansen, T and O M Faltinsen (2017). "Higher harmonic wave loads on a vertical cylinder in finite water depth". In: pp. 773–805.

Menter, FR, M Kuntz, and R Langtry (2003). "Ten years of industrial experience with the SST turbulence model". In: *Turbulence, heat and mass transfer*, p. 8.

Paulsen, Bo Terp (2013). "Efficient computations of wave loads on off shore structures". PhD thesis.

Paulsen, Bo Terp, Henrik Bredmose, and Harry B. Bingham (2014). "An efficient domain decomposition strategy for wave loads on surface piercing circular cylinders". In: *Coastal Engineering* 86, pp. 57–76.

Paulsen, Bo T. et al. (2014). "Forcing of a bottom-mounted circular cylinder by steep regular water waves at finite depth". In: *Journal of Fluid Mechanics* 755, pp. 1–34.

Rainey, Rod C T (2007). "Weak or strong nonlinearity: The vital issue". In: *Journal of Engineering Mathematics* 58.1-4, pp. 229–249.

Riise, Bjørn Hervold et al. (2018). "A note on the secondary load cycle for a monopile in irregular deep water waves". In: *Journal of Fluid Mechanics* 849, R1.

Rosetti, Guilherme F., Guilherme Vaz, and André L. C. Fujarra (2012). "URANS Calculations for Smooth Circular Cylinder Flow in a Wide Range of Reynolds Numbers: Solution Verification and Validation". In: *Journal of Fluids Engineering* 134.12, p. 121103.

Stringer, R. M., J. Zang, and A. J. Hillis (2014). "Unsteady RANS computations of flow around a circular cylinder for a wide range of Reynolds numbers". In: *Ocean Engineering* 87, pp. 1–9.

Sumer, B. Mutlu and Jorgen Fredsoe (2006). *Hydrodynamics Around Cylindrical structures*. Vol. 26.

Tromans, Peter S, A R Anatruk, and Paul Hagemeijer (1991). "A New Model for the Kinematics of Large Ocean Waves Application as a Design Wave". In: *Proceedings of the First International Offshore and Polar Engineering Conference* 8.August, pp. 64–71.

Yang, Y. and D. Rockwell (2002). "Wave interaction with a vertical cylinder: Spanwise flow patterns and loading". In: *Journal of Fluid Mechanics* 460, pp. 93–129.

Ye, Haixuan and Decheng Wan (2017). "Benchmark computations for flows around a stationary cylinder with high Reynolds numbers by RANS-overset grid approach". In: *Applied Ocean Research* 65, pp. 315–326.

Paper 6

Pressure impulse theory for a slamming wave on a vertical circular cylinder

* *This paper is submitted to the* ***Journal of Fluid Mechanics****.*

Amin Ghadirian[1], Henrik Bredmose[1]
[1] DTU Wind Energy, Nils Koppels Alle Building 403, DK-2800 Kgs. Lyngby, Denmark
E-mail: amgh@dtu.dk

Abstract

A pressure impulse model is presented for wave impact on vertical cylinders. The model is derived for a simplistic geometry and has the relative impact height, crest length and cylinder radius as effective variables. The last parameter, the maximum angle of impact is free and can be calibrated to yield the right force impulse.

A progression of simpler pressure impulse models are derived in terms of a 3D box generalization of the 2D wall model of Cooker and Peregrine 1995 and an axisymmetric model for vertical cylinders. The dependence to the model parameters are investigated in the simpler models and are linked to the behaviour of the 3D cylinder model.

The model is next validated against numerical results for a wave impact for a phase- and direction-focusing wave group. The maximum impact angle is determined by calibration against the force impulse. A good match of the pressure impulse fields is found. Further comparison to the force impulse of two common models in Marine Engineering reveals improved consistency for the present model. The model is found to provide a robust representation of the pressure impulse field, based on a limited number of input parameters. Its further validation and potential in force and response prediction is discussed.

Introduction

In the design process of offshore structures the slamming wave load calculations play an important role. One of the most commonly used approaches for vertical circular cylinders is based on the work done by Goda, Haranaka, and Kitahata 1966 formulated as

$$F_I(t) = \lambda\eta_b \pi \rho R C^2 \left(1 - \frac{C}{R}t\right), \tag{1}$$

where $\lambda\eta_b$ is the height of impact, C is the wave celerity, ρ is the fluid density and R is the cylinder's radius. The breaker front is vertical and moves with the celerity of the wave. Very often the maximum inline force per height is described as a function of a slamming coefficient, C_s, where $F_{I,max} = C_s \cdot \rho \cdot R \cdot V^2$. Therefore, in the formulation of Goda, Haranaka, and Kitahata 1966 $C_s = \pi$. Prior to Goda, Haranaka, and Kitahata 1966, Wagner 1932 developed a solution for the peak pressure during impact of a solid object on a still fluid in two-dimensions. The solution predicted a slamming coefficient of $C_s = 2\pi$. Later **Cointe1987** applied the method of matched asymptotic expansions to solve the boundary condition problem of the velocity potential and free surface of the flow around the structure. The model provides the same result as Wagner's theory for the slamming coefficient, $C_s = 2\pi$. The study further included the decay of the impulse force on the cylinder in time. More recently, Wienke and Oumeraci 2005 proposed a new formulation which extends the model of Wagner 1932 for the total duration of the impact in three-dimensions. Hallowell, Myers, and Arwade 2016 used measurements from a site test campaign of the Blyth wind farm off the coast of England to categorize and identify breaking waves and quantify the variability of their impact loads. The accuracy of several breaking wave limits and impact force models was analysed, and the impact force models were shown to represent the measurements with varying accuracy and to be sensitive to modelling assumptions. Their results showed that the mudline moments calculated using the model developed by Goda, Haranaka, and Kitahata 1966 were most consistent with the measurements, however, this consistency was claimed to be site and structure specific.

Since the duration of the impact on the structure is usually very short, the time integrated force impulse may be sufficient for an accurate response prediction. The pressure impulse theory is thus relevant in such cases. Further the theory gives spatial distribution of impulse over the structure. In Cooker and Peregrine 1995, the pressure impulse theory was derived for wave impact on a vertical wall in 2D. A parametric study was performed to identify the dependency to the ratio of the breaker height to the total depth and the length of the breaker. However, the model was not validated against measurements or other more comprehensive models. The approach was extended to more complicated configurations such as impact on an elastic wall by Korobkin and Malenica 2007, breaking wave impact on a wall in Iafrati and Korobkin 2006, breaking wave impact on permeable barriers by Cooker

2013 and wave impact on perforated structures by Korobkin 2008. Most recently Chatjigeorgiou et al. 2016 presented the three dimensional steep wave impact onto a vertical plate with finite width and used the results combined with the strip theory to model the time varying slamming load on a vertical cylinder. In a further paper, Chatjigeorgiou, Korobkin, and Cooker 2016 treated the three-dimensional hydrodynamic slamming problem on a vertical cylinder as a set of 2-D problems in the vertical direction. They found a closed form solution for the time dependent potential, the pressure impulse, the shape of the wave front and the slamming force as a function of time and height of the cylinder. Nevertheless, they did not validate the model against other models or measurements.

In the present paper a 3D pressure impulse model for a wave impact of a wedge-shaped geometry is presented. A 3D box generalization of the 2D wall model of Cooker and Peregrine 1995 is derived (§6) along with an axisymmetric impact model. The effective parameters of the axisymmetric impact model are investigated with reference to the behaviour of the 2 simpler models. The role of the maximum impact angle is discussed and a comparison to a realistic numerical wave impact is presented (§6). A summary and further discussion of the model application is presented in (§6).

Mathematical formulation

Even though the peak pressure of an impulse event varies unpredictably between each impact with the same characteristics, the pressure impulse does not change significantly. Hence, Cooker and Peregrine 1995 suggested the pressure impulse is a better quantity to model an impact event than the peak pressure. The speed of the fluid is much less than the speed of sound so the incompressibility assumption can be applied. In addition, the effect of viscosity is negligible. The pressure impulse P is defined by

$$P(\mathbf{x}) = \int_{t_b}^{t_a} p(\mathbf{x}, t)dt, \tag{2}$$

where t_b and t_a are the times immediately before and after impact respectively and pressure is denoted by p. Since the impact occurs in a very short time the convective terms in equation of motion are negligible so the horizontal Euler equation reads

$$\frac{\partial \mathbf{u}}{\partial t} = -\frac{1}{\rho}\nabla p. \tag{3}$$

After integration with respect to time through the impact interval the equation reads

$$\underline{u}_a - \underline{u}_b = -\frac{1}{\rho}\nabla P. \tag{4}$$

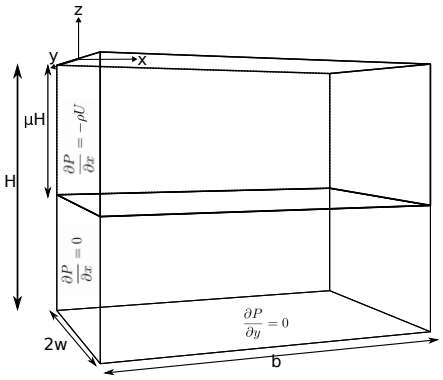

FIGURE 1: Definition sketch for 3D block impact on a flat plate.

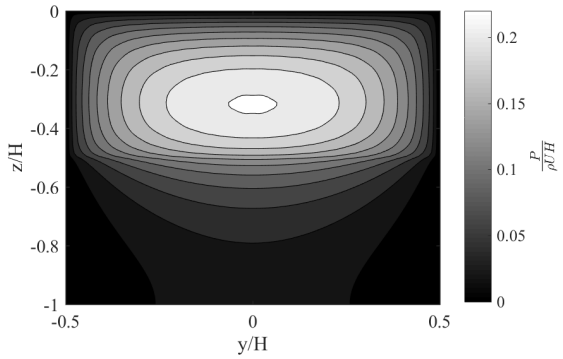

FIGURE 2: Pressure impulse of a finite-width fluid block on a flat vertical plate at x = 0 for $\mu = 0.5$, $W/H = 0.5$ and $b/H = 1$.

This equation can be rewritten by taking the divergence of both sides, which leads to the Laplace equation for the pressure impulse $\nabla^2 P = 0$. Following Cooker and Peregrine 1995, the pressure impulse field satisfies the boundary conditions $P = 0$ at the free surface; $\partial P/\partial n = 0$ at a stationary rigid body boundary and $\partial P/\partial n = \rho u_{nb}$ where the liquid meets a solid wall during impact.

Impact of an idealized finite-width wave on a vertical wall

The simplest case in three dimensions is to have a box shaped volume of fluid impacting a flat vertical wall. The domain and the boundaries for this problem is shown in figure 1. The flat plate is located at $x = 0$. The fluid is divided into two parts in the vertical direction: the fluid in $0 \geq z \geq -\mu H$ is the moving fluid with velocity U in the negative x direction while the fluid in $-\mu H > z \geq -H$ is standing still during the impact. The boundary conditions on the flat plate and on the bed are shown in the figure. On the other boundaries $P = 0$ must be satisfied.

The Laplace equation is solved using separation of variables and Fourier series analysis. The solution can be written as

$$P(x,y,z) = \sum_{m=1}^{\infty}\sum_{n=1}^{\infty}\left(A_{nm}\cos(L_m\frac{y}{W})\sin(K_n\frac{z}{H})\frac{\sinh(\sqrt{L_m^2(\frac{H}{W})^2+K_n^2}(\frac{b}{H}-\frac{x}{H}))}{\cosh(\sqrt{L_m^2(\frac{H}{W})^2+K_n^2}\frac{b}{H})}\right), \tag{5}$$

where $K_n = (n-1/2)\pi$, $L_m = (m-1/2)\pi$, and

$$A_{nm} = 4\rho UH\frac{(\cos(K_n\mu)-1)\sin(L_m)}{K_nL_m\sqrt{L_m^2(\frac{H}{W})^2+K_n^2}}. \tag{6}$$

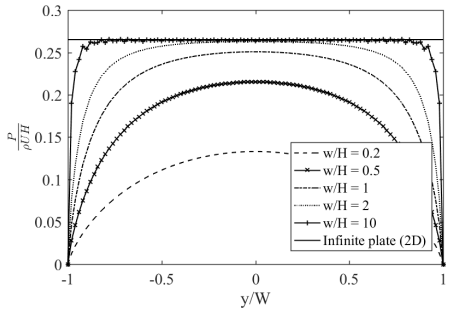

FIGURE 3: Pressure impulse as a function of width of the impacting block, plotted in the mid-height on the flat wall ($z/H = -\mu/2$ and $x/H = 0$).

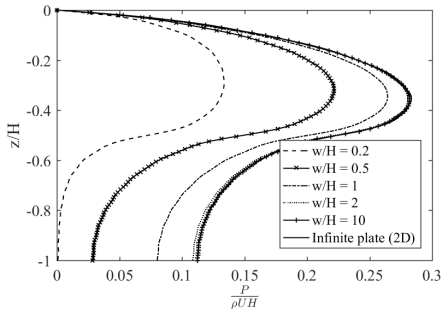

FIGURE 4: Pressure impulse as a function of width of the impacting block, plotted in the mid-width on the flat wall ($y/W = 0$ and $x/H = 0$).

For $W \to \infty$, (5) and (6) reduces to the solution of Cooker and Peregrine 1995. Additional to the 2D properties, (5) has an extra dependency to the second horizontal direction through the term $\cos(L_m y/W)$ and the coefficients in the hyperbolic functions. The pressure impulse field can thus be seen to depend on the three dimensionless parameters as follows:

$$\frac{P}{\rho U H}\left(\frac{x}{H}, \frac{y}{W}, \frac{z}{H}\right) = f\left(\frac{b}{H}, \mu, \frac{W}{H}\right). \tag{7}$$

The pressure impulse field thus depends on the relative length of the impacting block b/H, the relative height of the impact zone μ and the relative width of the block W/H. As an example, the result for the parameters $\mu = 0.5$, $W/H = 0.5$ and $b/H = 1$ is shown in figure 2. The pressure impulse extends in the middle of the block to lower heights than $-\mu H$ which means that part of the pressure impulse is carried by the bottom fluid. Convergence was achieved in this case with 30 components in each direction in (5).

The dependency of the pressure impulse on the width of the impacting block of fluid is shown in figure 3 in the depth of $z/H = -\mu H/2$ as a function of y/W. The pressure impulse is maximum at the centre of the plate ($y/W = 0$) and increases with width until the 2D limit is reached as marked by a solid line. At the middle of the plate this is achieved for $W/H \approx 2$ in the present case and is gradually achieved for larger W/H values towards the sides of the wall. In figure 4 the pressure impulse on the centre line of the plate is plotted as a function of height for the same parameters. As the width of the fluid box is increased, the results of the box impact approach the 2D case results.

Impact of an idealized all-directional wave on a cylinder

With the insight from the 3D box impact problem we proceed to impacts on cylinders. First the simple case of an axisymmetric impact is studied. A sketch of the domain and the boundary conditions is presented in figure 5.

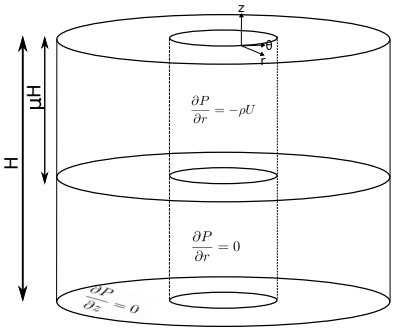

FIGURE 5: Definition sketch for axisymmetric impact on a vertical cylinder.

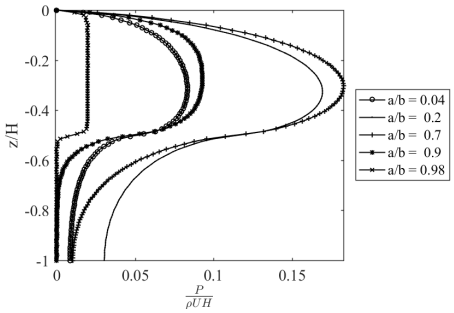

FIGURE 6: Pressure impulse of a axisymmetric wave impact on the wall of a cylinder with increasing a/b.

The domain is divided into two parts above and below $-\mu H$ with initially moving and standing still fluid respectively. The fluid, above $-\mu H$, is approaching in the radial direction towards the cylinder from all azimuthal angles. The boundaries on the walls are shown in this figure while all the other boundaries should satisfy $P = 0$.

The Laplace equation is solved in the cylindrical coordinate system to yield

$$P = \sum_{n=1}^{\infty} \left(A_n \frac{I_0(k_n \frac{r}{H}) + \alpha_n K_0(k_n \frac{r}{H})}{\partial_r \left(I_0(k_n \frac{r}{H}) + \alpha_n K_0(k_n \frac{r}{H}) \right)_{r=a}} \sin(k_n \frac{z}{H}) \right), \tag{8}$$

where $k_n = (n - 1/2)\pi$, ∂_r is the partial derivative with regards to r, I_0 and K_0 are the first and second modified Bessel functions of zeroth order and

$$A_n = 2\rho U I \frac{1 - \cos(k_n \mu)}{k_n}. \tag{9}$$

The modified Bessel functions I_0 and K_0 were chosen for the radial expansion due to their non-oscillatory variation, which is suitable for the impact problem. A linear combination of the two functions is used here to assure compliance with the boundary condition $P = 0$ at $r = b$ using the multiplier

$$\alpha_n = \frac{-I_0(k_n b/H)}{K_0(k_n b/H)}. \tag{10}$$

From (8), the non-dimensional pressure impulse on the cylinder wall depends on the relative outer radius of the impacting fluid b/H, the relative height of the impact region μ and the ratio of the inner to outer radius a/b:

$$\frac{P}{\rho U H}(\frac{r}{H}, \frac{z}{H}) = f(\frac{b}{H}, \mu, \frac{a}{b}). \tag{11}$$

The axisymmetric pressure impulse on the cylinder is shown in figure 6 for $b/H = 1$, $\mu = 0.5$ and varying radius radio. When the inner radius is

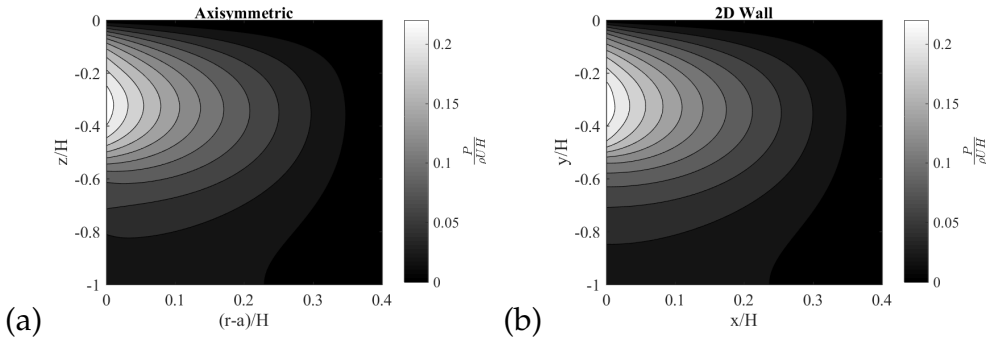

FIGURE 7: Pressure impulse for (a) an axisymmetric cylinder and (b) a 2D vertical wall.

increased, the cylinder wall delivers a larger impulse to decelerate the fluid and the pressure impulse increases. For the present values of μ and b/H, it reaches a maximum at a/b around 0.7 and decreases thereafter due to the decreasing initial momentum for $a/b \to 1$.

The axisymmetric solution can be compared to the case of impact of 2D wall case of from Cooker and Peregrine 1995. In this case, the radius of the cylinder must be large enough that the effect of the curvature is minimized. The pressure impulse field for the axisymmetric case of $b/H = 10.4$, $a/b = 0.96$ and the wall case of $b/H = 0.4$ are compared in figure 7. For both cases $\mu = 0.5$. A very similar behaviour of the two fields can be seen.

Impact of an idealized wave on a cylinder with azimuth limits

We now proceed to the 3D model of impact on a cylinder. The domain of the problem and its boundary conditions are shown in figure 8. In this case the fluid is wedge-shaped in the azimuthal direction divided into heights above and below $z = -\mu H$ while the part above is initially approaching the cylinder with velocity $U\cos(\theta)$ in the negative radial direction. Similar to the previous cases in all the other boundaries $P = 0$. The Laplace equation is solved in the cylindrical coordinate system to yield

$$P = \sum_{m=1}^{\infty}\sum_{n=1}^{\infty}\left(A_{n,m}\cos(L_m\theta/\theta_{max})\sin(k_n\frac{z}{H})\right.$$
$$\left.\frac{I_{L_m/\theta_{max}}(k_n\frac{r}{H}) + \alpha_{m,n}K_{L_m/\theta_{max}}(k_n\frac{r}{H})}{\partial_r\left(I_{L_m/\theta_{max}}(k_n\frac{r}{H}) + \alpha_{m,n}K_{L_m/\theta_{max}}(k_n\frac{r}{H})\right)_{r=a}}\right), \quad (12)$$

with $k_n = (n-1/2)\pi$, $L_m = (m-1/2)\pi$. Further $\alpha_{m,n}$ is chosen such that $P = 0$ at $r = b$ and

$$A_{n,m} = \frac{-2\rho U}{\theta_{max}}\int_{-\mu H}^{0}\left(\int_{-\theta_{max}}^{\theta_{max}}(\cos(\theta)\cos(L_m\theta/\theta_{max}))\,d\theta\sin(k_n\frac{z}{H})\right)dz. \quad (13)$$

In this case the non-dimensional pressure impulse depends on the maximum impact angle in addition to the parameters already defined for the

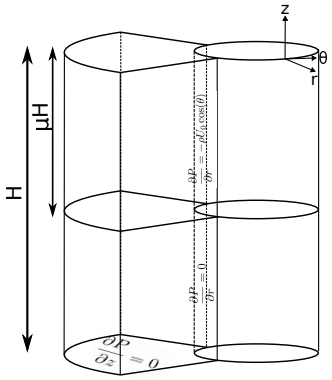

FIGURE 8: Definition sketch for wedge-shaped 3D impact on a vertical cylinder.

axisymmetric impact:

$$\frac{P}{\rho U H}\left(\frac{r}{H}, \theta, \frac{z}{H}\right) = f\left(\frac{b}{H}, \mu, \frac{a}{b}, \theta_{max}\right). \tag{14}$$

A parameter study was conducted to investigate the effect of the different parameters. The dependence to the relative length of the impacting wave b/H is shown in figure 9(a) for $\theta = 0$, $\mu = 0.5$, $a/H = 0.1$ and $\theta_{max} = \pi/4$. As b/H increases up to 0.35 the pressure impulse increases in all heights and then remains unchanged. This shows an asymptotic behaviour for increasing b/H. The same asymptotic behaviour was observed in the investigation performed by Cooker and Peregrine 1995 for the 2D flat plate case. We next investigate the dependence to the height of the impact region, μ, in figure 9(b). A width of $b/H = 0.3$ is used and μ, θ_{max} and a/H are identical to the values of figure 9(a). By the increase of μ the peak of the pressure impulse moves down as expected and increases the pressure impulse. The results from this figure are also similar to the ones shown in figure 5 of Cooker and Peregrine 1995.

The variation with respect to the relative inner radius a/b is investigated in figure 10(a) for $\mu = 0.5$, $\theta_{max} = \pi/4$ and $b/H = 0.3$. The pressure impulse increases as a/b increases up to $a/b = 0.5$. For a/b values larger than 0.67 the pressure impulse decreases similarly to the case shown for the axisymmetric impact on the cylinder wall. First the area that absorbs the impulse on the cylinder increases so the pressure impulse increases. However, at the same time the volume of fluid impacting on the cylinder is decreasing so at $a/b = 0.5 - 0.7$ the pressure impulse is at its maximum value.

The effect of the width of the fluid domain (in azimuth) is shown in figure 10(b). The constant parameters are $a/b = 0.33$, $b/H = 0.3$ and $\mu = 0.5$. As the width of the domain increases the pressure impulse also increases. This increase can be explained by the increase in the total impacting volume of fluid $V = ((b^2 - a^2) \cdot \theta_{max}) \cdot \mu \cdot H$ as θ_{max} increases. This conclusion is similar to the increasing pressure impulse of the 3D impact of the fluid on the flat vertical plate of figure 3. The rate of increase of the pressure impulse decreases as the azimuthal angle limit increases until it reaches its maximum

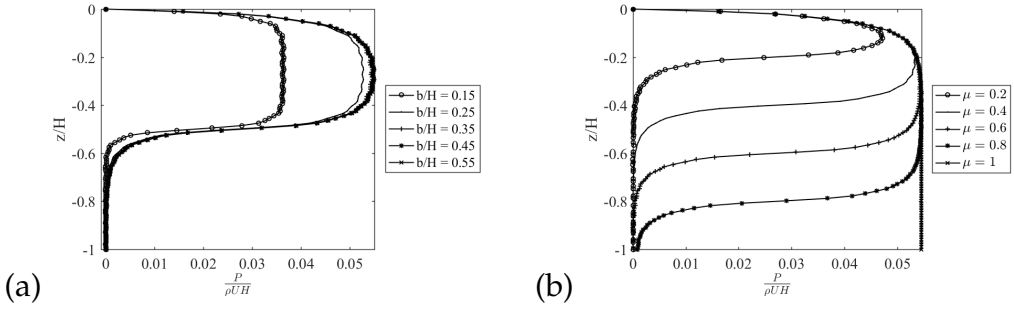

FIGURE 9: The pressure impulse at $\theta = 0$ as a function of height at the cylinder wall for (a) varying b/H and (b) varying μ.

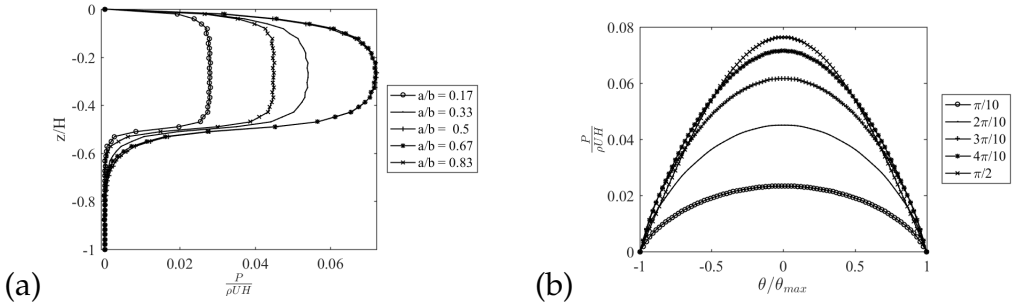

FIGURE 10: The pressure impulse at $\theta = 0$ as a function of height at the cylinder wall for (a) varying a/b and (b) varying θ_{max}.

at $\theta_{max} = \pi/2$.

Validation against CFD results

We now validate the model against a realistic wave impact. The chosen wave is a phase- and direction-focused wave group for a sea state of $H_s = 9.5$ m, $T_p = 12$ s in 33 m water depth with a cylinder diameter of 7 m. CFD results for this impact was presented by Ghadirian, Bredmose, and Dixen 2016. A snapshot of the wave just after the impact is shown in figure 11. The parameter a is given by the cylinder radius, H by the crest elevation over the bed, and b is chosen as the distance from the cylinder centre to the back of the wave crest at the still water level. Further μ is determined from the height of the breaker. Hereby $b/H = 0.64$, $\mu = 0.12$, $a/b = 0.13$ with θ_{max} left as the only free parameter.

In figure 12 the inline force time series from the CFD model is presented. The slamming effect on the force time series is shown by blue shade and the time instant of the snapshot of figure 11 is marked by a red star. The integral of the blue area is the same as the integrated pressure impulse on the cylinder wall. The value of θ_{max} in the model was therefore matched such that the impact force impulse of the CFD model was equal to the wall-integrated pressure impulse in the inline direction. This led to $\theta_{max} = \pi/3$.

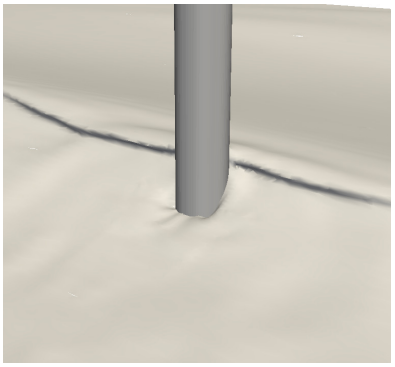

FIGURE 11: Snapshot of the wave breaking on a cylinder from CFD model results.

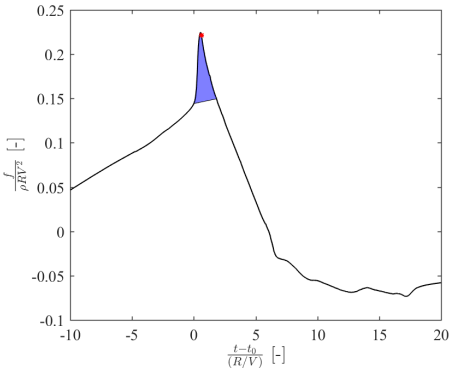

FIGURE 12: Inline force time series from the CFD model. The dashed blue region shows the effect of slamming.

The pressure on the cylinder from just before the impact was subtracted from all the time instants in the CFD results to isolate the impulsive pressures. Then the time integral from the beginning of the impulse until the end was calculated. The resulting pressure impulse is shown in figure 13(a). The largest pressure impulse is observed below $z/H = -0.05$ at $\theta/\theta_{max} = 0$ and the pressure impulse extends down to $z/H = -0.2$. Note that some of the extended effect is caused by the kinematics of the wave itself and not necessarily the slamming impact. It is observed that the pressure impulse decreases to around zero at the limits which shows that the chosen azimuthal limit is sensible.

The result of the pressure impulse model can be seen in figure 13(b). A general good consistency between the model and CFD pressure impulse distribution and magnitude is observed. The pressure impulse is localized in upper layer in both CFD and model results which is linked to the small breaker height ratio. The model result is based on a fit of θ_{max} to match the force impulse. However, since the force impulse is not generally available, the dependency of the total impulsive force to θ_{max} is shown in figure 14. The total impulsive force increases as the azimuthal angle limit increases up until $\pi/2$ where it reaches its maximum. The variation of the pressure impulse relative to θ_{max} is robust and homogeneous. Hence, calibration based on this parameter is possible for similar cases. The total force impulse of the model can be compared to the existing impact models of Goda, Haranaka, and Kitahata 1966 and Wienke and Oumeraci 2005. The force impulse calculated based on these models has about 190% and 100% over prediction respectively.

Summary and future work

Pressure impulse models for a 3D box, axisymmetric impact on a vertical cylinder and three-dimensional wave impact on a vertical cylinder have been derived. The model is formulated in a simplified wedge-shaped geometry

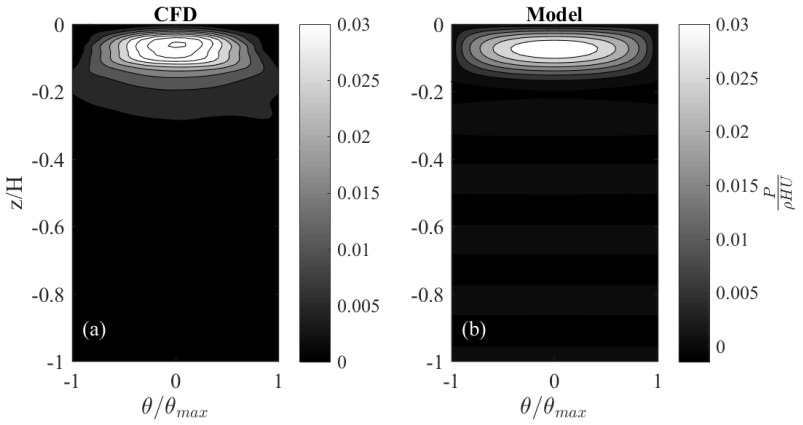

FIGURE 13: Pressure impulse contour plot from impact of a wave on a cylinder from (a) CFD model (b) the suggested model.

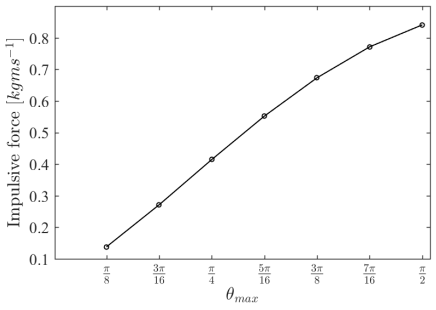

FIGURE 14: Total impulsive force as a function of θ_{max}.

and depends on the normalized crest length, impact zone height, inner radius and maximum impact angle. It is intended for calculation of slamming loads as an extension to standard force models. The parameter space was investigated and linked to the behaviour within the simpler models. We found that the pressure impulse increases with crest length up until an asymptotic limit, which appear to be effective for realistic wave impacts. The impact zone height governs the vertical extent of the pressure impulse distribution. The pressure impulse was further found to increase with inner radius due to the increased wall area and next to decrease due to the diminishing incident momentum. The only parameter that can not immediately be determined from the incident wave geometry is the maximum impact angle. In validation against a numerical wave impact, a value of $\theta = \pi/3$ was chosen through match of the numerical force impulse. This led to an encouraging match of the numerical pressure impulse field and thus provided a first and physically reasonable suggestion for a generic value. For the same wave parameters, the force impulse was over-predicted by 190% and 100% by two established force models. This underlines the models potential for further validation and application in structural load and response calculations.

Acknowledgement

This work was funded by the Innovation Fund Denmark and other partners as part of DeRisk project with grant number 4106-00038B. This support is gratefully acknowledged by the authors.

References

Chatjigeorgiou, Ioannis K., Alexander A. Korobkin, and Mark J. Cooker (2016). "Three-dimensional steep wave impact on a vertical plate with an open rectangular section". In: *Journal of Hydrodynamics* 28.4, pp. 523–533.

Chatjigeorgiou, Ioannis K et al. (2016). "Three-dimensional steep wave impact onto a vertical plate of finite width". In: *31st IWWWFB, 3-6 April, 2016, Plymouth, Michigan, USA*.

Cooker, Mark J. (2013). "A theory for the impact of a wave breaking onto a permeable barrier with jet generation". In: *Journal of Engineering Mathematics* 79.1, pp. 1–12.

Cooker, Mark J. and Howell Peregrine (1995). "Pressure-impulse theory for liquid impact problems". In: *Journal of Fluid Mechanics* 297, p. 193.

Ghadirian, A., H. Bredmose, and M. Dixen (2016). "Breaking phase focused wave group loads on offshore wind turbine monopiles". In: *Journal of Physics: Conference Series* 753.9, p. 092004.

Goda, Yoshimi, Suketo Haranaka, and Masaki Kitahata (1966). *Study on impulsive breaking wave forces on piles*. Tech. rep. 5, pp. 1–30.

Hallowell, S, A T Myers, and S R Arwade (2016). "Variability of breaking wave characteristics and impact loads on offshore wind turbines supported bymonopiles". In: *Wind Energy* 19, pp. 301–312.

Iafrati, A and AA Korobkin (2006). "Breaking wave impact onto vertical wall". In: *Proc. 4th Int. Conf. Hydroelas. Mar. Tech., Wuxi, China, 10–14 September*, pp. 139–148.

Korobkin, A. A. and Š. Malenica (2007). "Steep wave impact onto elastic wall". In: *International Workshop on Water Waves and Floating Bodies*. 1, pp. 2–5.

Korobkin, Alexander (2008). "Non-Classical Boundary Conditions in Water-Impact Problems". In: *IUTAM Symposium on Fluid-Structure Interaction in Ocean Engineering*. Dordrecht: Springer Netherlands, pp. 167–178.

Wagner, Herbert (1932). "Über Stoß- und Gleitvorgänge an der Oberfläche von Flüssigkeiten". In: *Zeitschrift für Angewandte Mathematik und Mechanik* 12.4.

Wienke, J. and H. Oumeraci (2005). "Breaking wave impact force on a vertical and inclined slender pile - Theoretical and large-scale model investigations". In: *Coastal Engineering* 52.5, pp. 435–462.

Technical University of Denmark
Department of Wind Energy
Frederiksborgvej 399
Building 118
4000 Roskilde
Denmark
Telephone 46 77 50 85

info@vindenergi.dtu.dk
www.vindenergi.dtu.dk